



---

**Universidad de Valladolid**

ESCUELA DE INGENIERÍAS INDUSTRIALES

DEPARTAMENTO DE INGENIERÍA QUÍMICA  
Y TECNOLOGÍA DEL MEDIO AMBIENTE

TESIS DOCTORAL:

**SYNTHESIS OF SUPPORTED CATALYSTS OF Co, Ni AND Ru  
USING SUPERCRITICAL CO<sub>2</sub> FOR BIOMASS  
VALORIZATION REACTIONS**

Presentada por Álvaro Sastre Cuadrillero para optar  
al grado de doctor por la Universidad de Valladolid

Dirigida por:

Dra. Ing. Gloria Esther Alonso Sánchez  
Prof. María José Cocero Alonso





---

**Universidad de Valladolid**

ESCUELA DE INGENIERÍAS

DEPARTAMENTO DE INGENIERÍA QUÍMICA  
Y TECNOLOGÍA DEL MEDIO AMBIENTE

TESIS DOCTORAL:

**SYNTHESIS OF SUPPORTED CATALYSTS OF Co, Ni AND Ru  
USING SUPERCRITICAL CO<sub>2</sub> FOR BIOMASS  
VALORIZATION REACTIONS**

Presentada por Álvaro Sastre Cuadrillero para optar al  
grado de doctor por la Universidad de Valladolid

Dirigida por:

Dra. Ing. Gloria Esther Alonso Sánchez  
Prof. María José Cocero Alonso



Memoria para optar al grado de Doctor,

Con Mención Doctor Internacional,

Presentada por el Ingeniero Químico:

Álvaro Sastre Cuadrillero

Valladolid, Junio de 2015



**UNIVERSIDAD DE VALLADOLID**  
**ESCUELA DE INGENIERÍAS INDUSTRIALES**

**Secretaría**

La presente tesis doctoral queda registrada en el folio  
número \_\_\_\_\_ del correspondiente libro de registro  
número \_\_\_\_\_

Valladolid, a \_\_\_\_\_ de \_\_\_\_\_ de 2015

Fdo. El encargado del registro



**Gloria Esther Alonso Sánchez**

Profesora Titular

Departamento de Ingeniería Química y Tecnología del Medio Ambiente

Universidad de Valladolid

y

**María José Cocero Alonso**

Catedrática

Departamento de Ingeniería Química y Tecnología del Medio Ambiente

Universidad de Valladolid

Certifican que:

ÁLVARO SASTRE CUADRILLERO ha realizado bajo su dirección el trabajo "*Syntheis of Supported Catalysts of Co, Ni and Ru using Supercritical CO<sub>2</sub> for Biomass Valorization Reactions*", en el Departamento de Ingeniería Química y Tecnología del Medio Ambiente de la Escuela de Ingenierías Industriales de la Universidad de Valladolid. Considerando que dicho trabajo reúne los requisitos para ser presentado como Tesis Doctoral expresan su conformidad con dicha presentación.

Valladolid, a \_\_\_\_\_ de \_\_\_\_\_ de 2015

Fdo. Gloria Esther Alonso Sánchez

Fdo. María José Cocero Alonso



Reunido el tribunal que ha juzgado la Tesis Doctoral titulada “*Syntheis of Supported Catalysts of (Co, Ni and Ru using Supercritical CO<sub>2</sub> for Biomass Valorization Reactions*” presentada por el Ingeniero Químico Álvaro Sastre Cuadrillero y en cumplimiento con lo establecido por el Real Decreto 99/2011 de 28 de enero de 2011 acuerda conceder por \_\_\_\_\_ la calificación de \_\_\_\_\_.

Valladolid, a \_\_\_\_\_ de \_\_\_\_\_ de 2015

PRESIDENTE

SECRETARIO

1<sup>er</sup> Vocal

2<sup>o</sup> Vocal

3<sup>er</sup> Vocal



*“There is no point in doing something in a  
supercritical fluid just because it’s neat.*

*Using the fluids must have some real advantage”*

---

*Val Krukonis*

*First International Symposium on Supercritical Fluids, 1988*



# INDEX

ABSTRACT .....	19
AIMS .....	23
CHAPTER I. INTRODUCTION .....	25
I.1. Introduction .....	26
I.2. Supercritical Fluids (SCFs) .....	27
I.3. Synthesis of Materials in Supercritical Fluids.....	31
I.4. Supercritical Fluid Deposition (SCFD).....	33
I.5. Metals in Catalysis and their applications .....	36
I.6. The importance of Support.....	37
I.7. References .....	38
CHAPTER II. COBALT-BASED CATALYSTS.....	44
II.1. Introduction.....	45
II.1.1. Cobalt-based Catalysts and their applications.....	45
II.1.2. Deposition of Cobalt using sc-CO <sub>2</sub> .....	47
II.2. Materials.....	48
II.2.1. Organometallic Precursor: CoCp <sub>2</sub> .....	48
II.2.2. Support: MCM-41 .....	48
II.3. Adsorption isotherms of CoCp <sub>2</sub> .....	50
II.3.1. Experimental Set-up for determination of Adsorption Isotherms.....	50
II.3.2. Results and discussions: Adsorption of CoCp <sub>2</sub> on MCM-41 .....	53
II.3.3. Adsorption Isotherms Modeling .....	54
II.3.4. Fittings and discussion .....	55
II.4. Supercritical Fluid Reactive Deposition of CoCp <sub>2</sub> on MCM-41 .....	58
II.4.1. Catalysts Synthesis Batch Device .....	58

II.4.2. Optimization: concentration, temperature and pressure.....	60
II.4.3. Kinetics of the process .....	62
II.4.3.1. Kinetics Model.....	64
II.4.4. Sequential loadings .....	66
II.4.5. Mass transfer limitations .....	66
II.4.6. Conclusions .....	69
II.5. Characterization of Co/MCM-41 catalysts .....	70
II.6. Activity Test: Gasification of Cellulose for Hydrogen production.....	76
II.6.1. Experimental Device.....	77
II.6.2. Thermogravimetric studies on Cellulose pyrolysis.....	78
II.6.3. Gas products analysis .....	79
II.6.4. Kinetics Model.....	83
II.6.5. Results and discussions .....	85
II.7. Conclusions.....	89
II.8. References .....	91
CHAPTER III. NICKEL-BASED CATALYSTS.....	98
III.1. Introduction.....	99
III.1.1. Nickel-based Catalysts and their applications .....	99
III.1.2. Deposition of Nickel using sc-CO <sub>2</sub> .....	101
III.2. Materials .....	102
III.2.1. Organometallic Precursor: NiCp <sub>2</sub> .....	102
III.2.2. Support: MCM-48.....	102
III.3. Adsorption isotherms of NiCp <sub>2</sub> .....	104
III.3.1. Results and discussions: Adsorption of NiCp <sub>2</sub> on MCM-48.....	104
III.3.3. Adsorption Isotherms Modeling .....	105

III.3.4. Fittings and discussion.....	107
III.3.5. Adsorption Kinetics .....	112
III.3.5.1. Adsorption Kinetics of NiCp <sub>2</sub> on MCM-48 .....	114
III.3.6. Adsorption Mechanism.....	115
III.3.6.1. Adsorption Mechanism of NiCp <sub>2</sub> on MCM-48.....	117
III.4. Supercritical Fluid Reactive Deposition of NiCp <sub>2</sub> on MCM-48 .....	120
III.4.1. Procedure of Synthesis.....	120
III.4.2. Results and discussion .....	121
III.5. Characterization of Ni/MCM-48 catalysts.....	123
III.6. Activity Test: Hydrogenation of Glucose for D-Sorbitol production.....	128
III.6.1. Experimental Device.....	128
III.6.2. Results and discussions.....	130
III.7. Conclusions.....	133
III.8. References.....	134
<b>CHAPTER IV. RUTHENIUM-BASED CATALYSTS .....</b>	<b>141</b>
IV.1. Introduction .....	142
IV.1.1. Ruthenium-based Catalysts and their applications.....	142
IV.1.2. Deposition of Ruthenium using sc-CO <sub>2</sub> .....	143
IV.2. Materials .....	145
IV.2.1. Organometallic Precursor: RuCp <sub>2</sub> .....	145
IV.2.2. Support: MCM-48 and activated carbon (AC).....	145
IV.3. Solubility of RuCp <sub>2</sub> in CO <sub>2</sub> .....	146
IV.3.1. Experimental Set-up for solubility measurements.....	146
IV.3.2. Results and discussion .....	149
IV.3.3. Modeling of solubility data of RuCp <sub>2</sub> in CO <sub>2</sub> .....	151

IV.3.3.1. Empirical Methods .....	152
IV.3.3.2. Equation of State (EoS) .....	153
IV.4. Adsorption isotherms of RuCp <sub>2</sub> .....	158
IV.4.1. Results and discussions: Adsorption of RuCp <sub>2</sub> .....	158
IV.4.2 Adsorption Isotherms Modeling: Fittings and discussion .....	161
IV.4.3. Adsorption Kinetics of RuCp <sub>2</sub> .....	169
IV.4.4. Adsorption Mechanism of RuCp <sub>2</sub> .....	172
IV.5. Continuous Supercritical Deposition of RuCp <sub>2</sub> .....	176
IV.4.1. Continuous Set-up for Catalysts Synthesis.....	176
IV.4.2. Results and discussion .....	177
IV.4.3. Kinetics of the continuous process .....	180
IV.6. Characterization of Ru/support catalysts.....	183
IV.7. Activity Test: Hydrolysis of Cellobiose for Glucose production .....	188
IV.7.1. Experimental Device .....	189
IV.7.2. Results and discussions .....	191
IV.8. Conclusions .....	194
IV.9. References .....	196
CONCLUSIONS .....	202
FUTURE WORK .....	206
APPENDIX .....	208
Characterization Techniques .....	209
Conventional Deposition Methods .....	217
About the author .....	218
Resumen (castellano).....	223

# Abstract

## Abstract

The aim of this PhD thesis is to study the stages to synthesize different supported metal catalysts in supercritical medium. It is expected to obtain nanocomposites that can be used to enhance the selectivity in reactions of biomass conversion to produce compounds with high added value.

In Chapter 1, a brief introduction on supercritical fluids, their properties and main uses in the synthesis of materials is presented; and some short notions about catalysis.

Then, after a literature review, it has been decided to start the work in Chapter 2 with the production of cobalt-based catalysts due to its numerous applications and because there was not any previous work in which supercritical technique would be used for its synthesis. Cobaltocene ( $\text{CoCp}_2$ ) has been selected as organometallic precursor owing to its relatively high solubility in  $\text{sc-CO}_2$ , and MCM-41 as support due to its sharp pore distribution, large surface area and thermal stability. To choose the optimal parameters of deposition process, the adsorption isotherm of  $\text{CoCp}_2$  on MCM-41 has been determined, where it can be observed that this system presents low adsorbate-adsorbent interactions with an equilibrium adsorptive capacity around 65 mg/g according to the predictions estimated by the fittings. After that, it can be concluded that deposition of cobaltocene on MCM-41 by a simple exposure of the dissolution of precursor is not enough to prepare these catalysts, being necessary to use the supercritical fluid reactive deposition (SCFRD) to promote the precipitation of metallic particles on the surface of support. This process has been optimized to find the combination of parameters that maximize the adsorption. At the end of this work, it was concluded that it is preferable to operate at 200 °C and 14 MPa during one hour with the precursor and support distributed through the reactor to solve the problems caused by mass transfer limitations. Besides, it has proved that it is possible to achieve high cobalt loadings by means of consecutives depositions (up to 15 %wt in only 3 batches). Then, Co/MCM-41 samples were characterized by different techniques and compared to other ones prepared by conventional synthesis methods, revealing that the catalysts prepared in  $\text{sc-CO}_2$  showed the best metal dispersion on the surface support (~10%) and small particles diameter (between 1 to 9 nm), accessible even inside the pores by reactive molecules. Finally, an activity test was carried out. Catalysts were tested in the gasification of cellulose, increasing the selectivity for hydrogen production from 7% to 30% as a result

of the promotion of tar, as it can be concluded with the fitting of the experimental data by a three-reaction model.

To continue the work, it has been decided to check the versatility and robustness of the supercritical process with a different precursor-support system, although very similar, in Chapter 3. In this sense, nickel-based catalysts from nickelocene ( $\text{NiCp}_2$ ) on MCM-48, other member of the family of MS41 silica mesoporous support, have been synthesized by SCFRD. For this purpose, the adsorption isotherms at  $70^\circ\text{C}$  of  $\text{NiCp}_2$  on MCM-48 have been extensively studied, revealing a completely different behavior. Experimental data have been adjusted by various models, being Toth equation which provided the best fit, and predicting a maximum value of adsorption of nickel around  $130\text{ mg/g}$  at  $70^\circ\text{C}$  and  $14\text{ MPa}$ . In order to have a better understanding of the process, its kinetics has been modeled by pseudo-first and pseudo-second order, in which it can be observed that this adsorption requires times higher than 10 hours. This fact it could be attributed to some diffusional limitation. To corroborate this theory an intraparticle and film-diffusion models have been used to analyze the experimental data and determine the adsorption mechanism. Results resolved that the external mass transport is the rate-controlling step for this system. With this information, it has been decided to use the SCFRD with the same temperature and pressure established as optimal conditional in Chapter 2. Ni/MCM-48 samples with metallic loadings between 2-5 %wt have been synthesized. These catalysts have been also characterized, revealing the existence of nickel oxides homogeneously distributed on the surface of support and BET areas around  $1000\text{ m}^2/\text{g}$ . The employment of high pressure has not modified the original pore structure, unlike catalysts prepared by direct synthesis where the TEM pictures showed irregular surfaces and collapsed pores. Finally, the activity of catalysts were tested in the selective conversion of glucose to sorbitol, reaching conversion of 6%, selectivity higher than 90 % and yields around 5 % in 30 minutes, similar to catalysts synthesized by wet impregnation and improving substantially data obtained by catalysts prepared by direct synthesis.

As conclusion, both in the first case of study about cobalt where the adsorption was practically non-existing, and in this last one about nickel in which the process is very slow, the SCFRD has proven to be a viable technique.

On the other hand, in Chapter 4, a continuous process for the synthesis of catalysts based on the supercritical fluid adsorption has been developed. With this aim, it was necessary to select an appropriate metal-support system, and start its study from the

beginning. First, the solubility of ruthenocene,  $\text{RuCp}_2$ , has been determined at 60 °C and different pressures by cloud point technique in a visual cell. Experimental data have been fitted by Chrastil and Peng-Robinson with good agreement. Results are consistent with data found in literature. Then, the adsorption of  $\text{RuCp}_2$  on two supports with different structure, one mesoporous (MCM-48) and other microporous (activated carbon) has been studied. Both cases have shown good results where the metallic loading in the support increased with the supercritical phase concentration, characteristic of monolayer deposition. Experiments conducted at different pressures (9, 11, 14, 17 and 20 MPa) have been revealed how the process is favored at low pressures. Following a similar analysis carried out in the previous chapter, experimental data have been adjusted by different models, being the three-parameter equations such as Redlich-Peterson or BET correlations which provide the best fit. The study seems to reveal that there is a direct relationship between the controlling step of the process and its kinetics. Although both mechanisms have complex mechanism with different stages involved, in the adsorption on activated carbon the controlling step is mainly the external transport, with a value of saturation limit of 80 mg/g after 10 hours, similar to nickel-based catalysts. On the other hand, the adsorption on MCM-48 is largely governed by pore diffusion, reaching loading up to 15 mg/g in shorter times, around 4 hours. Thanks to this information, ruthenium-based catalysts have been satisfactorily synthesized by supercritical fluid deposition in a continuous process, at 60 °C and 11 MPa. Different values of  $\text{CO}_2$  flows have been tested (15, 30 and 45 g/h) to avoid the problems owing to transfer limitations and fitted by first order model with acceptable average errors. Catalysts have been characterized and proved in the hydrolysis of cellobiose for glucose production. Ru/MCM-48 with metallic loading of 4 %wt have shown the highest yield, improving the process without catalysts from 18% to 48%, with selectivity around 90%. Besides, experiments with different loadings have been carried out, revealing that a higher amount of metal produce the collapse of pores and avoiding the contact with the active centers.

# Aims

## Aims

The main objective of this PhD thesis is the preparation of a family of supported metal catalysts in supercritical CO<sub>2</sub>, for selective and efficient conversion of biomass. Supercritical Fluid Deposition (SCFD) process is used for the deposition of three different metals, Co, Ni and Ru, on different supports, ordered mesoporous silica (MS41) and microporous carbon (AC)

Specifically, this research will focus on the optimization of the process of synthesis, for which several partial targets will be developed:

- Analysis of each stage of deposition process (solubility of the precursor, adsorption isotherms and kinetics).
- Study of the operational conditions, such as pressure, temperature, exposure time... and its effects on the process.
- Physico-chemical characterization of the nanocomposites (morphology, particle size, metal distribution...) by means of different techniques, such as BET, XRD, SEM, TEM...
- Evaluation of the activity and behavior of the catalysts in reactions associated with the valorization of biomass.

# CHAPTER I.

## Introduction

## I.1. Introduction

Chemistry is a branch of physical science that studies the composition, structure, properties and change of matter, including in this definition to humans and their interactions with the environment. Its applications cover a wide range of sectors, such as petrochemistry, cosmetics, pharmaceutical or food industry among others, representing an important economic activity [1].

In this sense, chemistry industry is partly responsible for the environmental problems caused by lot of its processes, as for example the air pollution due to the emissions produced by the combustion of fossil fuels or the burning of urban residues.

For this reason, Green Chemistry, also called sustainable chemistry, emerged in response to this quandary [2, 3]. This new philosophy of research and engineering encourages the design of goods and processes minimizing the use and generation of hazardous substances, but maintaining the quality of the end product. Paul Anastas and John C. Warner [4] coined this term in 1991 based on the concept proposed by Trevor Kletz [5] in 1978, and developed 12 principles which help to explain what the ideology means in practice.

In particular, laws 3 and 5 say that industrial processes should be designed to generate substances little or no dangerous to human health and the environment, and wherever practicable, the use of auxiliary agents (e.g. solvents) which are innocuous, or otherwise, with a low toxicity. According to this dogma, in recent years numerous researchers have been undertaken to replace the solvents employed in many industries by other reaction media such as ionic liquids [6-10] or supercritical fluids [11-15].

In this thesis, supercritical carbon dioxide (sc-CO<sub>2</sub>) is used as solvent that satisfies the principles of Green Chemistry; thus is a low toxic reactive whose critical parameters are easily accessible and therefore can minimize the energy consumption. Moreover, it can also be recycled by re-compress preventing its release into the atmosphere. The combination of all these aspects, together with its good transport properties, as will be discussed later in detail, makes the sc-CO<sub>2</sub> is an excellent resource to develop new technologies.

## I.2. Supercritical Fluids (SCFs)

A supercritical fluid (SCF) is defined as the state of a substance whose pressure and temperature are higher than their critical values [16]. Although strictly, in order to complete this definition is necessary to include other clause, and specify that this pressure must be below than the pressure required to condense it into a solid [17].

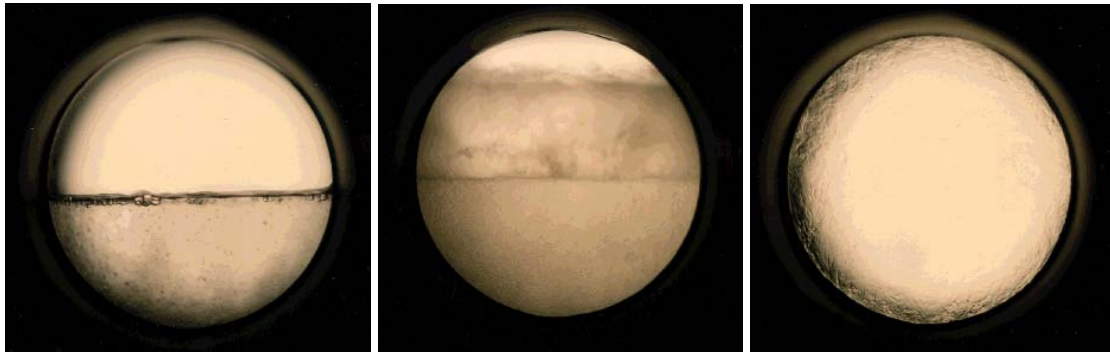


**Figure I-1.** Transition from two phases (gas/liquid, left picture) to only one homogenous phase in supercritical state (right picture) observed through a high-pressure view cell.

In this state, the phase boundary between liquid and gas is interrupted at the critical point, which involves the formation of a single homogenous phase, as shown in the figure I-1. Hence, it is possible for a substance to cross from a liquid state to the gas state without any phase transition by passing through the SC region (Figure I-2)

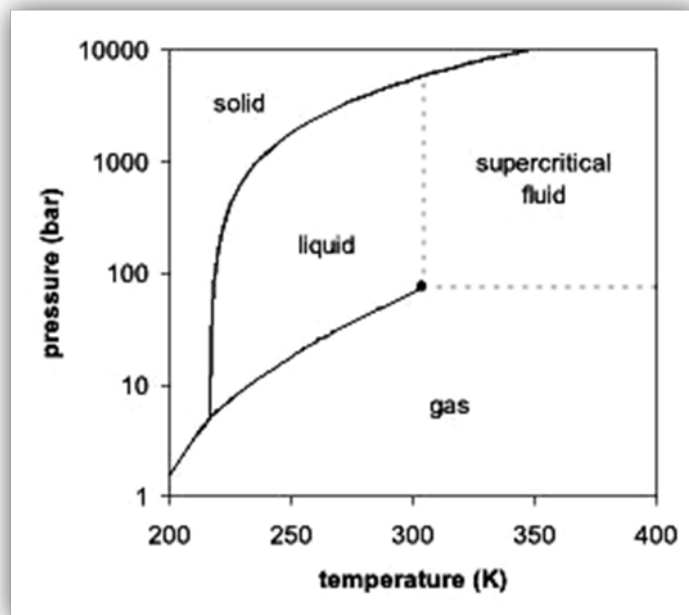


**Figure I-2.** P-T phase diagram of  $\text{CO}_2$ . The critical point is shown as filled circle [18].

## CHAPTER I. Introduction

Table I-1 includes the most commonly employed SCFs for syntheses and chemical reactions, with their critical parameters and physical properties together with its reference to find more detailed data.

**Table I-1.** Critical properties of some frequently used SCFs [18, 19].

<b>SCF</b>	<b>Name</b>	<b>T<sub>C</sub> (°C)</b>	<b>P<sub>C</sub> (bar)</b>	<b>ρ<sub>C</sub> (kg/m<sup>3</sup>)</b>
<b>CO<sub>2</sub></b>	Carbon dioxide	31.1	73.8	466
<b>H<sub>2</sub>O</b>	Water	374.0	220.6	322
<b>N<sub>2</sub>O</b>	Nitrous oxide	36.4	72.5	453
<b>NH<sub>3</sub></b>	Ammonia	132.4	113.2	235
<b>CH<sub>4</sub>O</b>	Methanol	239.5	80.8	273
<b>C<sub>2</sub>H<sub>6</sub></b>	Ethane	32.2	48.7	207
<b>C<sub>3</sub>H<sub>8</sub></b>	Propane	96.7	42.5	220
<b>C<sub>4</sub>H<sub>10</sub></b>	n-butane	152.0	38.0	228
<b>C<sub>5</sub>H<sub>12</sub></b>	n-pentane	196.6	33.7	232
<b>C<sub>6</sub>H<sub>6</sub></b>	Benzene	289.5	49.2	300
<b>SF<sub>6</sub></b>	Sulfur hexafluoride	45.5	37.6	737
<b>Xe</b>	Xenon	16.6	58.3	1099

Among them, sc-CO<sub>2</sub> has been primarily utilized in an industrial scale to replace toxic organic solvents used in the food industry for applications such as extraction of caffeine from coffee beans, hops and spices and tea leaves [20].

The main reason is that sc-CO<sub>2</sub> has a readily accessible at rather low temperatures, avoiding the degradation of thermally labile compounds. Furthermore, it is abundant, inexpensive and nonflammable. Finally, CO<sub>2</sub> is benign and nontoxic, considered as environmentally friendly, that leaves no residue on the treated medium.

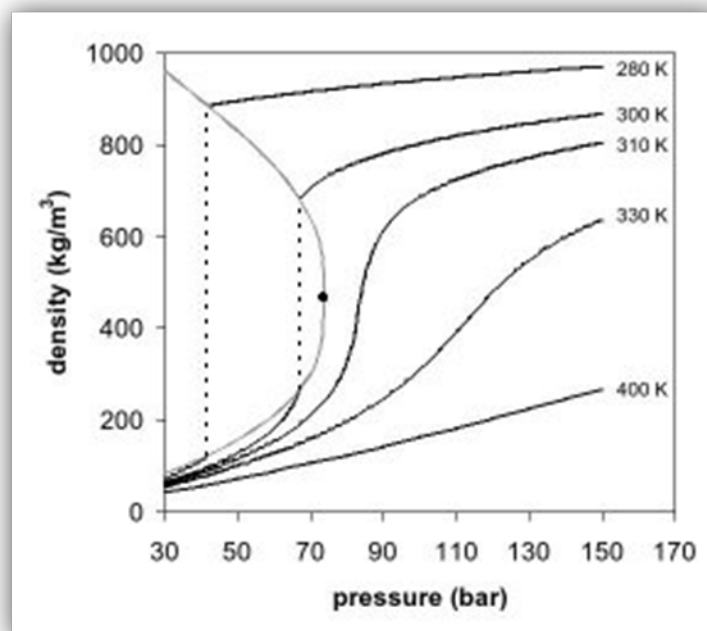
SCFs exhibit properties which in many ways are unique and differ substantially from its corresponding liquid or gaseous state. The properties of SCFs are frequently described as being intermediate between those of a gas and a liquid. Clear examples of this behavior are the density and transport properties as viscosity, diffusivity and thermal activity, as shown in Table I-2 where are collected typical values of these properties for liquid and gas at ambient conditions and for a SCF near the critical point. Although not all properties follow this tendency, as compressibility or heat capacity, for example, those are significantly higher in the “near-critical” region.

**Table I-2.** Comparison of physical properties of gases, liquids and SCFs

Property	Gas	SCF	Liquid
Density ( $\text{kg/m}^3$ )	0.5 – 2.0	200 – 500	500 – 1500
Viscosity ( $\text{mPa}\cdot\text{s}$ )	0.01 – 0.3	0.01 – 0.03	0.2 – 3.0
Diffusivity ( $\text{m}^2/\text{s}$ )	$10^{-5}$	$10^{-7}$	$10^{-9}$
Conductivity ( $\text{W/m}\cdot\text{K}$ )	0.01 – 0.02	0.05 – 1	0.1 – 0.2

SCFs have high densities, even in some cases at very high pressures, exceed to those of liquids. When working with a SCF, it is recommendable to refer to a plot of the dependence of density on pressure and temperature, since the density changes sharply with pressure in the compressible region, as it is shown in the figure I-3. Many of the properties of a SCF are governed primarily by its density bulk, such as its solvating power. Solubility increases with increasing pressure and thus density. Modest changes in either pressure or temperature, especially near to the critical point, can alter its solvating power over a wide range.

The possibility of using SCFs as “tunable solvents” not only for extraction but also for chemical reactions is one of the many interesting features related to their applications in modern synthesis.

**Figure I-3.** Density-pressure diagram for carbon dioxide [21].

On the other hand, the transport properties of SCFs also are modified with small variations in pressure and temperature. In the case of  $\text{CO}_2$ , its viscosity increases by

## CHAPTER I. Introduction

nearly a factor of 5 as the pressure raises from 7.7 to 30 MPa at 308 K. Gas-like viscosities of SCFs are substantially lower than those of conventional organic solvents. This fact enables easier contact between phases and contributes to enhance the mass transfer.

The binary diffusion coefficient ( $D_{12}$ ) of the solute in the SCFs is another important transport property to take into account. Generally, this coefficient  $D_{12}$  is much higher than in liquids, reaching values similar to gas diffusivities. It may translate into enhanced interphase mass transfer rates compared to conventional organic solvents. Besides, higher  $D_{12}$  values also cause higher fluxes inside the pores of solid matrices compared to organic solvents which may be advantageous in various applications such as impregnation of porous materials or regeneration of solid adsorbents.

### I.3. Synthesis of Materials in Supercritical Fluids

Nowadays, the preparation of materials with SCFs has been developed as a new research area of interest, and particularly in the field of nanoparticles. Polymeric materials, inorganic solids and organic compounds with uses as additives, drugs, cosmetic pigments, biomaterials, optics, catalysts or adsorbents, have been prepared with supercritical fluid technologies [22].

In the last decades, the research on particle production in sc-CO<sub>2</sub> has rapidly been growing, developing several methods to produce micro- and nano-particles [23]. Among them, one of the most precipitation process studied and used both an industrial scale and lab scale is the rapid expansion of supercritical solutions, known as RESS. In this method a pressurized solution of rapidly expanded through a nozzle, causing an extremely fast nucleation of the solid solute in a micronized form. Rapid expansion of a supercritical solution into a liquid solvent (RESOLV) is a modification of this technique, in which expansion occurs on a liquid solvent instead of sc-CO<sub>2</sub> in order to prevent the aggregation of the particles [24-28].

However, the SC fluid can also accomplish the function of anti-solvent, emerging new synthesis routes, such as GAS or SAS (Gas or supercritical anti-solvent). In these processes, a batch solution is expanded by mixing it with a supercritical solvent in a high pressure vessel. Due to the dissolution of the compressed gas, the expanded solvent exhibits a decrease of the solvent power and mixture becomes supersaturated, precipitating in the form of nanoparticles [29-31]. In the same way, particles from gas-saturated solutions or PGSS consists in dissolving a supercritical fluid into a solvent followed by a rapid depressurization of this mixture through a nozzle causing the formation of solid particles or liquid droplets, according to the system [32-35].

On the other hand, SC fluids can also act as reaction medium. In this group, the most common technique is the hydrothermal (or solvothermal) synthesis. By this technique, it is possible to synthesize nanoparticles by hydrolysis and dehydration reaction of metal salt solution in sub-critical or supercritical water [36-38] or other solvent [39-41]. One of the latest synthesis methods that have been developed is the SCF's microemulsions, where each droplet of water in sc-CO<sub>2</sub> works as a micro-reactor [42-45].

## CHAPTER I. Introduction

In this way, thanks to the possibility offered by supercritical fluids technology in order to control the size and shape of the products changing its operating conditions, all kinds of materials have been synthesized, such as nanoparticles, powder coatings, fibers, films, core-shell particles and supported nanocomposites.

Besides, this area has been recently combined to the chemistry of organometallic complexes for the manufacture of different composites, metal and metal oxides [46]. In the 90s, several pioneering studies [47-50] were conducted that thereafter led the advancement and development of new processes, which can be summarized in the following fields:

- 1) Use of organotransition metal complexes as homogeneous catalysts for reactions in SCFs and biphasic systems [51-54].
- 2) SCF extraction of heavy metal from various matrices by formation of metallic complexes [55-57].
- 3) Formation of inorganic powders with controlled size distribution by means of decomposition of organometallic complexes in SCFs [58-62].
- 4) Impregnation of polymers with different metal complexes in SCFs, and the subsequent transformation of the metal precursor within such matrices [63-68].
- 5) Incorporation of metallic nanoparticles into inorganic and carbonaceous porous substrates by SCF deposition [69-71].

This PhD work is focused on this last point and may contributed to go in deep in the incorporation of metallic nanoparticles into porous substrates by dissolution of organometallic complexes in sc-CO<sub>2</sub>.

## I.4. Supercritical Fluid Deposition

In recent years the interest towards nanostructured materials has grown tremendously [72-75] due to the advantages of nanoparticles associated with their small size and, therefore, their large surface area, making them very interesting from the standpoint of catalysts [76-80].

In this way, various research studies have been focused on enhancing the diffusion of more voluminous reactive molecules towards the active centers, creating new materials by depositing metal nanoparticles onto mesoporous materials, which have high surface areas and uniform pores structure.

There are several techniques for depositing metals on substrates, as well as preparing films and supported metal nanoparticles, including impregnation, co-precipitation, sol-gel deposition, chemical vapor deposition or microemulsions using organic stabilizing agents. Each one exhibits different advantages and disadvantages; but generally, the main drawback of these methods of synthesis is the control of the particle dimensions, including the size and distribution of particles, as well as the metal content into the matrix of the support. Moreover, the elimination of the surfactant may lead to agglomeration again due to the high temperatures employed and cause structural changes into the catalyst with a significant reduction of the support surface area and consequently, its catalytic activity.

But the main challenge for the development of nanostructured materials is the difficulty of reproducibility, size control and stabilization of nanoscale particles due to their tendency to react and agglomerate; since their properties are closely related to the manufacture or synthesis process.

In that sense, the use of supercritical fluids represents an alternative and a promising method of deposition of metal nanoparticles on the surface of solids and/or inside porous substrates [81-87]. Supercritical fluid deposition (SCFD) is a very simple and environmentally friendly procedure, which consists of the following stages.

Firstly, an organometallic precursor is dissolved by sc-CO<sub>2</sub> under optimal operation conditions (high pressure and moderate temperature) to favor its solubility in the

medium. Meanwhile, the resulting solution is exposing to the porous substrate with its subsequent adsorption onto the matrix of the support. After this impregnation, the metal complex can be converted to its metal form as shown in figure I-4.

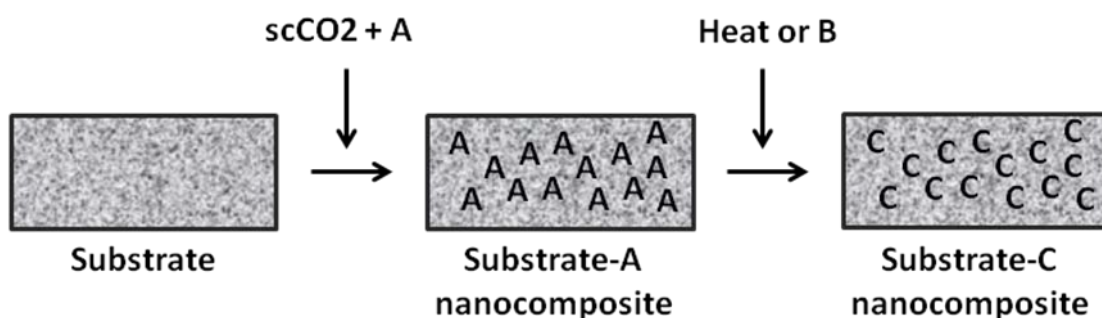


**Figure I-4.** Schematic diagram for SCFD method [88]

(A – organometallic precursor; B – reducing agent; C – metal nanoparticles)

Finally, the system is slowly decompressed, avoiding solvent residues or pore collapse associated with the agglomeration in aqueous catalysts preparation techniques.

The conversion of the adsorbed metal complex into metallic nanoparticles can be carried out by means of different procedures: by heating in an inert or hydrogen atmosphere as a catalyst prepared by conventional methods, or even before depressurization in the supercritical fluid phase.

Supercritical fluid reactive deposition (SCFRD) is used to refer to this last case where the reduction of the metal is included in the process of synthesis [89-91]. This technique is based on promoting the precipitation of metallic nanoparticles and their consequently deposition and growth over the porous, whereas the organic part of the precursor remains dissolved in the  $sc-CO_2$  and is released beside the gas.

For this, it can proceed in two ways: or injecting a reducing agent, such as hydrogen or an alcohol into the solution, or by thermal treatment to lead the breaking down of the precursor. Consequently, this one-pot process to prepare catalyst allows reducing operational times in comparison to other techniques.

SCFRD takes advantages of the unusual physical properties of  $sc-CO_2$ , different from those of ordinary liquids and gases, and easily adjustable with small variations of pressure and/or temperature. Thanks to this fact, density changes dramatically, being able to dissolve a wide range of organic and organometallic compounds compared with conventional liquids solvents. Furthermore, its low viscosity combined with its high

diffusivities enhance mass-transfer characteristics. On the other hand, low surface tension of sc-CO<sub>2</sub>, not only permits better penetration and wetting of pores than conventional solvents, but also avoids the pore collapse and modification of the structure how can occur on certain materials such as silica aerogel with liquid solvents.

## I.5. Metals in catalysis and their applications

Nowadays, the chemical industry converts raw materials or cheap chemicals, such as oil, natural gas, water, metals or minerals, into more than 70,000 different products. For this purpose, it is necessary to concern with pioneering valuable materials and associated techniques, which are often essential to related fields such as nanotechnology, fuel cells, bioengineering or catalysis. In particular, industrial catalysis plays an important role in the chemical industry and research. Catalysts are able to not only speed up reactions by providing an alternative pathway increasing the selective towards some products, but also replace a polluting chemical reaction with a more environmentally friendly alternative. Today, and in the future, catalysts are vital for the chemical industry and the progress of the companies, which pay close attention to the market development. The correct selection of the accurate catalyst can be the key to industrial success, making cheaper and more effective processes.

Focusing on heterogeneous catalysis, this field is in constant development: setting up innovative methods of synthesis and modern techniques of deposition of metals, creating original supports or trying to find out what is the most adequate catalyst for each reaction.

Noble metal based catalytic systems have been reported to exhibit high activities for most of reactions, and they are commonly used in numerous industrial applications. The main problem is that, in spite of acting as an inert in the reaction, with the passage of time they are deactivated and lose activity due to poisoning, fouling, coking... This fact implies the interruption of process operation for either replacement or regeneration of catalysts, losing time and investment.

According this outlook, extensive development and use of catalysts based on non-noble metals, such as Fe, Co or Ni, is considered to be preferred from the industrial standpoint, mostly due to economic reasons.

## I.6. The importance of support

Just as with metals, the choice of a precise support is a key aspect in the design of a catalyst.

The main role of a catalyst support is to affix the active centers, typically small metallic particles or transition metal oxides, which take part in the reaction later. In order to maximize their efficiency, it is crucial to ease the contact between the reactive molecules with the surface atoms of the nanomaterial-based catalysts.

According to this premise, there are great efforts to achieve stable supports with high surface areas where to distribute metallic nanoparticles. This task implies having a solid material capable not only to obtain catalytically active species homogeneously dispersed over the internal surface of the pores, but also they are accessible for reagents.

From the industrial standpoint, in the case of costly materials such as noble metals, small particles with a good distribution are economic necessities since they represent a large surface-to-volume ratio and thus greater catalytic utilization of the metal.

For this reason, maintenance of this dispersion under severe processing conditions is another function of the support, as the separation of the metallic nanoparticles inhibits their agglomeration.

Clearly, the primary function of the support is physical in nature, and effective dispersion is not dependent on any degree of metal-support interaction. However, it has been demonstrated that the morphology, physical and chemical characteristics of the supports have significant effects and that in certain cases the catalytic activities could indeed be influenced by them. Therefore, the support may be inert or participate in the catalytic reactions, for example due to its degree of acidity.

So taking these ideas into account, a large number of porous solid materials has been used as catalyst supports, although typically the most common are various kinds of carbon, alumina and silica.

## I.7. References

1. Alexander H., T., *C&EN's Global Top 50 Chemical Firms for 2014*. Chemical & Engineering News, 2014. **92**(30): p. 10-13.
2. Poliakoff, M., J.M. Fitzpatrick, T.R. Farre, and P.T. Anastas, *Green Chemistry: Science and Politics of Change*. Science, 2002. **297**.
3. Anastas, P.T. and M.M. Kirchhoff, *Origins, Currents Status, and Future Challenges of Green Chemistry*. Accounts of Chemical Research, 2002. **35**(9): p. 686-694.
4. Anastas, P.T. and J.C. Warner, *Green Chemistry Theory and Practice*. Oxford University Press, 1998.
5. Kletz, T.A., *What You Don't Have, Can't Leak*. Chemistry and Industry, 1978: p. 287-292.
6. Yang, Z. and W. Pan, *Ionic liquids: Green solvents for nonaqueous biocatalysis*. Enzyme and Microbial Technology, 2005. **37**(1): p. 19-28.
7. Cho, C.-W., Y.-C. Jeon, T.P.T. Pham, K. Vijayaraghavan, and Y.-S. Yun, *The ecotoxicity of ionic liquids and traditional organic solvents on microalga *Selenastrum capricornutum**. Ecotoxicology and Environmental Safety, 2008. **71**(1): p. 166-171.
8. Zhu, P., Y. Chen, L.Y. Wang, and M. Zhou, *Treatment of waste printed circuit board by green solvent using ionic liquid*. Waste Management, 2012. **32**(10): p. 1914-1918.
9. Dharaskar, S.A., K.L. Wasewar, M.N. Varma, D.Z. Shende, and C.K. Yoo, *Ionic Liquids: - The Novel Solvent for Removal of Dibenzothiophene from Liquid Fuel*. Procedia Engineering, 2013. **51**(0): p. 314-317.
10. Yan, N. and P.J. Dyson, *Solvents and Ionic Liquids*, in *Reference Module in Chemistry, Molecular Sciences and Chemical Engineering*. 2013, Elsevier.
11. Nalawade, S.P., F. Picchioni, and L.P.B.M. Janssen, *Supercritical carbon dioxide as a green solvent for processing polymer melts: Processing aspects and applications*. Progress in Polymer Science, 2006. **31**(1): p. 19-43.
12. Ramsey, E., Q. Sun, Z. Zhang, C. Zhang, and W. Gou, *Mini-Review: Green sustainable processes using supercritical fluid carbon dioxide*. Journal of Environmental Sciences, 2009. **21**(6): p. 720-726.
13. Machida, H., M. Takesue, and R.L. Smith Jr, *Green chemical processes with supercritical fluids: Properties, materials, separations and energy*. The Journal of Supercritical Fluids, 2011. **60**(0): p. 2-15.
14. de Melo, M.M.R., A.J.D. Silvestre, and C.M. Silva, *Supercritical fluid extraction of vegetable matrices: Applications, trends and future perspectives of a convincing green technology*. The Journal of Supercritical Fluids, 2014. **92**(0): p. 115-176.
15. Shirai, M., M. Osada, A. Yamaguchi, N. Hiyoshi, and O. Sato, *Chapter 15 - Utilization of Supercritical Fluid for Catalytic Thermochemical Conversions of Woody-Biomass Related Compounds*, in *Recent Advances in Thermo-Chemical Conversion of Biomass*, A.P.B.S.K. Sukumaran, Editor. 2015, Elsevier: Boston. p. 437-453.
16. McNaught, A.D. and A. Wilkinson, *IUPAC, Compendium of Chemical Terminology, the "Gold Book"*. 2006, Blackwell Scientific Publications, Oxford.

17. Jessop, P.G. and W. Leitner, *Supercritical Fluids as Media for Chemical Reactions*, in *Chemical Synthesis Using Supercritical Fluids*. 2007, Wiley-VCH Verlag GmbH. p. 1-36.
18. Bridgman, P.W., *Change of Phase under Pressure. I. The Phase Diagram of Eleven Substances with Especial Reference to The Melting Curve*. Physical Review, 1914. **3**(3): p. 153-203.
19. Angus, S., B. Armstrong, and K.M. Reuck, *International Thermodynamic Tables of the Fluid State*, ed. I.c.d. series. 1971, London, Butterworths.
20. Brunner, G., *Supercritical fluids: technology and application to food processing*. Journal of Food Engineering, 2005. **67**(1–2): p. 21-33.
21. Angus, S., B. Armstrong, and K.M. de Reuck, *International Thermodynamic Tables of the Fluid State - 3: Carbon Dioxide*. 1976.
22. Knez, Ž., E. Markočič, M. Leitgeb, M. Primožič, M. Knez Hrnčič, and M. Škerget, *Industrial applications of supercritical fluids: A review*. Energy, 2014. **77**(0): p. 235-243.
23. Jung, J. and M. Perrut, *Particle design using supercritical fluids: Literature and patent survey*. Journal of Supercritical Fluids, 2001. **20**: p. 179-219.
24. Huang, Z., G.-B. Sun, Y.C. Chiew, and S. Kawi, *Formation of ultrafine aspirin particles through rapid expansion of supercritical solutions (RESS)*. Powder Technology, 2005. **160**(2): p. 127-134.
25. Türk, M. and D. Bolten, *Formation of submicron poorly water-soluble drugs by rapid expansion of supercritical solution (RESS): Results for Naproxen*. The Journal of Supercritical Fluids, 2010. **55**(2): p. 778-785.
26. Ovaskainen, L., S. Chigome, N.A. Birkin, S.M. Howdle, N. Torto, L. Wågberg, and C. Turner, *Superhydrophobic polymeric coatings produced by rapid expansion of supercritical solutions combined with electrostatic deposition (RESS-ED)*. The Journal of Supercritical Fluids, 2014. **95**(0): p. 610-617.
27. Baseri, H. and M.N. Lotfollahi, *Formation of gemfibrozil with narrow particle size distribution via rapid expansion of supercritical solution process (RESS)*. Powder Technology, 2013. **235**(0): p. 677-684.
28. Keshmiri, K., A. Vatanara, O. Tavakoli, and N. Manafi, *Production of ultrafine clobetasol propionate via rapid expansion of supercritical solution (RESS): Full factorial approach*. The Journal of Supercritical Fluids, 2015. **101**(0): p. 176-183.
29. Esfandiari, N., *Production of micro and nano particles of pharmaceutical by supercritical carbon dioxide*. The Journal of Supercritical Fluids, 2015. **100**(0): p. 129-141.
30. Wang, H., H. Jiang, L. Kuang, and M. Zhang, *Synthesis of highly dispersed MnO<sub>x</sub>-CeO<sub>2</sub> nanospheres by surfactant-assisted supercritical anti-solvent (SAS) technique: The important role of the surfactant*. The Journal of Supercritical Fluids, 2014. **92**(0): p. 84-92.
31. Adeli, E., *A comparative evaluation between utilizing SAS supercritical fluid technique and solvent evaporation method in preparation of Azithromycin solid dispersions for dissolution rate enhancement*. The Journal of Supercritical Fluids, 2014. **87**(0): p. 9-21.
32. Cocero, M.J., Á. Martín, F. Mattea, and S. Varona, *Encapsulation and co-precipitation processes with supercritical fluids: Fundamentals and applications*. The Journal of Supercritical Fluids, 2009. **47**(3): p. 546-555.

33. Varona, S., S. Kareth, Á. Martín, and M.J. Cocero, *Formulation of lavandin essential oil with biopolymers by PGSS for application as biocide in ecological agriculture*. The Journal of Supercritical Fluids, 2010. **54**(3): p. 369-377.
34. Pestieau, A., F. Krier, P. Lebrun, A. Brouwers, B. Streel, and B. Evrard, *Optimization of a PGSS (particles from gas saturated solutions) process for a fenofibrate lipid-based solid dispersion formulation*. International Journal of Pharmaceutics, 2015. **485**(1–2): p. 295-305.
35. Bochon, I., S. Kareth, A. Kilzer, and M. Petermann, *Synthesis and powder generation of powder coatings using supercritical carbon dioxide*. The Journal of Supercritical Fluids, 2015. **96**(0): p. 324-333.
36. Ma, C.Y., J.J. Liu, Y. Zhang, and X.Z. Wang, *Simulation for scale-up of a confined jet mixer for continuous hydrothermal flow synthesis of nanomaterials*. The Journal of Supercritical Fluids, 2015. **98**(0): p. 211-221.
37. Zhu, K. and G. Hu, *Supercritical hydrothermal synthesis of titanium dioxide nanostructures with controlled phase and morphology*. The Journal of Supercritical Fluids, 2014. **94**(0): p. 165-173.
38. Kawasaki, S.-I., K. Sue, R. Ookawara, Y. Wakashima, A. Suzuki, Y. Hakuta, and K. Arai, *Engineering study of continuous supercritical hydrothermal method using a T-shaped mixer: Experimental synthesis of NiO nanoparticles and CFD simulation*. The Journal of Supercritical Fluids, 2010. **54**(1): p. 96-102.
39. Inoue, M., *Chapter 11.1.4 - Solvothermal Synthesis of Metal Oxides*, in *Handbook of Advanced Ceramics (Second Edition)*, S. Somiya, Editor. 2013, Academic Press: Oxford. p. 927-948.
40. Wang, M., C. Chen, B. Zhao, Q. Zeng, and D. He, *Solvothermal synthesis of nanostructured TiO<sub>2</sub> photocatalyst in supercritical CO<sub>2</sub> fluids*. Materials Letters, 2013. **109**(0): p. 104-107.
41. Leng, Y., W. Wang, L. Zhang, F. Zabihi, and Y. Zhao, *Fabrication and photocatalytical enhancement of ZnO-graphene hybrid using a continuous solvothermal technique*. The Journal of Supercritical Fluids, 2014. **91**(0): p. 61-67.
42. Malik, M.A., M.Y. Wani, and M.A. Hashim, *Microemulsion method: A novel route to synthesize organic and inorganic nanomaterials: 1st Nano Update*. Arabian Journal of Chemistry, 2012. **5**(4): p. 397-417.
43. Blattner, C., M. Zoumpantioti, J. Kröner, G. Schmeer, A. Xenakis, and W. Kunz, *Biocatalysis using lipase encapsulated in microemulsion-based organogels in supercritical carbon dioxide*. The Journal of Supercritical Fluids, 2006. **36**(3): p. 182-193.
44. Shimizu, R., A. Nibe, K. Sawada, Y. Enokida, and I. Yamamoto, *Preparation of hydrophobic platinum catalysts using a water-in-CO<sub>2</sub> microemulsion*. The Journal of Supercritical Fluids, 2008. **44**(1): p. 109-114.
45. Lu, L. and X. An, *Silver nanoparticles synthesis using H<sub>2</sub> as reducing agent in toluene–supercritical CO<sub>2</sub> microemulsion*. The Journal of Supercritical Fluids, 2015. **99**(0): p. 29-37.
46. Darr, J.A. and M. Poliakoff, *New Directions in Inorganic and Metal-Organic Coordination Chemistry in Supercritical Fluids*. Chemical Reviews, 1999. **99**(2): p. 495-542.
47. Wenclawiak, B. and F. Bickmann, *Fluid and supercritical CO<sub>2</sub> as eluent in metal chelate chromatography*. Analytical Chemistry, 1984. **319**: p. 305.
48. Banister, J.A., M.W. George, S. Grubert, S.M. Howdle, M. Jobling, F.P.A. Johnson, S.L. Morrison, M. Poliakoff, U. Schubert, and J.R. Westwell,

- Organometallic photochemistry in supercritical fluids: Reactions of cyclopentadienyl carbonyl and phosphine carbonyl complexes of manganese with dinitrogen.* Journal of Organometallic Chemistry, 1994. **484**(1–2): p. 129-135.
49. Lin, Y., N.G. Smart, and C.M. Wai, *Supercritical fluid extraction and chromatography of metal chelates and organometallic compounds.* TrAC Trends in Analytical Chemistry, 1995. **14**(3): p. 123-133.
50. Bayona, J.M., 18. *Development of supercritical fluid extraction procedures for the determination of organotin compounds in sediment,* in *Techniques and Instrumentation in Analytical Chemistry*, E.A.M. Ph. Quevauviller and B. Griepink, Editors. 1995, Elsevier. p. 465-487.
51. Rathke, J.W., R.J. Klingler, and T.R. Krause, *Propylene hydroformylation in supercritical carbon dioxide.* Organometallics, 1991. **10**: p. 1350-1355.
52. Dharmidhikari, S. and M.A. Abraham, *Rhodium supported on activated carbon as a heterogeneous catalyst for hydroformylation of propylene in supercritical carbon dioxide.* The Journal of Supercritical Fluids, 2000. **18**(1): p. 1-10.
53. Bektesevic, S., A.M. Kleman, A.E. Marteel-Parrish, and M.A. Abraham, *Hydroformylation in supercritical carbon dioxide: Catalysis and benign solvents.* The Journal of Supercritical Fluids, 2006. **38**(2): p. 232-241.
54. Koeken, A.C.J., S.J.M. de Bakker, H.M. Costerus, L.J.P. van den Broeke, B.-J. Deelman, and J.T.F. Keurentjes, *Evaluation of pressure and correlation to reaction rates during homogeneously catalyzed hydroformylation in supercritical carbon dioxide.* The Journal of Supercritical Fluids, 2008. **46**(1): p. 47-56.
55. Laintz, K.E., C.M. Wai, C.R. Yonker, and R.D. Smith, *Extraction of metal ions from liquid and solid materials by supercritical carbon dioxide.* Analytical Chemistry, 1992. **64**: p. 28-75.
56. Liang, M.-T., R.-C. Liang, C.-H. Lin, P.-J. Hsu, L.-Y. Wu, H.-F. Chen, Y.-W. Wu, and W.-C. Lee, *Metal extraction of a spiked solid with supercritical carbon dioxide.* The Journal of Supercritical Fluids, 2013. **79**(0): p. 324-329.
57. Erkey, C., *Supercritical carbon dioxide extraction of metals from aqueous solutions: a review.* The Journal of Supercritical Fluids, 2000. **17**(3): p. 259-287.
58. Reverchon, E. and R. Adami, *Nanomaterials and supercritical fluids.* The Journal of Supercritical Fluids, 2006. **37**(1): p. 1-22.
59. Shah, P.S., S. Husain, K.P. Johnston, and B.A. Korgel, *Nanocrystal arrested precipitation in supercritical carbon dioxide.* Journal of Physical Chemistry, 2001. **105**: p. 9433-9440.
60. Meziani, M.J., P. Pathak, F. Beacham, L.F. Allard, and Y.-P. Sun, *Nanoparticle formation in rapid expansion of water-in-supercritical carbon dioxide microemulsion into liquid solution.* The Journal of Supercritical Fluids, 2005. **34**(1): p. 91-97.
61. Haldorai, Y., J.-J. Shim, and K.T. Lim, *Synthesis of polymer-inorganic filler nanocomposites in supercritical CO<sub>2</sub>.* The Journal of Supercritical Fluids, 2012. **71**(0): p. 45-63.
62. Aymonier, C., A. Loppinet-Serani, H. Reverón, Y. Garrabos, and F. Cansell, *Review of supercritical fluids in inorganic materials science.* The Journal of Supercritical Fluids, 2006. **38**(2): p. 242-251.
63. Higginbotham, C.L., J.G.L. Yons, and J.E. Kennedy, 13 - *Polymer processing using supercritical fluids,* in *Advances in Polymer Processing*, S. Thomas and Y. Weimin, Editors. 2009, Woodhead Publishing. p. 384-401.

64. Hussain, Y.A. and C.S. Grant, *Ibuprofen impregnation into submicron polymeric films in supercritical carbon dioxide*. The Journal of Supercritical Fluids, 2012. **71**(0): p. 127-135.
65. Cooper, A.I., S.G. Kazarian, and M. Poliakoff, *Supercritical fluid impregnation of polyethylene films, a new approach to studying equilibria in matrices; the hydrogen bonding of fluoroalcohols to  $(\eta^5\text{-C}_5\text{Me}_5)\text{Ir}(\text{CO})_2$  and the effect on C-H activation*. Chemical Physics Letters, 1993. **206**(1-4): p. 175-180.
66. Tomasko, D.L., X. Han, D. Liu, and W. Gao, *Supercritical fluid applications in polymer nanocomposites*. Current Opinion in Solid State and Materials Science, 2003. **7**(4-5): p. 407-412.
67. Watkins, J.J. and T.J. McCarthy, *Polymer/metal nanocomposite synthesis in supercritical CO<sub>2</sub>*. Chemistry of Materials, 1995. **7**: p. 1991-1994.
68. Bozbağ, S.E. and C. Erkey, *Supercritical deposition: Current status and perspectives for the preparation of supported metal nanostructures*. The Journal of Supercritical Fluids, 2015. **96**(0): p. 298-312.
69. Erkey, C., *Preparation of metallic supported nanoparticles and films using supercritical fluid deposition*. The Journal of Supercritical Fluids, 2009. **47**(3): p. 517-522.
70. Caputo, G., I. De Marco, and E. Reverchon, *Silica aerogel-metal composites produced by supercritical adsorption*. The Journal of Supercritical Fluids, 2010. **54**(2): p. 243-249.
71. Aspromonte, S.G., Á. Sastre, A.V. Boix, M.J. Cocero, and E. Alonso, *Cobalt oxide nanoparticles on mesoporous MCM-41 and Al-MCM-41 by supercritical CO<sub>2</sub> deposition*. Microporous and Mesoporous Materials, 2012. **148**(1): p. 53-61.
72. Alonso, E., I. Montequi, S. Lucas, and M.J. Cocero, *Synthesis of titanium oxide particles in supercritical CO<sub>2</sub>: Effect of operational variables in the characteristics of the final product*. The Journal of Supercritical Fluids, 2007. **39**(3): p. 453-461.
73. Alonso, E., I. Montequi, and M.J. Cocero, *Effect of synthesis conditions on photocatalytic activity of TiO<sub>2</sub> powders synthesized in supercritical CO<sub>2</sub>*. The Journal of Supercritical Fluids, 2009. **49**(2): p. 233-238.
74. Bozbag, S.E., D. Sanli, and C. Erkey, *Synthesis of nanostructures materials using supercritical CO<sub>2</sub>: physical transformations*. Journal of Material Sciences, 2012. **47**: p. 2995-3025.
75. Bozbag, S.E., D. Sanli, and C. Erkey, *Synthesis of nanostructures materials using supercritical CO<sub>2</sub>: chemical transformations*. Journal of Material Sciences, 2012. **47**: p. 3469-3492.
76. Sinha Ray, S., *16 - Applications, environmental impact and future development of environmentally friendly polymer nanocomposites (EFPNCs)*, in *Environmentally Friendly Polymer Nanocomposites*, S.S. Ray, Editor. 2013, Woodhead Publishing. p. 467-477.
77. Fitzgerald, G., J. DeJoannis, and M. Meunier, *1 - Multiscale modeling of nanomaterials: recent developments and future prospects*, in *Modeling, Characterization, and Production of Nanomaterials*, V.K.T. Zhang, Editor. 2015, Woodhead Publishing. p. 3-53.
78. Pereira, S.R. and M.C. Coelho, *Can nanomaterials be a solution for application on alternative vehicles? – A review paper on life cycle assessment and risk analysis*. International Journal of Hydrogen Energy, 2015. **40**(14): p. 4969-4979.

79. Jiang, K. and A.O. Pinchuk, *Noble Metal Nanomaterials: Synthetic Routes, Fundamental Properties, and Promising Applications*, in *Solid State Physics*. 2015, Academic Press.
80. Wu, R., K. Zhou, C.Y. Yue, J. Wei, and Y. Pan, *Recent progress in synthesis, properties and potential applications of SiC nanomaterials*. *Progress in Materials Science*, 2015. **72**(0): p. 1-60.
81. Zhang, Y. and C. Erkey, *Preparation of supported metallic nanoparticles using supercritical fluids: A review*. *The Journal of Supercritical Fluids*, 2006. **38**(2): p. 252-267.
82. Yen, C.H., H.W. Lin, T.D. Phan, and C.S. Tan, *Chemical fluid deposition of monometallic and bimetallic nanoparticles on ordered mesoporous silica as hydrogenation catalysts*. *J Nanosci Nanotechnol*, 2011. **11**(3): p. 2465-9.
83. Cangül, B., L.C. Zhang, M. Aindow, and C. Erkey, *Preparation of carbon black supported Pd, Pt and Pd–Pt nanoparticles using supercritical CO<sub>2</sub> deposition*. *The Journal of Supercritical Fluids*, 2009. **50**(1): p. 82-90.
84. Garrido, E., C. Aymonier, L. Roiban, O. Ersen, C. Labrugère, P. Gaillard, and M. Lamirand-Majimel, *Noble metals supported on carbon nanotubes using supercritical fluids for the preparation of composite materials: A look at the interface*. *The Journal of Supercritical Fluids*, 2015. **101**(0): p. 110-116.
85. Bozbag, S.E., L.C. Zhang, M. Aindow, and C. Erkey, *Carbon aerogel supported nickel nanoparticles and nanorods using supercritical deposition*. *The Journal of Supercritical Fluids*, 2012. **66**(0): p. 265-273.
86. Morère, J., M.J. Tenorio, M.J. Torralvo, C. Pando, J.A.R. Renuncio, and A. Cabañas, *Deposition of Pd into mesoporous silica SBA-15 using supercritical carbon dioxide*. *The Journal of Supercritical Fluids*, 2011. **56**(2): p. 213-222.
87. Hunt, A.J., V.L. Budarin, J.W. Comerford, H.L. Parker, V.K. Lazarov, S.W. Breeden, D.J. Macquarrie, and J.H. Clark, *Deposition of palladium nanoparticles in SBA-15 templated silica using supercritical carbon dioxide*. *Materials Letters*, 2014. **116**(0): p. 408-411.
88. Erkey, C., *Chapter 5 - Synthesis of Nanostructured Composites of Metals*, in *Supercritical Fluid Science and Technology*, E. Can, Editor. 2011, Elsevier. p. 79-120.
89. Sanli, D. and C. Erkey, *Effect of polymer molecular weight and deposition temperature on the properties of silica aerogel/hydroxy-terminated poly(dimethylsiloxane) nanocomposites prepared by reactive supercritical deposition*. *The Journal of Supercritical Fluids*, 2015.
90. Wolff, S., M. Crone, T. Muller, M. Enders, S. Bräse, and M. Türk, *Preparation of supported Pt nanoparticles by supercritical fluid reactive deposition: Influence of precursor, substrate and pressure on product properties*. *The Journal of Supercritical Fluids*, 2014. **95**(0): p. 588-596.
91. Müller, S. and M. Türk, *Production of supported gold and gold–silver nanoparticles by supercritical fluid reactive deposition: Effect of substrate properties*. *The Journal of Supercritical Fluids*, 2015. **96**(0): p. 287-297.

# CHAPTER II.

## Cobalt-based Catalysts

## II.1. Introduction

### II.1.1. Cobalt-based Catalysts and their applications

Cobalt is one of the most deeply investigated transition metals for heterogeneous catalytic applications. In the form of supported single element or alloys, cobalt is an interesting active metal for the catalysis of several reactions.

Only in the petrochemical and plastic industries, where cobalt is used as both a hetero and homogeneous catalyst, account for 2,700 tons of cobalt (metal) per year.

Extended use of cobalt as catalyst is given in refineries, in the hydro-treating and desulphurisation of oil and gas to rid petroleum of sulfur impurities that interfere with the refining of liquid fuels.

The second major use of several cobalt compounds is the production of terephthalate acid (TPA) and di-methylterephthalate (DMT), used to manufacture resin for plastic bottles and also to make new ultra strong plastics for different applications. Moreover, the cobalt catalysts used in this field, known as cobalt soap, is also used in paints, varnishes and inks as “drying agents” through the oxidation drying oils and to improve the adhesion of steel to rubber in steel-belted radial tires.

The other large cobalt use is the hydroformylation where the end products are alcohols and aldehydes for plastics and detergent manufacture. In this case, cobalt can be introduced to the system as metal, oxide, hydroxide or as an inorganic salts, depend on the species involved in the reaction.

On the other hand, abundant literature has reported how cobalt-based catalysts can be applied in a wide variety of reactions with significant industrial interest. Recent studies suggested that cobalt-based catalysts supported on a wide range of metal oxide, such as zirconia, ceria, magnesia or alumina, provide similar activity to noble metal catalyst in the C-H and C-C bond cleavage [1, 2], even at low temperature [3, 4], useful for steam reforming process (SR) [1-8] for the generation of hydrogen-rich synthesis gas from light carbohydrates. Llorca et al. [9] reported the reaction selectivity increased in the order:  $\text{Co} >> \text{Ni} > \text{Rh} > \text{Pt} \sim \text{Ru} \sim \text{Cu}$  supported on  $\gamma\text{-Al}_2\text{O}_3$  from ethanol at 673K. Besides, it

## CHAPTER II. Cobalt-based Catalysts

has been demonstrated that cobalt reducibility, dispersion and interaction with support have important effects on the catalysts performance, playing an important role in the stability and selectivity. In order to improve its efficiency, promoted cobalt and several alloys with other metals such as Ni [10-12], Ru [7], Fe [13, 14] or Cu [14] are also under investigation.

But most research focuses on develop novel catalysts for Fischer-Tropsch synthesis (FTS) [15-25]. This reaction is one of the most efficient routes to produce hydrocarbon mixtures from syngas ( $\text{CO}_2$  and  $\text{H}_2$ ) derived from coal, natural gas or biomass, used for making chemicals and transportation fuels. Literature data reveal that cobalt-based catalysts are advantageous to the practical application due to the relatively high selectivity to long-chain paraffin, strong resistance toward deactivation, low activity for the competitive water-gas shift reaction and lower price than other choices. It was found that the FTS performance of catalysts is significantly governed by the type and structure of the support and thereby influenced dispersion of metal sites ( $\text{Co}^0$ ) and degree of reducibility, both of which are considered to be related to the nature of the support employed. According to this fact, various strategies have been investigated last years.

It is known that the dispersion of active cobalt on the surface of support requires some interaction between metal and support, since it can stabilize the catalyst against aggregation of active cobalt and deactivation. In order to achieve a high density of surface-active sites, different supports, such as titania, magnesia or zeolites, have been studies, even silica supports with mesoporous structure (MCM-41 and SBA-15) [16, 24, 25] and novel carbon nano-structured materials (CNFs, MWCNTs and CSc) [15, 22].

However, strong interaction with support also could decrease its reducibility creating non-reducible cobalt species, such as  $\text{CoAl}_2\text{O}_4$  and  $\text{CoTiO}_3$ . For this reason, some noble metal promoters, such as Ru, Pt or Re [18, 21], have been employed not only to enhance the reduction of cobalt oxide, but also inhibited carbon deposition during FTS.

Although these are the most increasing processes, there are other examples in which are getting promising developments recent years.

Unsupported bulk metal particles and several cobalt-based catalysts have exhibited good activity in ammonia synthesis [26, 27], improving their general catalyst properties,

mainly their thermostability with the additions of some promoters like cerium or barium.

Other field in which exists a growing interest is about how to eliminate the emission of  $\text{NO}_x$  from flue gases by selective catalytic reduction. Some studies [28, 29] have reported how the activity in the abatement of this kind of compounds with cobalt-based catalysts supported over zeolites, like MFI or FER, increased linearly with the metallic loading, and discuss about the role of Brønsted acid sites in presence of cobalt.

In this same sense, extensive efforts have been made to develop new cobalt-based oxide combustion catalysts in order to reduce the concentration of volatile organic compounds (VOCs) in the emission to the atmosphere mainly from industry, transports and residential/service sector [30-32]. Up to now, cobalt oxides such as  $\text{Co}_2\text{O}_3$  and  $\text{Co}_3\text{O}_4$  were reported to exhibit efficient catalytic performance for the oxidation of VOCs at low temperatures, resulting in considerable environmental and economic benefits in comparison to the traditional thermal oxidation.

### II.1.2. Deposition of cobalt using sc- $\text{CO}_2$

Up to our knowledge, there is only one published work about the SCFD of cobalt, that by Hunde and Watkins [33]. They reported the deposition of Co and Ni films directly onto a native oxide of Si wafers and onto TaN and TiN films supported on Si wafers, without the need of a catalytic layer, by  $\text{H}_2$  reduction of cobaltocene ( $\text{CoCp}_2$ ). For this deposition, reduction temperature of cobaltocene was varied in the range 285-320 °C and the pressure was modified between 22.0 MPa and 26.0 MPa. No significant deposition was observed below 280 °C and the operational times of the two steps were not varied.

## II.2. Materials

### II.2.1. Organometallic Precursor: CoCp<sub>2</sub>

Cobalt (II) bis-( $\eta^5$ -cyclopentadienyl), also known as cobaltocene (CoCp<sub>2</sub>) has been used as cobalt precursor in the present work because, it is known to be highly soluble in scCO<sub>2</sub> [34], and it has been used in the Co deposition of high purity thin films directly on silicon oxide [33].

CoCp<sub>2</sub> was provided by Sigma Aldrich and used as received.

### II.2.2. Support: MCM-41

MCM-41 (Mobil Composition of Matter N° 41) is the most popular mesoporous ordered silica material developed by Mobil Oil Corporation, with a hierarchical structure from a family of silicate and aluminosilicate solids.

This material consists of a regular arrangement of cylindrical mesopores which form a one-dimensional pore system. Its growing popularity is due to its sharp pore distribution (with diameter between 2 and 6.5 nm), and hence to its large surface area (1200 – 1500 m<sup>2</sup>/g) and pore volume. Moreover, its pore diameter can be easily adjusted at the time of its synthesis.

Spherical MCM-41 materials have been synthesized following the literature procedure reported by Szegedi et al. [35].

In this process, 2 g of n-hexadecyltrimethylammonium-bromide (C<sub>16</sub>TMABr, Sigma Aldrich) is dissolved in 42 ml of de-ionized water and mixed with 48 ml of absolute ethanol. 13 ml of aqueous ammonia solution (29 w/w %) is added to this clear solution and stirred for 15 min. Under uninterrupted stirring 4 ml of tetraethylorthosilicate (TEOS, 98% GC, Sigma Aldrich) is added drop-wise in a couple of minutes. Finishing the addition of TEOS the gel formation immediately begins. The resulting gel having the molar composition of 1 TEOS:0.3 C<sub>16</sub>TMABr:11 NH<sub>3</sub>:144 H<sub>2</sub>O:58 EtOH is stirred for 2 h and aged for 20 h at 35 °C temperature.

The white precipitate is filtered and washed several times until neutral pH is reached. Finally, the mixture is aged at 100 °C without stirring for a further 12-24 h. Template removal is carried out by heating the samples up to 600 °C at a heating rate of 2 °C/min,

followed by isothermal treatment at the same temperature for 6 h. This preparation method is represented in figure II-1.

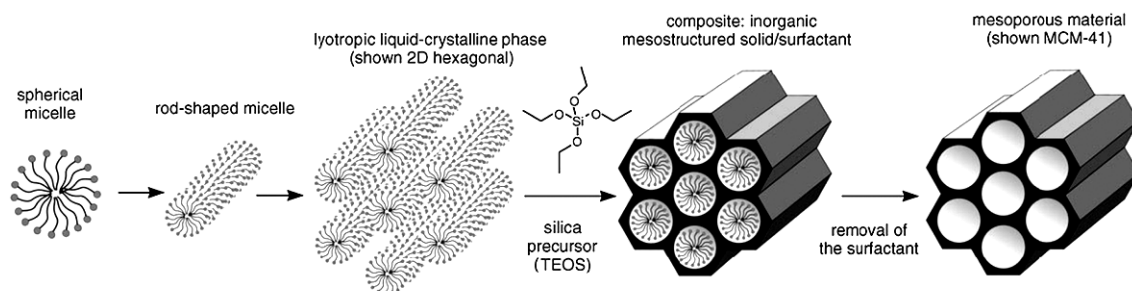


Figure II-1. Schematic illustration of MCM-41 preparation

In conclusion, having considered the possible reactions in which our samples can be tested and, once elected both precursor and support, the research work performed in cobalt catalysts has been divided into four sections:

1. Determination of adsorption isotherms of  $\text{CoCp}_2$  on MCM-41
2. Study of operational variables in the SCFRD synthesis of Co/MCM-41 catalysts
3. Characterization of the Co/MCM-41 catalysts
4. Catalytic activity tests of Co/MCM-41 in the gasification of cellulose

### II.3. Adsorption isotherms of CoCp<sub>2</sub>

Supercritical fluids have been used to impregnate some compounds into different materials in order to improve or change its properties. There are several examples in the literature, especially on polymeric and inorganic supports for pharmaceutical proposes and metal coatings [36-39]. Even there exists an industrial scale plant for wood treatment using organic fungicides based on this principle in Denmark since 2002 [40].

However, these kinds of studies are still scarce in the literature and there is a lack of fundamental understanding of the adsorption process at supercritical conditions. In this adsorption not only the concentration and temperature should be considered, but also pressure and density play an important role in its kinetics and equilibrium.

Up to now, only a few organometallic compounds on porous supports have been studied in sc-CO<sub>2</sub>. The adsorption equilibrium of [Pd(hfac)<sub>2</sub>] on silica SBA-15 and the influence of temperature, pressure and density in the process has been examined [41]. The adsorption isotherms of [Pt(CODMe<sub>2</sub>)] on different supports, such as carbon aerogels, silica gel tablets or monolithic silica have been reported [42, 43]. And the adsorption process of Ru(COD)tmhd<sub>2</sub> on carbon in sc-CO<sub>2</sub> has been also studied [44].

In this section the adsorption of a cobalt organometallic precursor of the family of metallocenes (CoCp<sub>2</sub>) on the mesoporous support (MCM-41) in supercritical CO<sub>2</sub> is studied.

In first place, the adsorption isotherms are determined using a batch configuration, followed by its subsequent modeling in order to reach a better understanding of its nature and thus, continue with the research on a larger scale. Due to the easy oxidation of this precursor, its solubility in CO<sub>2</sub> has been estimated from bibliographic data [34].

#### II.3.1. Experimental Set-up for Determination of Adsorption Isotherms

The determination of adsorption isotherms and kinetics was carried out in a high pressure reaction chamber. In figure II-2, a scheme of this plant is reported.

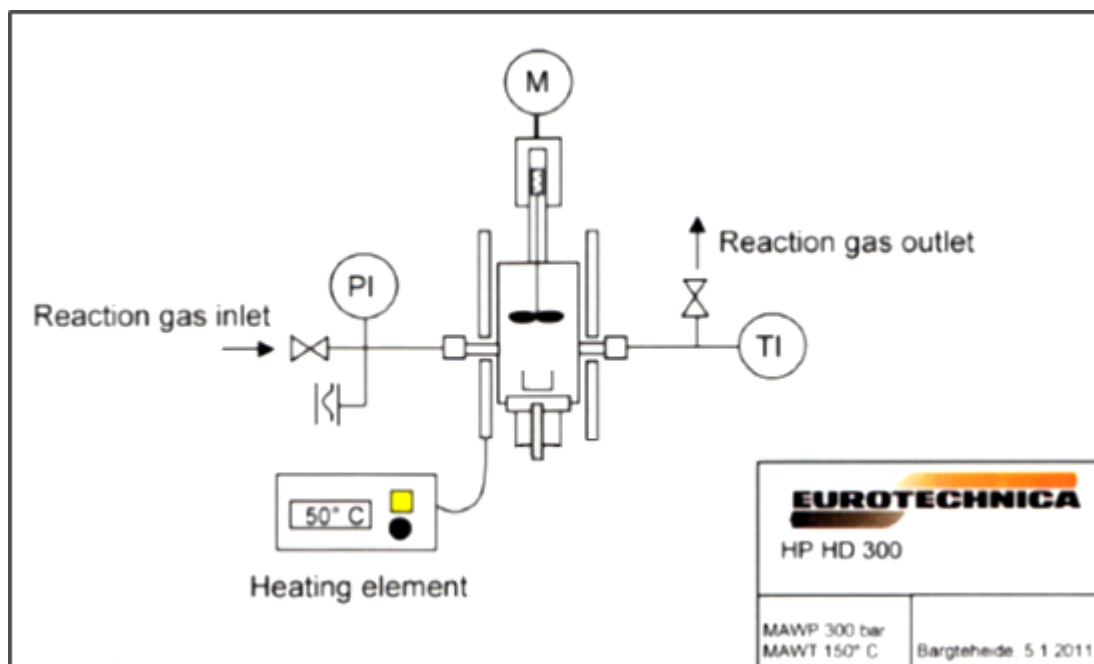


**Figure II-2.** Flow sheet of the experimental device for adsorption isotherms and kinetics determination

This chamber (HP HD300) is built out of SS316-Ti, has an internal volume approximately 25 ml, supporting 30 MPa and 150 °C as maximum operating conditions. A picture of this chamber is presented in figure II-3.

A magnetic driven agitator (12 VDC with transformer 230 VAC) is installed at the top of the reaction chamber in order to ensure a homogenous medium. The temperature of the vessel was controlled by means of an electrical jacket (230 VAC; 50/60 Hz) connected to a digital display and a NiCr-Ni thermocouple with a  $\pm 0.1$  °C accuracy; and pressure inside the chamber is measured by a pressure Gauge between 0.1-40 MPa.

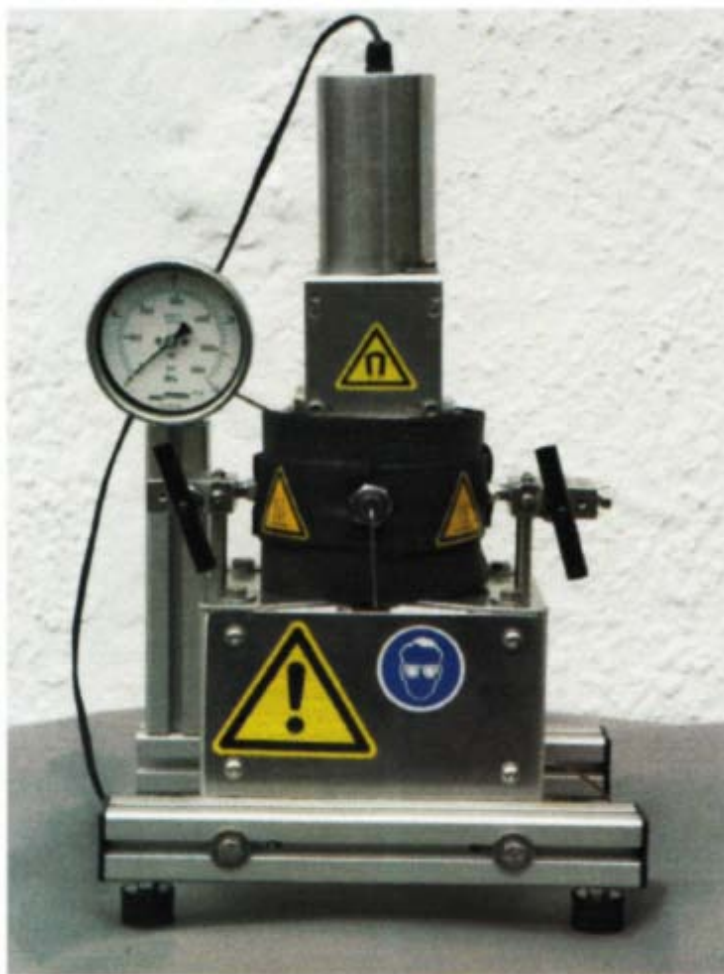


**Figure II-3.** Stirred tank reactor

At the beginning, an amount of support and precursor are introduced into the chamber in a small container through the bottom connection. This closure is mounted again tighten rather softly the nut by wrench to avoid deform the seals set (PTFE, carbon graphite and non ferrous materials). The CO<sub>2</sub> is pumped with a dosing pump Milton Roy Dosapro, MILROYALD (up to 0.6 l/h and 24 MPa) and heated up to operational conditions. The fluid, which contains the dissolved precursor, is constantly mixed with a magnetic coupled stirrer during different times. Finally, at the end of each experiment, the fluid is slowly depressurized in order to prevent the sweeping along particles and recover the products for further analysis.

Experiments were carried out at constant temperature (T=70 °C) for 24 hours, varying the amount of precursor at different CO<sub>2</sub> pressures. The choice of this working temperature is based on bibliographic data [34] and previous results, which have demonstrated that the adsorption process is favored by moderate temperatures.

### II.3.2. Results and discussion: Adsorption of $\text{CoCp}_2$ on MCM-41

At 70°C and 11MPa the estimated solubility of  $\text{CoCp}_2$  in SC- $\text{CO}_2$  is 350 mg/L , according to the literature data [34]. This precursor has a high solubility in comparison with another precursors of cobalt, such as  $\text{Co}(\text{thd})_3$  and in comparison with precursors of other metals with the same ligands, as  $\text{RuCp}_2$  and  $\text{NiCp}_2$ , that have also been used in this PhD thesis.

Figure II-4 shows the adsorption isotherm for  $\text{CoCp}_2$  on MCM-41 at 70 °C and 11 MPa.

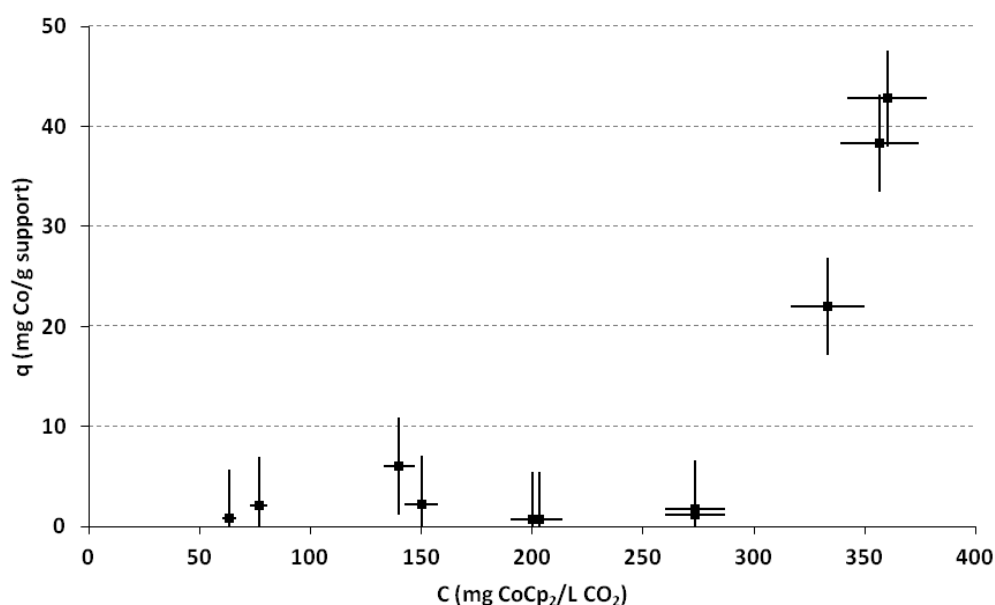


**Figure II-4.** Adsorption isotherms for  $\text{CoCp}_2$  on MCM-41 at 70 °C and 11 MPa

As can be seen in the figure II-4, the metallic loading in the solid  $q$  is practically non-existent for a wide range of concentrations down to a point where the adsorptive capacity increases exponentially. The shape of the isotherm is concave upward and presents a vertical asymptote corresponding to the vapor pressure of the adsorbate (i.e. condensation) [45].

This means that the second layer is more strongly adsorbed than the first one, an effect related to the existence of attractive interactions between the adsorbed molecules. In these cases, however, the adsorbent still has finite saturation capacity and the isotherm could have a horizontal asymptote [46].

This behavior is characteristic when the adsorbate-adsorbent interaction is low or conversely, there is a greater affinity for the fluid medium (isotherm of type III), at least

in the entire concentrations range investigated, from 0 to close to the saturation of fluid phase. Although this type of isotherm is unusual, it can be found several examples in the literature, such as bromine or iodine on silica gel, or water over some hydrophobic rubbers, plastics, synthetic fibers or graphitized carbon [47].

On the other hand, competition between the solvent and the solute for the support adsorbent sites may also be possible, especially for systems involving low solubility or weak adsorbing solute species [48]. However, this phenomenon may be diminished at supercritical conditions [49], since the transport coefficients are enhanced. Besides, MCM-41 surface does not interact very strongly with CO<sub>2</sub> according to other authors [50, 51].

Since the acquisition of adsorption data from a type III system is the most confused and ambiguous at low concentrations, more isotherms will not be determined experimentally and it will be proceeded to its modeling.

### II.3.3. Adsorption Isotherms Modeling

Several authors have been tried to predict isotherms of type III with anti-Langmuir models [46, 52]. This means that it could be modeled by using a Langmuir model with negative association equilibrium constant [46], but although this modification provides good fits, its parameters lack physical sense.

Another option is the use of an exponential equation as the following expression:

$$q = A \cdot B^C \quad (\text{Eq. 1})$$

where  $A$  and  $B$  are constants, and  $C$  is the concentration of organometallic precursor in the fluid phase (mg/L). Worth mentioning that this model is only recommendable for low concentrations, since at very high initial concentrations, it predicts depositions that tend to infinity.

To solve all these drawbacks, the isotherms describing best this type of behavior are generally referred to an S-shape isotherm and they are often best modeled using the quadratic isotherm model, where the initial curvature is negative. The easiest equation of this kind of models is known as sigmoid function:

$$q = \frac{q_s}{[1+\exp(-a \cdot C-b)]} \quad (\text{Eq. 2})$$

where  $q_s$  is the adsorptive capacity,  $a$  is related to saturation concentration, and  $b$  depends on the minimum concentration which must be overcome to start adsorption.

On the other hand, among all these options, BET adsorption isotherm model [53] is the most used alternative to study this kind of systems; whose equation is able to reproduce any singularity in adsorption process, even different kinds of isotherms as a function of the relationship between its parameters.

$$q = \frac{Q_m \cdot K_{BET} \cdot C_e}{(C_m - C_e) \cdot [1 + (K_{BET} - 1) \cdot (C_e / C_m)]} \quad (\text{Eq. 3})$$

where  $q$ , the equilibrium adsorption capacity (mg/g);  $Q_m$ , the theoretical isotherm monolayer capacity (mg/g);  $K_{BET}$  is the BET adsorption isotherm constant (L/mg); and  $C_m$ , the adsorbate monolayer concentration (mg/L).

#### II.3.4. Fittings and discussion

To adjust the isotherm parameters and conclude which is the best model for describing the equilibrium, it is necessary to calculate the mean squared error, defined in Eq. 4:

$$MSE = \frac{1}{n} \sum_{i=1}^n |q_i^{exp} - q_i^{cal}|^2 \quad (\text{Eq. 4})$$

Figure II-5 shows the adjustment provided by the models described aforementioned; and the Table II-1 summarizes the characteristic parameters and mean squared error of each of them.

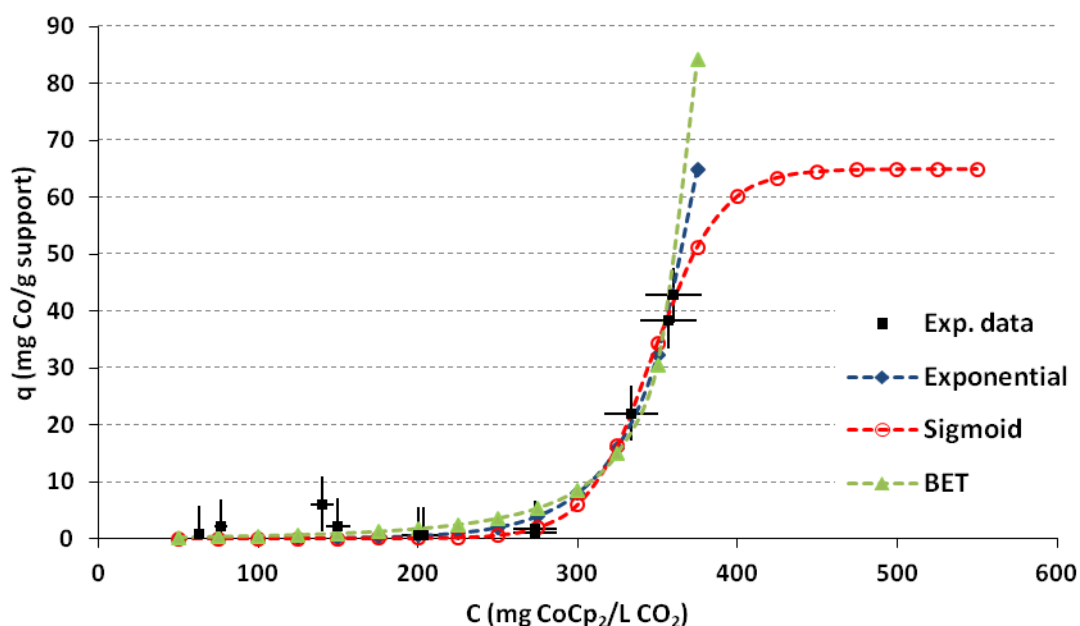


**Figure II-5.** Experimental data (■) and fit by Exponential (-◆-), Sigmoid (-○-) and BET (-▲-) correlations for adsorption isotherms of CoCp<sub>2</sub> on MCM-41 at 70 °C and 11 MPa

**Table II-1.** Fitted model parameters and average deviation for the adsorption equilibrium of CoCp<sub>2</sub> on MCM-41 in sc-CO<sub>2</sub>: Exponential, Sigmoid and BET

<b>MODEL</b>	<b>Isotherm 70°C and 11 MPa</b>
<b>Exponential</b>	
<i>A</i>	0.0017
<i>B</i>	1.028
<i>MSE</i>	1.68
<b>Sigmoid</b>	
<i>q<sub>s</sub> (mg/g)</i>	64.89
<i>a (L/mg)</i>	0.048
<i>b</i>	-16.786
<i>MSE</i>	1.41
<b>BET</b>	
<i>K<sub>BET</sub> (L/mg)</i>	0.0083
<i>Q<sub>m</sub> (mg/g)</i>	109.93
<i>C<sub>m</sub> (mg/L)</i>	414.60
<i>MSE</i>	2.08

First, note that all model fit neatly within the range of studied concentration, with an average error  $\leq 2$ ; however, predictions about the progression of the adsorption process vary significantly from each other.

The exponential equation works nicely as empirical model with only two constants, quickly and easily; nevertheless, no valid information is achieved from the analysis of its parameters.

On the other hand, BET isotherms provides similarly exponential curve, that is, a multilayer adsorption; but in this case, attending to its characteristic parameters, it is possible to draw several conclusions. BET adsorption isotherm constant ( $K_{BET}$ ) is slightly larger than the pre-exponential factor in the previous model, which results in superior metallic loadings as it can be observed at high concentration in Figure II-5. This means that the affinity of the metallocene by itself and the crystal growth rate predicted by this model is higher.

Also, according to the results shown in the Table II-1, it is possible to obtain homogeneous monolayer depositions with loadings around 110 mg/g (theoretical monolayer capacity); and that to achieve this goal, an initial precursor concentration higher than 415 mg/L is needed.

Conversely, sigmoid function predicts a completely different behavior.

In the first place, this model assumes that there exists a maximum concentration at which the substrate is saturated, and therefore, it cannot be obtained depositions higher than 65 mg/g, well below even the prognosticated monolayer deposition by BET model. Nonetheless, the adsorbate saturation concentration  $C_S$ , at which this loading is achieved, is very close to that estimated by BET isotherm, around 420 mg/L.

All in all, we are dealing with an adsorbate-adsorbent system which is not favorable under current conditions for supercritical fluid deposition process (SCFD). This is why we propose including a reaction step (SCFRD) in order to promote the precipitation of metal nanoparticles over the support surface after the rupture of the precursor in the fluid phase.

This rupture can be promoted by a reducing agent or by thermal decomposition as it has already been described in the Introduction of this PhD thesis. In our case, we have chosen to cause a temperature rise above the decomposition temperature of the precursor, precipitating the metal whereas the organic part remains dissolved into the supercritical phase. The whole optimization process will be developed in the next chapter.

## II.4. Supercritical Fluid Reactive Deposition of $\text{CoCp}_2$ on MCM-41

In the previous section, it has been concluded that for the deposition of cobalt from  $\text{CoCp}_2$  on MCM-41 is not enough simple exposure of a solution of the precursor over the support, since the adsorption is not favorable. For this reason, it has raised the alternative of the supercritical fluid reactive deposition (SCFRD).

In this chapter, different tests will be performed in order to optimize the process, analyzing its operational variables and their consequential effects, such as pressure, temperature, time and even its reactor configuration.

### II.4.1. Catalyst Synthesis Batch Device

The deposition experiments were carried out in batch process in a high-pressure vessel constructed out of stainless steel with an internal volume of 100 ml. Since conventional salts used in aqueous impregnation are not soluble in  $\text{sc-CO}_2$ , metal complexes such as organometallic compounds or chelates complexes are used.

The experimental set-up, given in Fig. II-6, operates up to 30 MPa pressure and 400 °C as maximum allowable working conditions.

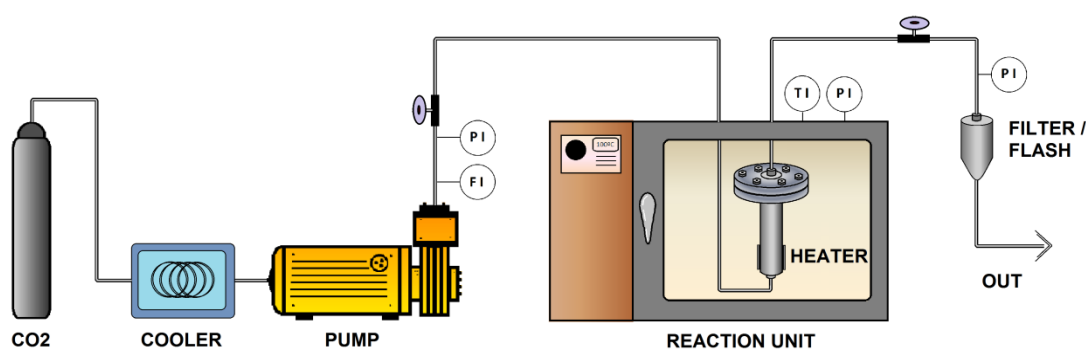


**Figure II-6.** Experimental device for the synthesis of catalysts by SFRD (batch process)

A dosing pump Milton Roy Dosapro (flow rate up to 6.2 l/h and 33 MPa maximum pressure) was used to move the  $\text{CO}_2$  into the reactor. To ensure the liquid state of the  $\text{CO}_2$  for its pumping, the fluid is previously cooled in a bath with a mixture (50/50, ethylene glycol/water) refrigerated with an immersion cooler JULABO model FT402

and external Pt-100 sensor. Mass flow meter and a pressure Gauge are installed in the output of the pump.

At the beginning of each experiment, support and organometallic precursor, 150 mg and 100 mg respectively, were placed into the vessel, separated by wire mesh to allow the circulation of sc-CO<sub>2</sub> and avoid their direct contact (Fig. II-7). The reactor is equipped with two wall electrical resistances (250 W) located at the bottom to promote the convective flow of sc-CO<sub>2</sub>, and a K-Thermocouple connected to a controller PID BS-2100 to measure and manage the temperature with a  $\pm 0.1$  °C accuracy. Pressure is also recorded by means of a pressure transmitter ATSA TPR-14/STD, <1% accuracy and range for up to 40 MPa, and displayed in a BS-2100. All this reaction section is located inside an oven Memmert (Universal Oven Model UF110) to minimize the amount of heat losses.

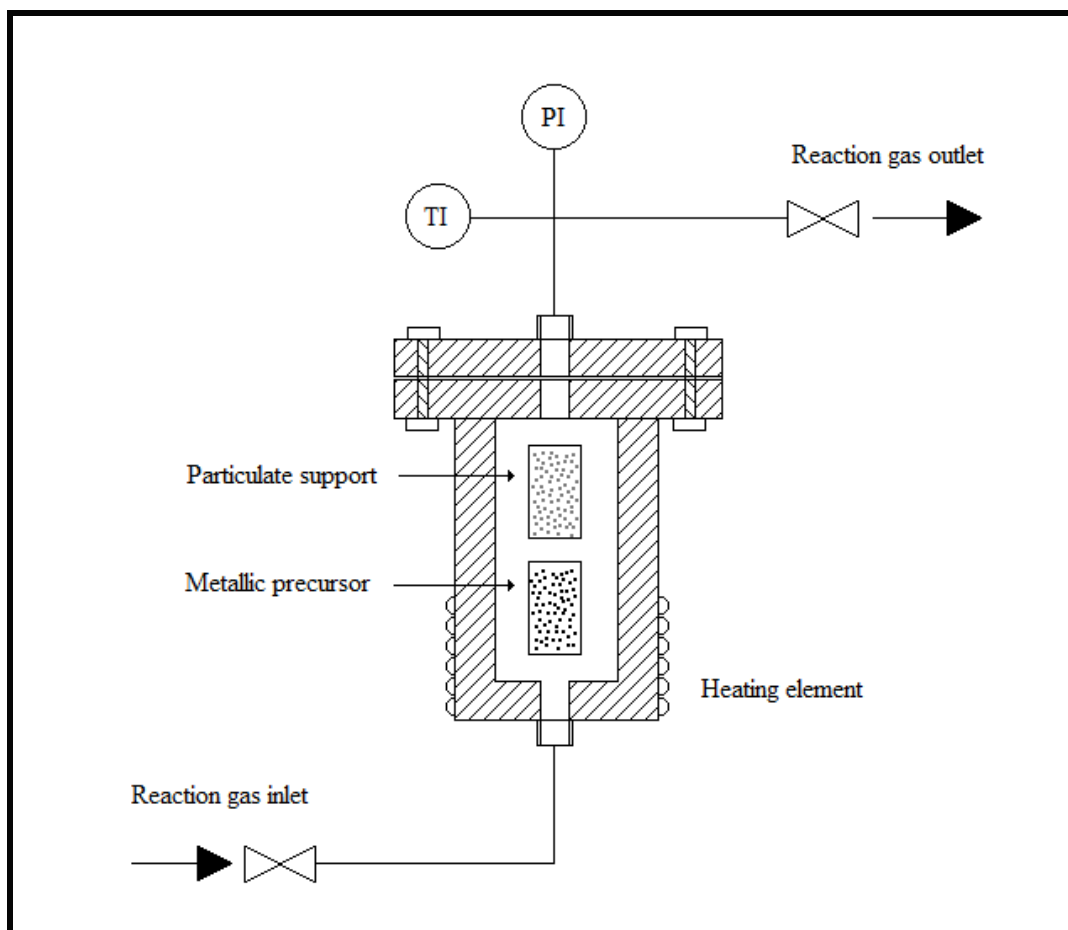


**Figure II-7.** Detail of the distribution of reactants (support and precursor) within deposition chamber

During the first step, precursor is dissolved by sc-CO<sub>2</sub> under optimal operation conditions to favor its solubility. Meanwhile, precursor adsorption onto the support from the medium takes place during the desired adsorption time. After this adsorption

## CHAPTER II. Cobalt-based Catalysts

step, temperature is increased to 200 °C to break down the organometallic compound, with its subsequent precipitation of the metallic nanoparticles during the desired decomposition time. Afterwards, the system is isochorically cooled down to subcritical conditions, and CO<sub>2</sub> is released from the reactor over a period approximately 30 min, which implies a slowly depressurization to atmospheric pressure to avoid drag metallic nanoparticles which are adsorbed over the support surface.

As a safeguard against pollutant emissions of remaining precursor dissolved by the fluid, a flash vessel is located in the output line and a pressure regulator Metal Work model MR-BIT 1/8 with maximum allowable pressure of 1.3 MPa.

### II.4.2. Optimization: concentration, temperature and pressure

This process of synthesis, SCFRD, consists of two consecutive steps: 1) precursor dissolution and adsorption, and 2) precursor decomposition. Each of them has different conditions of pressure and temperature, which must be chosen carefully, besides the initial precursor concentration.

The first stage in which the precursor is dissolved in the supercritical medium and the adsorption on the surface support is initiated, is performed in the same conditions as the previous experiments to determine its isotherm. That is to say, at constant temperature  $T_1 = 70$  °C and pressure  $P_1 = 11$  MPa. Taking into account the shape of the adsorption isotherm of CoCp<sub>2</sub> on MCM-41, it has been decided to work always with an initial mass of precursor above the maximum amount that can be dissolved in CO<sub>2</sub>. According to the experimental results, a maximum deposition loading in this stage of around 6.5 % wt is expected attending the saturation value of sigmoid model used in its isotherm.

Nonetheless, in the second stage in which the precursor is broken down to facilitate the precipitation of metallic nanoparticles, it is necessary to increase the temperature. This temperature is chosen based on the precursor thermogravimetric analysis (TGA), wherein the decomposition temperature ( $T_d$ ) of the compound is identified through its mass loss, and verified by means of the FT-IR spectra of the precursor. The figure II-8 shows the TGA profile of this cobalt precursor, CoCp<sub>2</sub>.

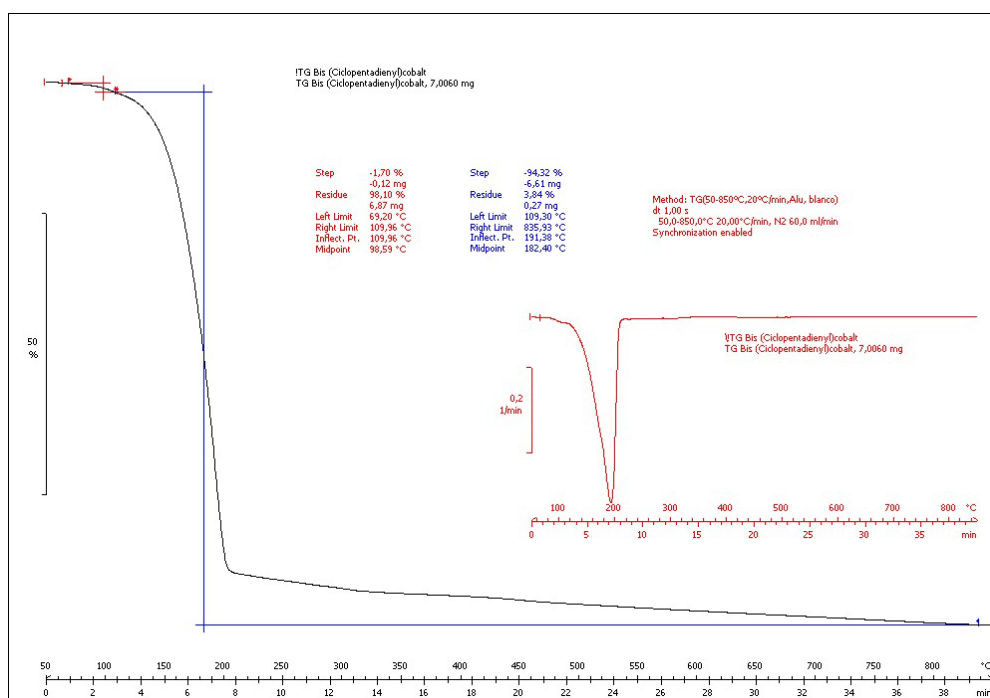


Figure II-8. TGA profile for  $\text{CoCp}_2$

As can be seen from the figure II-8, the  $T_d$  of  $\text{CoCp}_2$  is found around  $180\text{ }^\circ\text{C}$ , so a temperature of  $T_2 = 200\text{ }^\circ\text{C}$  is chosen as the temperature for the second stage of the process, about  $20\text{ }^\circ\text{C}$  above its  $T_d$ , as recommended in literature [54].

As a result of this temperature rise and batching at constant volume, the pressure increases drastically. For safety reasons and experimental device limitations, the pressure is relieved, having to choose a new pressure value for this second stage. The pressure itself has not any role in the decomposition step, but due to the operation in a constant volume cell, with a specific maximum operation pressure, it is necessary to vent partially the fluid phase, and therefore, some of the dissolved precursor is released.

In order to select the suitable pressure, a series of experiments were performed by changing the study variable between 9 and 20 MPa. As it is not yet possible to establish an optimum operating time, it was decided to fix that each stage lasts 3 hours. This implies that every batch involves about 8 hours of operation, including the conditioning and decompression.

Table II-2 summarizes these results, where it can be observed that this process presents a maximum of cobalt loading, for a pressure  $P_2 = 14\text{ MPa}$ , hence this value has been chosen as pressure for the second stage.

## CHAPTER II. Cobalt-based Catalysts

**Table II-2.** Metallic loading (%wt) deposited by SCFRD (2 steps)  
1<sup>st</sup> – 3h, 70 °C and 11 MPa; 2<sup>nd</sup> – 3 h, 200 °C and at different pressures

Pressure (MPa)	Co (%wt)
9	2.61
11	2.52
14	2.90
17	2.55
20	2.08

According to these previous results, conditions for the 1<sup>st</sup> stage (CoCp<sub>2</sub> solubilization and adsorption) have been fixed in T<sub>1</sub> = 70 °C and P<sub>1</sub> = 11 MPa; and the 2<sup>nd</sup> stage (thermal degradation of CoCp<sub>2</sub>) in T<sub>2</sub> = 200 °C and P<sub>2</sub> = 14 MPa.

### II.4.3. Kinetics of the process

In this section, the kinetics of the process will be discussed in order to reduce the operational times for each of the stages involved, in order to increase its effectiveness.

For this purpose, a set of experiments with the conditions selected in the preceding paragraph were carried out, varying the duration of its stage. In Table II-3 the values obtained for metallic loading, alongside the timing for each stage in hours are presented.

**Table II-3.** Effect of time on cobalt loading of the final material Co/MCM41

Sample	1 <sup>st</sup> step (min) <sup>a</sup>	2 <sup>nd</sup> step (min) <sup>b</sup>	Co (%wt)
1	60	0	0.07
2	120	0	0.05
3	180	0	0.08
4	180	60	1.20
5	180	120	1.39
6	180	180	2.64
7	0	60	2.90
8	0	120	3.30
9	0	180	3.24

a) Conditions: 70 °C and 11 MPa

b) Conditions: 200 °C and 14 MPa

According to these results, several conclusions can be drawn. In first place, it is checked again that no good results are obtained independently of exposure time by using only the supercritical fluid deposition without the precursor breakdown (Co %wt < 0.1), since the adsorption is very unfavorable and the solubilized precursor is vented together with the CO<sub>2</sub> during the depressurization of the vessel.

Incorporating a second stage of reaction, higher metal depositions are achieved as a function of operation time, as expected. However, by eliminating the first step of precursor dissolution completely and, performing the breaking thereof directly, higher loadings are attained in less time. Actually, the first stage cannot be really eliminated, since dissolution takes place during the heating up of the system because it is a batch process. This non stationary period lasts 20 minutes.

This divergence in results may be due to the way of operating. When the deposition process is performed in two stages, a controlled decompression of the medium must be performed after the temperature increase, thus losing solubilized precursor; whereas when only the second stage is directly carried out, more precursor is available.

Then, henceforth it will operate directly with the conditions of the second stage (200 °C and 14 MPa), considering therefore that the precursor dissolution is a quick process that takes place during heating up period. The figure II-9 shows the progression of the metal loading versus time, conducting experiences at 14 MPa and 200 °C at different times.

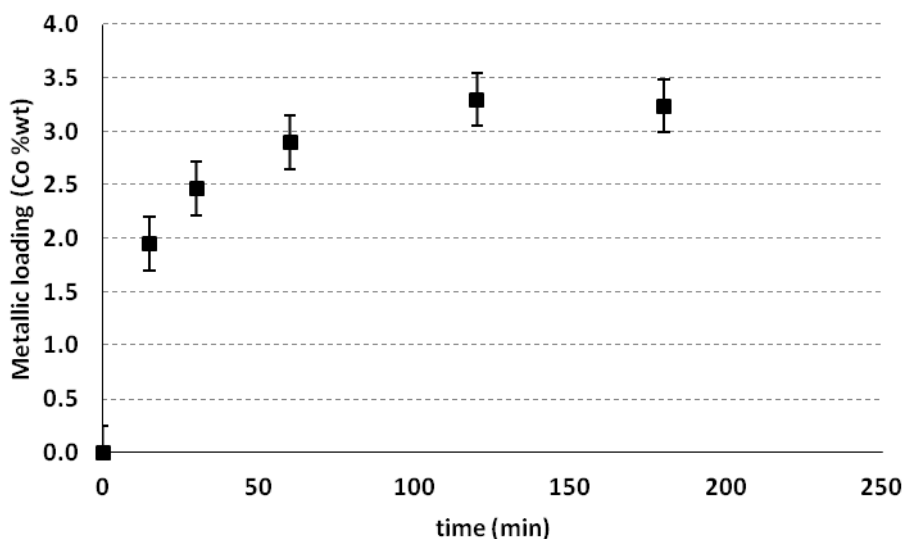


**Figure II-9.** Progression of metallic loading versus exposure time at 200 °C and 14 MPa

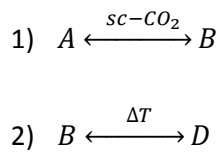
As can be seen, the metal loading increases in the support with time up to a maximum concentration of 3.4 %wt of cobalt at 60-120 min. This means that during approximately the first hour, the coating of the support takes place through the channels and refilling the pores of the matrix in order to form a monolayer of cobalt over the support surface. Beyond this time kinetics is limited by another factor.

### II.4.3.1. Kinetics Model

For a deeper understanding of what actually happens, a model that explains the physics of the process is proposed.

SCFRD consists of two sequential steps; the first one is the dissolution of the precursor in sc-CO<sub>2</sub>, whereas the second stage involves the precipitation of the metal over the support and its adsorption.

Based on the aforementioned, this process has been explained as serial reaction kinetics:



Where *A* is the organometallic precursor in solid state, *B* is the precursor dissolved into the sc-CO<sub>2</sub>, and *D* represents the metallic nanoparticles adsorbed over the support.

All kinetics are considered of first order. If the process takes place in a well-mixed batch reactor without variation in volume, the following balances can be considered:

$$\frac{dC_A}{dt} = r_2 - r_1 \approx -k_1 \cdot C_A \quad (\text{Eq. 5})$$

$$\frac{dC_B}{dt} = r_1 - r_2 - r_3 \approx k_1 \cdot C_A - k_3 \cdot C_B \quad (\text{Eq. 6})$$

$$\frac{dC_D}{dt} = r_3 = k_3 \cdot C_B \quad (\text{Eq. 7})$$

Taking into account that the equilibrium is displaced to the species *B* in the first reaction due to the solubility of the precursor in sc-CO<sub>2</sub>, and considering the initial concentration of *A* is *C<sub>A0</sub>*, integration of Equation 5 is as follows:

$$\int_{C_{A0}}^{C_A} \frac{dC_A}{C_A} = -k_1 \cdot \int_0^t dt \quad (\text{Eq. 8})$$

$$C_A = C_{A0} \cdot \exp(-k_1 \cdot t) \quad (\text{Eq. 9})$$

On the other hand, the dependence of the concentration *C<sub>B</sub>* with time can be determined by combining the mass balance (Eq. 6) and the above equation which indicates the change in *C<sub>A</sub>* with time (Eq. 9):

$$\frac{dC_B}{dt} + k_3 \cdot C_B = k_1 \cdot C_{A0} \cdot \exp(-k_1 \cdot t) \quad (\text{Eq. 10})$$

$$C_B = \frac{k_1 \cdot C_{A0}}{(k_3 - k_1)} [\exp(-k_1 \cdot t) - \exp(-k_3 \cdot t)] + C_{B0} \cdot \exp(-k_3 \cdot t) \quad (\text{Eq. 11})$$

Finally, the concentration  $C_D$  can be obtained by means of the global balance:

$$C_{A0} + C_{B0} + C_{D0} = C_A + C_B + C_D \quad (\text{Eq. 12})$$

$$C_D = C_{A0} + C_{B0} + C_{D0} \left[ 1 - \left( \frac{k_3}{k_3 - k_1} \right) \exp(-k_1 \cdot t) \right] + \left[ \left( \frac{k_1 \cdot C_{A0}}{k_3 - k_1} \right) - C_{B0} \right] \cdot \exp(-k_3 \cdot t) \quad (\text{Eq. 13})$$

According to this model, being  $C_{B0} = C_{D0} = 0$ , the concentration of species A, ie the precursor in solid state, decreases exponentially; while the species B has a maximum because of, on one hand it is created by dissolving the precursor in sc-CO<sub>2</sub>, and at the same time it disappears by effect of temperature, precipitating the metal particles on the substrate and forming the species D.

The suggested model of two serial reactions is adjusted to experimental data. Figure II-10 shows this fit.

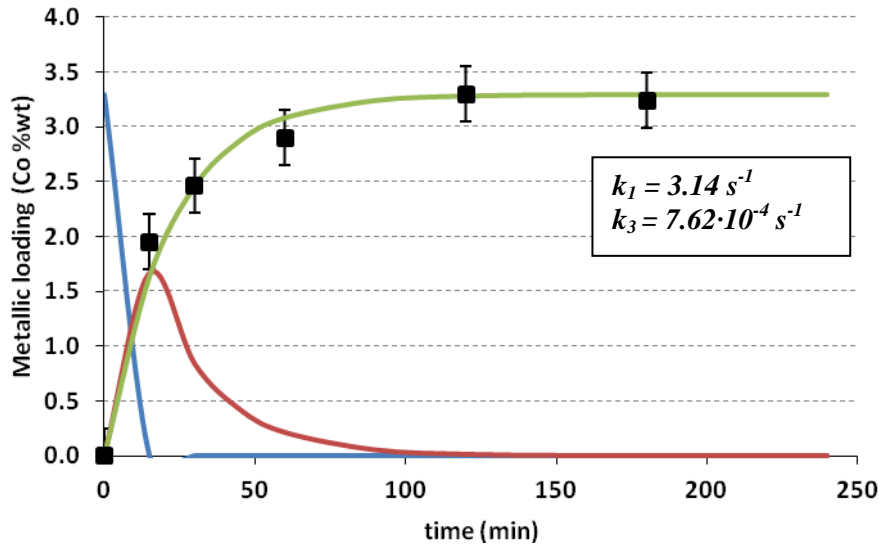


**Figure II-10.** Simulation curves for SCFRD as serial reaction kinetics: (■) Experimental values; (Blue line —) Evolution of precursor in solid state; (Red line —) precursor dissolved in sc-CO<sub>2</sub>; and (Green line —) metallic nanoparticles adsorbed on the support

As can be seen from values of the kinetics constants ( $k$ ), it can be drawn again that the first step of dissolution is very fast compared to the adsorption stage and not limiting for the process.

## CHAPTER II. Cobalt-based Catalysts

Thereupon, basing on the results obtained in this section, it is established an optimal operational time of one hour.

### II.4.4. Sequential loadings

Up to now, we have only managed to reach a metallic loading around 3 %wt. For catalytic purposes, it will be interesting to have higher metallic loadings. For this reason, consecutive sequential loadings have been carried out in order to obtain a catalyst (Co/MCM41) with higher amounts of Co [55].

Table II-4 shows the amount of cobalt achieved after each batch, with a duration of 1 hour per batch.

**Table II-4.** Metallic loading (Co %wt) after each successive batch

<b>Sample</b>	<b>N. batches</b>	<b>Co (%wt)</b>
<b>1</b>	<b>1</b>	<b>3.24</b>
<b>2</b>	<b>2</b>	<b>4.40</b>
<b>3</b>	<b>3</b>	<b>6.00</b>

Results indicate that it is possible to get a material Co/MCM41 with a metallic loading of 6 %wt after only 3 batches.

### II.4.5. Mass transfer limitations

Due to the configuration of the experimental device, the synthesis process is carried out into the reactor without external stirring. To facilitate as far as possible the homogeneity of the solution, the electrical resistances are located at the bottom of the vessel, as it is shown in the figure II-11, to favor the creation of convective currents.

Inside the high pressure reactor, the support and precursor are located inside two glass vials separated by means of wire mesh. Precursor is located in the lower part and the support occupies the upper vial. This kind of configuration has been called “column” type.

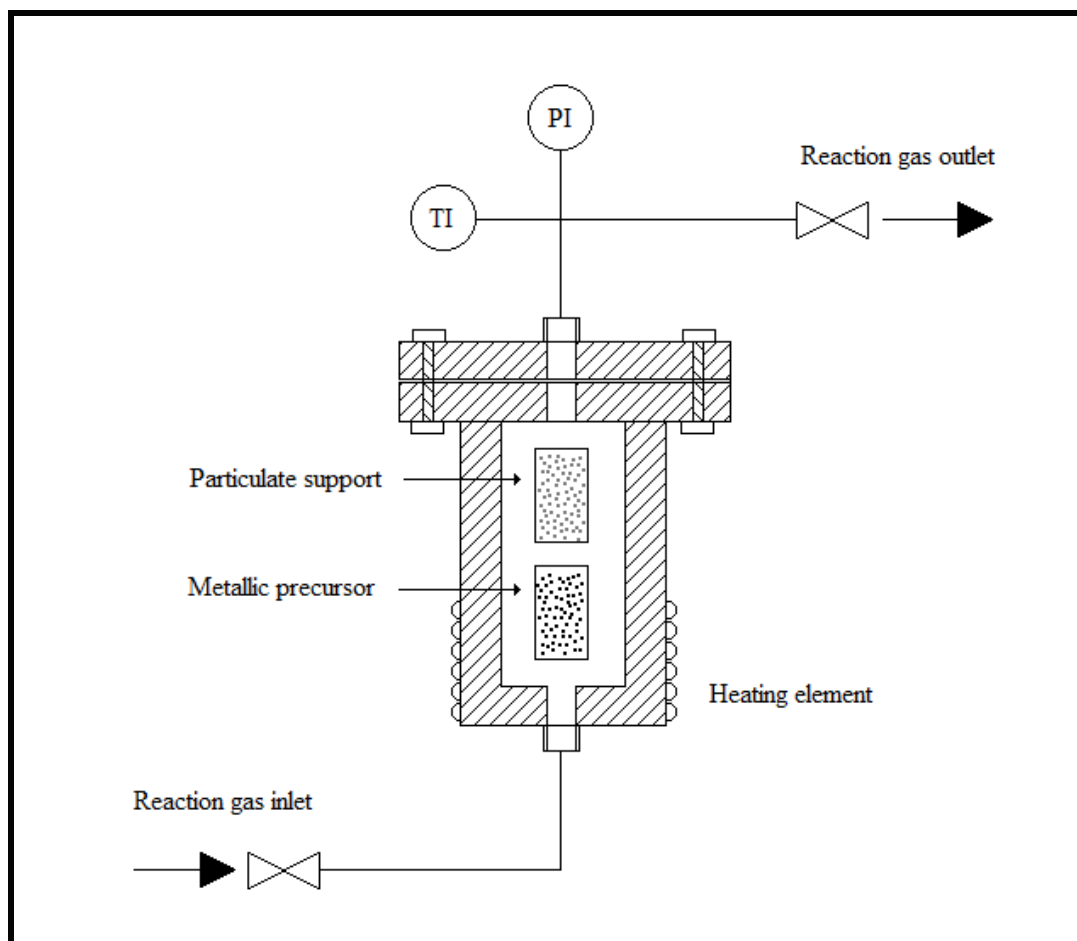


**Figure II-11.** “Column configuration”, precursor at the bottom and support at the top

Since the support is disposed as a fixed bed, it was decided to test whether all along the vial the same deposition was obtained, or conversely there was some mass transfer limitation. For this reason, the metal content from the same sample was analyzed at three different heights, as it is indicated in figure II-12.

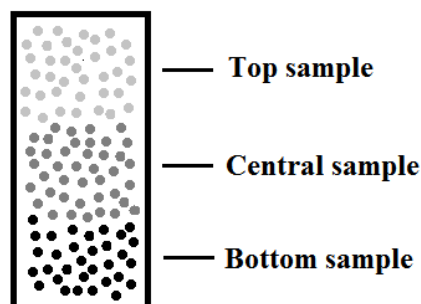


**Figure II-12.** Sampling at different heights

The results showed that there was a certain divergence, with a concentration gradient of up to 20% if the initial amount of support was too high, so a new configuration in the form of placing the reactants was contemplated in order to avoid the observed mass transfer limitations.

To avoid bed length was too long, reagents were separated on lower amounts in several vials and placed alternately as shown in the attached figure, maintaining the total mass of both precursor and support. This new configuration is called “sandwich” and a scheme of it is presented in Fig. II-13.

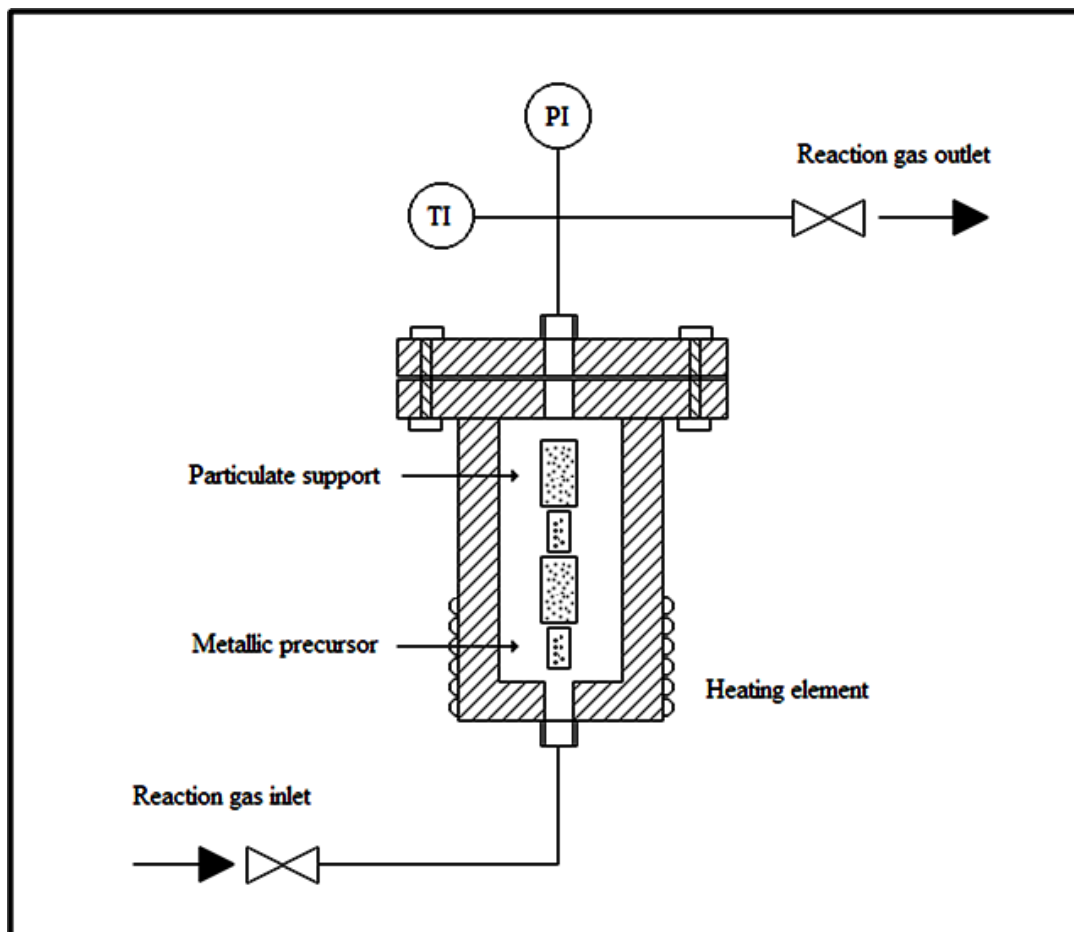


Figure II-13. “Sandwich configuration”, precursor and support alternatively placed

The experiments of sequential loadings were repeated under the same conditions but with this new “sandwich” configuration, to test its effect. The results are compared in the table II-5.

Table II-5. Metallic loading (%wt) after each successive batch;  
comparison between configurations: “column” and “sandwich” type

“Column” configuration			“Sandwich” configuration		
Sample	N. batches	Co (%wt)	Sample	N. batches	Co (%wt)
1	1	3.24	4	1	5.80
2	2	4.40	5	2	13.72
3	3	6.00	6	3	16.58

Surprisingly, the improvement allows to obtaining nanocomposites with really higher metallic loadings to 16 %wt, showing that this “sandwich” configuration improves mass transfer in the system.

#### II.4.6. Conclusions

In short, in this chapter we have optimized the process of synthesis of Co/MCM41 catalysts by SCFRD, as summarized in the following table II-6. Under these conditions it has been achieved metallic loading around 6 %wt of Co in just one hour, and successive batches of one hour have led to metal content of around 13.7 and 16.5 %wt respectively.

**Table II-6.** Optimal conditions for synthesis of cobalt nanocomposites by SCFRD

<b>PARAMETER</b>	<b>OPTIMIZATION</b>
<b>Operation</b>	Batch
<b>1<sup>st</sup> stage of adsorption</b>	Unnecessary
<b>Configuration</b>	“Sandwich”
<b>Temperature</b>	200 °C
<b>Pressure</b>	14 MPa
<b>Time</b>	1 hour

It is noteworthy that these working conditions of temperature (200 °C) and pressure (14 MPa) are quite softer than those recommended by Hunde et al. [33] for film formation from  $\text{CoCp}_2$  onto native oxide of silica wafers, which operated with temperatures above 285 °C and pressures up to 26 MPa.

## II.5. Characterization of cobalt-based catalyst

At the beginning of the experimental work, MCM-41 were treated with pure sc-CO<sub>2</sub> under different operational conditions (T and P), and it was checked that the mesoporous structure were not disturb in any case, and no apparent variations in the value of the surface and volume parameters with respect to untreated raw material was observed.

The content of cobalt in the final composite materials Co/MCM-41 was analyzed by ICP and XRF analyzers. Those analytical techniques, and their equipments, together with the rest of characterization techniques used in this PhD thesis are presented in the appendix.

Textural properties such as BET area, and pore parameters, of MCM-41 and the final composite materials, are collected in the Table II-7. For comparison, a catalyst of Co/MCM-41 has been prepared by wet impregnation using Co(NO<sub>3</sub>)<sub>2</sub> as precursor, and it is identified by -WI.

**Table II-7.** Metal loading and textural properties of support and Co-based catalysts.

<b>Sample</b>	<b>%Metal</b>	<b>BET (m<sup>2</sup>/g)</b>	<b>d<sub>p</sub> (nm)</b>	<b>V<sub>p</sub> (cm<sup>3</sup>/g)</b>
<b>MCM-41</b>	---	1300	4.6	0.80
<b>*Co(L)MCM41-WI</b>	6.4	1198	4.2	0.56
<b>*Co(L)MCM41-SC</b>	5.8	1134	3.9	0.29
<b>*Co(H)MCM41-SC</b>	16.5	420	1.8	0.36

\* (L) refers to a low metallic loading and (H) a high loading, obtained by several consecutives batches

The data show that BET surfaces areas is slightly decreased for the catalysts with low cobalt loading. However, when the cobalt content is increased up to 16.5 %wt, pores are filled with the metal and both pore parameters and BET surface area are dramatically decreased. According to the literature, such behavior could be attributed to modification of the pore distribution of silica due to the presence of Co, by reducing the mesopore volume even with low Co content and adding some microporosity with the highest Co content and the segregated Co<sub>3</sub>O<sub>4</sub> phase or other spinels [29].

In order to further identify the cobalt species in these catalysts, the TPR, XPS and XRD of the samples are examined.

The reducibility of the cobalt species are studied by TPR. Fig. II-14 shows the TPR profiles of the following catalysts: (a) Co(L)MCM41-WI, (b) Co(L)MCM41-SC and (c) Co(H)MCM41-SC.

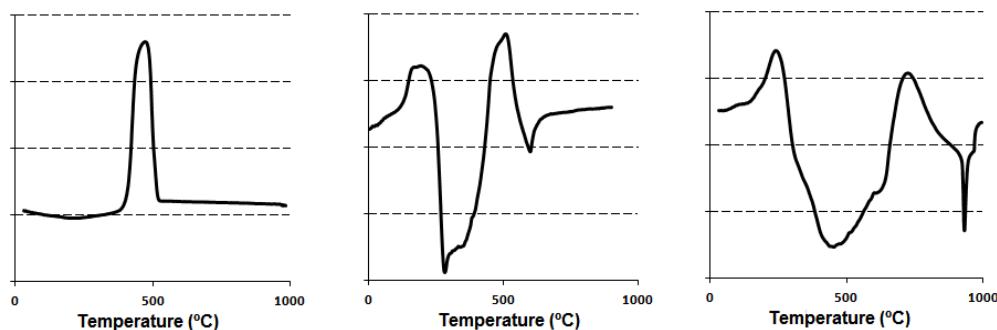


**Figure II-14.** TPR profile: a) Co(L)MCM41-WI; b) Co(L)MCM41-SC; and c) Co(H)MCM41-SC

In TPR measurements of the catalysts prepared by WI, only one reduction region has been observed at around 460°C (figure II-14a). This peak is assigned to the reduction of the cobalt oxide species  $\text{Co}^{2+}$  to metallic cobalt according to the following equation [30]:



However, profile displayed in the samples prepared by SCFRD provides a completely different and rather strange behavior. Throughout the analysis, the detector recorded negative signals, which would imply hydrogen production. This fact could be due to organic remnants from precursor adsorbed on the support, which decompose by thermal effect releasing hydrogen, thus explaining the abrupt slope around 250 °C in figure. II-14b and figure II-14c.

Leaving aside this phenomenon, both profiles show a peak at high temperature above 700°C (more pronounced at higher concentrations), which is attributed to cobalt silicate [56, 57]. In view of this, it has decided to reduce the samples prepared by WI at 500 °C, and catalysts prepared by SCFRD at two different temperatures, 500 and 800 °C, to evaluate its effect on the metallic nanoparticles, and consequently on its activity.

To complete the study addressing the problem from another perspective, the surface composition of catalysts were studied by XPS, whose results are shown in Fig. II-15.

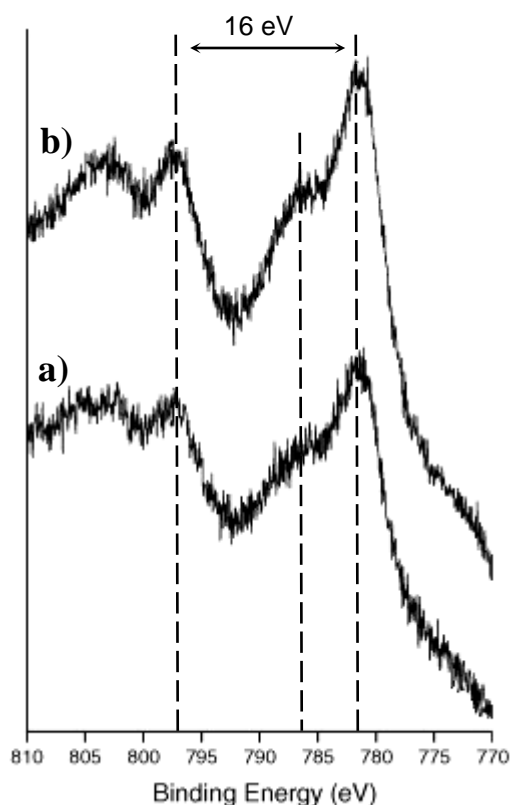


**Figure II-15.** XPS spectra of a) Co(L)MCM41-SC and b) Co(H)MCM41-SC

The main peak appears at 781 eV (Co  $2p_{3/2}$ ), with an intense satellite peak at 786 eV. Moreover, another peak appears at 797 eV (Co  $2p_{1/2}$ ). These binding energies correspond to cobalt oxide species  $\text{Co}^{2+}$  highly dispersed [58].

X-ray diffraction (XRD) analysis was employed to investigate the crystal phase. The XRD patterns of supported cobalt catalysts after calcination (at 800°C for 3h) are shown in Fig. II-16. The broad line centered at around  $2\theta=22^\circ$  is due to the silica support. The XRD spectra of samples prepared by SCFRD give distinct diffraction peaks arising at  $44.2^\circ$  (111),  $51.5^\circ$  (200) and  $75.8^\circ$  (220), which can be all indexed to Co metal in face-centered cubic structure (JCPDS 15-806). However, in the XRD pattern of the sample synthesized by WI can be observed two different peaks at  $41.6^\circ$  (100) and  $47.5^\circ$  (101), which reveal the coexistence of two different crystallization phases of cobalt, cubic and hexagonal closed-packed (JCPDS 5-727) in the bulk.

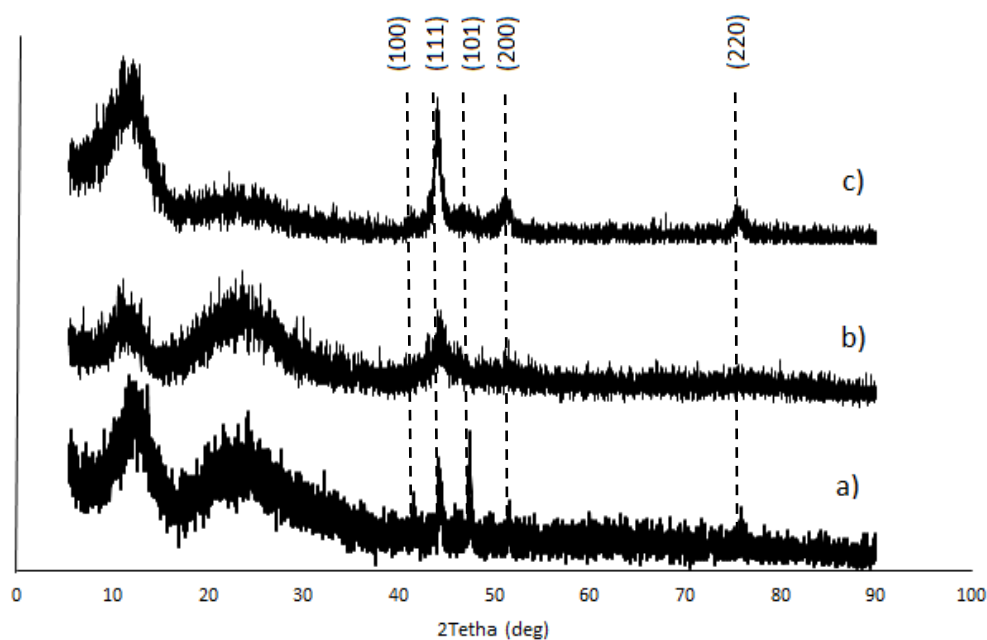


**Figure II-16.** XRD pattern of catalysts (a) Co(L)MCM41-WI, (b) Co(L)MCM41-SC and (c) Co(H)MCM41-SC

On the other hand, the morphology and nanoparticles distribution were observed on electron microscopy. SEM images in Fig. II-17 show spherical particles with an average diameter of about 500 nm, where appear metallic nanoparticles homogenously dispersed over the surface of the support with sizes less than 30 nm.

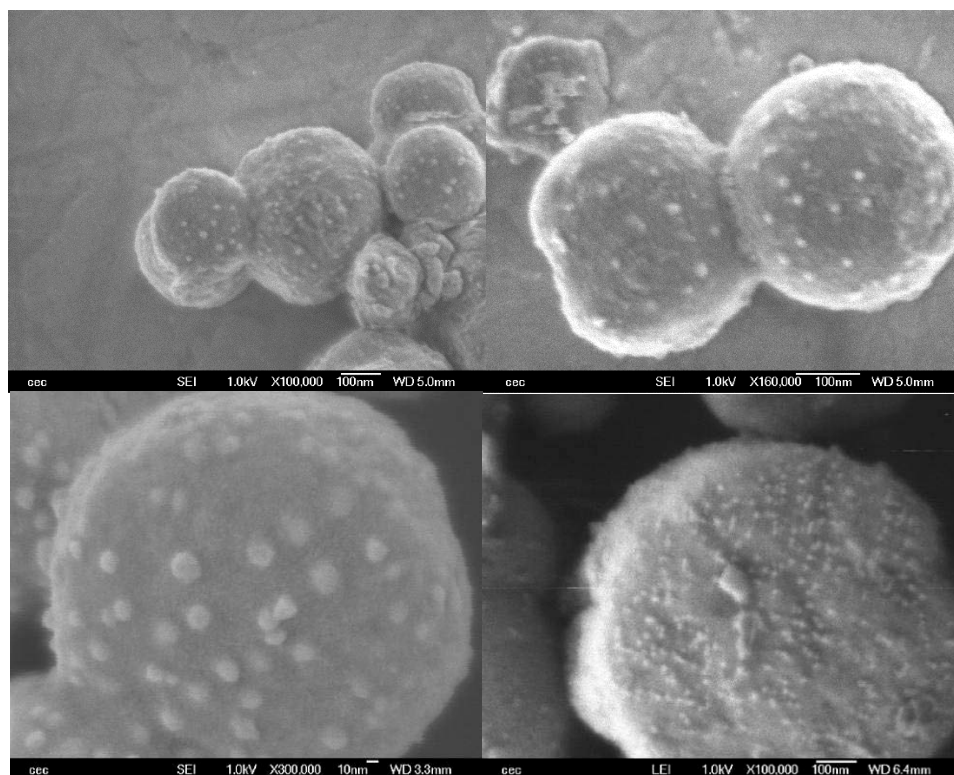


**Figure II-17.** SEM images of Co(H)MCM41-SC with metallic nanoparticles dispersed over the surface of the support

## CHAPTER II. Cobalt-based Catalysts

In TEM pictures (Fig. II-18), the intact pore structure can be identified and regular channels in the support after working with pressure. Besides, it can be sensed certain gradient of color from the inside of the support (with darker areas) towards the outside (lighter areas), implying that the metal is not only deposited on the external surface but also inside the pores.

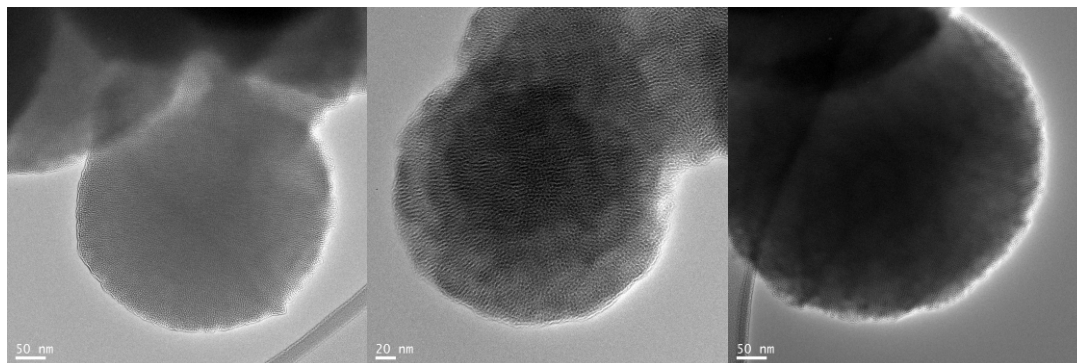


**Figure II-18.** TEM pictures of Co(L)MCM41-SC: pore structure and channels

Increasing the metal loading, samples still maintain the ordered pore structure of the support, but various cobalt nanoparticles appear located on the outer surface, assuming that the channels are filled.

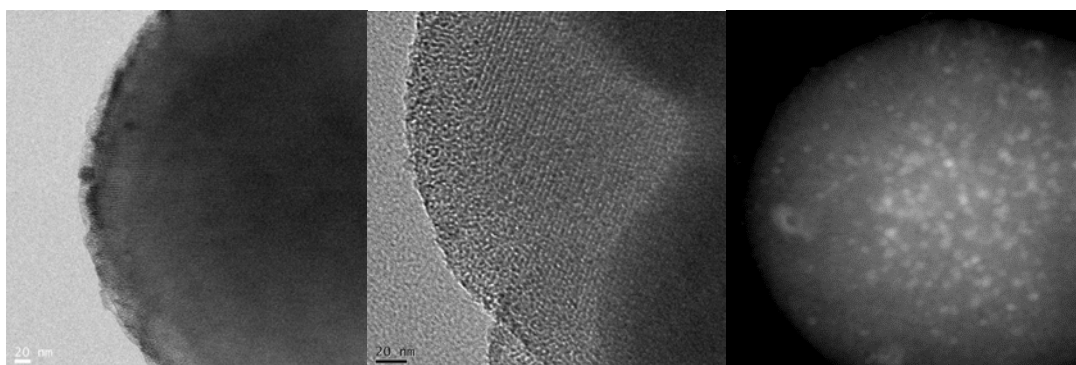


**Figure II-19.** TEM pictures of Co(H)MCM41-SC: (A) Metallic nanoparticles, (B) intact pore structure and channels of support, (C) BSE-Image

This premise is verified with MAPPING pictures (Fig. II-20), where it is possible to observe the homogeneous distribution of the metal into the support.

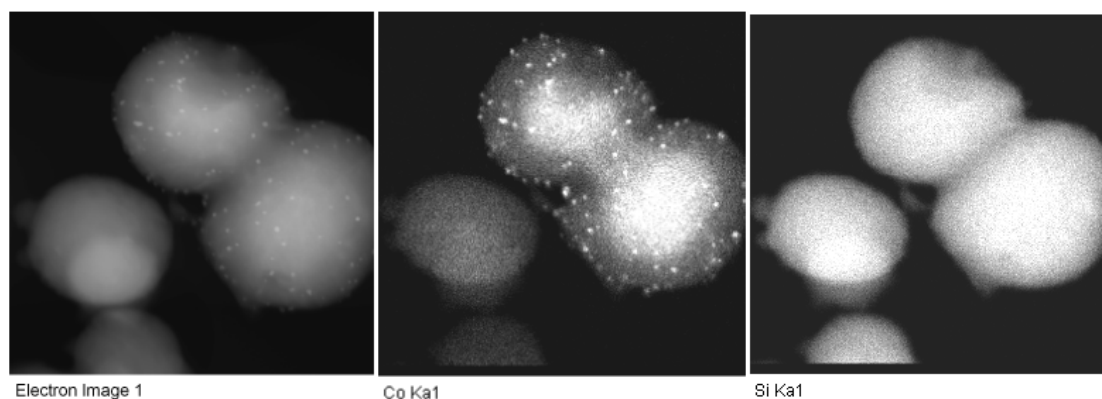


**Figure II-20.** X-Ray TEM/EDX Mapping for Co(H)MCM41-SC:  
(A) electron image, (B) Co  $\kappa\alpha$  and (C) Si  $\kappa\alpha$ .

However, to check if all active species are accessible inside the pores and can be easily reached by reactive molecules, hydrogen chemisorption was employed, showing the results for catalysts prepared by WI and SCFRD calcined at two different temperatures (500 and 800 °C) in the table II-8:

**Table II-8.** Metal dispersion results of Co-based catalysts by hydrogen chemisorptions.

Catalyst	% Metal dispersion	Metallic surface area ( $\text{m}^2/\text{g}_{\text{sample}}$ )	Metallic surface area ( $\text{m}^2/\text{g}_{\text{metal}}$ )	Crystallite Size (nm)
Co(L)MCM41-WI	0.05	0.02	0.34	1974
Co(L)MCM41-SC-500	2.19	0.89	14.82	45.50
Co(L)MCM41-SC-800	10.82	4.40	73.23	9.20
Co(H)MCM41-SC-500	3.22	3.61	21.76	30.98
Co(H)MCM41-SC-800	8.15	9.15	55.14	12.22

In view of these results, several conclusions can be drawn. First, although WI method can deposit cobalt onto a mesoporous material such as MCM-41 even with high loads, it seems not to be accessible. Nevertheless, the samples prepared by SCFRD show better metal dispersion and smaller particle diameters. This difference could be explained thanks to the high diffusivity of precursor dissolved in  $sc\text{-CO}_2$  compared to the WI method, allowing it to enter with relative ease through the pores and channels of support.

On the other hand, an increase in the metallic loading involves higher particles, and thus lower effective areas, as would be expected. In regard to the reduction temperature, these values show that it is necessary to use temperatures higher than 800 °C in order to achieve a complete activation of the catalyst, just as it was observed in TPR measurements formerly. According to these results, it is possible to obtain nanoparticles with sizes about 10 nm and a good dispersion of the metal over the surface of the support by means of SCFRD without their subsequently sintering produced by high temperatures.

## II.6. Activity Test: Gasification of cellulose for hydrogen production

Energy shortage and environmental pollution are two main challenges we have to deal with in the future. This situation has promoted numerous researches on the use of biomass and agricultural waste in energy conversion processes [59-62]. The principal benefit conferred by this technology is that bio-energy is an immense source of renewable and sustainable energy (~220 billion dry tones/year [63]), contributing approximately 12% of the global primary energy supply nowadays [64].

Following this trend, many techniques have been developed to produce hydrogen-rich gas or syngas from biomass [65-68]. Generally, the conventional gasification is carried out at 700-1000 °C and atmospheric pressure, where many by-products are generated, such as NO<sub>x</sub>, SO<sub>2</sub>, fly ash and tar.

In particular, tar formation is one of the major issues to be solved. This is a complex mixture of condensable hydrocarbons comprising single-ring to 5-ring aromatic compounds plus other oxygen-containing hydrocarbons and complex polyaromatic hydrocarbons (PAHs) [69, 70].

For pure cellulose, the kinetics of the primary reaction have been extensively studied; but by comparison, the secondary reaction of tar reforming are less well understood [71].

Several studies suggest the use of supercritical water as reaction medium [72-75] to reduce the process temperature, since the formation of most of these compounds starts at higher temperatures [76].

By contrast, other authors propose to use supported catalysts in order to achieve higher conversion efficiency in conventional gasification process. Numerous metals, such as Ni [77, 78], Ru [73, 74] or Pt [79], have been tested, showing in all cases a remarkable improvement in hydrogen production.

In this sense, it is not intended to avoid the formation of these compounds (PAHs), but rather they are recombined and degraded into smaller molecules, releasing H<sub>2</sub> during the reaction [69, 80-82].

### II.6.1. Experimental device

The activity of catalysts was tested by means of the gasification-pyrolysis of cellulose to produce hydrogen. These experiments were carried out in a TGA apparatus (TGA-DSC 1, METTLER TOLEDO) at different heating rates (10, 20 and 40 °C/min) up to 1000 °C. Fig. II-21 shows the diagram of these experiments.

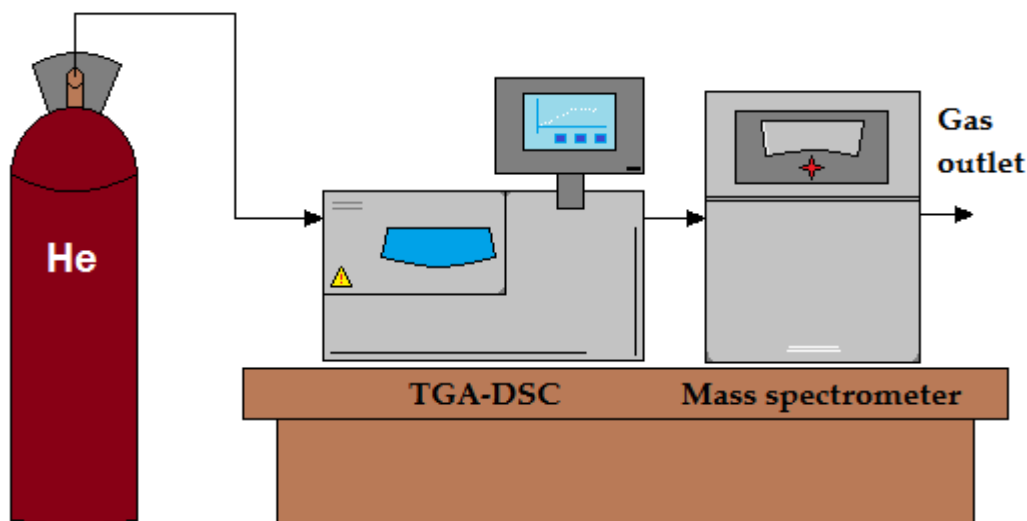


**Figure II-21.** Scheme of the experimental setup for the activity test

The following operating conditions were chosen from previous studies in TGA analysis [83, 84] in order to avoid the effects of heat and mass transfer limitations: sample weight was kept at 10 mg (catalyst + cellulose) and a constant flow rate of 20 Nml/min of helium (99.99%) was used as carrier gas to provide an inert atmosphere. The experimental error of these measurements was calculated, obtaining an error for all studied samples of  $\pm 0.5\%$  in weight loss measurements and  $\pm 2$  °C in temperature measurement.

The gas products coming from the thermal analysis were analyzed in a mass spectrometer (Thermostar-GSD 320/quadrupole mass analyzer; PFEIFFER VACUUM) with an electron ionization voltage at 70 eV and provided mass spectra up to 300 a.m.u. The interface was wrapped with heating wire to circumvent condensation of exhausting gases.

## II.6.2. Thermogravimetric studies on cellulose pyrolysis

The mass loss curves and the differential thermogravimetric (TGA/DTG) profiles of the cellulose (alone and catalyzed) as a function of temperature at a heating rate of 20 °C/min during the pyrolysis process are shown in Fig. II-22, which reveal marked differences between the pyrolysis behavior in presence of various catalysts. Table II-9 summarizes the most relevant pyrolysis characteristics for cellulose gasification.

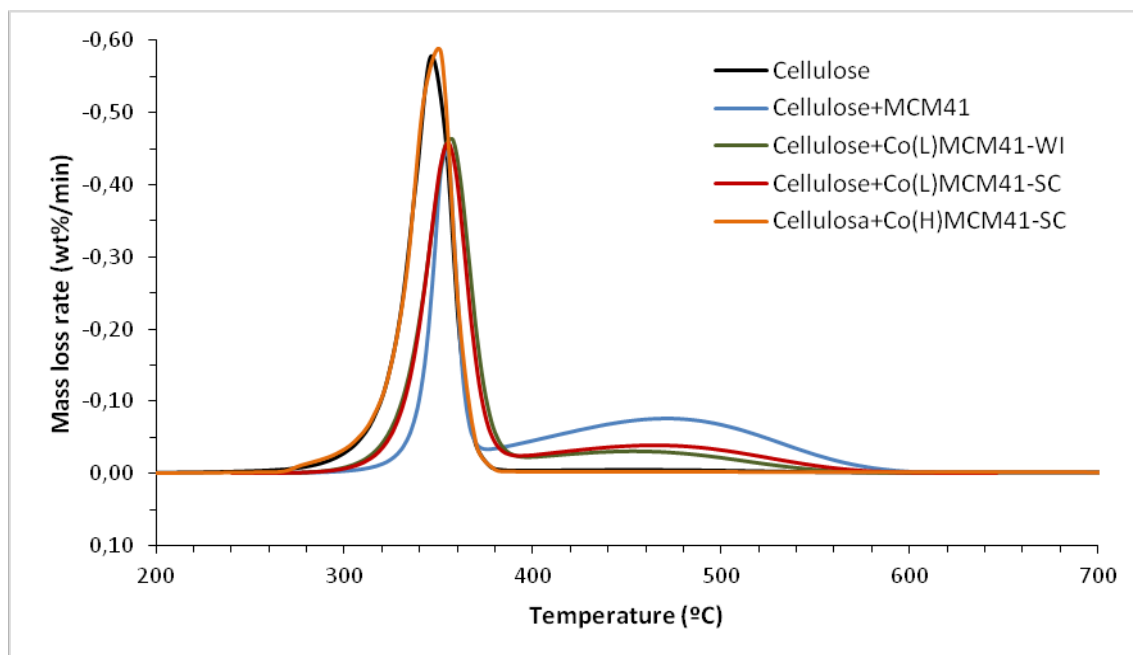


**Figure II-22.** TGA/DTG profiles of pyrolysis process of cellulose at a heating rate of 20°C

\*WI – catalysts prepared by wet impregnation; SC – by SCFRD

\*\* (L) – low metallic loading ~5%; (H) – high metallic loading ~15%

**Table II-9.** Pyrolysis characteristic parameter for cellulose gasification

	Cellulose	Cel+MCM41		Cel+WI		Cel+SC(L)		Cel+SC(H)
	1 <sup>st</sup> peak	1 <sup>st</sup> peak	2 <sup>nd</sup> peak	1 <sup>st</sup> peak	2 <sup>nd</sup> peak	1 <sup>st</sup> peak	2 <sup>nd</sup> peak	1 <sup>st</sup> peak
$T_{\text{pyr}}^{\text{a}}$ (°C)	268	302		293		293		270
$T_{\text{p0}}^{\text{b}}$ (°C)	268	302	372	293	391	293	397	270
$T_{\text{pf}}^{\text{c}}$ (°C)	380	372	600	391	583	397	555	380
$T_{\text{p}}^{\text{d}}$ (°C)	346	360	477	358	481	358	457	351
$(\text{dw}/\text{dt})_{\text{max}}^{\text{e}}$ (wt.%/min)	0.58	0.46	0.07	0.45	0.04	0.44	0.03	0.57
Residue yield (wt.%)	6.3	4.4		5.5		6.1		4.5

<sup>a</sup>  $T_{\text{pyr}}$  - Temperature at which the pyrolysis started

<sup>b</sup>  $T_{\text{p0}}$  - Initial peak temperature

<sup>c</sup>  $T_{\text{pf}}$  - Final peak temperature

<sup>d</sup>  $T_{\text{p}}$  - Peak temperature

<sup>e</sup>  $(\text{dw}/\text{dt})_{\text{max}}$  - Maximum weight loss rate

The decomposition of cellulose, in which 93% by weight was lost, took place between 268 and 380 °C, reaching its maximum value at 346 °C. It can be noticed the pronounced DTG profile of the cellulose presenting a weight loss rate of 0.58 wt%/min. During this stage, a complex set of reactions as denitration and deacetylation, scission of C-O, C-C and C-H bonds might take place [85].

The use of MCM-41 in this reaction promotes the production of tar, as shown in Fig. II-22. Cellulose starts to decompose at a higher temperature (302 °C), reducing its weight loss rate from 360 °C. Therefore, a second peak appears in the DTG profile between 372 and 600 °C. This second peak is related to the oxidation of the char and tar formed during the devolatilization stage [86] favored by the slight acidity of the support.

Cobalt-based catalysts, prepared both by WI and SCFRC with the same metal loading, exhibit analogous TGA/DTG profiles to that of cellulose with bare MCM-41t, as can be seen from Fig. II-22. However, the temperature in which the second peak appears is delayed until 391 and 397 °C respectively, as well as a reduction in mass loss in the second peak. Apparently, this behavior could be attributed to a shielding effect caused by the metallic particles on the surface, reducing the useful area of contact with the support and thus, hindering the reaction of tar with the acid sites of the support. By contrast, another authors [80] explain that metal accelerate the oxidation of char and tar to volatiles.

This effect is multiplied when the metal loading is increased, obtaining similar TGA-DTG profiles to the decomposition of cellulose alone with only one peak at 380 °C, being necessary other kind of analysis, such as the identification and quantification of the flue gases, to determine what really happens and propose a theory.

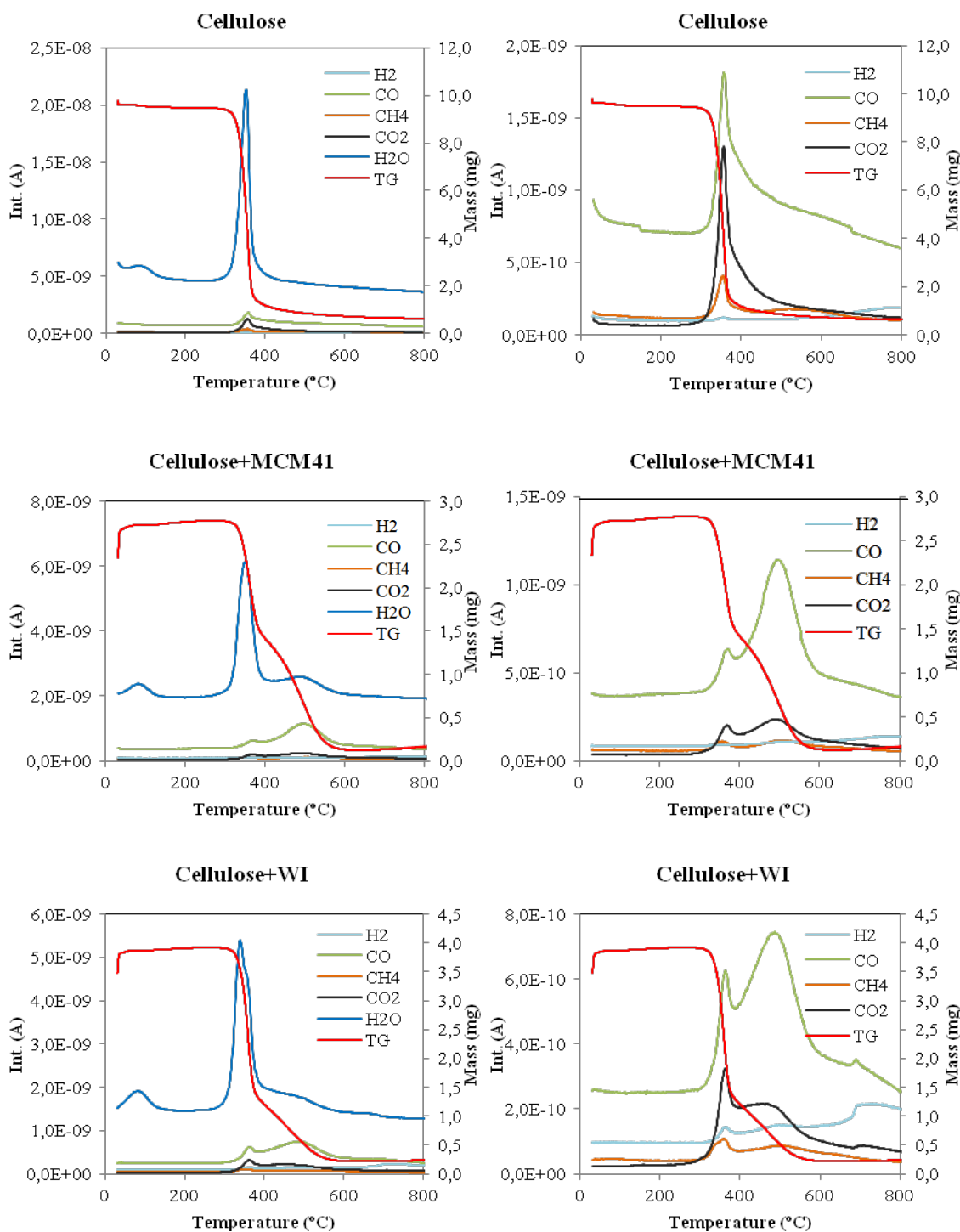
### II.6.3. Gas products analysis

The pyrolysis behavior of biomass by means of TGA-MS has been studied by different authors [83, 84, 87]. TGA-MS measurements reproduce the evolution and distribution of the main gas products during the process. The present work was focused on the main volatile products of cellulose degradation on the basis of both their relative intensities and relevancy. H<sub>2</sub>, CH<sub>4</sub>, H<sub>2</sub>O, CO and CO<sub>2</sub>, and assigned to the ion/mass intensities

## CHAPTER II. Cobalt-based Catalysts

(m/z) 2, 16, 18, 30 and 44, respectively (according to the database of National Institute of Standards and Technology, NIST) [88].

Mass spectrometry analyses for cellulose pyrolysis are shown in Fig. II-23, and data about H<sub>2</sub> selectivity summarized in Table II-10.



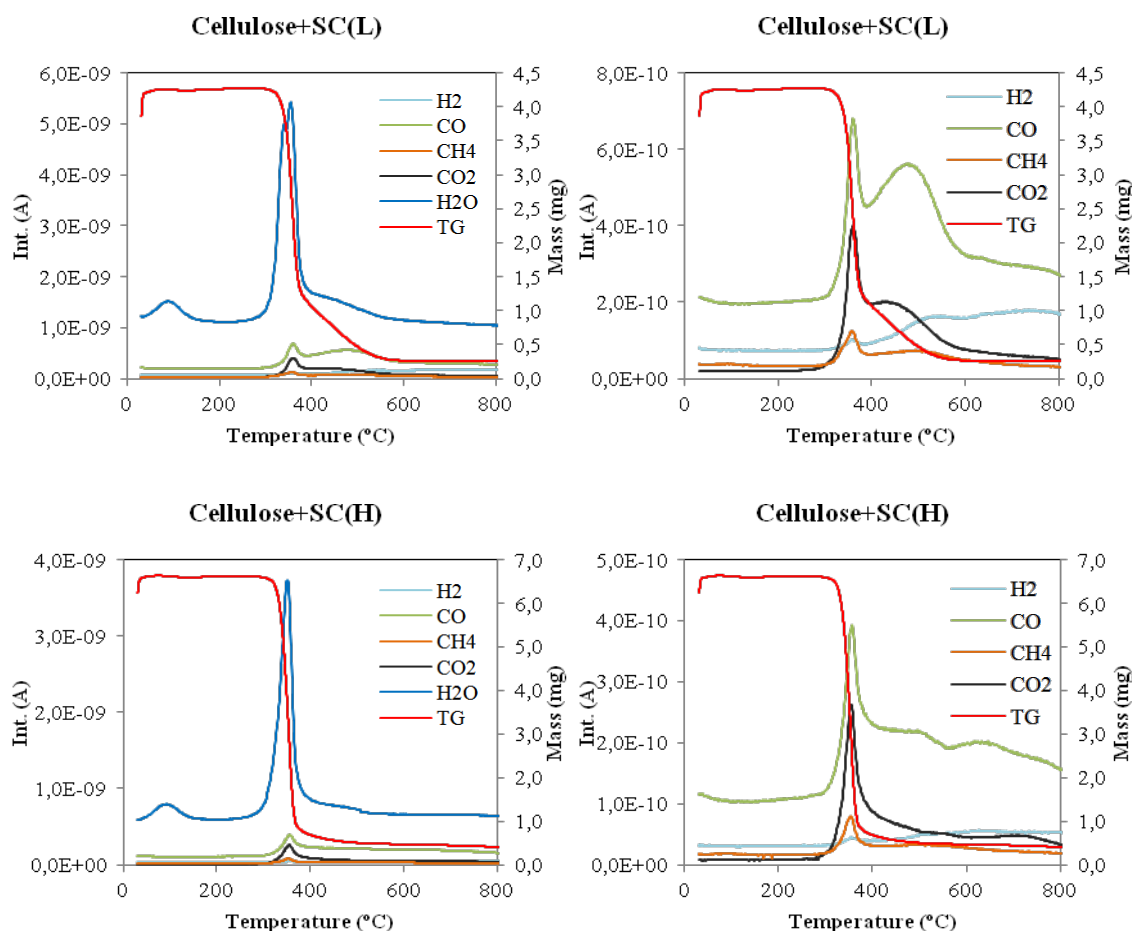


**Figure II-23.** TGA-MS spectra of combustion process of cellulose at a heating rate of 20°C  
 \*H<sub>2</sub>, CO, CH<sub>4</sub>, CO<sub>2</sub> and water have been represented in the graphics of the left column;  
 while in the right column, water has been removed for a better understanding of the process

**Table II-10.** Selectivity of H<sub>2</sub>/CO ratio analyzed by mass spectrometry

\*Catalysts synthesized by SCFRD were tested at 2 reduction temperatures: 500 °C and 800 °C

	H <sub>2</sub> /CO
Cellulose	7.61
Cellulose + MCM41	19.59
Cel + Co(L)MCM41-WI	29.19
Cel + Co(L)MCM41-SC/500	29.62
Cel + Co(L)MCM41-SC/800	28.74
Cel + Co(H)MCM41-SC/500	25.04
Cel + Co(H)MCM41-SC/800	25.72

As aforementioned, the pyrolysis of cellulose occurred in a relatively narrow range of temperature (300-400 °C) coincidental with the major emission peak for all products at the devolatilization stage and in good agreement with its maximum DTG peak. The main gas detected was in all cases H<sub>2</sub>O, followed by CO and CO<sub>2</sub>.

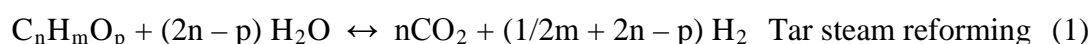
The first peak at low temperatures (<150 °C) represented the drying process of the samples, losing the moisture and very light volatiles compounds. Secondly, the main

## CHAPTER II. Cobalt-based Catalysts

peak (between 300 and 400 °C) is related to the degradation of glycosyl units in cellulose which produces four well-identified products (H<sub>2</sub>O, CH<sub>4</sub>, CO and CO<sub>2</sub>) and leading to the formation of char residue. Xie et al. [89] stated that during this process the complete decomposition of glycosidic structures proceeded. Furthermore, rapid depolymerization of cellulose turned into the breakdown of the molecule, producing a variety of low molecular weight products [90], reducing the selectivity of the reaction. Then, CO and CO<sub>2</sub> were continuously evolved, increasing the production of CH<sub>4</sub> around 500 °C. The evolution of these gases is associated to carbonate decomposition, consequence of the loss of carbonyl and carboxyl groups previously formed by the oxidation of hydroxyl groups [90]. Finally, most of the H<sub>2</sub> emission was observed at high temperatures, over 700 °C, corresponding to char decomposition.

TGA-MS spectra of cellulose with MCM-41 reveal the same stages, but in this case the most of the main volatiles products were detected as of 400 °C. The selectivity of H<sub>2</sub>/CO ratio increases from 7.6 to 19.6% due to new reaction mechanisms promoted by the slight acidity of the support.

The product distribution in the last stage at temperatures above 500 °C, suggested that secondary reaction took place. These reactions could be attributed to tar cracking (1 and 2), being CO<sub>2</sub>, CH<sub>4</sub> and H<sub>2</sub> mainly formed [91]. This fact could explain the decrease in the mass loss rate observed in TGA profiles as result of greater tar production.



The incorporation of cobalt-based catalysts enhances the production of H<sub>2</sub>. At temperatures lower than 400 °C, H<sub>2</sub> was produced as CH<sub>4</sub> and -CH<sub>3</sub> groups are consumed, attributed to CH<sub>4</sub> steam reforming reaction (3) [92].



On the other hand, the production of H<sub>2</sub> was still increasing above 500 °C, reducing the amount of CO. This fact could be explained thanks to the promotion of water-gas shift reaction by cobalt nanoparticles.



If the results obtained by different catalysts preparation methods are compared, several conclusions can be drawn.

Both techniques achieve the same selectivity of H<sub>2</sub>/CO ratio, around 30%. However, the major production of H<sub>2</sub> with the catalyst prepared by WI was obtained over 700 °C, related to char decomposition. On the contrary, catalyst prepared by SFRD enabled superior yields at lower temperatures, finding smaller peaks for CH<sub>4</sub>, CO and CO<sub>2</sub> over 500 °C and thereby reducing operational temperature.

As shown in the data of Table II-10, the selectivity of H<sub>2</sub> decreased slightly from 30 to 25% with increasing the metal loading of the catalyst. These results are in agreement with other authors [93], where it has been obtained an optimum value for this reaction between 6-10 wt%. Comparing the profiles, it can be noticed the reactions proposed previously were slowed, obtaining a figure similar to decomposition of cellulose alone.

Regarding the reduction temperature of catalysts, it has not been found significant differences in either the evolution profiles of emitted gases or hydrogen selectivity to justify the activation of the catalyst at 800 °C.

### II.6.4. Kinetics Model

It has been proposed a three-reaction model in which cellulose breaks down into gaseous products and intermediate decomposition compounds (charcoal and tar) via three simultaneous reactions [94]. According to previous results obtained by Broido and other researches [95], below approximately 280°C, the formation of char and permanent gas is assumed to be favored, while above this temperature, it is the formation of tar which is preferential due to the predominant depolymerization reactions associated to the breakage of glycosidic bonds. Figure II-24 describes the proposed mechanism, where each path is completed adding the decomposition of each charcoal to volatiles and with the vaporization of liquids phases [96].

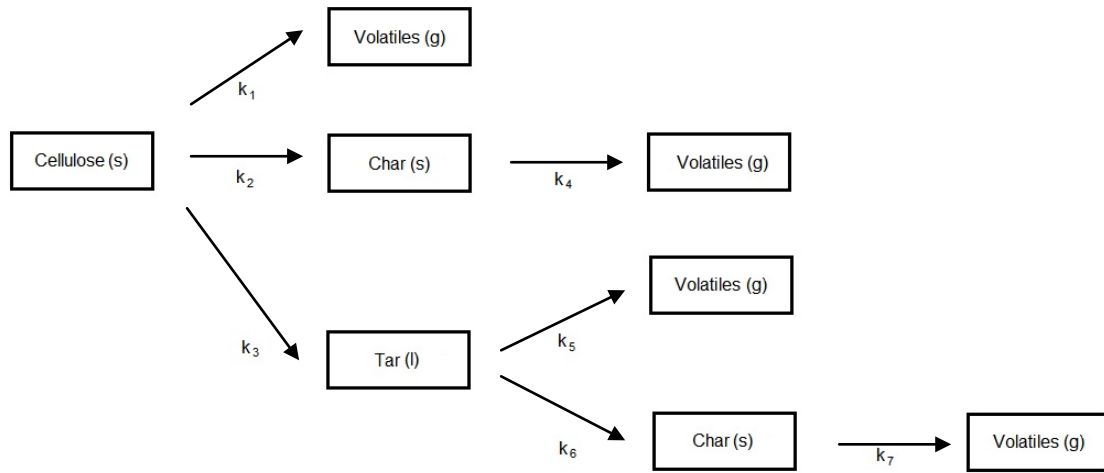


**Figure II-24.** Reaction mechanism proposed

Kinetics is divided in two groups, real reaction kinetics for the solid materials, and mass transfer kinetics for the liquid phase. There are two options for the former: a first order reaction (5) and an autocatalytic reaction (6). The first one is the most extended option in literature [97-100]; nevertheless, the second one is proposed because its response is very similar to the behavior of the biomass observed in previous works and studies [101]. Both kinetic equations consider an Arrhenius dependence with temperature.

$$r_i = k_{0_i} \cdot e^{-\frac{E_{a_i}}{R \cdot T}} \cdot m_j^{n_i} \quad (5)$$

$$r_i = k_{0_i} \cdot e^{-\frac{E_{a_i}}{R \cdot T}} \cdot m_j^{n_i} \cdot (1 - \alpha_i \cdot m_j)^{\beta_i} \quad (6)$$

The coefficient  $\alpha_i$  is the initialization factor which indicates the resistance of the cellulose against the degradation and it is used to establish the initial value of the reaction velocity. Usually, this parameter is fixed at 0.99 as typical value for this kind of reactions [101]. The coefficient  $\beta_i$  is the acceleration factor and represents how fast the degradation is once it has started. The autocatalytic kinetic can explain the dramatic changes in total mass at a narrow interval of temperatures better than a first order kinetics.

Kinetics in liquid phase is based in the mass transfer to gas phase which is reproduced by the partial mass transfer coefficient of the gas phase (7)

$$r_i = h \cdot S \cdot (C_j^* - C_j) \quad (7)$$

As the operating pressure is the atmospheric, the equilibrium concentration is obtained from the ideal gas equation and the vapor pressure obtained from the Antoine equation.

$$C_j^* = \frac{P_j^*}{R \cdot T} \quad (8)$$

In addition, the transfer area can be considered as a function of the mass in the solid, so the final expression for the mass transfer kinetics is as follow:

$$r_i = h \cdot (C_j^*) \cdot m_j^{nl_i} \quad (9)$$

### II.6.5. Results and discussion

Figures II-25 to II-29 show the experimental (dotted line) compared to the predicted curve (solid line) and the evolution of different compounds obtained by the kinetic model described previously for cellulose pyrolysis at a heating rate of 20 °C/min and a constant ratio metal/cellulose of 0.05. In the experiment carried out with MCM-41, the same relationship as if it had a load of 5 %wt was remained, so that all the experiences were comparable.

It can be noticed that the proposed mechanism adequately reproduces the experimental values, with an average absolute deviation around 7%. The calculated kinetic parameters are presented in Table II-11.

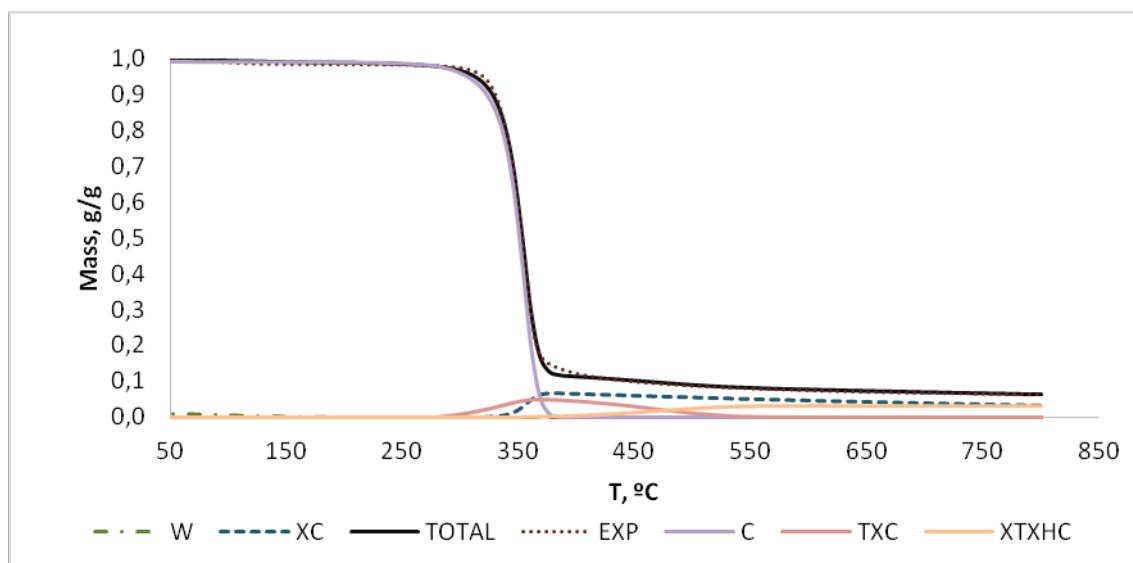


**Figure II-25.** Real TGA and predicted curve by the autocatalytic model together with the evolution of the intermediate products for cellulose pyrolysis at a heating rate of 20 °C/min:  
\*W) water, XC) char, C) cellulose, TXC) tar, and XTXHC) char from tar

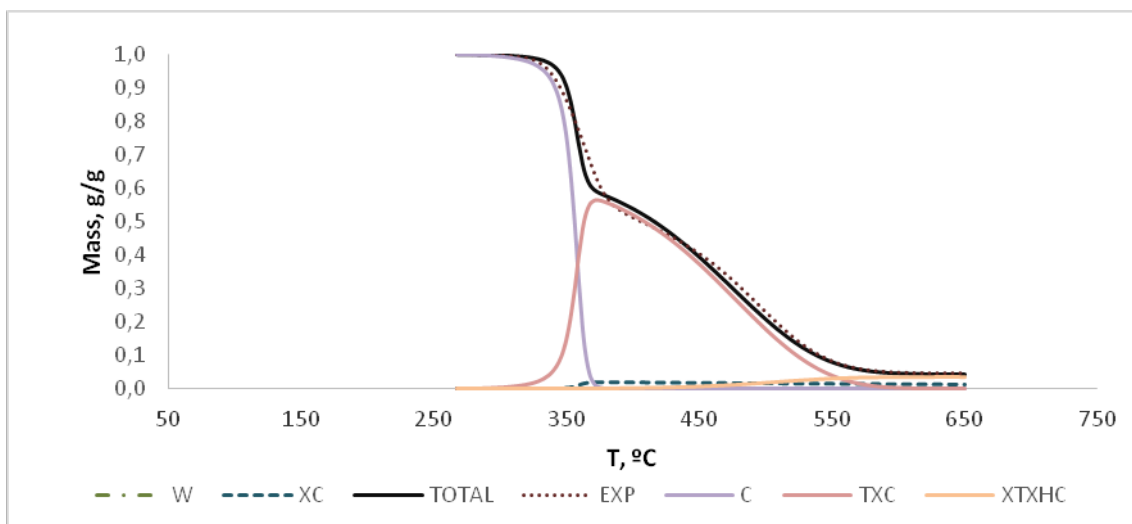


**Figure II-26.** Real TGA and predicted curve by the model proposed together with the evolution of the intermediate products for cellulose pyrolysis at a heating rate of 20 °C/min with MCM41:  
 \*W) water, XC) char, C) cellulose, TXC) tar, and XTXHC) char from tar

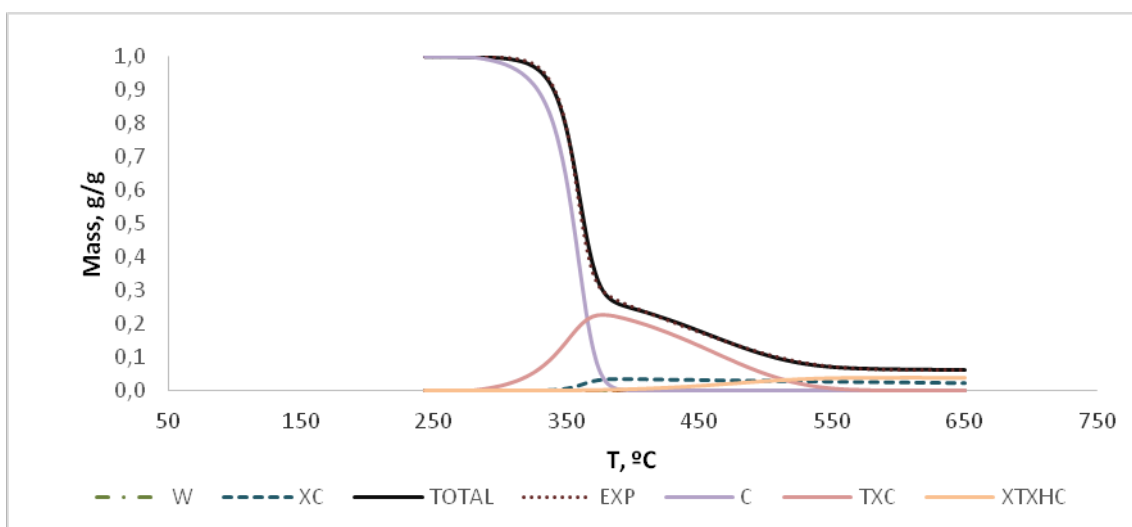


**Figure II-27.** Real TGA and predicted curve by the model proposed together the evolution of the intermediate products for cellulose combustion at a heating rate of 20 °C/min with Co(L)MCM41-WI  
 \*W) water, XC) char, C) cellulose, TXC) tar, and XTXHC) char from tar

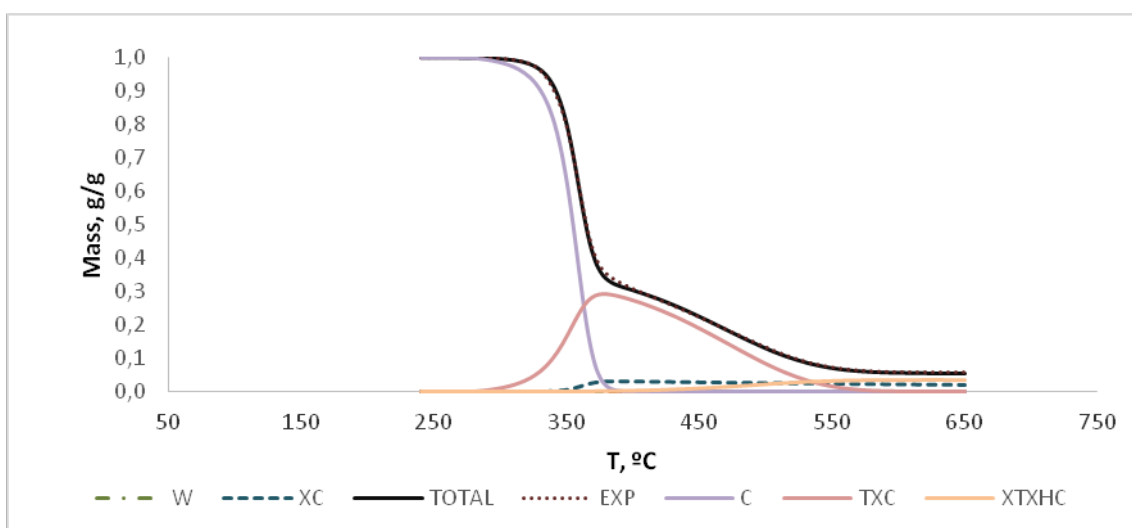


**Figure II-28.** Real TGA and predicted curve by the model proposed together the evolution of the intermediate products for cellulose combustion at a heating rate of 20 °C/min with Co(L)MCM41-SC  
 \*W) water, XC) char, C) cellulose, TXC) tar, and XTXHC) char from tar

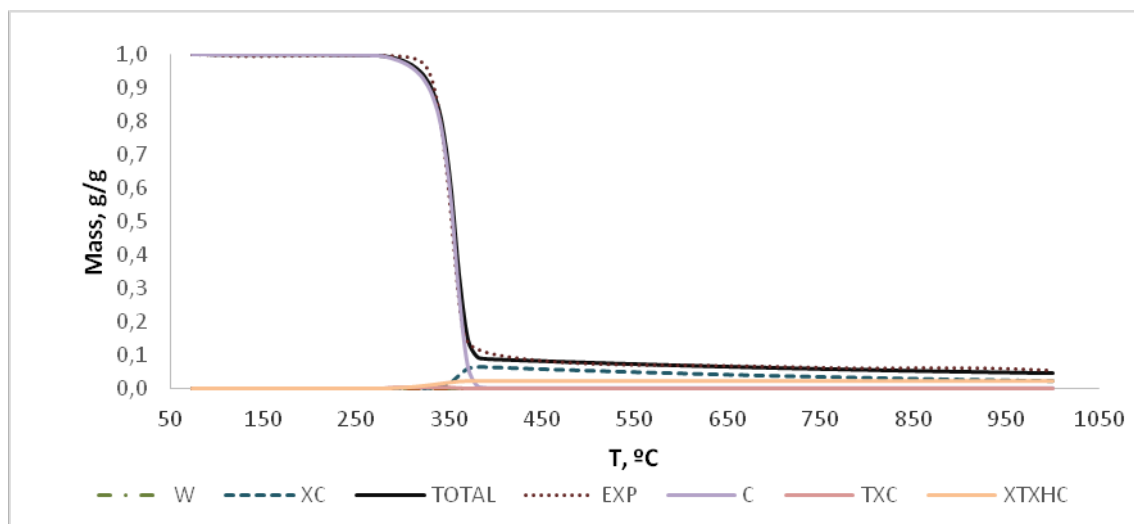


**Figure II-29.** Real TGA and predicted curve by the model proposed together the evolution of the intermediate products for cellulose combustion at a heating rate of 20 °C/min with Co(H)MCM41-SC  
\*W) water, XC) char, C) cellulose, TXC) tar, and XTXHC) char from tar

**Table II-11.** Kinetics parameters for each reaction fitted by the model

	<b>R<sub>1</sub></b>			<b>R<sub>2</sub></b>			<b>R<sub>3</sub></b>			<b>R<sub>5</sub></b>		<b>R<sub>6</sub></b>		
	<b>K</b>	<b>E</b>	<b>r</b>	<b>K</b>	<b>E</b>	<b>R</b>	<b>k</b>	<b>E</b>	<b>R</b>	<b>K</b>	<b>E</b>	<b>k</b>	<b>e</b>	<b>R</b>
Cellulose	25.14	5.68	1.39	31.91	7.19	1.90	2.97	7.22	0	14.41	8.59	45.99	9.18	0
Cellulose + MCM41	25.14	5.88	1.39	31.77	7.72	1.91	13.37	5.24	1.36	14.61	8.14	38.42	10.66	1.40
Cellulose + Co(L)/MCM41-WI	25.14	5.88	1.39	31.77	7.72	1.91	12.34	6.34	0.69	13.06	8.04	38.44	10.19	1.39
Cellulose + Co(L)/MCM41-SC	25.14	5.88	1.39	31.77	7.72	1.91	11.98	6.69	0.47	13.33	7.96	38.57	9.82	1.39
Cellulose + Co(H)/MCM41-SC	25.14	5.69	1.39	31.91	7.19	1.90	1.38	6.54	0	18.38	4.78	46.34	5.90	0

*k*: Pre-exponential factor for the reaction [ $e^3 \cdot \text{min}^{-1}$ ]

*e*: Activation energy of the reaction:  $E_a/R$  [ $e^3 \cdot K$ ]

*r*: Acceleration factor [--]

\*Reactions 4 and 7 are very slow ( $k < 10^{-3}$ ) and do not influence the calculations

In the test with only cellulose, the thermal break starts at 270 °C with the fractionation of the cellulose and continues until 400 °C, obtaining charcoal as residue beyond this temperature. This behavior of cellulose thermal decomposition kinetics is summarized in Table II-11 and it agrees with previous works [102].

The use of an autocatalytic kinetics is justified by the very steep slope obtained in the thermal decomposition of cellulose, as seen in TGA profiles. In case of using first order kinetics, extremely high Pre-exponential factors are obtained. However, the autocatalytic model provides more reasonable values. The physical explanation of the employ of an autocatalytic kinetics is that solid polymers, such as cellulose, once they start to decompose are more likely to be attacked by external agents, and therefore increase their degradation rate as if were a chain reaction.

## CHAPTER II. Cobalt-based Catalysts

Adding cobalt-based catalysts, all experiences showed almost the same kinetic behavior, except in tar formation reaction ( $R_3$ ), supporting the conclusions drawn by TGA profiles.

In contact with the catalyst, gases produced by the first reaction ( $R_1$ ) were recombined, leading the formation of tar. According to the estimations obtained by the proposed kinetics model, the activation energy of  $R_3$  decreases, the pre-exponential factor increases considerably and also acquires autocatalytic nature. Furthermore, the reaction  $R_6$ , which corresponds to the formation of new char from tar, it also becomes to be autocatalytic. Apparently, the gasification of cellulose in this way produces a larger amount of tar, predominantly composed of polycyclic aromatic hydrocarbons (PAH), which in turn increases the selectivity for hydrogen.

Increasing the metal loading, kinetic parameters are similar to that obtained in the initial test where no catalyst is used. A new mechanism for reaction  $R_3$  is observed, losing its autocatalytic character, which supports the results obtained in TGA profiles discussed above.

## II.7. Conclusions

In conclusion, in this chapter cobalt-based catalysts have been synthesized on MCM-41 from cobaltocene ( $\text{CoCp}_2$ ) as organometallic precursor by means of supercritical fluid reactive deposition. For this, we have developed the following fundamental aspects:

- ✓ It has been determined that the adsorption isotherm of  $\text{CoCp}_2$  on MCM-41 is concave upward (type III), characteristic of low adsorbate-adsorbent interactions. The experimental data have been fitted by exponential, sigmoid and BET model, with average error lower than 2%, and predicting a theoretical value for the equilibrium adsorptive capacity around 65 mg/g.
- ✓ Due to the unfavorable adsorption of this organometallic complex ( $\text{CoCp}_2$ ) on this support (MCM-41), Supercritical Fluid Deposition must be followed by an in situ decomposition reaction, leading to the named process supercritical Fluid Reactive Deposition.
- ✓ SCFRD has been optimized for the synthesis of Co/MCM-41 catalysts. This is a one-pot process which consists of one stage of 60 min at 200 °C and 14 MPa. To solve the problems caused by mass transfer limitations, a new configuration in “sandwich” type has been proposed, in which precursor and support are placed alternatively inside the reactor.
- ✓ It has been proved that SCFRD is viable for the manufacture of catalysts with high metallic loading through consecutive depositions, achieving cobalt loads higher than 15 %wt.
- ✓ Co/MCM-41 catalysts have been characterized by different techniques and compared to other samples prepared by conventional synthesis methods. The results showed that catalysts prepared by SCFRD have better metal dispersion over the surface and smaller particle diameters, accessible even inside the pores by reactive molecules. Increasing the metal loading, catalysts showed cobalt crystals located on the outer surface. The adsorbed cobalt species corresponds to the  $\text{Co}_3\text{O}_4$  spinel, being necessary temperatures up to 800 °C to reduce the catalysts.

## CHAPTER II. Cobalt-based Catalysts

- ✓ Catalysts have been tested in the gasification of cellulose for H<sub>2</sub> production. These experiences have revealed that the cobalt catalysts prepared by SCFRD increase the selectivity of the process from 7% to 30% as a result of the promotion of tar production. Experimental data have been fitted by a three-reaction model, with average absolute deviation around 7%, with the purpose of study the evolution of the different compounds obtained in the cellulose pyrolysis, and therefore, demonstrating the effect of the cobalt changing the reaction mechanism to tar formation.

II.8. References

1. Passos, A.R., L. Martins, S.H. Pulcinelli, C.V. Santilli, and V. Briois, *Effect of the balance between Co(II) and Co(0) oxidation states on the catalytic activity of cobalt catalysts for Ethanol Steam Reforming*. *Catalysis Today*, 2014. **229**: p. 88-94.
2. Pairojpiriyakul, T., E. Croiset, W. Kiatkittipong, K. Kiatkittipong, A. Arpornwichanop, and S. Assabumrungrat, *Hydrogen production from catalytic supercritical water reforming of glycerol with cobalt-based catalysts*. *International Journal of Hydrogen Energy*, 2013. **38**(11): p. 4368-4379.
3. Chiou, J.Y.Z., C.-L. Lee, K.-F. Ho, H.-H. Huang, S.-W. Yu, and C.-B. Wang, *Catalytic performance of Pt-promoted cobalt-based catalysts for the steam reforming of ethanol*. *International Journal of Hydrogen Energy*, 2014. **39**(11): p. 5653-5662.
4. Garbarino, G., P. Riani, M.A. Lucchini, F. Canepa, S. Kawale, and G. Busca, *Cobalt-based nanoparticles as catalysts for low temperature hydrogen production by ethanol steam reforming*. *International Journal of Hydrogen Energy*, 2013. **38**(1): p. 82-91.
5. Papadopoulou, E., D. Delimaris, A. Denis, A. Machocki, and T. Ioannides, *Alcohol reforming on cobalt-based catalysts prepared from organic salt precursors*. *International Journal of Hydrogen Energy*, 2012. **37**(21): p. 16375-16381.
6. Zhang, G., Y. Du, Y. Xu, and Y. Zhang, *Effects of preparation methods on the properties of cobalt/carbon catalyst for methane reforming with carbon dioxide to syngas*. *Journal of Industrial and Engineering Chemistry*, 2014. **20**(4): p. 1677-1683.
7. Pereira, E.B., P.R. de la Piscina, and N. Homs, *Efficient hydrogen production from ethanol and glycerol by vapour-phase reforming processes with new cobalt-based catalysts*. *Bioresour Technol*, 2011. **102**(3): p. 3419-23.
8. Niu, W., D. Ren, Y. Han, Y. Wu, and X. Gou, *Optimizing preparation of carbon supported cobalt catalyst for hydrogen generation from NaBH<sub>4</sub> hydrolysis*. *Journal of Alloys and Compounds*, 2012. **543**: p. 159-166.
9. Llorca, J., *Efficient Production of Hydrogen over Supported Cobalt Catalysts from Ethanol Steam Reforming*. *Journal of Catalysis*, 2002. **209**(2): p. 306-317.
10. Busca, G., U. Costantino, T. Montanari, G. Ramis, C. Resini, and M. Sisani, *Nickel versus cobalt catalysts for hydrogen production by ethanol steam reforming: Ni-Co-Zn-Al catalysts from hydrotalcite-like precursors*. *International Journal of Hydrogen Energy*, 2010. **35**(11): p. 5356-5366.
11. Chen, L., C.K.S. Choong, Z. Zhong, L. Huang, Z. Wang, and J. Lin, *Support and alloy effects on activity and product selectivity for ethanol steam reforming over supported nickel cobalt catalysts*. *International Journal of Hydrogen Energy*, 2012. **37**(21): p. 16321-16332.
12. Resini, C., M. Concepción Herrera Delgado, S. Presto, L.J. Alemany, P. Riani, R. Marazza, G. Ramis, and G. Busca, *Yttria-stabilized zirconia (YSZ) supported Ni-Co alloys (precursor of SOFC anodes) as catalysts for the steam reforming of ethanol*. *International Journal of Hydrogen Energy*, 2008. **33**(14): p. 3728-3735.
13. de la Peña O'Shea, V.A., R. Nafria, P. Ramírez de la Piscina, and N. Homs, *Development of robust Co-based catalysts for the selective H<sub>2</sub>-production by*

- ethanol steam-reforming. The Fe-promoter effect.* International Journal of Hydrogen Energy, 2008. **33**(13): p. 3601-3606.
14. Casanovas, A., M. Roig, C. de Leitenburg, A. Trovarelli, and J. Llorca, *Ethanol steam reforming and water gas shift over Co/ZnO catalytic honeycombs doped with Fe, Ni, Cu, Cr and Na.* International Journal of Hydrogen Energy, 2010. **35**(15): p. 7690-7698.
  15. Xiong, H., M.A.M. Motchelaho, M. Moyo, L.L. Jewell, and N.J. Coville, *Cobalt catalysts supported on a micro-coil carbon in Fischer–Tropsch synthesis: A comparison with CNTs and CNFs.* Catalysis Today, 2013. **214**: p. 50-60.
  16. Xiong, H., Y. Zhang, K. Liew, and J. Li, *Ruthenium promotion of Co/SBA-15 catalysts with high cobalt loading for Fischer–Tropsch synthesis.* Fuel Processing Technology, 2009. **90**(2): p. 237-246.
  17. Griboval-Constant, A., A. Butel, V.V. Ordonsky, P.A. Chernavskii, and A.Y. Khodakov, *Cobalt and iron species in alumina supported bimetallic catalysts for Fischer–Tropsch reaction.* Applied Catalysis A: General, 2014. **481**: p. 116-126.
  18. Parnian, M.J., A. Taheri Najafabadi, Y. Mortazavi, A.A. Khodadadi, and I. Nazzari, *Ru promoted cobalt catalyst on  $\gamma$ -Al<sub>2</sub>O<sub>3</sub>: Influence of different catalyst preparation method and Ru loadings on Fischer–Tropsch reaction and kinetics.* Applied Surface Science, 2014. **313**: p. 183-195.
  19. Grams, J., A. Ura, and W. Kwapiński, *ToF-SIMS as a versatile tool to study the surface properties of silica supported cobalt catalyst for Fischer–Tropsch synthesis.* Fuel, 2014. **122**: p. 301-309.
  20. Shimura, K., T. Miyazawa, T. Hanaoka, and S. Hirata, *Fischer–Tropsch synthesis over alumina supported cobalt catalyst: Effect of crystal phase and pore structure of alumina support.* Journal of Molecular Catalysis A: Chemical, 2014. **394**: p. 22-32.
  21. Cook, K.M., H.D. Perez, C.H. Bartholomew, and W.C. Hecker, *Effect of promoter deposition order on platinum-, ruthenium-, or rhenium-promoted cobalt Fischer–Tropsch catalysts.* Applied Catalysis A: General, 2014. **482**: p. 275-286.
  22. Davari, M., S. Karimi, A. Tavasoli, and A. Karimi, *Enhancement of activity, selectivity and stability of CNTs-supported cobalt catalyst in Fischer-Tropsch via CNTs functionalization.* Applied Catalysis A: General, 2014.
  23. Liu, C., J. Li, Y. Zhang, S. Chen, J. Zhu, and K. Liew, *Fischer–Tropsch synthesis over cobalt catalysts supported on nanostructured alumina with various morphologies.* Journal of Molecular Catalysis A: Chemical, 2012. **363-364**: p. 335-342.
  24. Martínez, A.n., C. López, F. Márquez, and I. Díaz, *Fischer–Tropsch synthesis of hydrocarbons over mesoporous Co/SBA-15 catalysts: the influence of metal loading, cobalt precursor, and promoters.* Journal of Catalysis, 2003. **220**(2): p. 486-499.
  25. Wu, H., Y. Yang, H. Suo, M. Qing, L. Yan, B. Wu, J. Xu, H. Xiang, and Y. Li, *Effect of TiO<sub>2</sub> promotion on the structure and performance of silica-supported cobalt-based catalysts for Fischer–Tropsch synthesis.* Journal of Molecular Catalysis A: Chemical, 2014. **390**: p. 52-62.
  26. Karolewska, M., E. Truszkiewicz, B. Mierzwa, L. Kępiński, and W. Raróg-Pilecka, *Ammonia synthesis over cobalt catalysts doped with cerium and barium. Effect of the ceria loading.* Applied Catalysis A: General, 2012. **445-446**: p. 280-286.

27. Karolewska, M., E. Truskiewicz, M. Wściseł, B. Mierzwa, L. Kępiński, and W. Raróg-Pilecka, *Ammonia synthesis over a Ba and Ce-promoted carbon-supported cobalt catalyst. Effect of the cerium addition and preparation procedure*. Journal of Catalysis, 2013. **303**: p. 130-134.
28. Campa, M.C., I. Luisetto, D. Pietrogiacomini, and V. Indovina, *The catalytic activity of cobalt-exchanged mordenites for the abatement of NO with CH<sub>4</sub> in the presence of excess O<sub>2</sub>*. Applied Catalysis B: Environmental, 2003. **46**(3): p. 511-522.
29. Campa, M.C., *Catalytic activity of Co-ZSM-5 for the abatement of NO<sub>x</sub>, with methane in the presence of oxygen*. Applied Catalysis B: Environmental, 1996. **8**: p. 315-331.
30. Yan, Y., L. Wang, and H. Zhang, *Catalytic combustion of volatile organic compounds over Co/ZSM-5 coated on stainless steel fibers*. Chemical Engineering Journal, 2014. **255**: p. 195-204.
31. Ulla M.A., S.R., Lombardo E., Daniell W., Knözinger H., *Catalytic combustion of methane on Co/MgO: characterisation of active cobalt sites*. Applied Catalysis B: Environmental, 2001. **29**: p. 217-229.
32. Jiang, Z., J. Yu, J. Cheng, T. Xiao, M.O. Jones, Z. Hao, and P.P. Edwards, *Catalytic combustion of methane over mixed oxides derived from Co-Mg/Al ternary hydrotalcites*. Fuel Processing Technology, 2010. **91**(1): p. 97-102.
33. Hunde, E.T. and J.J. Watkins, *Reactive Deposition of Cobalt and Nickel Films from Their Metallocenes in Supercritical Carbon Dioxide Solution*. Chemistry of Materials, 2004. **16**(3): p. 498-503.
34. Aschenbrenner, O., S. Kemper, N. Dahmen, K. Schaber, and E. Dinjus, *Solubility of  $\beta$ -diketonates, cyclopentadienyls, and cyclooctadiene complexes with various metals in supercritical carbon dioxide*. The Journal of Supercritical Fluids, 2007. **41**(2): p. 179-186.
35. Szegedi, Á., Z. Kónya, D. Méhn, E. Solymár, G. Pál-Borbély, Z.E. Horváth, L.P. Biró, and I. Kiricsi, *Spherical mesoporous MCM-41 materials containing transition metals: synthesis and characterization*. Applied Catalysis A: General, 2004. **272**(1-2): p. 257-266.
36. Domingo, C., J. García-Carmona, M.A. Fanovich, and J. Saurina, *Study of adsorption processes of model drugs at supercritical conditions using partial least squares regression*. Analytica Chimica Acta, 2002. **452**(2): p. 311-319.
37. Yoon, S.-D. and H.-S. Byun, *Molecularly imprinted polymers for selective separation of acetaminophen and aspirin by using supercritical fluid technology*. Chemical Engineering Journal, 2013. **226**(0): p. 171-180.
38. Byun, H.-S., D.-S. Yang, and S.-H. Cho, *Synthesis and characterization of high selective molecularly imprinted polymers for bisphenol A and 2,4-dichlorophenoxyacetic acid by using supercritical fluid technology*. Polymer, 2013. **54**(2): p. 589-595.
39. Cao, L., C. Ma, J. Wang, and P. Chen, *Synthesis of polymer-copper(II) complexes in supercritical carbon dioxide*. The Journal of Supercritical Fluids, 2013. **75**(0): p. 152-158.
40. Gamse, T., *Industrial applications and current trends in supercritical fluid technologies*. Hemijka Industrija, 2005. **59**: p. 207-212.
41. Tenorio, M.J., C. Pando, J.A.R. Renuncio, J.G. Stevens, R.A. Bourne, M. Poliakov, and A. Cabañas, *Adsorption of Pd(hfac)<sub>2</sub> on mesoporous silica SBA-15 using supercritical CO<sub>2</sub> and its role in the performance of Pd-SiO<sub>2</sub> catalyst*. The Journal of Supercritical Fluids, 2012. **69**: p. 21-28.

42. Bozbag, S.E., N.S. Yasar, L.C. Zhang, M. Aindow, and C. Erkey, *Adsorption of Pt(cod)me<sub>2</sub> onto organic aerogels from supercritical solutions for the synthesis of supported platinum nanoparticles*. The Journal of Supercritical Fluids, 2011. **56**(1): p. 105-113.
43. Aschenbrenner, O., N. Dahmen, K. Schaber, and E. Dinjus, *Adsorption of Dimethyl(1,5-cyclooctadiene)platinum on Porous Supports in Supercritical Carbon Dioxide*. Industrial & Engineering Chemistry Research, 2008. **47**(9): p. 3150-3155.
44. Zhang, Y., B. Cangul, Y. Garrabos, and C. Erkey, *Thermodynamics and kinetics of adsorption of bis(2,2,6,6-tetramethyl-3,5-heptanedionato) (1,5-cyclooctadiene) ruthenium (II) on carbon aerogel from supercritical CO<sub>2</sub> solution*. The Journal of Supercritical Fluids, 2008. **44**(1): p. 71-77.
45. Kast, W., *Physical Adsorption on Heterogeneous Solids. Von M. Jaroniec und R. Madey. Elsevier Science Publishers, Amsterdam – New York 1988. XIV, 353 S., zahlr. Abb. u. Tab., geb., US-\$ 131,50*. Chemie Ingenieur Technik, 1989. **61**(9): p. 766-766.
46. Cavazzini, A., G. Bardin, K. Kaczmarski, P. Szabelski, M. Al-Bokari, and G. Guiochon, *Adsorption equilibria of butyl- and amylbenzene on monolithic silica-based columns*. Journal of Chromatography, 2002. **957**: p. 111-126.
47. Kayranli, B., *Adsorption of textile dyes onto iron based waterworks sludge from aqueous solution; isotherm, kinetic and thermodynamic study*. Chemical Engineering Journal, 2011. **173**(3): p. 782-791.
48. Kikic, I., P. Alessi, A. Cortesi, S.J. Macnaughton, N.R. Foster, and B. Spicka, *An experimental study of supercritical adsorption equilibria of salicylic acid on activated carbon*. Fluid Phase Equilibria, 1996. **117**(1-2): p. 304-311.
49. Subra, P., A. Vega-Bancel, and E. Reverchon, *Breakthrough curves and adsorption isotherms of terpene mixtures in supercritical carbon dioxide*. The Journal of Supercritical Fluids, 1998. **12**(1): p. 43-57.
50. López-Aranguren, P., J. Fraile, L.F. Vega, and C. Domingo, *Regenerable solid CO<sub>2</sub> sorbents prepared by supercritical grafting of aminoalkoxysilane into low-cost mesoporous silica*. The Journal of Supercritical Fluids, 2014. **85**: p. 68-80.
51. Domingo, C., J. García-Carmona, M.A. Fanovich, J. Llibre, and R. Rodríguez-Clemente, *Single or two adsorption processes at supercritical conditions: an experimental study*. Journal of Supercritical Fluids, 2001. **21**(2): p. 147-157.
52. Samuelsson, J., T. Undin, and T. Fornstedt, *Expanding the elution by characteristic point method for determination of various types of adsorption isotherms*. J Chromatogr A, 2011. **1218**(24): p. 3737-42.
53. Brunauer, S., P.H. Emmet, and E. Teller, *Adsorption of Gases in Multimolecular Layers*. Journal of American Chemical Society, 1938. **60**: p. 309-319.
54. Fehrenbacher, U., O. Grosshardt, T. Hirth, O. Aschenbrenner, and N. Dahmen, *Reactive decomposition of metals in supercritical fluids: Investigation of the solubility and decomposability of metal organic substances*. 10th European Meeting on Supercritical Fluids, 2005: p. Colmar, France.
55. Bayrakçeken, A., B. Cangül, L.C. Zhang, M. Aindow, and C. Erkey, *PtPd/BP2000 electrocatalysts prepared by sequential supercritical carbon dioxide deposition*. International Journal of Hydrogen Energy, 2010. **35**(21): p. 11669-11680.
56. Sewell, G.S., E. van Steen, and C.T. O'Connor, *Use of TPR/TPO for characterization of supported cobalt catalysts*. Catalysis Letters, 1996. **37**: p. 255-260.

57. Ernst, B., A. Bensaddik, L. Hilaire, P. Chaumette, and A. Kiennemann, *Study on a cobalt silica catalyst during reduction and Fischer-Tropsch reaction: In situ EXAES compared to XPS and XRD*. *Catalysis Today*, 1998. **39**: p. 329-341.
58. Chu, W., P. Chernavskii, L. Gengembre, G. Pankina, P. Fongarland, and A. Khodakov, *Cobalt species in promoted cobalt alumina-supported Fischer-Tropsch catalysts*. *Journal of Catalysis*, 2007. **252**(2): p. 215-230.
59. Balat, H. and E. Kirtay, *Hydrogen from biomass – Present scenario and future prospects*. *International Journal of Hydrogen Energy*, 2010. **35**(14): p. 7416-7426.
60. Kirtay, E., *Recent advances in production of hydrogen from biomass*. *Energy Conversion and Management*, 2011. **52**(4): p. 1778-1789.
61. Dascomb, J., A. Krothapalli, and R. Fakhrai, *Thermal conversion efficiency of producing hydrogen enriched syngas from biomass steam gasification*. *International Journal of Hydrogen Energy*, 2013. **38**(27): p. 11790-11798.
62. Chang, A.C.C., L.-S. Chang, C.-Y. Tsai, and Y.-C. Chan, *Steam reforming of gasification-derived tar for syngas production*. *International Journal of Hydrogen Energy*, 2014. **39**(33): p. 19376-19381.
63. Torres, W., S. Pansare, and J. Goodwin, *Hot gas removal of tars, ammonia, and hydrogen sulfide from biomass gasification gas*. *Catalysis Reviews*, 2007. **494**(407-456).
64. Yu, Y., X. Lou, and H. Wu, *Some recent advances in hydrolysis of biomass in hot-compressed water and its comparisons with other hydrolysis methods*. *Energy & Fuels*, 2008. **22**: p. 46-60.
65. Tanksale, A., J.N. Beltramini, and G.M. Lu, *A review of catalytic hydrogen production processes from biomass*. *Renewable and Sustainable Energy Reviews*, 2010. **14**(1): p. 166-182.
66. Kalinci, Y., A. Hepbasli, and I. Dincer, *Biomass-based hydrogen production: A review and analysis*. *International Journal of Hydrogen Energy*, 2009. **34**(21): p. 8799-8817.
67. Saxena, R.C., D. Seal, S. Kumar, and H.B. Goyal, *Thermo-chemical routes for hydrogen rich gas from biomass: A review*. *Renewable and Sustainable Energy Reviews*, 2008. **12**(7): p. 1909-1927.
68. Chang, A.C.C., H.-F. Chang, F.-J. Lin, K.-H. Lin, and C.-H. Chen, *Biomass gasification for hydrogen production*. *International Journal of Hydrogen Energy*, 2011. **36**(21): p. 14252-14260.
69. Font Palma, C., *Modelling of tar formation and evolution for biomass gasification: A review*. *Applied Energy*, 2013. **111**: p. 129-141.
70. Ferreira, M.M.C., *Polycyclic aromatic hydrocarbons: a QSPR study*. *Chemosphere*, 2001. **44**: p. 125-146.
71. Fagbemi, L., L. Khezami, and R. Capart, *Pyrolysis products from different biomasses: application to the thermal cracking of tar*. *Applied Energy*, 2001. **69**: p. 293-306.
72. Ding, N., R. Azargohar, A.K. Dalai, and J.A. Kozinski, *Catalytic gasification of cellulose and pinewood to H<sub>2</sub> in supercritical water*. *Fuel*, 2014. **118**: p. 416-425.
73. Hao, X., L. Guo, X. Zhang, and Y. Guan, *Hydrogen production from catalytic gasification of cellulose in supercritical water*. *Chemical Engineering Journal*, 2005. **110**(1-3): p. 57-65.
74. Yamamura, T., T. Mori, K.C. Park, Y. Fujii, and H. Tomiyasu, *Ruthenium(IV) dioxide-catalyzed reductive gasification of intractable biomass including*

- cellulose, heterocyclic compounds, and sludge in supercritical water*. The Journal of Supercritical Fluids, 2009. **51**(1): p. 43-49.
75. Reddy, S.N., S. Nanda, A.K. Dalai, and J.A. Kozinski, *Supercritical water gasification of biomass for hydrogen production*. International Journal of Hydrogen Energy, 2014. **39**(13): p. 6912-6926.
  76. Loppinet-Serani, A. and C. Aymonier, *Chapter 7 - Hydrolysis in Near- and Supercritical Water for Biomass Conversion and Material Recycling*, in *Supercritical Fluid Technology for Energy and Environmental Applications*, V.A. Fan, Editor. 2014, Elsevier: Boston. p. 139-156.
  77. Wu, C., L. Wang, P.T. Williams, J. Shi, and J. Huang, *Hydrogen production from biomass gasification with Ni/MCM-41 catalysts: Influence of Ni content*. Applied Catalysis B: Environmental, 2011. **108-109**: p. 6-13.
  78. Wu, C., Z. Wang, J. Huang, and P.T. Williams, *Pyrolysis/gasification of cellulose, hemicellulose and lignin for hydrogen production in the presence of various nickel-based catalysts*. Fuel, 2013. **106**: p. 697-706.
  79. Irmak, S., M. Kurtuluş, A. Hasanoglu, and O. Erbatur, *Gasification efficiencies of cellulose, hemicellulose and lignin fractions of biomass in aqueous media by using Pt on activated carbon catalyst*. Biomass and Bioenergy, 2013. **49**: p. 102-108.
  80. Su, S., Y. Chi, R. Chang, R. Hu, and N. Li, *Analysis of the catalytic steam gasification mechanism of biomass*. International Journal of Hydrogen Energy, 2015. **40**(2): p. 935-940.
  81. Hosoya, T., H. Kawamoto, and S. Saka, *Cellulose–hemicellulose and cellulose–lignin interactions in wood pyrolysis at gasification temperature*. Journal of Analytical and Applied Pyrolysis, 2007. **80**(1): p. 118-125.
  82. Hosoya, T., H. Kawamoto, and S. Saka, *Pyrolysis gasification reactivities of primary tar and char fractions from cellulose and lignin as studied with a closed ampoule reactor*. Journal of Analytical and Applied Pyrolysis, 2008. **83**(1): p. 71-77.
  83. Sanchez-Silva, L., D. Lopez-Gonzalez, J. Villasenor, P. Sanchez, and J.L. Valverde, *Thermogravimetric-mass spectrometric analysis of lignocellulosic and marine biomass pyrolysis*. Bioresour Technol, 2012. **109**: p. 163-72.
  84. Lopez-Gonzalez, D., M. Fernandez-Lopez, J.L. Valverde, and L. Sanchez-Silva, *Thermogravimetric-mass spectrometric analysis on combustion of lignocellulosic biomass*. Bioresour Technol, 2013. **143**: p. 562-74.
  85. Li, X.-G., *High-resolution thermogravimetry of cellulose esters*. Journal of Applied Polymer Science, 1999. **71**(4): p. 573-578.
  86. Xingping, K., Y. Tianhua, H. Ying, S. Yang, H. Yeguang, and L. Rundong. *The Effect of Biomass Components on the Co-combustion Characteristics of Biomass with Coal*. in *Digital Manufacturing and Automation (ICDMA), 2011 Second International Conference on*. 2011.
  87. Huang, Y.F., P.T. Chiueh, W.H. Kuan, and S.L. Lo, *Pyrolysis kinetics of biomass from product information*. Applied Energy, 2013. **110**(0): p. 1-8.
  88. *NIST Chemistry WebBook*. 2015, Linstrom, P.J.
  89. Xie, X., B. Goodell, D. Zhang, D.C. Nagle, Y. Qian, M.L. Peterson, and J. Jellison, *Characterization of carbons derived from cellulose and lignin and their oxidative behavior*. Bioresource Technology, 2009. **100**(5): p. 1797-1802.
  90. Cheng, K., W.T. Winter, and A.J. Stipanovic, *A modulated-TGA approach to the kinetics of lignocellulosic biomass pyrolysis/combustion*. Polymer Degradation and Stability, 2012. **97**(9): p. 1606-1615.

91. Huang, Y.F., W.H. Kuan, P.T. Chiueh, and S.L. Lo, *Pyrolysis of biomass by thermal analysis–mass spectrometry (TA–MS)*. Bioresource Technology, 2011. **102**(3): p. 3527-3534.
92. Widyawati, M., T.L. Church, N.H. Florin, and A.T. Harris, *Hydrogen synthesis from biomass pyrolysis with in situ carbon dioxide capture using calcium oxide*. International Journal of Hydrogen Energy, 2011. **36**(8): p. 4800-4813.
93. Zhao, M., N.H. Florin, and A.T. Harris, *Mesoporous supported cobalt catalysts for enhanced hydrogen production during cellulose decomposition*. Applied Catalysis B: Environmental, 2010. **97**(1-2): p. 142-150.
94. Agrawal, R.K., *Kinetics of reactions involved in pyrolysis of cellulose I. The three reaction model*. The Canadian Journal of Chemical Engineering, 1988. **66**(3): p. 403-412.
95. Broido, A. and F.J. Kilzer, *Speculations on the nature of cellulose pyrolysis*. Pyrodynamics, 1965. **2**: p. 151-163.
96. Cabeza, A., F. Sobrón, F.M. Yedro, and J. García-Serna, *Autocatalytic kinetic model for thermogravimetric analysis and composition estimation of biomass and polymeric fractions*. Fuel, 2015. **148**: p. 212-225.
97. Kastanaki, E., D. Vamvuka, P. Grammelis, and E. Kakaras, *Thermogravimetric studies of the behavior of lignite-biomass blends during devolatilization*. Fuel Processing Technology, 2002. **77**: p. 159-166.
98. Mangut, V., E. Sabio, J. Gañán, J.F. González, A. Ramiro, C.M. González, S. Román, and A. Al-Kassir, *Thermogravimetric study of the pyrolysis of biomass residues from tomato processing industry*. Fuel Processing Technology, 2006. **87**(2): p. 109-115.
99. Słopiecka, K., P. Bartocci, and F. Fantozzi, *Thermogravimetric analysis and kinetic study of poplar wood pyrolysis*. Applied Energy, 2012. **97**: p. 491-497.
100. Zabaniotou, A., O. Ioannidou, E. Antonakou, and A. Lappas, *Experimental study of pyrolysis for potential energy, hydrogen and carbon material production from lignocellulosic biomass*. International Journal of Hydrogen Energy, 2008. **33**(10): p. 2433-2444.
101. Capart, R., L. Khezami, and A.K. Burnham, *Assessment of various kinetic models for the pyrolysis of a microgranular cellulose*. Thermochimica Acta, 2004. **417**(1): p. 79-89.
102. Wiederschain, G.Y., *Polysaccharides. Structural diversity and functional versatility*. Biochemistry (Moscow), 2007. **72**(6): p. 675-675.

# CHAPTER III.

## Nickel-based

## Catalysts

## III.1. Introduction

### III.1.1. Nickel-based Catalysts and their applications

Nickel-based catalysts are widely employed and help to the competitiveness of a number of major industries thanks to their high activity at room temperature.

Among which include man-made fibres and auto parts, where two major raw materials used in nylon production, adipic acid and caprolactum, are obtained from cyclohexane which is, in turn, produced from benzene using a nickel-based catalytic process [1].

Then also, much of the production of oils and fats derived from natural sources, such as palm and vegetable oils, used in the manufacture of a wide range of food products, including, inter alia, cooking oils, spreads, ready meals or bread, depends on nickel-catalyst technology. Even fertilizer industry, which generates sales of more than Euro 14 billion, principally in arable farming, is based on nickel-based catalysts for the ammonia production. But above all, nickel-based catalysts find their main application in petroleum refining. In this industry, Raney nickel is widely employed for hydro-treating (hydro-denitrogenation to reduce  $\text{NO}_x$  and hydro-desulphurisation to reduce  $\text{SO}_x$ ), in such a way that it is possible to obtain levels below the legally required.

Apart of these applications, different kinds of nickel-based catalysts supported over porous aluminium and silica are preferred choice for hydro-cracking and hydro-processing due to their ability to adsorb huge quantities of hydrogen thereby greatly increasing the efficiency of the reactions. Additionally, nickel is less costly relative to other competing materials of the platinum group.

But the field which the use of nickel-based catalysts is solidifying more and more is in the production of syngas as alternative to the use of fossil fuels. For this purpose, there are several technologies that could be applied, the same that have been extensively used for the natural gas reforming.

One of these processes is the steam reforming of liquefied natural gas (mainly composed of methane) [2-7], ethanol [8] or aqueous fraction of bio-oil [9, 10]. Nickel-based catalysts have shown appropriate activity and selectivity towards hydrogen production at a much lower cost than others noble metals, both in fixed-bed and

### CHAPTER III. Nickel-based Catalysts

fluidized-bed reactors. However, these catalysts suffer from significant deactivation caused by carbon deposition and sintering due to the extremely operational conditions, leading to loss of active surface. For these reasons, researches are trying to solve this drawback confronting it from different perspectives: the use of promoters (Zn, Mg, Zr... [5, 8]), acid supports ( $\text{SiO}_2$  or  $\text{Al}_2\text{O}_3$  [3, 5]) and regeneration treatments [4].

But the most promising process for syngas production is the  $\text{CO}_2$  reforming of  $\text{CH}_4$  or dry reforming (DRM), and all the network reactions that can be included in this process are also catalyzed by nickel.

Nickel-based catalysts are replacing noble metals, such as Ru, Rh and Pt, for DRM due to their relative economic feasibility and availability. But, once more, their use is limited due to their high tendency toward coking and subsequent deactivation. Side reactions, including  $\text{CH}_4$  cracking [11], the Boundary reaction and reverse water gas shift reaction, lead to carbon deposition [12]. Furthermore, the endothermic nature of the reaction means high temperatures need to be utilized resulting in a greater tendency toward sintering of metal. In this sense, to prevent or reduce the coke formation and improve the catalytic performance, it has been published numerous papers studying the most important parameters: the nature of the support [13-15], the catalysts preparation method [16, 17] and the presence of modifiers [18, 19].

On the other hand, currently, in the middle of growing concern about depletion of fossil fuel reserves and pollution, a very attractive alternative for the continuously increasing energy demands is the generation of hydrogen from renewable resources such as biomass. The use of nickel-based catalysts in the biomass gasification process cannot only increase the  $\text{H}_2$  yield, but also decrease the size of the reactor as result of the enhancement in the reaction rate. As in the previous cases, various catalyst supports, metal additives and synthesis methods have been developed. Some of the most commonly used include alumina, silica and magnesium oxide as supports, and Rh, Ru, Co, Fe and Cu as promoters to improve their stability [20, 21].

Other example is the process of  $\text{CO}_2$  methanation, developed by Sabatier and Senderens the 1902s [22], has only become common on an industrial scale since the 1970s thanks to the use of catalysts, mainly Rh, Ru or Pd. But recently, a number of nickel-based

catalysts supported on different solids have been tested, showing high selectivity for methane and relatively low price [23-26].

Besides, there are hundreds of paper and patents published [27-32] on the use of nickel as catalyst for the hydrogenation of organic compounds, due to its ability to hydrogenate virtually any type of functional group, among them being carbon-carbon double bond, carbonyl (aldehydic and ketonic), nitro, azide, nitrile and oxime groups.

### III.1.2. Deposition of nickel using sc-CO<sub>2</sub>

Up to our knowledge, there are few papers related to the deposition of Ni nanoparticles by means of SCFD on porous supports. Peng et al. [33] have demonstrated the hydrogenolysis of NiCp<sub>2</sub> can take place through a self-catalyzed process at low temperature (< 70 °C) in sc-CO<sub>2</sub> both onto carbon nanotubes and on flat surfaces. Bozbag et al. [34] reported the synthesis by impregnating the activated carbon with Ni(acac)<sub>2</sub> in sc-CO<sub>2</sub> at 30 MPa and 60 °C followed by thermal chemical treatment using H<sub>2</sub> at atmospheric pressure, achieving metallic loadings up to 6.5 %wt with an average nanoparticle size around 12 nm. In this study, the adsorption isotherm of the system Ni(acac)<sub>2</sub>-AC was also studied. Similarly, using this same organometallic precursor (Ni(acac)<sub>2</sub>), Taylor et al. [35] have prepared nickel-based catalysts supported on carbon nanotube/fiber and aluminosilicate using sc-MeOH for the hydrogen production in the gasification of biomass in supercritical water, with metal loadings much higher (60-70 %wt). Finally, Hunde et al [36] have published the film formation from NiCp<sub>2</sub> onto Si, TaN and TiN via chemical fluid deposition at temperatures between 175 and 200 °C and pressures from 19 to 23 MPa. In this paper, the films were found to be essentially free from ligand-derived contamination, using a high-pressure cold-wall reactor, and therefore, restricting the deposition to the heated substrates only.

## III.2. Materials

### III.2.1. Organometallic Precursor: NiCp<sub>2</sub>

Nickel (II) bis-( $\eta^5$ -cyclopentadienyl), known as nickelocene (NiCp<sub>2</sub>) has been selected as precursor for the SCFD of nickel. By using the same ligands as in the case of cobalt-based catalysts synthesis, some comparative results can be concluded related with kind of metal. The solubility of NiCp<sub>2</sub> in sc-CO<sub>2</sub> is reported in literature [37], and according to these values, solubility of NiCp<sub>2</sub> is up to 1.5 times lower of CoCp<sub>2</sub>. Nonetheless, solubility of this precursor is higher than that of other organometallic compounds, such as Ni(acac)<sub>2</sub> or Ni(thd)<sub>2</sub>, which are completely insoluble at low pressures [37].

Nickelocene was supplied by Sigma Aldrich, and used without further treatment; nevertheless, due to its ease for oxidation, its management was conducted in a glovebox under inert nitrogen atmosphere.

### III.2.2. Support: MCM-48

MCM-48 is one of the most widely employed mesoporous support in the industry due to its structural characteristics, resistance and slight acidity. For all these reasons, this support has been selected to bring greater durability at nickel-based catalysts, which are very susceptible to poisoning coke.

The cubic MCM-48, a member of M41S, has attracted much attention for its interwoven and branched three-dimension mesoporous channel systems, which can be used as a promising adsorbent in separation techniques, catalyst and even a template for the synthesis of other nanostructures or molecular sieves. Similarly to MCM-41, this material has a narrow pore size distribution, usually in the range 1.6 – 3.8 nm, which has a slight mesoporosity index higher than its equivalent MCM-41; and large surface area (~1200 m<sup>2</sup>/g). Besides temperature, also the importance of small amounts of ethanol, formed by the hydrolysis of the silicate source TEOS, is pointed out as the driving force for the transformations to occur by altering the surfactant packing parameter within the micellar surfactant templates. A few researches described the possibilities of obtaining different phases at room temperature [38], which demonstrate the transition from an MCM-41 hexagonal structure into a cubic or lamellar phase by

adding small quantities of alcohol to the reaction mixture, adopting the role of cosurfactant.

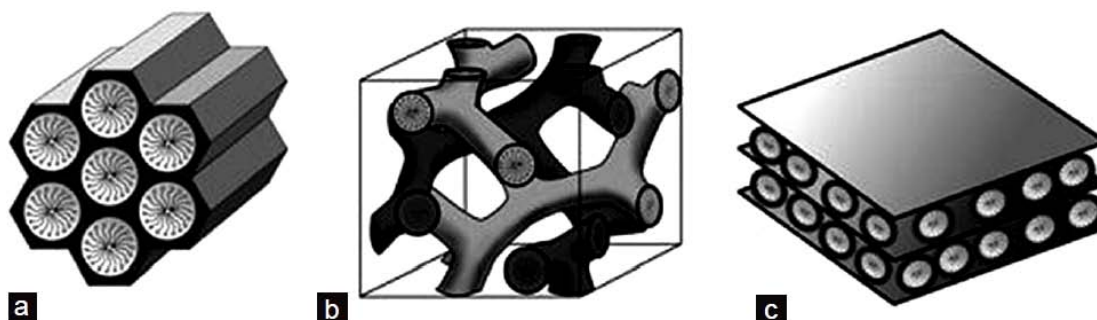


**Figure III-1.** Structures of mesoporous M41S materials:

a) MCM-41 (2D hexagonal), b) MCM-48 (3D cubic), and c) MCM-50 (1D lamellar)

According to this information, to synthesize cubic MCM-48 materials, the same recipe described previously for the synthesis of MCM-41 was employed, applying the modification proposed by Liu et al. [38]. In this case, 18 ml of absolute ethanol is added and mixed at the beginning of the preparation instead of 48 ml, thus the final molar composition of the gel is 1 TEOS:0.3 C<sub>16</sub>TMABr:11 NH<sub>3</sub>:144 H<sub>2</sub>O:22 EtOH.

---

For all these reasons, the process of SCFRD has been used to prepare nickel catalysts (Ni/MCM-48), and different aspects have been studied:

1. Determination of adsorption isotherms of NiCp<sub>2</sub> on MCM-48 and proposal of a mechanism
2. Synthesis of Ni/MCM-48 catalysts by means of SCFRD method in batch
3. Characterization of the Ni/MCM-48 catalysts
4. Catalytic activity tests of the former Ni/MCM-48 catalysts in the hydrogenation of glucose for sorbitol production

### III.3. Adsorption Isotherms of NiCp<sub>2</sub>

#### III.3.1. Experimental adsorption isotherms

Adsorption isotherms were determined by means of the same procedure explained in Chapter II of this thesis for cobalt catalysts. Similarly to procedure described for CoCp<sub>2</sub> in section II.3, various amounts of precursor NiCp<sub>2</sub> were introduced into the stirred vessel, while the support mass was constant. In all the experiments, the adsorption chamber was previously heated up to the desired temperature ( $T=70\text{ }^{\circ}\text{C}$ ), and the liquefied CO<sub>2</sub> was pumped into the vessel up to the wanted pressure. Experimental data for the adsorption isotherms for NiCp<sub>2</sub> on MCM-48 at 70 °C for pressures of 11, 14 and 17 MPa are represented in Fig. III-2.

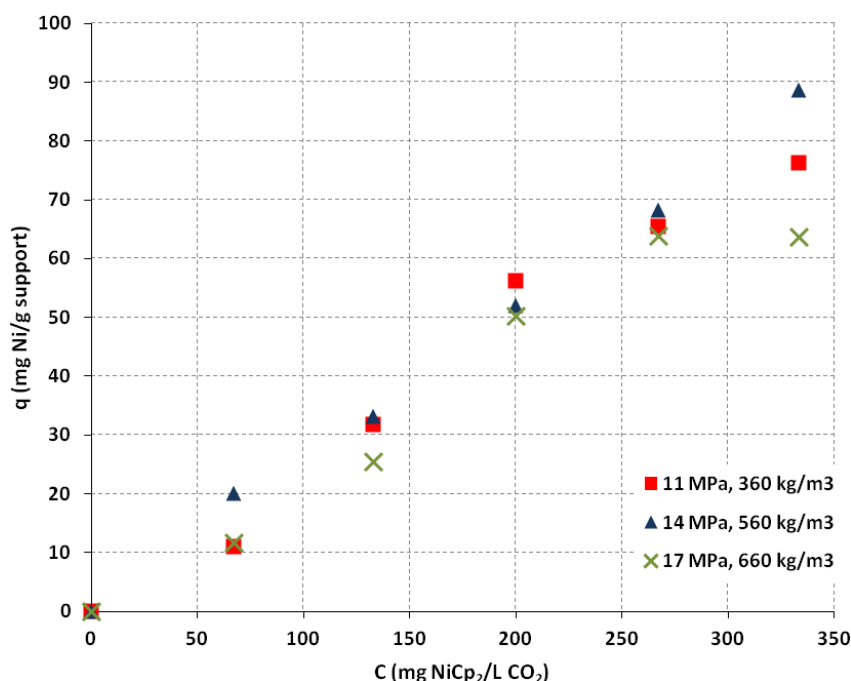


**Figure III-2.** Adsorption isotherms of NiCp<sub>2</sub> on MCM-48 at 70 °C and different pressures in sc-CO<sub>2</sub>

Results show that the metallic loading deposited over the support increases with the concentration, whatever the pressure. The three isotherms show a change in their curvature at a NiCp<sub>2</sub> concentration of around 100 and 150 mg/L CO<sub>2</sub>. This behavior is typical of an isotherm of type IV, whose shape is related to the existence of both micro- and meso-pores.

Comparing the isotherms according to their variation with pressure, it can be observed as the equilibrium adsorptive capacity ( $q$ ) is practically the same at three pressures at

low concentrations; whereas at high concentrations, increases slightly from 11 to 14 MPa, whereas from 14 to 17 MPa,  $q$  decreases; finding a maximum at 14 MPa.

This optimum pressure for the adsorption process is unique for each precursor-support combination, and depends on the affinity between them and the fluid medium, as well as intermolecular forces that govern them. An example with similar result is the adsorption of hydroxybenzoic acid on PMA [39], which experiences at 12, 16 and 20 MPa found an maximum at the intermediate pressure inside the range studied.

### III.3.2. Adsorption isotherm Modeling

To design large-scale adsorption processes, it is necessary to understand in which way the adsorption is influenced by different variables such as mass transfer effects [40-43] and equilibrium consideration [44-47]. For this reason, the experimental data obtained previously have been fitted with the most common adsorption isotherm models, i.e. Langmuir or Freundlich models.

#### Langmuir

The Langmuir isotherm is the simplest and most useful isotherm for describing both physical and chemical adsorption. In its formulation, this empirical model assumes monolayer adsorption (the adsorbed layer is one molecule in thickness) in a finite number of defined localized sites, without lateral interaction or steric hindrance and transmigration. This isotherm is a two-parameter model, which is usually written as Equation 1:

$$q = \frac{k \cdot q_s \cdot C}{1 + k \cdot C} \quad (\text{Eq. 1})$$

where  $q$  is the adsorbed quantity (mg of metal/g of support);  $C$  the concentration of the adsorbate in the bulk gas phase (mg<sub>precursor</sub>/L); and the two parameters to adjust,  $q_s$  and  $k$  are, respectively, the saturation limit and the Langmuir constant.

It is often very useful to add a degree of freedom to this model through an additional linear term, very recommendable for adsorbents which contain non-selective sites, like carbon. This new expression is presented as Equation 2:

$$q = \frac{k' \cdot q'_s \cdot C}{1 + k' \cdot C} + \lambda \cdot C \quad (\text{Eq. 2})$$

where  $\lambda C$  term takes into account the heterogeneity of the sorbent surface.

### Freundlich

Another empirical model commonly used is the Freundlich isotherm. This is the earliest known relationship describing the non-ideal and reversible adsorption. Moreover, this model can be applied to multilayer adsorption, with non-uniform distribution and affinities over heterogeneous surface. Freundlich isotherm describes the linearity of adsorption capacity as a function of adsorbate concentration when adsorption data are plotted on a log-log scale (Eq. 3):

$$q = K_F \cdot C^{1/n} \quad (\text{Eq. 3})$$

where  $K_F$  and  $n$  are empirical constants.

### Redlich-Peterson

The Redlich-Peterson model contains three parameters and it can be considered as a hybrid isotherm featuring both Langmuir and Freundlich isotherms. It establishes a linear dependence on concentration in the numerator and an exponential function in the denominator to represent adsorption equilibrium over a wide concentration range. For this, it can be applied either in homogeneous or heterogeneous systems due to its versatility, as shown follows (Eq. 4):

$$q = \frac{K_{RP} \cdot C}{1 + a_R \cdot C^g} \quad (\text{Eq. 4})$$

$K_{RP}$ ,  $a_R$  and  $g$  (being  $0 < g < 1$ ) are the three isotherm constants which characterize this model.

Multilayer physisorption isotherms

Brunauer-Emmett-Teller isotherm [48, 49], most known as BET, is a theoretical equation employed for multilayer adsorption systems. It can be described as follows in Equation 5:

$$q = \frac{Q_s \cdot K_{BET} \cdot C_e}{(C_s - C_e) \cdot [1 + (K_{BET} - 1) \cdot (C_e / C_s)]} \quad (\text{Eq. 5})$$

where  $q$ , the equilibrium adsorption capacity (mg/g);  $Q_s$ , the theoretical isotherm saturation capacity (mg/g);  $K_{BET}$  is the BET adsorption isotherm constant (L/mg); and  $C_s$ , the adsorbate saturation concentration (mg/L), maybe several layers. As  $K_{BET}$  and  $C_e / C_s$  are much greater than 1, this equation can be simplified as:

$$q = \frac{Q_s}{1 - (C_e / C_s)} \quad (\text{Eq. 6})$$

III.3.3. Fittings and discussion

To adjust the isotherm parameters and conclude which is the best model for describing the equilibrium, it is necessary to calculate the mean squared error, defined as (Eq. 7):

$$MSE = \frac{1}{n} \sum_{i=1}^n |q_i^{exp} - q_i^{cal}|^2 \quad (\text{Eq. 7})$$

Experimental data were fitted using the sorption models explained in the previous section (Langmuir, Freundlich, Redlich-Peterson and BET). Adjusted parameters and average error are given in the Table III-1, followed by their graphical representation for each model in Figures. III-3 to III-7.

## CHAPTER III. Nickel-based Catalysts

**Table III-1.** Fitted model parameters and average deviation for the adsorption equilibrium for NiCp<sub>2</sub> on MCM-48 in sc-CO<sub>2</sub>: Langmuir, Freundlich, Redlich-Peterson and BET

	<i>Isotherm 1</i> <i>11 MPa</i>	<i>Isotherm 2</i> <i>14 MPa</i>	<i>Isotherm 3</i> <i>17 MPa</i>
<b>Langmuir</b>			
<i>k</i> (L/mg)	0.0048	0.0038	0.0056
<i>q<sub>s</sub></i> (mg/g)	114.57	134.95	94.77
<i>MSE</i>	7.31	7.92	8.15
<b>Modified Langmuir</b>			
<i>k'</i> (L/mg)	0.0012	0.0002	0.0017
<i>q'<sub>s</sub></i> (mg/g)	115.01	139.16	95.03
<i>λ</i> (L/mg)	0.130	0.237	0.089
<i>MSE</i>	3.65	1.45	7.89
<b>Freundlich</b>			
<i>K<sub>F</sub></i> ((mg/g)/(mg/L) <sup>1/n</sup> )	0.36	0.32	0.24
<i>n</i>	1.08	1.04	1.04
<i>MSE</i>	3.81	1.59	8.39
<b>Redlich-Peterson</b>			
<i>K<sub>RP</sub></i> (mg/g)	14.75	14.76	14.74
<i>a<sub>R</sub></i> (L/mg) <sup>g</sup>	30.05	30.04	30.05
<i>g</i>	0.13	0.11	0.16
<i>MSE</i>	4.02	2.03	8.37
<b>BET</b>			
<i>K<sub>BET</sub></i> (L/mg)	5.86	6.25	10.66
<i>Q<sub>s</sub></i> (mg/g)	128.71	140.20	77.93
<i>C<sub>s</sub></i> (mg/L)	2250	2437	2010
<i>MSE</i>	4.00	3.66	8.15

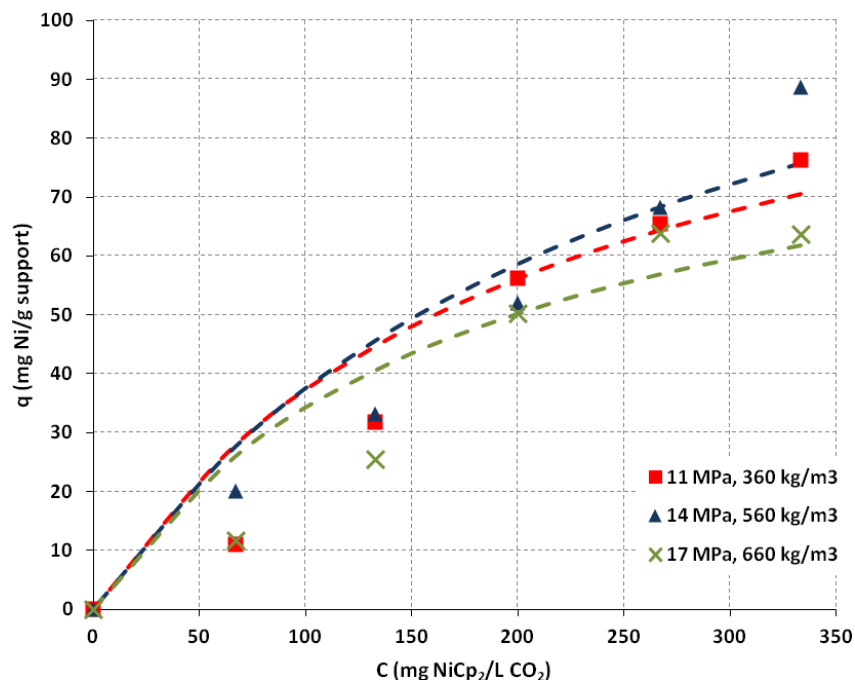


**Figure III-3.** Experimental data (symbols) and fit by Langmuir (lines) for adsorption isotherms of NiCp<sub>2</sub> on MCM-48 at 70 °C and: (■) 11 MPa; (▲) 14 MPa; (×) 17 MPa.

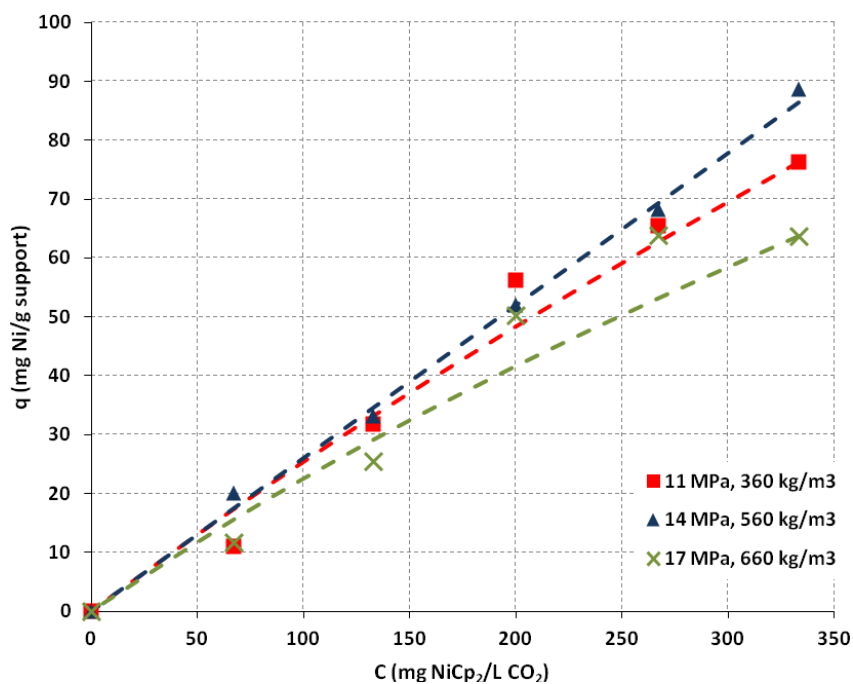


**Figure III-4.** Experimental data (symbols) and fit by Modified Langmuir (lines) for adsorption isotherms of NiCp<sub>2</sub> on MCM-48 at 70 °C and: (■) 11 MPa; (▲) 14 MPa; (X) 17 MPa.

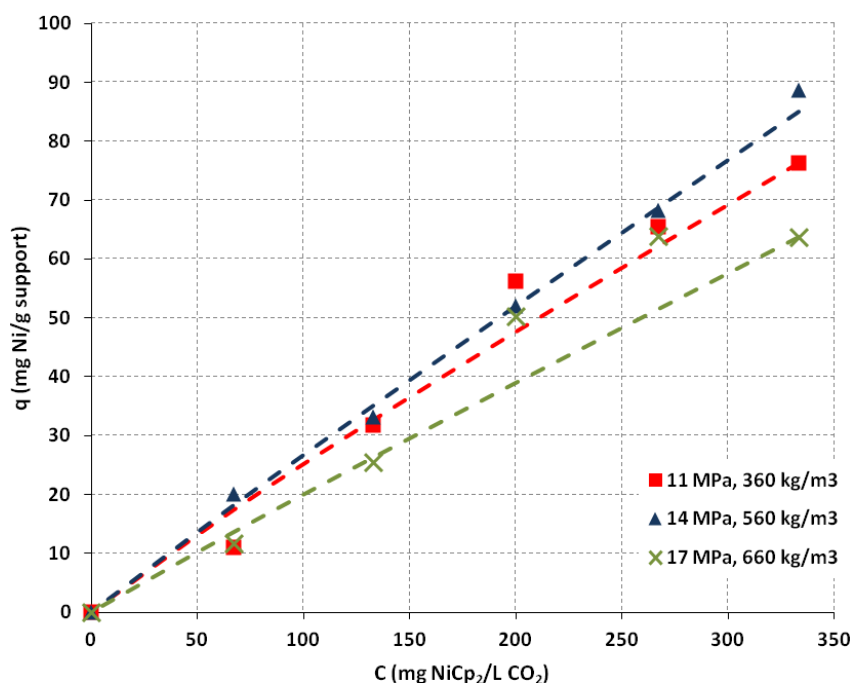


**Figure III-5.** Experimental data (symbols) and fit by Freundlich (lines) for adsorption isotherms of NiCp<sub>2</sub> on MCM-48 at 70 °C and: (■) 11 MPa; (▲) 14 MPa; (X) 17 MPa.

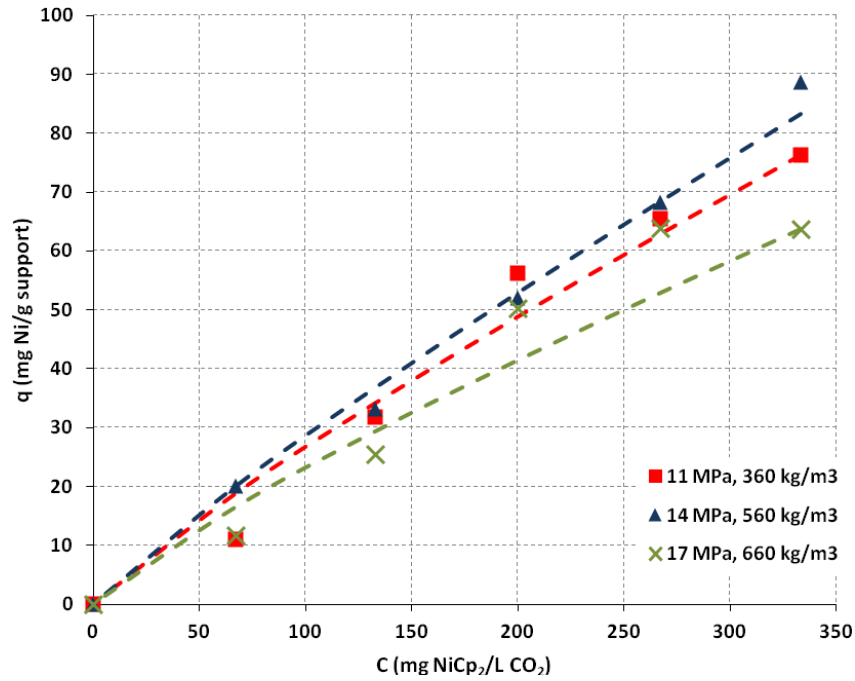


**Figure III-6.** Experimental data (symbols) and fit by Redlich-Peterson (lines) for adsorption isotherms of NiCp<sub>2</sub> on MCM-48 at 70 °C and: (■) 11 MPa; (▲) 14 MPa; (X) 17 MPa.

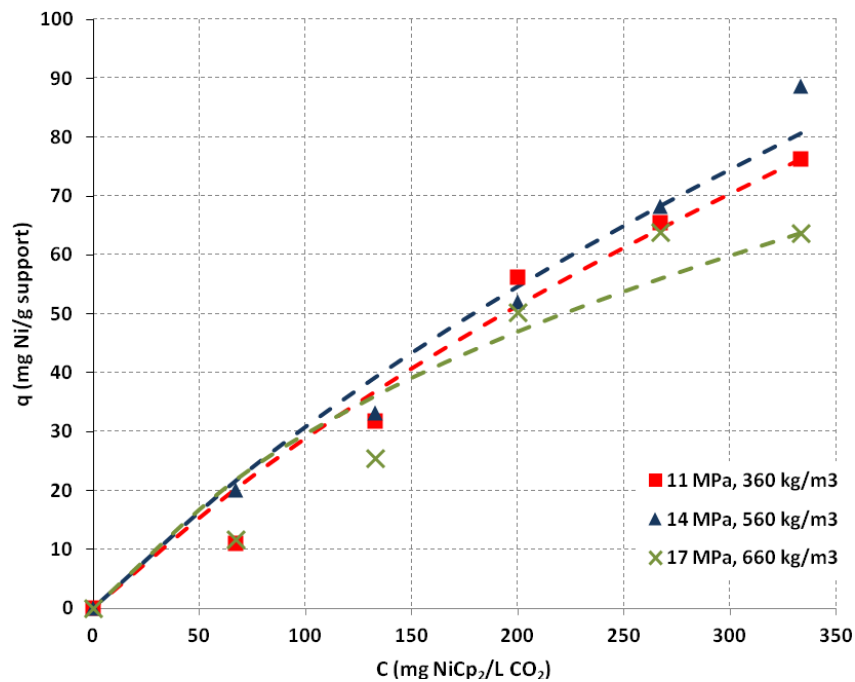


**Figure III-7.** Experimental data (symbols) and fit by BET (lines) for adsorption isotherms of NiCp<sub>2</sub> on MCM-48 at 70 °C and: (■) 11 MPa; (▲) 14 MPa; (X) 17 MPa.

Langmuir model provide the worst fitting, with an average error around 8%. Moreover, the value of  $q_s$  obtained by this model (95 mg/g at 17 MPa) does not fit compared with the experimental value of 62 mg/g.

On the other hand, Modified Langmuir, Freundlich and Redlich-Peterson correlated satisfactorily the experimental data at low concentration, with errors MSE between 1-3. However, they are unable to reproduce the plateau occurring at higher concentrations. Thus, it seems that this system differs significantly from ideal monolayer adsorption on a plane surface.

According to the data summarized in the table III-1, even BET model is not capable of reproducing the shape of the isotherms throughout the range of concentrations and pressures. For this reason, it has been proposed to use the Toth model.

This is an empirical equation gives correct limits at both low and high concentration, which was developed to represent the adsorption of a monolayer, but with an energetic heterogeneity of the adsorption sites.

$$q = q_m \frac{k_T \cdot C}{[1+(k_T \cdot C)^t]^{1/t}} \quad (\text{Eq. 8})$$

where  $q_m$  is the monolayer adsorption capacity (mg/g) and  $k_T$  is the characteristic parameter of this model (L/mg). When  $t = 1$ , this model equals the Langmuir one, expressed for ideal surfaces. For this, this parameter is generally considered as a characteristic of the system heterogeneity, caused by the solid, the solute or by a combination of them. The results are given in the Table III-2 and Figure III-8.

**Table III-2.** Fitted model parameters and average deviation for the adsorption equilibrium for NiCp<sub>2</sub> on MCM-48 in sc-CO<sub>2</sub>: Toth

	<i>Isotherm 1</i> <i>11 MPa</i>	<i>Isotherm 2</i> <i>14 MPa</i>	<i>Isotherm 3</i> <i>17 MPa</i>
<b>Toth</b>			
$k_T$ (L/mg)	0.0025	0.0020	0.0039
$q_m$ (mg/g)	100.15	130.00	64.98
$T$	4.09	15.00	23.99
$MSE$	2.99	1.45	3.06

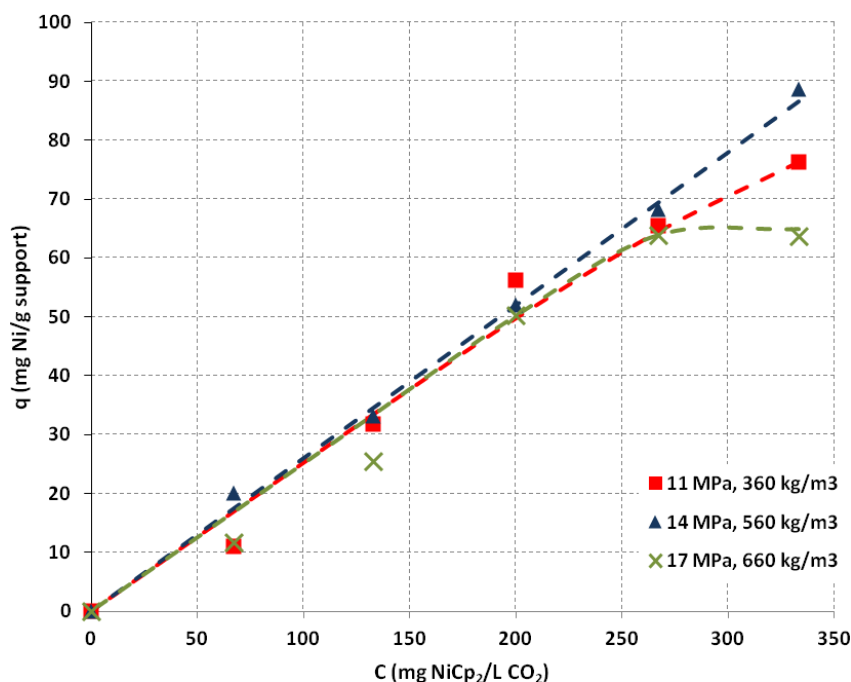


**Figure III-8.** Experimental data (symbols) and fit by Toth (lines) for adsorption isotherms of NiCp<sub>2</sub> on MCM-48 at 70 °C and: (■) 11 MPa; (▲) 14 MPa; (×) 17 MPa.

As can be seen in the figure, this curve pattern has a saturation limit when concentration becomes high, and the adjusted values for  $q_m$  (65 mg/g) are closer to the experimental values of the plateau (62 mg/g). Toth model is clearly the most appropriated to represent the sorption equilibrium of NiCp<sub>2</sub> on MCM-48.

According to these results and taking into account the saturation values estimated by Toth model, the optimum working pressure would be 14 MPa.

### III.3.4. Adsorption Kinetics

The kinetics of adsorption is often complex because the mechanism depends on the physical and chemical properties of the adsorbent as well as the mass transport process. In this sense, a wide variety of kinetics model have been formulated [50-55].

In the present study, pseudo-first order and pseudo-second order models have been selected to study the adsorption rate behavior of precursors over the surface of the supports, as these are the simplest models able to describe the process in a quite plausible way.

In these two models, all the adsorption steps such as external diffusion, pore diffusion and surface adhesion are lumped together [56]. It is assumed that the difference between the equilibrium concentration and the average solid phase concentration is the driving force for the adsorption.

### Pseudo-first order model

This model is based on the assumption that the adsorption rate is proportional to the number of free adsorption sites. The rate expression associated to the process can then be expressed as:

$$\frac{dq_i}{dt} = k_f \cdot (q_s - q_i) \quad (\text{Eq. 9})$$

where  $q_s$  and  $q_i$  (mg/g) represent the amount of solute adsorbed at the equilibrium or saturation limit and, at a given point of time respectively; and  $k_f$  ( $\text{h}^{-1}$ ) is first order rate constant [50].

After integration of Eq. 9 with the next boundary conditions:  $q_{i0}=0$  and  $q_{i\infty}=q_s$  ; this equation is then given by the expression:

$$q_i = q_s \cdot (1 - e^{-k_f \cdot t}) \quad (\text{Eq. 10})$$

### Pseudo-second order model

In the previous model, reversible interactions with the equilibrium are established between the molecules of the solid and the surface of the support. In contrast, second order kinetic model assumes that the rate-controlling step is most likely to involve chemical interactions leading to binding of solute to the support by means of strong covalent bonding [57, 58]. For this, pseudo-second order model is selected to check whether chemisorption is the rate-controlling factor in this process [55].

This model is based on the assumption that the adsorption rate is linearly related to the square of the number of unoccupied sites, and thus, the kinetic rate can be calculated as:

$$\frac{dq_i}{dt} = k_s \cdot (q_s - q_i)^2 \quad (\text{Eq. 11})$$

where  $k_s$  is the second order rate constant ( $\text{g} \cdot \text{mg}^{-1} \cdot \text{h}^{-1}$ ).

Applying the same boundary conditions that in the pseudo-first order model, integrating, Eq. 11 becomes:

$$q_i = \frac{q_s^2 \cdot k_s \cdot t}{1 + q_s \cdot k_s \cdot t} \quad (\text{Eq. 12})$$

To obtain the parameters and estimate the accuracy of the fit of the kinetics models, an error function based on the normalized standard deviation was calculated, as is reported in the literature:

$$\Delta q(\%) = \sqrt{\frac{\sum[(q_{exp} - q_{model})/q_{exp}]^2}{N-1}} \cdot 100 \quad (\text{Eq. 13})$$

where  $\Delta q$  is the normalized standard deviation;  $q_{exp}$  and  $q_{model}$  are the experimental and estimated amounts of solute adsorbed; and  $N$  is the number of data points [59].

### III.3.4.1. Adsorption kinetics of NiCp<sub>2</sub> on MCM-48

In order to determine a correct operational time, the kinetics of adsorption was studied, modeling its behavior by means of a pseudo-first order and pseudo-second order models, recently explained. Experimental metallic loading versus time and profiles predicted by both models are represented in Fig. III-9, together the kinetics parameters and standard deviation, which are summarized in Table III-3.

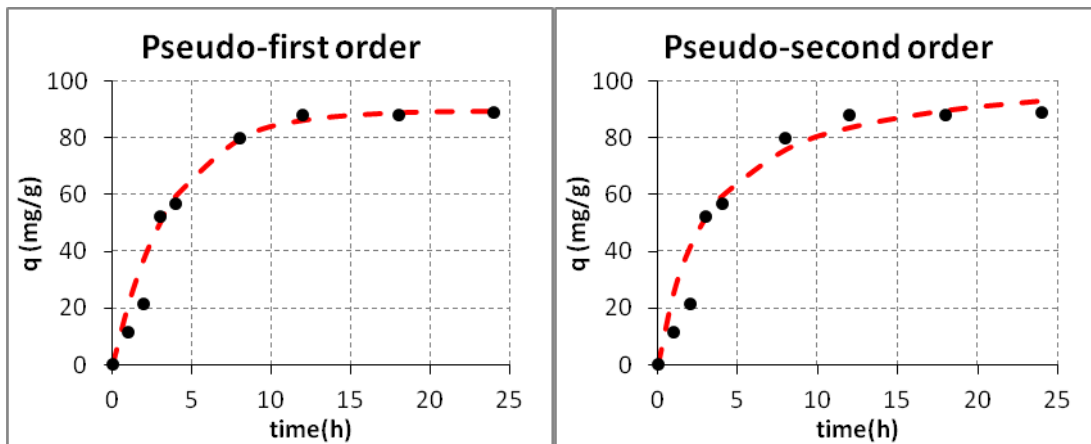


**Figure III-9.** Adsorption of NiCp<sub>2</sub> on MCM-48 at 70 °C and 14 MPa: Experimental data (●) and pseudo-first and second order fits (dotted line).

**Table III-3.** Kinetics parameters for adsorption of NiCp<sub>2</sub> on MCM-48: pseudo-first and second order.

Model	Rate constant ( <i>k</i> )	Saturation limit ( <i>q<sub>s</sub></i> )	Std. deviation ( $\Delta q$ )
Pseudo-first order	0.274	89.52	2.3
Pseudo-second order	0.003	104.67	3.4

According to these results, both models provide good fittings with similar average standard deviation lower than 4%. However, if a deeper analysis is carried out, it can be concluded that pseudo-first order model represents with greater reliability the reality. If values of saturation limit ( $q_s$ ) are compared, it is verified as this value estimated by pseudo-first order model (~90 mg/g) is virtually the same as obtained in the experiences; whereas in the case of the pseudo-second order model, this value is much higher (~105 mg/g), which would mean that after 24 hours of experimentation, equilibrium has not yet been reached and therefore, the kinetics is much slower.

Finally, attending to these conclusions, working time necessary to optimize the higher metallic loading is around 10 hours. However, since in the field of catalysis there is no need as high metallic loadings (~5%), and due to the limitations in equipment, it has been decided to work with shorter times, in order to try to reach an acceptable metallic loading in much less time, thus reducing operational costs; considering that times of 3 hours will be enough.

### III.3.5. Adsorption Mechanism

For an appropriate interpretation of experimental data, it is essential to identify the controlling step of the adsorption process. According to Fick's second law of diffusion, adsorption is considered to involve the following consecutive steps:

- The external resistance (or film diffusion) to mass transfer, which refers the transport of the adsorbate molecules across the fluid towards the external surface of the adsorbent.
- Particle diffusion (or intra-particle diffusion), where adsorbate molecules travel within the pores.
- Adsorption of the solute on the interior surface of the adsorbent.

### Intraparticle diffusion model

As the above kinetics models were not able to identify the diffusion mechanism, results were then analyzed by using the intra-particle diffusion model, based on the theory developed by Weber and Morris [60, 61], and tested by McKay and Poots [62]. This is an empirically found functional relationship, which predicts the rate-controlling step. The adsorption capacity is expressed by linearization of the following equation:

$$q_t = k_i \cdot t^{1/2} + C \quad (\text{Eq. 14})$$

where  $k_i$  is the intraparticle diffusion rate constant which can be evaluated from the slope of the straight line of  $q_t$  versus  $t^{1/2}$ ; and  $C$  represents the intercept, which value gives an idea about the thickness of boundary layer [63-65], i.e., larger the intercept, greater will be the boundary layer effect.

Although this model was initially designed for adsorption on solids in aqueous solutions, the density of supercritical fluids are similar to the values of the liquids due to the pressure that working; therefore, it also allows its use in this field [66, 67].

According to this model, the Weber-Morris plot should be a straight line and pass through the origin if the rate limiting process is only due to the intraparticle diffusion. Otherwise, when the plot does not pass through the origin, this is indicative of some degree of boundary layer control, and therefore, some other mechanism along the intraparticle diffusion is also involved. When multi-linearity is observed, then different steps with different rate constants are implicated in the mechanism [68]. The slope of the linear portion corresponding to each step indicates the rate of adsorption, being the lowest one, the rate-controlling step.

### Boyd's film-diffusion model

In order to complete the analysis, kinetics data have been treated by the expression given by Boyd et al. [69, 70], which single-resistance model assumes the main resistance to diffusion is in the boundary layer surrounding the adsorbent particle. Hence, this model can also be used to determine the actual rate-controlling step, and is expressed as:

$$F = 1 - \frac{6}{\pi^2} \sum_{n=1}^{\infty} \frac{1}{n^2} \exp(-n^2 B_t) \quad (\text{Eq. 15})$$

where  $F$  is the fractional attainment of equilibrium at different times, given by:

$$F = \frac{q_t}{q_e} \quad (\text{Eq. 16})$$

where  $q_t$  and  $q_e$  are the amount of metal adsorbed per gram of support (mg/g) at time  $t$  (h) and equilibrium, respectively.

Substituting Eq. 15 in Eq. 16, and for  $F < 0.85$ , the function  $B_t$  can be simplified to:

$$B_t = -0.4977 - \ln(1 - F) \quad (\text{Eq. 17})$$

The calculated  $B_t$  values is plotted against time  $t$  (h) to predict the mechanistic steps involve in the adsorption process, i.e., whether the adsorption takes place via particle diffusion or film diffusion mechanism. If the plot is linear and passes through the origin, then pore diffusion controls the rate of mass transfer; however, if the plot is nonlinear or linear but does not pass through the origin, then it can be concluded that film-diffusion or chemical reaction also plays major role on the adsorption rate [63, 71, 72].

### III.3.5.1. Adsorption mechanism of NiCp<sub>2</sub> on MCM-48

First, the Weber-Morris plot is shown below, revealing three different regions in the adsorption process of NiCp<sub>2</sub> on MCM-48,

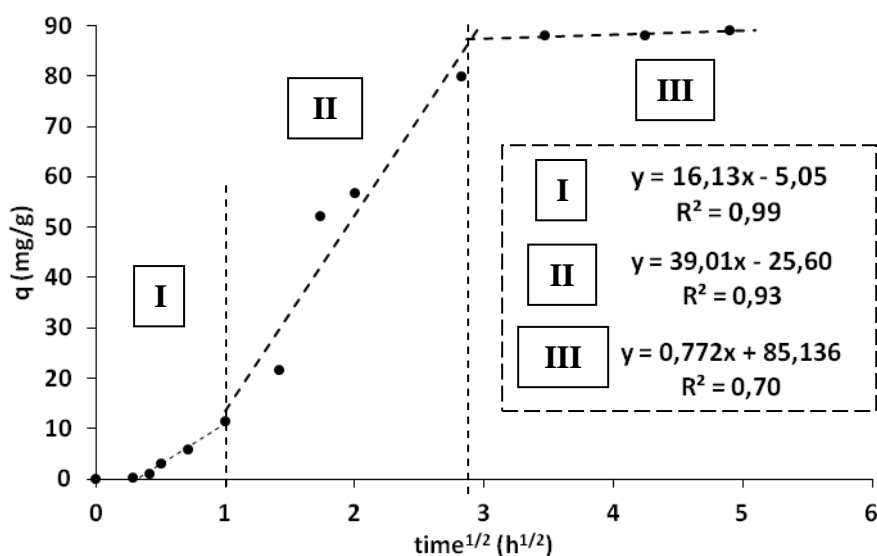


**Figure III-10.** Prediction of intraparticle diffusion model for adsorption of NiCp<sub>2</sub> on MCM-48 at 14 MPa and 70 °C

### CHAPTER III. Nickel-based Catalysts

First region I is related to external mass transport and direct adsorption over the external support surface, i.e. the boundary layer diffusion. According to the values of kinetic constant  $k_i$ , the slope in this region is the lowest. This means that the diffusion from the fluid phase to the surface of the support is the rate-controlling step. Moreover, as shown in the Fig. III-10, this stage seems to be the predominant for a very long time, largely delaying the adsorption process, as was concluded after its kinetic analysis.

On its behalf, the second region II, despite being much faster as can be seen in the value of its slope, also prevails over a very long period of time (6-7 hours) until reaching a metallic loading close to the equilibrium concentration. During this stage, the pore diffusion controls the rate of mass transfer.

After achieving an upcoming concentration to saturation, the adsorption speed decreases drastically (region III), because the support is not able to collect more metal producing a slow crystal growth.

Although high regression coefficient  $R^2$  values are obtained, and therefore, this model seems to fit correctly the experimental data, it is necessary to continue with the analysis. For this reason, the proposed hypothesis about the mechanisms governing the process could be corroborated through the study of another model, such as Boyd's film-diffusion model, which is represented in Fig. III-11.

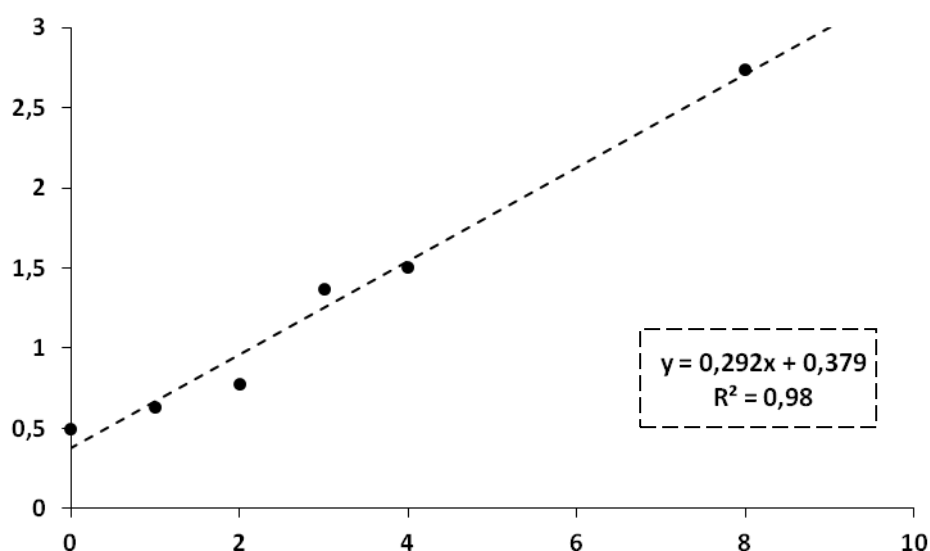


**Figure III-11.** Boyd plot for adsorption of NiCp<sub>2</sub> on MCM-48 at 14 MPa and 70 °C

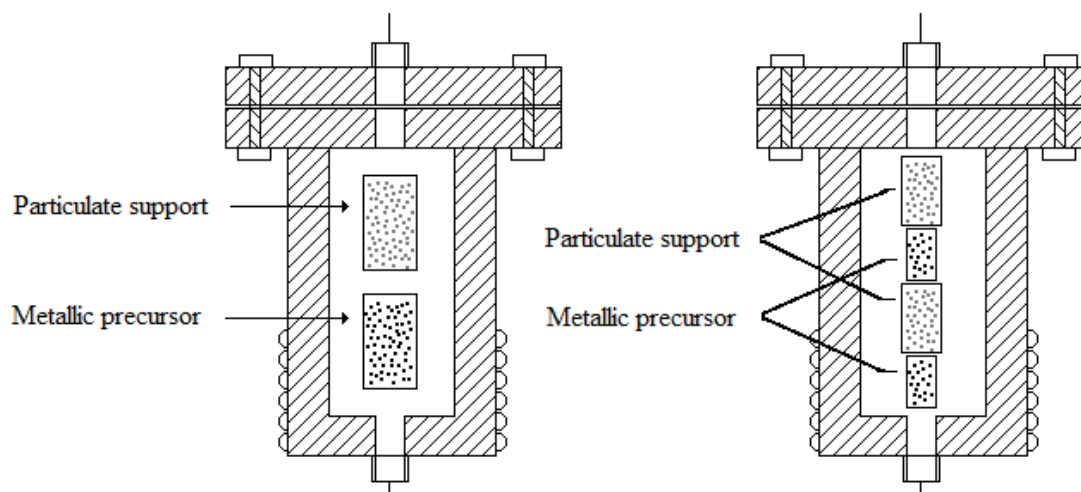
According to the high regression coefficient value  $R^2$ , Boyd's model fits very well the experimental data.

Fig. III-6 shows a straight line with an intercept value and slope value very high; this fact suggests that the adsorption process of NiCp<sub>2</sub> on MCM-48 is limited by the external mass transport. However, even though the intraparticle diffusion plays a major role in the kinetics of the process; the low value of intercept, near to zero, hints at that the mechanism is more complicated and therefore, the pore diffusion is also involved in it.

### III.4. Supercritical Fluid Reactive Deposition of Ni on MCM-48

#### III.4.1. Procedure of synthesis

Ni/MCM-48 catalysts with metallic loading around 2 %wt have been prepared for further characterization and comparison in reaction with other samples prepared by conventional methods, thereby validating the synthesis process. Nickel-based catalysts were prepared by using the supercritical fluid reactive deposition (SCFRD). The experimental device employed was the same as for the preparation of cobalt-based catalysts (Chapter II). The support (MCM-48) and nickel precursor ( $\text{NiCp}_2$ ) are located inside the high pressure reactor, separated by means of wire mesh. In these experiments, the two reactor configuration presented in the chapter of cobalt catalysts (Section II.4I), “column” and “sandwich” (Fig. III-12), have been tested.



**Figure III-12.** Different configuration: “Column” and “sandwich”

Then,  $\text{CO}_2$  is compressed to 14 MPa and heated up rapidly (in less than 20 minutes) up to 200 °C; assuming that the precursor is dissolved during this short step of conditioning process practically instantaneously. Afterwards, these conditions are maintained for one hour in batch while the deposition takes place, whereupon, the system is slowly decompressed and the composite materials are recovered from the reactor without any residues.

The selected pressure (14 MPa) and temperature (200 °C) are similar to that cobalt deposition. Precursor thermogravimetric analysis (TGA), in figure III-13, confirms that this temperature is high enough to ensure the breakdown of the  $\text{NiCp}_2$ .

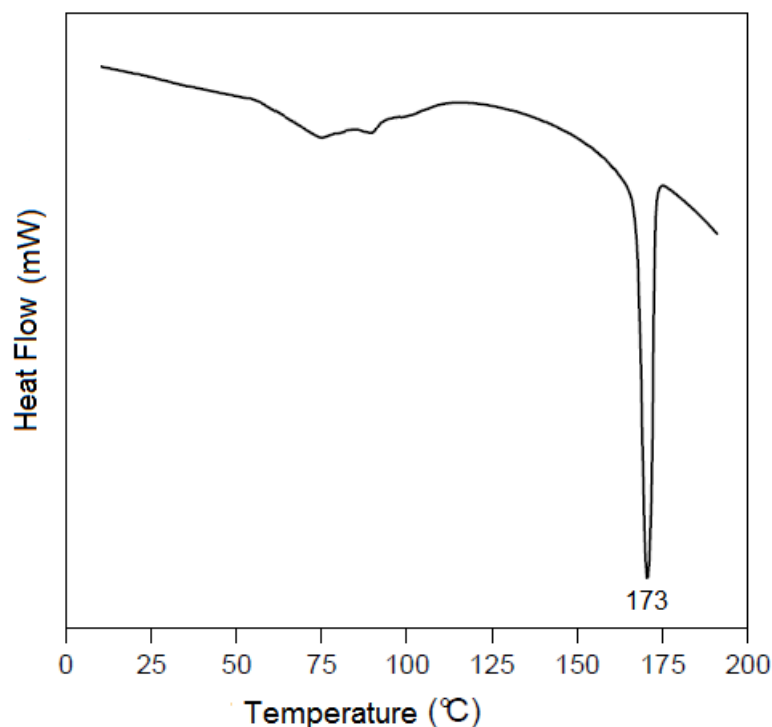


**Figure III-13.** DSC heating profile of NiCp<sub>2</sub>

Finally, several consecutive loadings were also performed to assess whether this results in greater concentration in metallic nanoparticles homogeneously dispersed on the support matrix or on the contrary, this caused the crystal growth of the nanoparticles of nickel.

### III.4.2. SCFRD Results and Discussion.

The table III-4 shows the results of analyzing the concentration of nickel metal in the prepared samples.

**Table III-4.** Nickel metallic loading (% wt) at 14 MPa, 200 °C and 1 hour

Sample <sup>a)</sup>	Methodology	Nickel loading (% wt)
Ni/MCM-48	Column configuration 1 loading	<b>2.81</b>
Ni/MCM-48'	Column configuration 1 loading	<b>2.75</b>
Ni/MCM-48''	Column configuration 1 loading	<b>2.60</b>
Ni <sub>(x1)</sub> /MCM-48 <sub>(x2)</sub>	Sandwich configuration 1 loading	<b>2.44</b>
Ni <sub>(x2)</sub> /MCM-48 <sub>(x2)</sub>	Sandwich configuration 2 sequential loadings	<b>3.70</b>
Ni <sub>(x3)</sub> /MCM-48 <sub>(x2)</sub>	Sandwich configuration 3 sequential loadings	<b>4.21</b>

- a) Samples have been named as follows, Ni<sub>(xx)</sub>/MCM-48<sub>(x2)</sub>, indicating in the first bracket, the number of consecutive loads, and in the second one, the sandwich configuration

### CHAPTER III. Nickel-based Catalysts

The first three experiments were carried out under the same conditions (14 MPa, 200 °C and 1 hour) and configuration, a glass vial with the precursor below, and another one above with the support. The nickel concentration in all of them turned out to be very similar, with an average value of 2.7 %wt and a standard deviation lower than 0.1, demonstrating the robustness of this process.

On the other hand, if these values are compared to the results obtained from the adsorption kinetic study in the previous section, it can be observed that incorporating the precursor decomposition step after the adsorption process, both kinetics and efficacy are enhanced, just as with cobalt-based catalysts. In this case, an increased in nickel concentration closed to 140% is obtained, from the maximum metallic loading obtained only by adsorption of 1.14%wt, to a current value of 2.70 %wt in only one hour of operation.

Experiments with the morphology of sandwich type, in which there are several vials of precursor and support alternately inside the reactor, reveal no improvement taking into account only their metallic loading. However, this work methodology does allow us to obtain a greater amount of product in a single operation.

Lastly, the depositions conducted in sequential loadings have achieved increasing concentrations of metal. But in this case, unlike what was observed by working with Co/MCM-41, the rising in metallic loading decreases considerably from one batch to the next. As shown in the data from Table II-4, the increase in nickel concentration after the second deposition is around 52%, compared with 14% which was obtained after the third batch.

In conclusion, SCFRD method has proven to be a valuable and versatile process with a reasonable repeatability, allowing be applied to other metal-support systems with acceptable efficiencies, starting with operational conditions similar to other systems, without requiring a very large study for its optimization.

### III.5.Characterization of Ni/MCM-48 catalysts

For proper comparison, catalysts were prepared by the three aforementioned techniques with a similar metallic loading, around 3%. The amount of Ni was analyzed by XRF. Table III-5 summarizes the content of Ni-doped on MCM-48 samples, together with other structural data of interest.

**Table III-5.** Structural properties of nickel-based catalysts

Sample	Ni (wt.%)	$S_{BET}$ (m <sup>2</sup> /g)	$d_p$ (nm)	$V_p$ (cm <sup>3</sup> /g) <sup>(a)</sup>
MCM48	---	1641	3.6	0.90
Ni/MCM48-WI	2.95	1545	2.9	0.56
Ni/MCM48-DS	2.79	800	1.2	0.42
Ni/MCM48-SC	2.75	977	1.4	0.45

a) Pore volume (assuming pores are filled with liquid adsorbate)

Data from Table III-5 show how the deposition of nanoparticles over the surface of the support decreases the volume of pore (from 0.9 to around 0.5 cm<sup>3</sup>/g), adding some microporosity ( $d_p < 2$ nm) and therefore, a gradual decrease in the surface area is observed.

On the other hand, the reducibility of the nickel species was studied by TPR profiles, as it is shown the following figures.

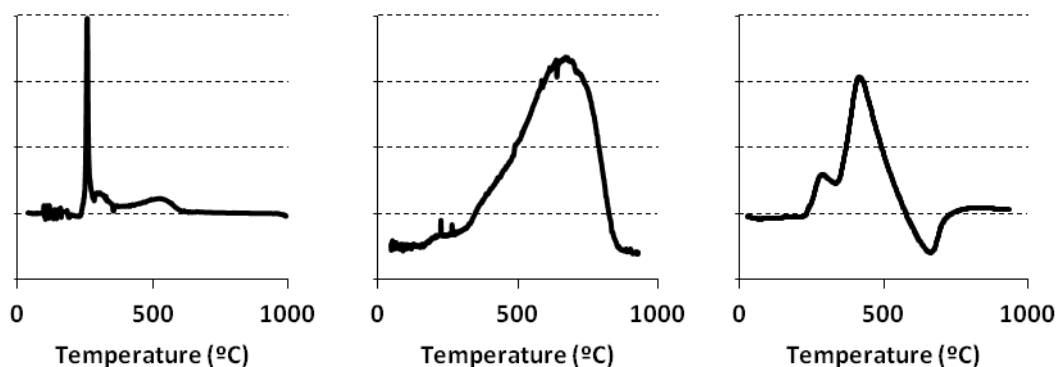


**Figure III-14.** TPR profiles: a) Ni/MCM48-WI; b) Ni/MCM48-DS; and c) Ni/MCM48-SC

TPR profile of catalysts prepared by WI shows 3 peaks. The first and the sharpest peak is observed at around 250 °C (Fig. III-14), which is assigned to the reduction of the nickel oxide species Ni<sup>2+</sup> to metallic form [73].



The presence of this reduction region reveals that deposited nickel shows a slight interaction with the support, characteristic of physisorption, which can lead to a short

### CHAPTER III. Nickel-based Catalysts

useful life of the catalyst. Later, around 300 and 520 °C, two small humps appear. Indicating the existence of some faint traces of hydroxysilicates [74, 75] linked to the support surface.

Conversely, TPR profile for catalysts prepared by DS exhibits a wide reduction region from 230 to 800 °C, with a maximum around 680 °C. This strange behavior is a sign of the presence of small particles of nickel oxides, both Ni<sup>2+</sup> and Ni<sup>3+</sup>, stabilized over the matrix of the support, effect that it only presents in low concentration. Finally, as can be observed in TPR profile for SFRD samples, there are two main peaks. The first one appears at 280 °C; whereas the second is found around 400 °C, with a very steep slope with increasing temperature, even reaching negative values in the output signal from the equipment. This fact reveals not only the existence of nickel oxides, which are reduced at low temperatures; but also the deposition of traces of organometallic precursor, which releases hydrogen after its decomposition. As conclusion, a temperature of 800 °C has been chosen for the activation of catalysts and their subsequent activity test. Then, reduction of the different nickel species has been proved by XRD.

XRD was also employed to characterize the nickel species present at the catalyst prior to its reduction. However, there was no obviously characteristic diffraction peaks on the NiO particles appeared in the XRD patterns of the nickel-based catalysts. According to literature, when the Ni content is lower than 10%, it is unable to identify any species, since the peaks are almost invisible [26], as shown the Fig III-15. This fact is due to that at low concentration, the metallic nanoparticles are much finer and with a more uniform dispersion.

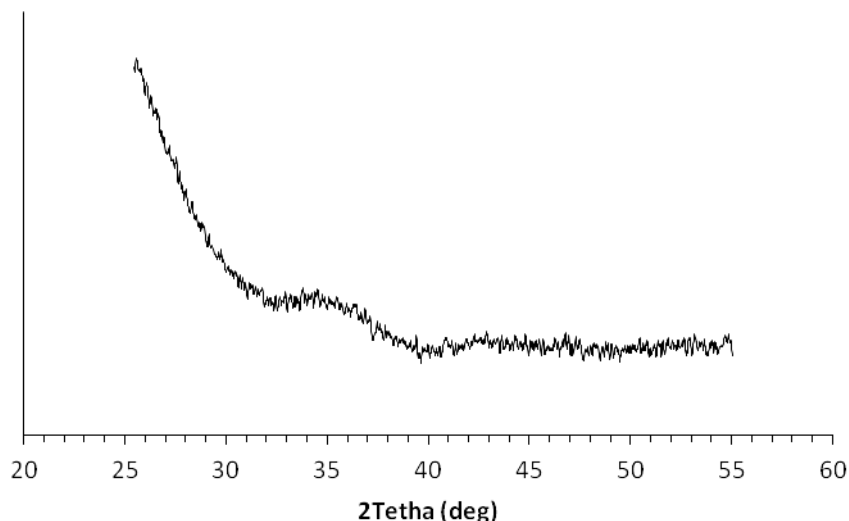


**Figure III-15.** XRD pattern of the catalyst Ni/MCM48

Nevertheless, if the analysis is repeated on a smaller range of angles, it is possible to identify two peaks (Fig. III-16). The main peak for checking the presence of nickel appears at  $44^\circ$ , which is related to several species of nickel (Ni in cubic and hexagonal crystallization phase, NiO and  $\text{Ni}_2\text{O}_3$ ). Also, another peak is observed at around  $36^\circ$ , which could be associated to NiO, slight shifted. The presence of these two unique peaks suggests that in fact the more likely it is that both species coexist in the bulk, and therefore the nickel is in form of a mixed oxide (spinel  $\text{Ni}_{1.875}\text{O}_2$ )

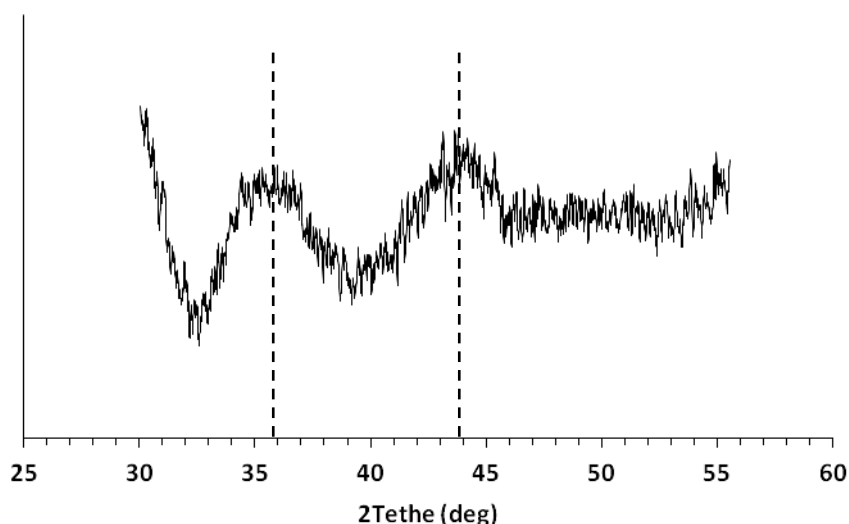


**Figure III-16.** XRD pattern of the catalyst Ni/MCM48 in the range  $2\text{Theta}=30^\circ\text{-}55^\circ$

Following with the characterization of the catalysts, an electron microscopy was used in order to study the morphology of the nanocomposites, besides the distribution of metal.

### CHAPTER III. Nickel-based Catalysts

Figure III-17 shows spherical particles of support with an average diameter of about 200 nm and metallic nanoparticles dispersed on the surface.

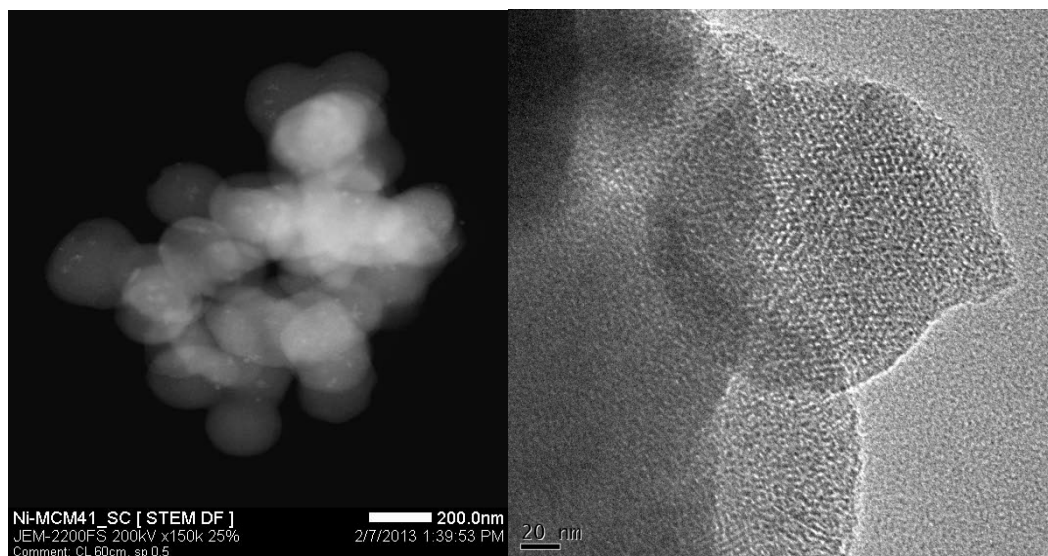


**Figure III-17.** TEM pictures of Ni/MCM48-SC: (A) BSE-Image: homogenous particles support with nanoparticles on surface, (B) detail: intact pore structure and channels

As occurred with the deposition of cobalt, both pores and channels can be distinguished in Fig. III-17, which confirms that SCFRD, despite working at high pressure, does not modify the original structure of the support under any circumstances.

This is the case for example of samples prepared by DS, as can be seen in the attached figure, where the outline of the particle has scaled appearance (Fig. III-18).

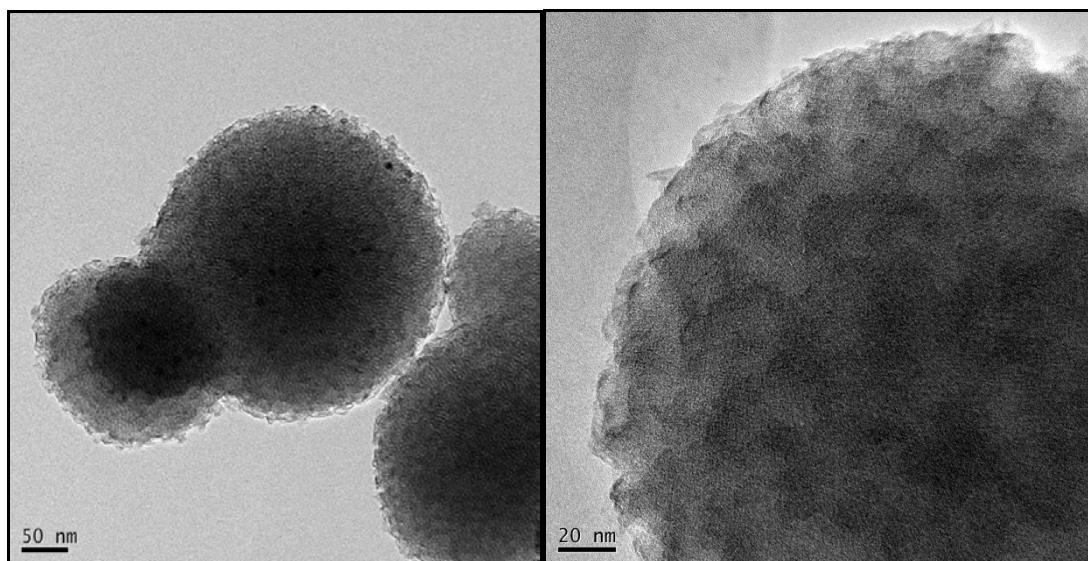


**Figure III-18.** TEM pictures for Ni/MCM48-DS: detail of the irregular surface, broken by the deposition process

The distribution of the metal was observed by means of a MAPPING picture (Fig. III-19).

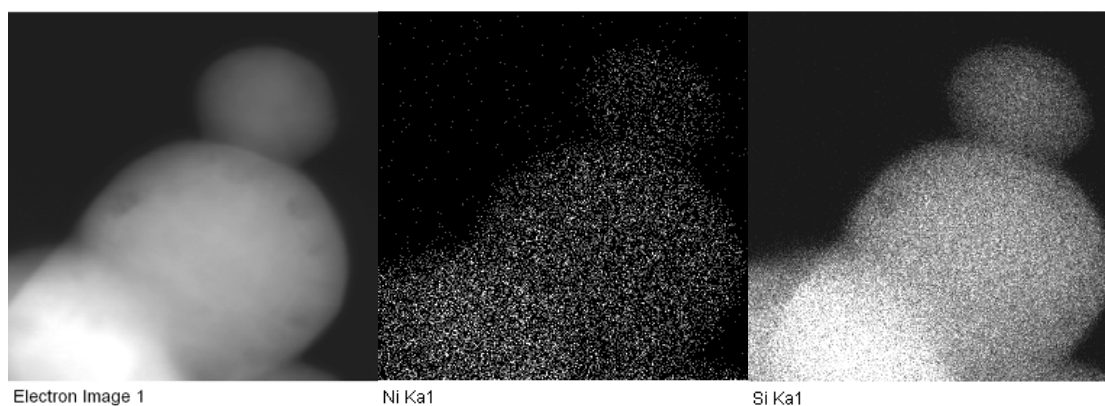


**Figure III-19.** X-Ray TEM/EDX Mapping for Ni/MCM48-SC:  
(A) electron image, (B) Ni  $\kappa\alpha$  and (C) Si  $\kappa\alpha$

In these images, the homogenous distribution of the metal throughout the catalysts prepared by SCFRD is observed, being perfectly distributed both surface and inside the support, without detecting any gradient of concentration or uncoated areas; and corroborating the conclusion drawn above after analysis of the XRD profile.

### III.6. Activity Test: Hydrogenation of Glucose for D-Sorbitol production

Extensive literature deals with biomass conversion to chemicals with high added value [76-81], revealing a new field of study in the choice and synthesis of innovative catalysts in order to increase the selectivity of the reaction. This arises in response to the problematic presented by the degradation of biomass, with complex reaction mechanism and large number of undesirable byproducts [82].

Among the wide range of chemical intermediate, D-sorbitol is one of the most versatile products, used in confections, cosmetics, toothpaste, care products, but particularly as additive in the food industry [83-85].

The catalytic hydrogenation of cellulose into D-sorbitol has been extensively studied in the literature [86-91]. The current industrial is performed with Raney-type nickel catalyst, promoted by various transition metals [92, 93]. Nickel-based catalysts present numerous advantages in this process, exhibiting high activity at low price. But most important is that because of their high density, it is very easy to separate it from the liquid phase in order to recycle it.

In recent years, low ruthenium loading catalysts have been tried to replace nickel-based catalyst, despite being much more expensive, as showing less or no deactivation [94-96]. However, for certain pharmacological and food applications where a free metal waste product is required, ruthenium-based catalysts cannot be implemented either because of their greater toxicity, or by the increase in separations costs incurred.

Therefore, in this chapter, the catalytic activity of the Ni/MCM48 composite materials prepared by SCFRD is confirmed following the hydrogenation of glucose to sorbitol.

#### III.6.1. Experimental device

Catalytic hydrogenation of glucose experiments were carried out in a stainless-steel high pressure reactor (Berghof BR-25) with an internal volume of 25 mL, magnetic stirred and fitted up with a PID for temperature control. This set-up has nitrogen and

hydrogen feeding lines, purge and vent line. Both gases,  $N_2$  and  $H_2$ , are supplied by Carbueros Metálicos (Spain).

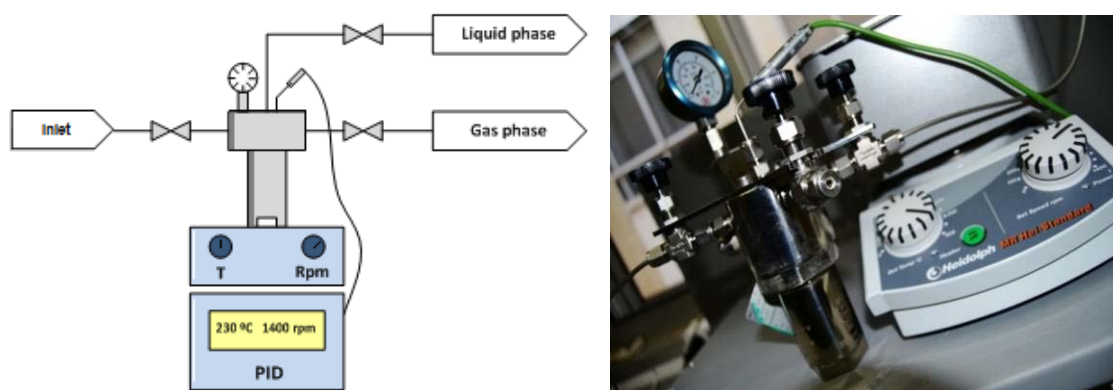


**Figure III-20.** Hydrogenation reactor scheme and photograph

All activity tests for the hydrogenation of glucose were performed at 120 °C and 2.5 MPa  $H_2$ -pressure, under constant stirring rate (1400 rpm) during the desired time. These operating conditions were chosen as optimal for this reaction, based on preceding studies carried out in our High Pressure Research Group [97].

Experiments start with the location of the catalyst in the reactor, previously reduced under  $H_2$  at conditions established by TRP analysis during 1 hour. Cellulose /Ni ratio in all experiments was around 40, as suggested in the literature [97].

After flashing the reactor with  $N_2$  for 10 minutes to remove any oxidizing atmosphere within the reaction chamber,  $H_2$  is fed whereas the reactor is heated up to 120 °C. Once the set point is reached, a solution of glucose (7.5 g/L) is pumped by means of a HPLC pump Jasco model PU-2080 Plus (flow rate range of 1  $\mu$ L to 10 ml per minute and max. pressure of 22 MPa). At the end of each experiment, the reaction is suddenly interrupted by immersing the reactor in an ice bath. Finally, the sample is centrifugated and filtered to recover the catalysts.

Liquid products are analyzed in a HPLC column (SUGAR SC-1011 from Shodex), at 80 °C and flow of 0.8 mL/min, with water Milli-Q as mobile phase. To identify the different sugars, polyols and their derivatives, a Water IR detector was used.

Finally, D-Glucose conversion and D-Sorbitol selectivity and yield, were calculated using Equations 18-20.

$$\%C = \frac{(\text{moles Glucose}_i - \text{moles Glucose}_f)}{\text{moles Glucose}_i} \cdot 100 \quad (\text{Eq. 18})$$

$$\%S = \frac{\text{moles Sorbitol}_f}{(\text{moles Glucose}_i - \text{moles Glucose}_f)} \cdot 100 \quad (\text{Eq. 19})$$

$$\%Y = \frac{\text{moles Sorbitol}_f}{\text{moles Glucose}_i} \cdot 100 \quad (\text{Eq. 20})$$

### III.6.2. Results and discussion

Repeated activity test under the same conditions at different time, only changing the catalyst employed, has been conducted. The results are shown in the Fig. III-21, where the conversion of cellulose is plotted versus time.

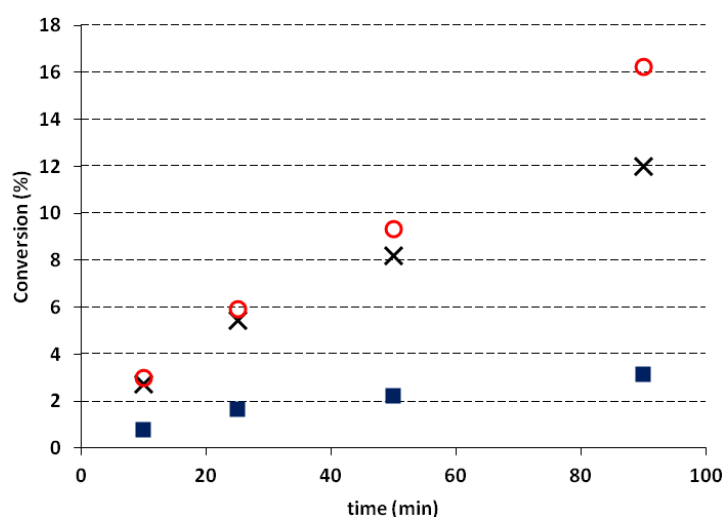


**Figure III-21.** Conversion of glucose versus time at 120 °C and 2.5 MPa (Cellulose/Ni ~ 40):  
(X) Ni/MCM48-SC; (O) Ni/MCM48-WI; and (■) Ni/MCM48-DS

As can be seen, the catalysts prepared by DS presents the smallest activity, reaching a conversion value around 3% after 90 min of reaction. This fact might result from the plugging of the pores and rupture of the channels that was observed in its TEM pictures, avoiding the contact between the reactive and active phase.

By contrast, both catalysts synthesized by WI and SC, show a similar behavior at low time, achieving, for example, the same conversion of 5% in less than 30 minutes. However, after 90 min of operation, both conversions are separated slightly, slowing the reaction produced by the supercritical catalyst. Many authors have already referred to

this behavior, caused by the catalyst deactivation due to intensive coke deposition, being more pronounced the lower the size of the metallic particles [98, 99].

For better evaluation of the influence of this phenomenon in the reaction, the experimental data were fitted to a first order kinetics (Eq. 21).

$$C_i = C_0 \cdot e^{-k \cdot t} \quad (\text{Eq. 21})$$

where  $C_i$  and  $C_0$  represent the concentration at a given point of time and, the initial concentration respectively (g/L);  $k$  is the kinetics constant ( $\text{L/g}_{\text{cat}} \cdot \text{min}^{-1}$ ), and  $w$  is the mass of catalyst per unit volume ( $\text{g}_{\text{cat}}/\text{L}$ ).

Fig. III-22 shows the fitting provided by a first order kinetics model; and the table 6 summarizes the kinetics data with their error, as well as also the conversion, selectivity and yield of the reaction to a particular time of 30 minutes.

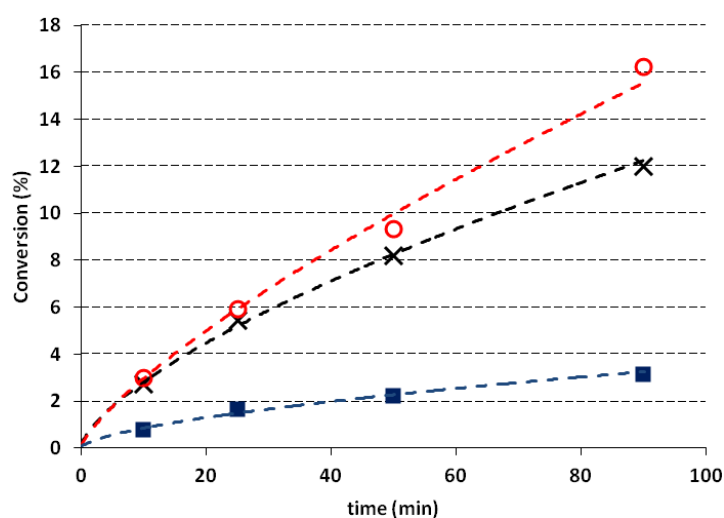


**Figure III-22.** Conversion of glucose versus time at 120 °C and 2.5 MPa (Cellulose/Ni ~ 40):  
Experimental data: (X) Ni/MCM48-SC; (O) Ni/MCM48-WI; and (■) Ni/MCM48-DS  
and the fit provided by first-order kinetics (dotted line)

**Table III-6.** Conversion, average selectivity and yield of hydrogenation of glucose for D-Sorbitol production at 120 °C, 2.5 MPa and 30 minutes, kinetics constant  $k$  and  $R^2$

Catalyst	Conversion (%)	Selectivity (%)	Yield (%)	$k$ ( $\text{L/g}_{\text{cat}} \cdot \text{min}^{-1}$ )	$R^2$
Ni/MCM48-SC	5.67	92.45	5.26	$9.7 \cdot 10^{-3}$	0.99
Ni/MCM48-WI	5.96	96.04	5.96	$7.4 \cdot 10^{-3}$	0.94
Ni/MCM48-DS	1.67	68.36	1.11	$1.6 \cdot 10^{-3}$	0.99

Kinetics constant data reinforce the conclusion drawn above over the catalyst prepared by DS; where besides, if attention is paid to its low selectivity, this provides unacceptable yields (~1%) which would entail substantial costs in separation operations.

### CHAPTER III. Nickel-based Catalysts

Nevertheless, the kinetics constant of the catalysts prepared by WI and SC have the same order, with a very similar value ( $\sim 10^{-2} \text{ min}^{-1}$ ). Moreover, not only seems that catalysts synthesized by SC are equal to the kinetics those prepared by conventional method, but also attending to their yield in the process, provide significant values (5-6%), comparable to the rest.

In conclusion, in this chapter it has been demonstrated that supercritical fluid reactive deposition method (SCFRD) is entirely feasible for the synthesis of nickel-based catalysts.

Catalysts prepared with metallic loading between 2-3% have been tested and compared with other synthesized by conventional methods (WI and DS) in the hydrogenation of glucose for D-Sorbitol production, not only to check their activity, but also to test their selectivity.

Results have shown that catalysts have led to the formation of D-Sorbitol, reaching a glucose conversion around 5% and higher selectivities at 90% in 30 minutes, improving substantially data obtained by DS catalysts and comparable to those of the WI catalysts.

### III.7. Conclusions

In conclusion, in this chapter Ni/MCM-48 catalysts have been synthesized by SCFRD using nickelocene ( $\text{NiCp}_2$ ) as organometallic precursor. During the course of its development, the following partial results have been obtained:

- ✓ It has been determined that the adsorption isotherm of  $\text{NiCp}_2$  on MCM-48 is of type IV, related to the existence of both micro- and meso-pores. Experimental data have been adjusted by different models, being Toth equation which provided the best fit, and predicting a maximum value of adsorption of nickel around 130 mg/g at 14 MPa.
- ✓ The adsorption kinetics of  $\text{NiCp}_2$  on MCM-48 has been fitted to pseudo-first and pseudo-second order with similar results and average standard deviations lower than 4%, estimating time required greater than 10 hours for the adsorption. This process is so slow because the external mass transport is the rate-controlling step, as intraparticle diffusion and film-diffusion models suggest.
- ✓ Ni/MCM-48 catalysts with metallic loading between 2-5 %wt have been synthesized by SCFRD. In this case, the same conditions of temperature (200 °C) and pressure (14 MPa) for the preparation of cobalt-based catalysts have been used, demonstrating the versatility and robustness of the process.
- ✓ Nickel catalysts have been characterized by different techniques and compared to other ones prepared by WI and DS methods. The samples showed BET areas around 1000  $\text{m}^2/\text{g}$  with a slight decrease in the pore volume. TPR profiles revealed very different behaviors according to the synthesis method employed, suggesting the existence of nickel oxides. Microscopy images for samples prepared by SCFRD showed a homogeneous distribution of the metal throughout the support without modifying the original pore structure, unlike catalysts prepared by DS.
- ✓ The activity of the catalysts prepared by SCFRD has been tested in the selective conversion of glucose to sorbitol, reaching a conversion of 6 %, selectivity higher than 90 % and yields around 5 % in 30 minutes, similar to catalysts synthesized by WI and improving substantially data obtained by catalysts prepared by DS. Experimental data have been satisfactorily fitted to a first order kinetics, obtained a value for the kinetics constant of  $9.7 \cdot 10^{-3} \text{ min}^{-1}$ .

### III.8. References

1. Voorhoeve, R.J.H. and J.C.M. Stuiver, *The mechanism of the hydrogenation of cyclohexene and benzene on nickel-tungsten sulfide catalysts*. Journal of Catalysis, 1971. **23**(2): p. 243-252.
2. Bang, Y., S.J. Han, J.G. Seo, M.H. Youn, J.H. Song, and I.K. Song, *Hydrogen production by steam reforming of liquefied natural gas (LNG) over ordered mesoporous nickel–alumina catalyst*. International Journal of Hydrogen Energy, 2012. **37**(23): p. 17967-17977.
3. Majewski, A.J., J. Wood, and W. Bujalski, *Nickel–silica core@shell catalyst for methane reforming*. International Journal of Hydrogen Energy, 2013. **38**(34): p. 14531-14541.
4. Hashemnejad, S.M. and M. Parvari, *Deactivation and Regeneration of Nickel-Based Catalysts for Steam-Methane Reforming*. Chinese Journal of Catalysis, 2011. **32**(1): p. 273-279.
5. Nieva, M.A., M.M. Villaverde, A. Monzón, T.F. Garetto, and A.J. Marchi, *Steam-methane reforming at low temperature on nickel-based catalysts*. Chemical Engineering Journal, 2014. **235**: p. 158-166.
6. Shen, K., X. Wang, X. Zou, X. Wang, X. Lu, and W. Ding, *Pre-reforming of liquefied petroleum gas over nickel catalysts supported on magnesium aluminum mixed oxides*. International Journal of Hydrogen Energy, 2011. **36**(8): p. 4908-4916.
7. Zou, X., X. Wang, L. Li, K. Shen, X. Lu, and W. Ding, *Development of highly effective supported nickel catalysts for pre-reforming of liquefied petroleum gas under low steam to carbon molar ratios*. International Journal of Hydrogen Energy, 2010. **35**(22): p. 12191-12200.
8. Han, S.J., Y. Bang, J. Yoo, J.G. Seo, and I.K. Song, *Hydrogen production by steam reforming of ethanol over mesoporous Ni–Al<sub>2</sub>O<sub>3</sub>–ZrO<sub>2</sub> xerogel catalysts: Effect of nickel content*. International Journal of Hydrogen Energy, 2013. **38**(20): p. 8285-8292.
9. Bimbela, F., M. Oliva, J. Ruiz, L. García, and J. Arauzo, *Hydrogen production via catalytic steam reforming of the aqueous fraction of bio-oil using nickel-based coprecipitated catalysts*. International Journal of Hydrogen Energy, 2013. **38**(34): p. 14476-14487.
10. Morlanés, N., *Reaction mechanism of naphtha steam reforming on nickel-based catalysts, and FTIR spectroscopy with CO adsorption to elucidate real active sites*. International Journal of Hydrogen Energy, 2013. **38**(9): p. 3588-3596.
11. Lua, A.C. and H.Y. Wang, *Decomposition of methane over unsupported porous nickel and alloy catalyst*. Applied Catalysis B: Environmental, 2013. **132-133**: p. 469-478.
12. Abelló, S., C. Berrueco, and D. Montané, *High-loaded nickel–alumina catalyst for direct CO<sub>2</sub> hydrogenation into synthetic natural gas (SNG)*. Fuel, 2013. **113**: p. 598-609.
13. Lovell, E., Y. Jiang, J. Scott, F. Wang, Y. Suhardja, M. Chen, J. Huang, and R. Amal, *CO<sub>2</sub> reforming of methane over MCM-41-supported nickel catalysts: altering support acidity by one-pot synthesis at room temperature*. Applied Catalysis A: General, 2014. **473**: p. 51-58.

14. Zhang, L., L. Li, Y. Zhang, Y. Zhao, and J. Li, *Nickel catalysts supported on MgO with different specific surface area for carbon dioxide reforming of methane*. Journal of Energy Chemistry, 2014. **23**(1): p. 66-72.
15. Tao, K., L. Shi, Q. Ma, D. wang, C. Zeng, C. Kong, M. Wu, L. Chen, S. Zhou, Y. Hu, and N. Tsubaki, *Methane reforming with carbon dioxide over mesoporous nickel–alumina composite catalyst*. Chemical Engineering Journal, 2013. **221**: p. 25-31.
16. Fukuhara, C., R. Hyodo, K. Yamamoto, K. Masuda, and R. Watanabe, *A novel nickel-based catalyst for methane dry reforming: A metal honeycomb-type catalyst prepared by sol–gel method and electroless plating*. Applied Catalysis A: General, 2013. **468**: p. 18-25.
17. Ranjbar, A. and M. Rezaei, *Preparation of nickel catalysts supported on CaO.2Al<sub>2</sub>O<sub>3</sub> for methane reforming with carbon dioxide*. International Journal of Hydrogen Energy, 2012. **37**(8): p. 6356-6362.
18. Bereketidou, O.A. and M.A. Goula, *Biogas reforming for syngas production over nickel supported on ceria–alumina catalysts*. Catalysis Today, 2012. **195**(1): p. 93-100.
19. Huang, L., F. Zhang, R. Chen, and A.T. Hsu, *Manganese-promoted nickel/alumina catalysts for hydrogen production via auto-thermal reforming of ethanol*. International Journal of Hydrogen Energy, 2012. **37**(21): p. 15908-15913.
20. Chan, F.L. and A. Tanksale, *Review of recent developments in Ni-based catalysts for biomass gasification*. Renewable and Sustainable Energy Reviews, 2014. **38**: p. 428-438.
21. Phuhiran, C., T. Takarada, and S. Chaiklangmuang, *Hydrogen-rich gas from catalytic steam gasification of eucalyptus using nickel-loaded Thai brown coal char catalyst*. International Journal of Hydrogen Energy, 2014. **39**(8): p. 3649-3656.
22. Sabatier, P. and J.B. Senderens, *Comptes Rendus de l'Académie des Sciences Paris*, 1902. **134**: p. 514.
23. Rahmani, S., M. Rezaei, and F. Meshkani, *Preparation of promoted nickel catalysts supported on mesoporous nanocrystalline gamma alumina for carbon dioxide methanation reaction*. Journal of Industrial and Engineering Chemistry, 2014.
24. Rahmani, S., M. Rezaei, and F. Meshkani, *Preparation of highly active nickel catalysts supported on mesoporous nanocrystalline  $\gamma$ -Al<sub>2</sub>O<sub>3</sub> for CO<sub>2</sub> methanation*. Journal of Industrial and Engineering Chemistry, 2014. **20**(4): p. 1346-1352.
25. Ando, H., *Effect of Metal Additives on the Hydrogenation of Carbon Dioxide over Nickel Catalyst Prepared by Sol-gel Method*. Energy Procedia, 2013. **34**: p. 517-523.
26. Zhang, J., Z. Xin, X. Meng, and M. Tao, *Synthesis, characterization and properties of anti-sintering nickel incorporated MCM-41 methanation catalysts*. Fuel, 2013. **109**: p. 693-701.
27. Azadi, P., S. Khan, F. Strobel, F. Azadi, and R. Farnood, *Hydrogen production from cellulose, lignin, bark and model carbohydrates in supercritical water using nickel and ruthenium catalysts*. Applied Catalysis B: Environmental, 2012. **117–118**(0): p. 330-338.

28. Cao, Y.-l., J.-w. Wang, Q.-f. Li, N. Yin, Z.-m. Liu, M.-q. Kang, and Y.-l. Zhu, *Hydrolytic hydrogenation of cellulose over Ni-WO<sub>3</sub>/SBA-15 catalysts*. Journal of Fuel Chemistry and Technology, 2013. **41**(8): p. 943-949.
29. Upare, P.P., M.-G. Jeong, Y.K. Hwang, D.H. Kim, Y.D. Kim, D.W. Hwang, U.H. Lee, and J.-S. Chang, *Nickel-promoted copper-silica nanocomposite catalysts for hydrogenation of levulinic acid to lactones using formic acid as a hydrogen feeder*. Applied Catalysis A: General, 2015. **491**(0): p. 127-135.
30. Liang, G., L. He, H. Cheng, C. Zhang, X. Li, S.-i. Fujita, B. Zhang, M. Arai, and F. Zhao, *ZSM-5-supported multiply-twinned nickel particles: Formation, surface properties, and high catalytic performance in hydrolytic hydrogenation of cellulose*. Journal of Catalysis, 2015. **325**(0): p. 79-86.
31. Harrad, M.A., B. Boualy, L. El Firdoussi, A. Mehdi, C. Santi, S. Giovagnoli, M. Nocchetti, and M. Ait Ali, *Colloidal nickel(0)-carboxymethyl cellulose particles: A biopolymer-inorganic catalyst for hydrogenation of nitro-aromatics and carbonyl compounds*. Catalysis Communications, 2013. **32**(0): p. 92-100.
32. Song, Q., J. Cai, J. Zhang, W. Yu, F. Wang, and J. Xu, *Hydrogenation and cleavage of the C-O bonds in the lignin model compound phenethyl phenyl ether over a nickel-based catalyst*. Chinese Journal of Catalysis, 2013. **34**(4): p. 651-658.
33. Peng, Q., J.C. Spagnola, and G.N. Parsons, *Self-Catalyzed Hydrogenolysis of Nickelocene: Functional Metal Coating of Three-Dimensional Nanosystems at Low Temperature*. Journal of The Electrochemical Society, 2008. **155**(9): p. D580-D582.
34. Bozbag, S.E., L.C. Zhang, M. Aindow, and C. Erkey, *Carbon aerogel supported nickel nanoparticles and nanorods using supercritical deposition*. The Journal of Supercritical Fluids, 2012. **66**(0): p. 265-273.
35. Taylor, A.D., G.J. DiLeo, and K. Sun, *Hydrogen production and performance of nickel based catalysts synthesized using supercritical fluids for the gasification of biomass*. Applied Catalysis B: Environmental, 2009. **93**(1-2): p. 126-133.
36. Hunde, E.T. and J.J. Watkins, *Reactive Deposition of Cobalt and Nickel Films from Their Metallocenes in Supercritical Carbon Dioxide Solution*. Chemistry of Materials, 2004. **16**(3): p. 498-503.
37. Aschenbrenner, O., S. Kemper, N. Dahmen, K. Schaber, and E. Dinjus, *Solubility of  $\beta$ -diketonates, cyclopentadienyls, and cyclooctadiene complexes with various metals in supercritical carbon dioxide*. The Journal of Supercritical Fluids, 2007. **41**(2): p. 179-186.
38. Liu, S., P. Cool, O. Collart, P. Van der Voort, E.F. Vansant, O.I. Lebedev, G. Van Tendeloo, and M. Jiang, *The influence of the alcohol concentration on the structural ordering of mesoporous silica: cosurfactant versus cosolvent*. Journal of Physical Chemistry, 2003. **107**: p. 10405-10411.
39. Diankov, S., D. Barth, A. Vega-Gonzalez, I. Pentchev, and P. Subra-Paternault, *Impregnation isotherms of hydroxybenzoic acid on PMMA in supercritical carbon dioxide*. The Journal of Supercritical Fluids, 2007. **41**(1): p. 164-172.
40. Alessi, P., A. Cortesi, I. Kikic, and R. Kittel, *Supercritical adsorption and desorption measurements using a new automated apparatus*, in *Process Technology Proceedings*, R. Ph. Rudolf von and T. Ch, Editors. 1996, Elsevier. p. 687-692.
41. Harikrishnan, R., M.P. Srinivasan, and C.B. Ching, *Adsorption of ethyl benzene on activated carbon from supercritical CO<sub>2</sub>*. AIChE Journal, 1998. **44**(12): p. 2620-2627.

42. Charniak, C.L., T.E. Wetzel, G.L. Aranovich, and M.D. Donohue, *Monte Carlo simulations of phase transitions and adsorption isotherm discontinuities on surface compression*. J Colloid Interface Sci, 2008. **324**(1-2): p. 9-14.
43. Aranovich, G.L. and M.D. Donohue, *Diffusion in fluids with large mean free paths: Non-classical behavior between Knudsen and Fickian limits*. Physica A: Statistical Mechanics and its Applications, 2009. **388**(17): p. 3355-3370.
44. Shigeta, T. and T. Nitta, *Monte Carlo simulation for distribution equilibrium between supercritical fluid and slit pores*, in *Process Technology Proceedings*, R. Ph. Rudolf von and T. Ch, Editors. 1996, Elsevier. p. 327-332.
45. Nitta, T. and T. Shigeta, *Computer simulation studies of adsorption characteristics in supercritical fluids*. Fluid Phase Equilibria, 1998. **144**: p. 245-256.
46. Cocero, M.J. and J. García, *Mathematical model of supercritical extraction applied to oil seed extraction by CO<sub>2</sub> + saturated alcohol: Desorption model*. Journal of Supercritical Fluids, 2001. **20**: p. 229-243.
47. Alonso, E., F.J. Cantero, J. García, and M.J. Cocero, *Scale-up for a process of supercritical extraction with adsorption of solute onto active carbon. Application to soil remediation*. Journal of Supercritical Fluids, 2002. **24**: p. 123-135.
48. Brunauer, S., P.H. Emmet, and E. Teller, *Adsorption of Gases in Multimolecular Layers*. Journal of American Chemical Society, 1938. **60**: p. 309-319.
49. Ebadi, A., J.S. Soltan Mohammadzadeh, and A. Khudiev, *What is the correct form of BET isotherm for modeling liquid phase adsorption?* Adsorption, 2009. **15**(1): p. 65-73.
50. Lagergren, S., *Zur theorie der sogenannten adsorption gelöster stoffe*. Kungliga Svenska Vetenskapsakademiens, 1998. **24**(4): p. 1-39.
51. Ho, Y.S., J.C.Y. Ng, and G. McKay, *Kinetics of Pollutant Sorption by Biosorbents: Review*. Separation and Purification Methods, 2000. **29**(2): p. 189-232.
52. Ho, Y.-S., *Citation review of Lagergren kinetic rate equation on adsorption reactions*. Scientometrics, 2004. **59**(1): p. 171-177.
53. Tseng, R.-L., F.-C. Wu, and R.-S. Juang, *Characteristics and applications of the Lagergren's first-order equation for adsorption kinetics*. Journal of the Taiwan Institute of Chemical Engineers, 2010. **41**(6): p. 661-669.
54. Ho, Y.S. and G. McKay, *Comparative sorption kinetic studies of dye and aromatic compounds onto fly ash*. Journal of Environmental Science and Health, Part A, 1999. **34**(5): p. 1179-1204.
55. Ho, Y.S. and G. McKay, *Pseudo-second order model for sorption processes*. Process Biochemistry, 1999. **34**: p. 451-465.
56. Do, D.D. and H.D. Do, *Non-isothermal effects on adsorption kinetics of hydrocarbon mixtures in activated carbon*. Separation and Purification Technology, 2000. **20**: p. 49-65.
57. Ho, Y.S. and G. McKay, *Sorption of dye from aqueous solution by peat*. Chemical Engineering Journal, 1998. **70**: p. 115-124.
58. Borah, J.M., J. Sarma, and S. Mahiuddin, *Adsorption comparison at the  $\alpha$ -alumina/water interface: 3,4-Dihydroxybenzoic acid vs. catechol*. Colloids and Surfaces A: Physicochemical and Engineering Aspects, 2011. **387**(1-3): p. 50-56.

59. Serna-Guerrero, R. and A. Sayari, *Modeling adsorption of CO<sub>2</sub> on amine-functionalized mesoporous silica. 2: Kinetics and breakthrough curves*. Chemical Engineering Journal, 2010. **161**(1-2): p. 182-190.
60. Weber Jr, W.J. and C.J. Morris, *Kinetics of Adsorption on Carbon from Solution*. Journal of the Sanitary Engineering Division, 1963. **89**(2): p. 31-60.
61. Weber Jr, W.J., *ADSORPTION PROCESSES*, in *XXIVth International Congress of Pure and Applied Chemistry*. 1974, Butterworth-Heinemann. p. 375-392.
62. McKay, G. and V.J.P. Poots, *Kinetics and diffusion processes in colour removal from effluent using wood as an adsorbent*. Journal of Chemical Technology and Biotechnology, 1980. **30**(1): p. 279-292.
63. Hameed, B.H., I.A.W. Tan, and A.L. Ahmad, *Adsorption isotherm, kinetic modeling and mechanism of 2,4,6-trichlorophenol on coconut husk-based activated carbon*. Chemical Engineering Journal, 2008. **144**(2): p. 235-244.
64. Abramian, L. and H. El-Rassy, *Adsorption kinetics and thermodynamics of azo-dye Orange II onto highly porous titania aerogel*. Chemical Engineering Journal, 2009. **150**(2-3): p. 403-410.
65. Yousef, R.I., B. El-Eswed, and A.a.H. Al-Muhtaseb, *Adsorption characteristics of natural zeolites as solid adsorbents for phenol removal from aqueous solutions: Kinetics, mechanism, and thermodynamics studies*. Chemical Engineering Journal, 2011. **171**(3): p. 1143-1149.
66. Albarelli, J.Q., R.B. Rabelo, D.T. Santos, M.M. Beppu, and M.A.A. Meireles, *Effects of supercritical carbon dioxide on waste banana peels for heavy metal removal*. The Journal of Supercritical Fluids, 2011. **58**(3): p. 343-351.
67. Caputo, G., M. Scognamiglio, and I. De Marco, *Nimesulide adsorbed on silica aerogel using supercritical carbon dioxide*. Chemical Engineering Research and Design, 2012. **90**(8): p. 1082-1089.
68. Loganathan, S., M. Tikmani, S. Edubilli, A. Mishra, and A.K. Ghoshal, *CO<sub>2</sub> adsorption kinetics on mesoporous silica under wide range of pressure and temperature*. Chemical Engineering Journal, 2014. **256**: p. 1-8.
69. Boyd, G.E., A.W. Adamson, and L.S. Myers, *The Exchange Adsorption of Ions from Aqueous Solutions by Organic Zeolites: Kinetics*. Journal of American Chemical Society, 1947. **69**: p. 2836-2848.
70. Reichenberg, D., *Properties of ion exchange resins in relation to their structure. Kinetics of exchange*. Journal of American Chemical Society, 1953. **75**: p. 589-597.
71. Oladoja, N.A., A. C.O., and Y.B. Oladimeji, *Kinetics and Isotherm Studies on Methylene Blue Adsorption onto Ground Palm Kernel Coat*. Journal of engineering and environmental sciences, 2008. **32**: p. 303-312.
72. Zulfikar, M.A., H. Stetiyanto, and S.D. Djajanti, *Effect of temperature and kinetic modelling of lignosulfonate adsorption onto powdered eggshell in batch systems*. Journal of Science and Technology, 2013. **35**(3): p. 309-316.
73. Rynkowski, J.M., T. Paryjczak, and M. Lenik, *Characterization of alumina supported nickel-ruthenium systems*. Applied Catalysis A: General, 1995. **126**: p. 257-271.
74. Clause, O., L. Bonneviot, and M. Che, *Effect of the preparation method on the thermal stability of silica-supported nickel oxide as studied by EXAFS and TPR techniques*. Journal of Catalysis, 1992. **138**: p. 195-205.
75. Laribi, M., K. Bachari, R. Chebout, and M. Touati, *Synthesis, characterization and catalytic application of the nickel containing mesoporous silica*. Journal of

- the Association of Arab Universities for Basic and Applied Sciences, 2012. **12**(1): p. 42-47.
76. Corma, A., S. Iborra, and A. Velty, *Chemical Routes for the Transformation of Biomass into Chemicals*. Chemical Reviews, 2007. **107**(6): p. 2411-2502.
  77. Bhaskar, T. and A. Pandey, *Chapter 1 - Advances in Thermochemical Conversion of Biomass—Introduction*, in *Recent Advances in Thermo-Chemical Conversion of Biomass*, A.P.B.S.K. Sukumaran, Editor. 2015, Elsevier: Boston. p. 3-30.
  78. Lan, W., G. Chen, X. Zhu, X. Wang, and B. Xu, *Progress in techniques of biomass conversion into syngas*. Journal of the Energy Institute, 2015. **88**(2): p. 151-156.
  79. Matthiesen, J., T. Hoff, C. Liu, C. Pueschel, R. Rao, and J.-P. Tessonnier, *Functional carbons and carbon nanohybrids for the catalytic conversion of biomass to renewable chemicals in the condensed phase*. Chinese Journal of Catalysis, 2014. **35**(6): p. 842-855.
  80. Tekin, K., S. Karagöz, and S. Bektaş, *Hydrothermal conversion of woody biomass with disodium octaborate tetrahydrate and boric acid*. Industrial Crops and Products, 2013. **49**(0): p. 334-340.
  81. Zhang, J., M. Sun, X. Liu, and Y. Han, *Catalytic oxidative conversion of cellulosic biomass to formic acid and acetic acid with exceptionally high yields*. Catalysis Today, 2014. **233**(0): p. 77-82.
  82. Gallezot, P., *Chapter 1 - Metal Catalysts for the Conversion of Biomass to Chemicals*, in *New and Future Developments in Catalysis*, S.L. Suib, Editor. 2013, Elsevier: Amsterdam. p. 1-27.
  83. Gallezot, P., *Direct routes from biomass to end-products*. Catalysis Today, 2011. **167**(1): p. 31-36.
  84. Liu, G.J., H.G. Cai, Y.G. Liu, and T.F. Su, *Study on influencing factors in preparing C2-C3 polyols with Ry/C hydrogenolysis sorbitol*. Journal of Industrial Science & Technology, 2009. **26**: p. 497-499.
  85. Marash, S., H. Janshekar, and N. Takei. *Sorbitol CEH report*, <http://www.keh.sric.sri.com/public/reports/693.1000/1999>. 1999.
  86. Guo, X., X. Wang, J. Guan, X. Chen, Z. Qin, X. Mu, and M. Xian, *Selective hydrogenation of D-glucose to D-sorbitol over Ru/ZSM-5 catalysts*. Chinese Journal of Catalysis, 2014. **35**(5): p. 733-740.
  87. Negahdar, L., P.J.C. Hausoul, S. Palkovits, and R. Palkovits, *Direct cleavage of sorbitol from oligosaccharides via a sequential hydrogenation-hydrolysis pathway*. Applied Catalysis B: Environmental, 2015. **166–167**(0): p. 460-464.
  88. Li, Y., Y. Liao, X. Cao, T. Wang, L. Ma, J. Long, Q. Liu, and Y. Xua, *Advances in hexitol and ethylene glycol production by one-pot hydrolytic hydrogenation and hydrogenolysis of cellulose*. Biomass and Bioenergy, 2015. **74**(0): p. 148-161.
  89. Han, J.W. and H. Lee, *Direct conversion of cellulose into sorbitol using dual-functionalized catalysts in neutral aqueous solution*. Catalysis Communications, 2012. **19**(0): p. 115-118.
  90. Xi, J., Y. Zhang, Q. Xia, X. Liu, J. Ren, G. Lu, and Y. Wang, *Direct conversion of cellulose into sorbitol with high yield by a novel mesoporous niobium phosphate supported Ruthenium bifunctional catalyst*. Applied Catalysis A: General, 2013. **459**(0): p. 52-58.

91. Negoi, A., K. Triantafyllidis, V.I. Parvulescu, and S.M. Coman, *The hydrolytic hydrogenation of cellulose to sorbitol over M (Ru, Ir, Pd, Rh)-BEA-zeolite catalysts*. *Catalysis Today*, 2014. **223**(0): p. 122-128.
92. Liang, G., L. He, H. Cheng, W. Li, X. Li, C. Zhang, Y. Yu, and F. Zhao, *The hydrogenation/dehydrogenation activity of supported Ni catalysts and their effect on hexitols selectivity in hydrolytic hydrogenation of cellulose*. *Journal of Catalysis*, 2014. **309**(0): p. 468-476.
93. Meryemoglu, B., A. Hesenov, S. Irmak, O.M. Atanur, and O. Erbatur, *Aqueous-phase reforming of biomass using various types of supported precious metal and raney-nickel catalysts for hydrogen production*. *International Journal of Hydrogen Energy*, 2010. **35**(22): p. 12580-12587.
94. Wang, H., L. Zhu, S. Peng, F. Peng, H. Yu, and J. Yang, *High efficient conversion of cellulose to polyols with Ru/CNTs as catalyst*. *Renewable Energy*, 2012. **37**(1): p. 192-196.
95. Zhang, J., B. Hou, X. Wang, Z. Li, A. Wang, and T. Zhang, *Inhibiting effect of tungstic compounds on glucose hydrogenation over Ru/C catalyst*. *Journal of Energy Chemistry*, 2015. **24**(1): p. 9-14.
96. Lazaridis, P.A., S. Karakoulia, A. Delimitis, S.M. Coman, V.I. Parvulescu, and K.S. Triantafyllidis, *D-Glucose hydrogenation/hydrogenolysis reactions on noble metal (Ru, Pt)/activated carbon supported catalysts*. *Catalysis Today*, 2015.
97. Romero, A., A. Sastre, A. Nieto-Márquez, and E. Alonso, *Preparacion de catalizadores mesoporosos de Ni y Ru para la hidrogenación selectiva de D-Glucosa*. I Encuentro de Jóvenes Investigadores de la SECAT, Málaga, España, 22-24 Junio 2004.
98. Forzatti, P. and L. Lietti, *Catalyst deactivation*. *Catalysis Today*, 1999. **52**(2-3): p. 165-181.
99. Liu, D., W.N.E. Cheo, Y.W.Y. Lim, A. Borgna, R. Lau, and Y. Yang, *A comparative study on catalyst deactivation of nickel and cobalt incorporated MCM-41 catalysts modified by platinum in methane reforming with carbon dioxide*. *Catalysis Today*, 2010. **154**(3-4): p. 229-236.

CHAPTER IV.  
Ruthenium-based  
Catalysts

## IV.1. Introduction

### IV.1.1. Ruthenium-based Catalysts and their applications

Ruthenium is a rare transition metal belonging to the platinum group. Thanks to this proximity, it can be used as a versatile catalyst but at a much lower price, especially in applications in organic and pharmaceutical chemistry. Ruthenium catalysts can be a very powerful tool in synthetic chemistry for selective catalysis of such oxidative transformations as asymmetric epoxidation of alkenes, generation of dioxygen species, dihydroxylation of olefins or oxidative dehydrogenation of alcohols.

In particular from the industrial standpoint, ruthenium catalysts are widely employed in metathesis reaction, with Grubbs' catalysts being the most well-known in the field of olefin metathesis. This reaction is one of the most important tools for constructing carbon-carbon double bonds in organic synthesis, materials science and biochemistry. In this case, ruthenium-based catalysts are highly applicable due to their excellent tolerance of a variety of functional groups, and stability in air and a variety of solvents [1-5].

Similarly, in fine chemistry and pharmacy, useful families of hydrogen-transfer catalysts have been developed based on ruthenium. This alternative, which consists in the addition of hydrogen to a molecule from a source other than gaseous H<sub>2</sub> in presence of a catalyst, is being increasingly used in the area of organic synthesis industry, in part because of the inconvenience and expense of using gaseous H<sub>2</sub>. These catalysts, ruthenium complexes, are mainly employed for reduction of ketones, aldehydes and imines to alcohols and amines, respectively [6-8].

On the other hand, ruthenium-based catalysts are generally accepted to be superior to iron or other transition metals. For this reason, many studies are trying to replace them in reactions which require relatively high temperature and pressure to achieve certain productivity. One example is the synthesis of ammonia from hydrogen and nitrogen, where different ruthenium-based catalysts supported have been tested, over BaTiO<sub>2</sub> [9] and carbon [10], with promising results.

Even in the field of the energy carrier, where a great deal of research efforts has been devoted to find suitable hydrogen storage materials ensuring the safe and economical way, ruthenium-based catalysts are earning a spot. Akbayrak et al [11, 12] have reported how ruthenium supported over silica or nanotitania is one of the most active catalyst for the hydrogen generation from ammonia-borane under mild conditions.

But overall, most of research about ruthenium-based catalysts is focused on hydrogenation reactions [13-20]. For example, in the hydrogenation of benzene to cyclohexane, the IFP process in industry uses nickel-based catalysts at temperature above 200°C under 50 bar, but these forcing conditions will lead to poor life-time performance and promote side reactions such as isomerization and hydrocracking, decreasing the selectivity of cyclohexane decline. In view of these arguments, numerous researchers are trying to replace these kinds of catalysts for other ruthenium-based alloy catalysts [13, 14].

In the same way, in glucose hydrogenation where D-sorbitol is produced using nickel-based catalysts e.g. Raney Nickel, novel ruthenium-based catalysts have been developed due to their resistance to chemical attack, showing no leaching [15, 16]. Increasingly, multiple hydrogenation reactions are being catalyzed by new types of ruthenium-based catalysts, even at severe operation conditions such as the transformation of CO<sub>2</sub> to formic acid under 20-40 MPa and at 353-423 K [17].

#### IV.1.2. Deposition of ruthenium using sc-CO<sub>2</sub>

There are a few articles studying the deposition of ruthenium on different supports using supercritical technology. Yen et al. [21] have reported the synthesis of Ru/MCM-41 nanocomposites using Ru(cod)(thmd)<sub>2</sub> as precursor at 150 °C, 10 MPa of CO<sub>2</sub> and 10 MPa of H<sub>2</sub>. In this manner, they have achieved a good distribution of the metallic nanoparticles with an average size of 3.4 nm. Similarly, Kim et al. [22] have synthesized Ru nanodots on Si substrates and HfO<sub>2</sub> films. In this case, Ru<sub>3</sub>(CO)<sub>12</sub> is dissolved into the sc-CO<sub>2</sub> for 1 hour at 90 °C and 23 MPa. Then the solution is pumped into a deposition chamber where H<sub>2</sub> gas was supplied. On the other hand, ruthenium-based catalysts have been also prepared on activated carbon [23-25] by means of sc-CO<sub>2</sub> with the use of a co-solvent (methanol and ethanol). The effects of the temperature,

#### CHAPTER IV. Ruthenium-based Catalysts

pressure, and amount of co-solvent is discussed, obtaining at the optimum condition Ru loading of 2 %wt at 45 °C and 10 MPa. Besides, the catalysts have been tested; in particular, catalysts of Ru/AC prepared by Xu et al. [24] have exhibited a reaction rate 1.5 times higher than commercial catalysts for the hydrogenation of glucose.

## IV.2. Materials

### IV.2.1. Organometallic Precursor: RuCp<sub>2</sub>

As in the case of cobalt and nickel, bis-( $\eta^5$ -cyclopentadienyl)ruthenium or ruthenocene has been chosen as the organometallic precursor for the synthesis of ruthenium catalysts. RuCp<sub>2</sub> was supplied by Sigma Aldrich and used without further treatment.

### IV.2.2. Supports: MCM-48 and activated carbon (AC)

In this case, two different supports have been used for comparison: MCM-48 (previously employed with the nickel catalysts) and activated carbon.

This last support, activated carbon (AC), is a form of carbon processed to have small low-volume pores, obtaining a strong character of microporosity (diameter of pore < 2 nm) in contrast to the M41S supports employed up to the moment in this PhD thesis. Their properties and reactivity are easily modified with different surface functional groups, making this support into the ideal candidate for many industrial and chemical applications, such as medical uses, gas purification, fuel storage, sound absorption or environmental processes inter alia.

In this case, AC was supplied by Sigma Aldrich, reference number 53663, activated charcoal Norit<sup>®</sup> (SX ultra), steam activated and acid washed, powders with an average diameter between 0.15 and 0.25 mm (R1). Elemental analysis was carried out by XRF, where were detected basically Si (~0.7 %wt), Fe (~0.3 %wt), S (~0.2 %wt), and traces of K, Na, Ti and Mg.

---

Briefly, taking into account the above (alternative reactions, precursor and supports), the discussion about the ruthenium catalysts will be developed as follows:

1. Determination of solubility of RuCp<sub>2</sub> in sc-CO<sub>2</sub>
2. Study and modeling of the adsorption isotherms of RuCp<sub>2</sub> on MCM-48 and AC
3. Development of SCFD of RuCp<sub>2</sub> in continuous process
4. Characterization of the prepared Ru-based catalysts prepared
5. Activity test of the Ru-based catalyst in the hydrolysis of cellobiose

### IV.3. Solubility of RuCp<sub>2</sub> in CO<sub>2</sub>

From an industrial point of view, the production of metal nanoparticles using sc-CO<sub>2</sub> could be very useful for numerous applications as it has been previously described in the Introduction of this thesis, but nowadays we are still far from being able to design a large-scale process.

To understand what really happens in the process and to reach a deeper knowledge of it, it is necessary to study the fundamentals and thermodynamics of the process. Aspects such as the solubility of the precursor in sc-CO<sub>2</sub> phase, and the adsorption kinetics on the substrate must be studied since they are not included among the literature data.

So far, in the development of this PhD thesis, unstable organometallic precursors, such as CoCp<sub>2</sub> or NiCp<sub>2</sub>, have been employed and the measurement of their solubilities in sc-CO<sub>2</sub> was not performed experimentally. Their fast degradation and complex formation make not possible these experiments. In these cases, solubility values have been taken from the literature using the few available values [26, 27].

On the other hand, RuCp<sub>2</sub> is a compound enough stable to be used without major precaution in combination with normal grade supercritical CO<sub>2</sub>, because the atomic number, Z, of its metal center is much higher.

#### IV.3.1. Experimental set-up for solubility measurements

The solubility of the organometallic precursor RuCp<sub>2</sub> in sc-CO<sub>2</sub> was determined in a high pressure visual cell at the Chemical and Biological Engineering Dept. in Koç University, Sarıyer, Istanbul, under the supervision of Prof. Dr. Can Erkey.

The solubility was determined by means of the cloud point method. This procedure is based on the visual observation through a sapphire window of a change in the behavior of a solution with a well-known concentration, in this case, the suddenly precipitation of the precursor dissolved in the supercritical fluid when the pressure is decreasing.

A visual observation in a constant volume high pressure view cell equipped with two sapphire windows of 3.2 cm diameter at each side, poly(ether ether ketone) O-rings and rupture disk. The experimental setup that was used for the measurements is depicted in Figures IV-1 and IV-2.

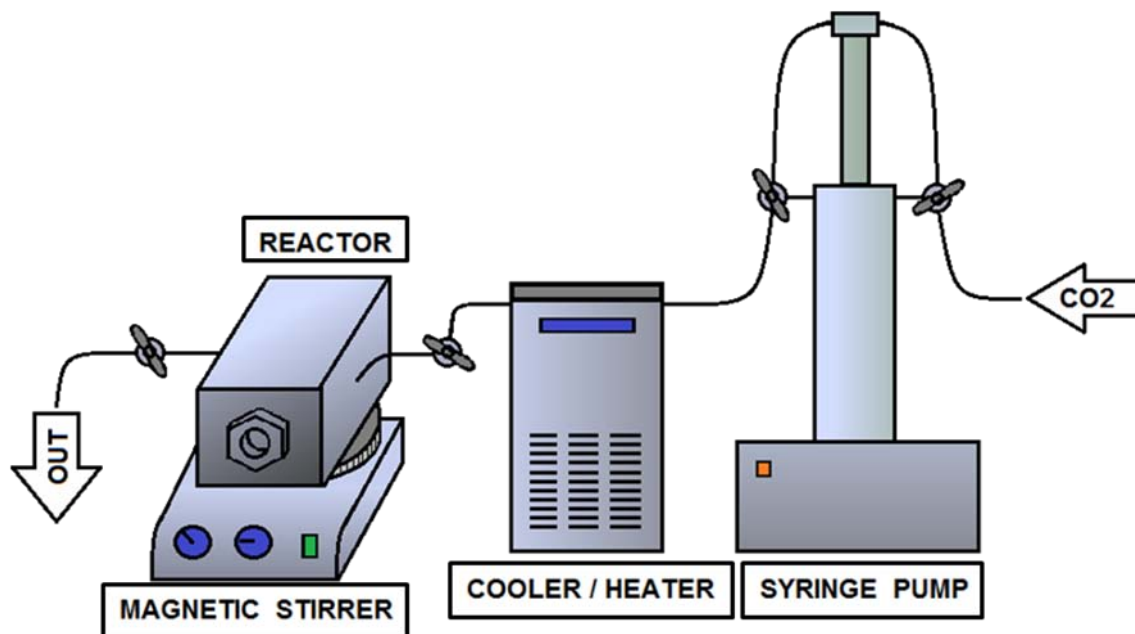


Figure IV-1. Diagram of the device for the solubility experiments



Figure IV-2. High pressure visual cell with sapphire windows and O-rings

## CHAPTER IV. Ruthenium-based Catalysts

A syringe pump (Teledyne ISCO model 260D) was used for the transfer of CO<sub>2</sub> into the high pressure vessel. The accuracy of the syringe pump pressure transducer was  $\pm 0.1$  MPa. Another pressure transducer (Omega PX4100) and a thermocouple (Omega GTMQSS-062G-6) were employed to record the temperature and pressure inside the vessel with a  $\pm 0.1$  °C and  $\pm 0.1$  MPa accuracy, respectively. The temperature of the vessel was controlled by circulating water through the machined internal channels of the vessel using a circulating heater (Cole-Parmer model 12108-15). The temperature of the syringe pump was controlled at 25 °C with a circulating heater (Cole-Parmer model 12108-15) by circulating water through the jacket around the cylinder housing of the pump. A magnetic stirrer was used to mix the contents of the vessel.

Initially, a certain amount of precursor is weighed and placed inside the vessel. After it is sealed, connected to the syringe pump and flushed with CO<sub>2</sub> at atmospheric pressure in order to remove the air inside the vessel. While keeping the inlet valve of the vessel closed, the syringe pump is started and the desired pressure is attained in the line between the syringe pump and the vessel. The inlet valve of the vessel is then opened and liquid CO<sub>2</sub> is charged into the vessel until the set pressure is attained in the vessel. Subsequently, the inlet valve is closed and a single phase mixture is obtained in the vessel which has a clear, homogenous appearance. During the addition of CO<sub>2</sub>, the volume change in the pump cylinder is recorded. The mass of CO<sub>2</sub> that is transferred into the vessel is determined using the density of CO<sub>2</sub> at the pump conditions and the volume change of CO<sub>2</sub> in the pump cylinder. Consequently, the composition of the binary mixture is calculated from masses of precursor and CO<sub>2</sub> added to the vessel. Following the addition of the CO<sub>2</sub> at room temperature, the temperature of the vessel is brought to the experimental conditions using the circulating heater. During the charging of CO<sub>2</sub>, the mixture in the vessel is continuously mixed with the stir bar to provide the homogeneity.

After a homogenous, single-phase mixture of precursor and CO<sub>2</sub> is obtained inside the high pressure vessel, the outlet valve is slightly opened and adjusted to achieve a slow rate of depressurization ( $\sim 0.007$  MPa/s) at constant temperature. During the depressurization, the single phase mixture in the vessel was continuously observed from the sapphire windows. As the pressure is lowered at which dissolved solids are no longer completely soluble, the behavior of the mixture changes precipitating the precursor around the stirrer, as shown in figure IV-3.



**Figure IV-3.** Detail of the cloud point through the sapphire window, with the first precipitated precursor,  $\text{RuCp}_2$  in  $\text{sc-CO}_2$

It is important to note that the composition of the outlet stream and the mixture inside the vessel do not change during depressurization as long as the mixture is homogenous and single-phase. Therefore, it is also possible to make successive measurements at the same conditions as long as the outlet flow is immediately stopped right after the detection of the changes to check the value.

The measurements were repeated for various compositions which were obtained by charging the vessel with different amounts of precursor.

### IV.3.2. Results and discussion

Figure III-4 shows the experimental values of  $\text{RuCp}_2$  solubility in  $\text{sc-CO}_2$  at 60 °C. For each experiment, the measurement was carried out at least three times to verify the value and minimize the statistical error derived from the accuracy of instruments and statistical error ( $\leq 5\%$ ). The density of pure  $\text{CO}_2$  was calculated from Wagner equation of state [28], with an estimated uncertainty range from 0.03 to 0.05% in density. The minimum absolute error in solubility is estimated to be  $\pm 10^{-5}$  mol/mol.

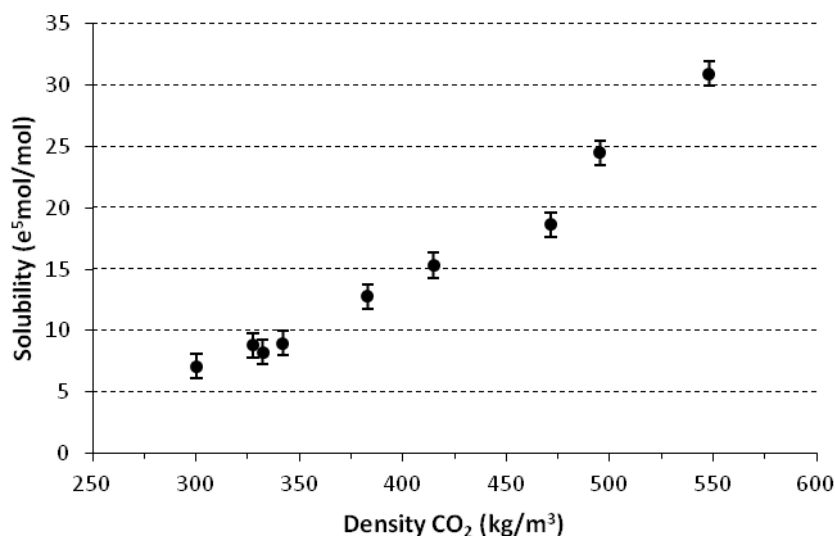


**Figure IV-4.** Experimental data: Molar solubility of  $\text{RuCp}_2$  in  $\text{sc-CO}_2$  at  $60\text{ }^\circ\text{C}$

As it is shown in Fig. IV-4, solubility increases with pressure due to an increase in  $\text{CO}_2$  density, and therefore in solvation power. Values are in agreement with that reported in previous literature [26] measured by a dynamic-gravimetric method.

On the other hand, the solubility of different ruthenium organometallic precursors can be compared considering the influence of its complex structure, several conclusions can be drawn. The figure IV-5 shows the solubility of  $\text{RuCp}_2$  together two other complexes extracted from recent literature [29].

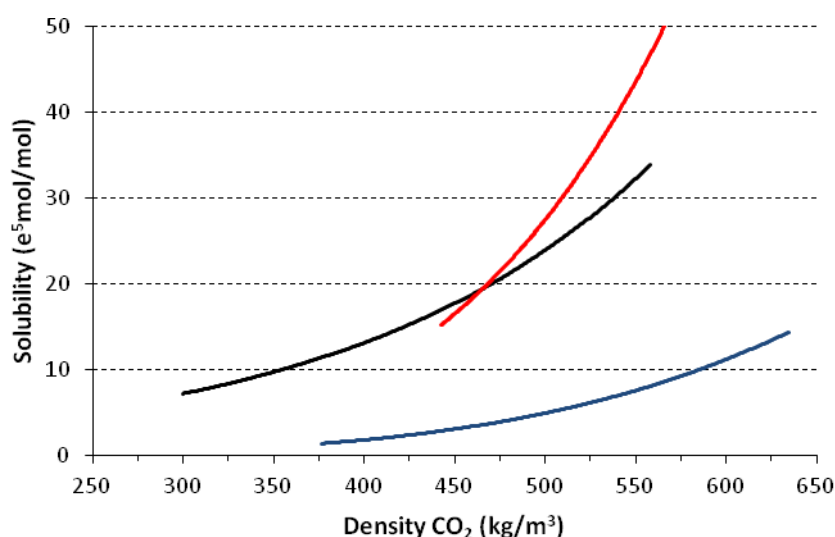


**Figure IV-5.** Solubility in  $\text{sc-CO}_2$  at  $60\text{ }^\circ\text{C}$  of (Black)  $\text{RuCp}_2$  [this work], (Red)  $\text{Ru}(\text{thd})_2(\text{cod})$  [29], and (Blue)  $\text{Ru}(\text{acac})$  [29]

In general, solubility increases with a higher number of ligands per molecule and, accordingly, with the increasing oxidation state of the metal. This is usually related to the better shielding of the positive charge of the metal centre by the bulkier ligands [30].

As can be seen in figure IV-5, this theory is verified for *acac* complex, which presents the lowest solubility in all the studied pressure range; but if the other two compounds ( $\text{Cp}_2$  and  $(\text{thd})_2(\text{cod})$ ) are analyzed, it can be observed a crossover phenomenon at density around  $450 \text{ kg/m}^3$ . This implies that, when working in the vicinity of the critical region (at low pressures), in terms of solubility, it is better to use  $\text{RuCp}_2$  as precursor; whereas away from the critical point (in the region of higher pressures), it is preferable the use of trivalent complexes such as  $\text{Ru}(\text{thd})_2(\text{cod})$ .

Finally, since the purpose of this PhD thesis is to develop a continuous deposition process, we must choose a precursor whose time of solubilization is low, since this will determine the residence time in the saturation bed. The dissolution rate of  $\text{RuCp}_2$  observed through the visual cell was lower than 1 hour, in comparison to 3 h for  $\text{Ru}(\text{thd})_2(\text{cod})$  reported in the literature [29].

### IV.3.3. Modeling of solubility data of $\text{RuCp}_2$ in $\text{CO}_2$

In this section, experimental data of  $\text{RuCp}_2$  solubility in  $\text{sc-CO}_2$  at  $60^\circ\text{C}$  are fitted to predict the solubility behavior of this organometallic precursor in  $\text{sc-CO}_2$ . Usually, classical thermodynamic models can be categorized into three types: equations of state (EoS), models based on the excess Gibbs free energy or activity coefficient (such as UNIFAC or NRTL), and empirical methods [31-34].

Although the solubility of many compounds are good correlated by means of EoS, even in supercritical media [35, 36]; in this case, the use of organometallic complexes- $\text{scCO}_2$  system presents several difficulties; its complexity, non-ideality and non-linearity hinder to predict its behavior.

First, solubility is influenced by the intermolecular forces between the molecules in the solution [31]. On one hand, metals and cyclopentadienyl anions connected by  $\pi$ -bonds, which is not a “real” bond; and on the other hand, the electrons of the Cp are coordinated to the metal center because of its nature as carbanion. Metallocenes have

partial negative charges on the electronegative Cp's and a large partial positive charge on its electropositive metal atom, allowing for the electron-deficient parts act as a Lewis acid and the metallic center atom as Lewis base.

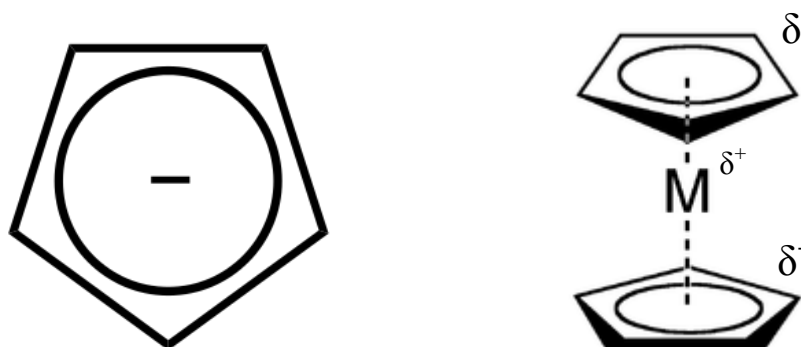


**Figure IV.6.** Ciclopentadienyl and bis( $\eta^5$ -ciclopentadienyl)*metal*: charge distribution

In the same way, *sc*-CO<sub>2</sub> has a large quadrupole moment which plays an important role in its solvating power [37], leading the clustering of solvent molecules around the solute [38].

Besides, various limitations remain in the ability of EoS to predict systems with metal-based complexes due to three main causes: the lack of critical properties data and sublimation pressure for relatively non-volatile solids, the extreme asymmetric sizes and energies of the components in SC solutions, and the highly condensable solutions that lead to solvent clustering around the solute.

Hence, for all these reasons, before trying to fit the experimental data by means of thermodynamic models based on EoS, such as Peng-Robinson or Soave-Redlich-Kwong, it is necessary the employment of others alternative and easier models for this kind of systems, such as empirical methods, in order to evaluate the discrepancies that may exist between the model and reality.

### IV.3.1. Empirical methods

According to these reasons, several groups have developed empirical equations for phase equilibrium calculations of mixtures of solid substances in *sc*-CO<sub>2</sub>. Mendez-Santiago and Teja [39, 40], for example, applied a semiempirical equation including three parameters for each binary system, which has been extended by other authors to model the behavior of similar systems [29]. But the most extended alternative

correlation to predict the solubilities of numerous compounds even in sc-CO<sub>2</sub> was proposed by Chrastil [41].

In this method, the solubility data are correlated as a function of sc-CO<sub>2</sub> density with the assumption that the molecules of a solute associates with a certain number of molecules of gas with the formation of a solvate complex, in equilibrium with the gas (Eq. 1):

$$\ln S = k \cdot \ln \rho_{\text{CO}_2} + C \quad (\text{Eq. 1})$$

where  $S$  is the solubility of precursor expressed as  $\text{kg solute} \cdot \text{m}^{-3}$  of sc-CO<sub>2</sub>; and the SC fluid density,  $\rho_{\text{CO}_2}$  in  $\text{kg} \cdot \text{m}^{-3}$ ;  $k$  is a constant for the solute-solvent system which denotes the grade of solvation of the solute in the fluid; and  $C$  is a constant dependent on the temperature and related to the volatility of the solute.

The Chrastil equation parameters were calculated by minimizing the difference between experimental and calculated solubility, according to the objective function presented in the next equation (Eq. 2):

$$\%AARD = \frac{100}{n} \sum_{i=1}^n \frac{|S_i^{\text{exp}} - S_i^{\text{cal}}|}{S_i^{\text{exp}}} \quad (\text{Eq. 2})$$

The good agreement between estimated values by Chrastil equation with experimental data is shown in Fig. IV-7, together its parameters summarized in Table IV-1.

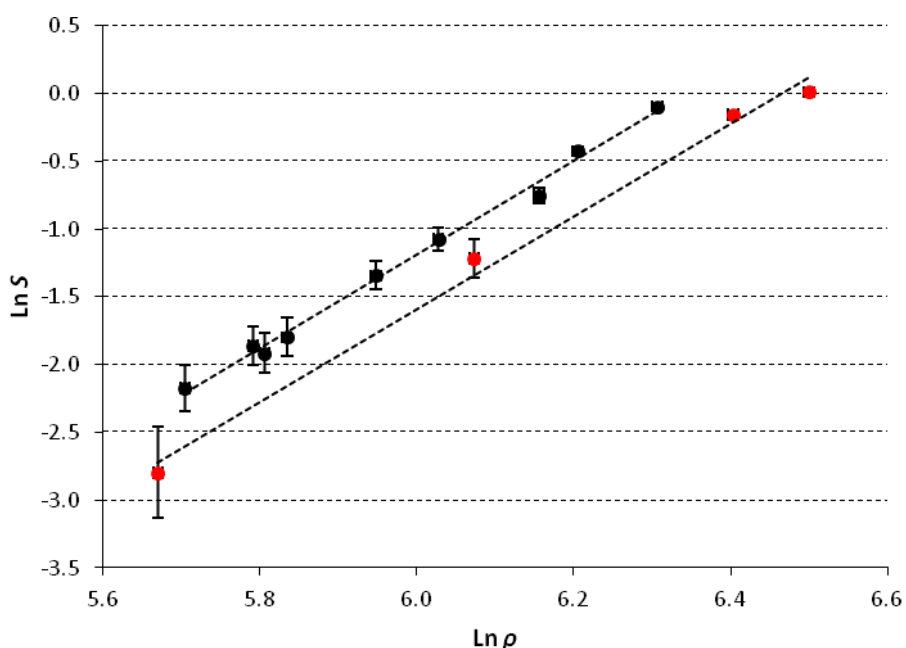


**Figure IV-7.** Solubility of RuCp<sub>2</sub> in sc-CO<sub>2</sub> as a function of density: ● experimental values at 60 °C; ● experimental data from literature [26]; dotted line calculated with Chrastil equation. The error bars correspond with the accuracy of the data points presented in Table IV-1.

**Table IV-1.** Chrastil equation parameters and absolute error

Data	Temp. (°C)	k	C	%AARD
Experimental	60	3.46	-21.95	7.75
Literature [26]	60	3.43	-22.19	11.92

In both curves the same trend in the solubility can be observed, finding a slight difference between the absolute values owing to the different techniques employed for measurements.

### IV.3.3.2. Equations of state (EoS)

Among the different models based on EoS, Peng-Robinson cubic equation of state (PR-EoS) together with Van der Waals-1 mixing rules has been used to correlate the solubility of RuCp<sub>2</sub> in CO<sub>2</sub>, as it has shown good results in a quick and efficient way previously, even with supercritical fluids [42-45].

At equilibrium, the fugacity of RuCp<sub>2</sub> (component *i*) in the solid phase is equal to the fugacity in the SC phase:

$$\hat{f}_i^{solid} = \hat{f}_i^{SCF} \quad (\text{Eq. 3})$$

In the solid phase, the fugacity is given by the following expression:

$$\hat{f}_i^{solid} = x_i(P_i)_{sbl}(\hat{\phi}_i)_{sbl} \exp \left[ \frac{1}{RT} \int V_S dP \right] \quad (\text{Eq. 4})$$

where  $x_i$  is the mole fraction of RuCp<sub>2</sub> in the solid phase,  $(P_i)_{sbl}$  is the sublimation pressure of the pure solid,  $(\hat{\phi}_i)_{sbl}$  is the fugacity coefficient in the solid phase at sublimation,  $V_S$  is the molar volume,  $R$  the gas constant and,  $T$  the temperature. The term in brackets is called the Poynting factor (PF).

On the other hand, the fugacity in the SC phase:

$$\hat{f}_i^{SCF} = y_i P (\hat{\phi}_i)_{SCF} \quad (\text{Eq. 5})$$

where  $y_i$  is the mole fraction of  $\text{RuCp}_2$  in the SC phase,  $(\hat{\phi}_i)_{SCF}$  is the fugacity coefficient in the SC phase and,  $P$  the pressure.

Replacing both terms in Eq. 1, the Equation 6 is obtained:

$$y_i P (\hat{\phi}_i)_{CO_2} = x_i (P_i)_{sbl} (\hat{\phi}_i)_{sbl} \exp \left[ \frac{1}{RT} \int V_S dP \right] \quad (\text{Eq. 6})$$

Since the solid can be taken to be pure,  $x_i$  is unity, so Eq. 6 can be rearranged as:

$$y_i = \frac{(\hat{\phi}_i)_{sbl} (P_i)_{sbl} P^F}{(\hat{\phi}_i)_{CO_2} P} \quad (\text{Eq. 7})$$

In most cases,  $(\hat{\phi}_i)_{sbl}$  can be assumed to be unity since the sublimation pressure of this kind of compounds is very low; however, for the calculation of  $(\hat{\phi}_i)_{SCF}$  it is necessary to apply to PR-EoS.

$$P = \frac{RT}{V-b} - \frac{a(T)}{V(V+b)+b(V-b)} \quad (\text{Eq. 8})$$

where  $a$  and  $b$  are the Van der Waals energy and volume parameters respectively. These constants in the mixture have been computed using the classical mixing rules:

$$a = \sum_i \sum_j x_i x_j a_{ij} \quad (\text{Eq. 9})$$

$$a_{ij} = \sqrt{a_i a_j} (1 - k_{ij}) \quad (\text{Eq. 10})$$

$$b = \sum_i \sum_j x_i x_j b_{ij} \quad (\text{Eq. 11})$$

$$b_{ij} = \frac{b_i + b_j}{2} (1 - l_{ij}) \quad (\text{Eq. 12})$$

where

$$a_i = 0.45724 \alpha (T_{ri}, \omega_i) \frac{R^2 T_{ci}^2}{P_{ci}} \quad (\text{Eq. 13})$$

$$\alpha = [1 + (0.37464 + 1.54226\omega - 0.26992\omega^2)(1 - T_r^{0.5})^2] \quad (\text{Eq. 14})$$

$$\omega = -1.0 - \log(P_r^{sat})_{T_r=0.7} \quad (\text{Eq. 15})$$

$$b_i = 0.07780 \frac{RT_{ci}}{P_{ci}} \quad (\text{Eq. 16})$$

For the application of this equation, it is mandatory to know the critical properties of the substances (critical pressure  $P_c$  and critical temperature  $T_c$ ) and the acentric factor  $\omega$ . For  $\text{CO}_2$ , these properties are reported in data bases [46]. However, for  $\text{RuCp}_2$ , this information is not available owing to this kind of organometallic compounds undergo thermal degradation at temperatures below  $T_c$ ; and on the other hand, it cannot be estimated by group contribution methods, i.e. Joback, because of their special electronic configuration, as already indicated above.

As solution, it has been proposed to use the critical properties of ferrocene ( $\text{FeCp}_2$ ), due to its great similarity since it belongs to the same kind of compounds (metallocenes), which were recently measured by means of a pulse-heating method [47].

In addition, to facilitate the calculation, a single-parameter mixing rule ( $k_{ij}$ ) has been used to describe the interaction between components. This parameter has been calculated correlating the experimental solubility data minimizing the following expression:

$$f(T, P, T_c, P_c, k_{ij}) = \sum_i \left[ \frac{(y_{i,cal} - y_{i,exp})}{y_{i,exp}} \right]^2 \quad (\text{Eq. 17})$$

The critical properties and obtained interaction parameter are presented in Table IV-2, and the PR-EoS prediction is compared with experimental data in Figure IV-8, with an average deviation of 4.4%

**Table IV-2.** PR-EoS parameters

<b>Parameter</b>	<b>Value</b>
<b>Critical temperature (<math>T_c</math> / °C)</b>	512
<b>Critical pressure (<math>P_c</math> / MPa)</b>	3.61
<b>Acentric factor (<math>\omega</math>)</b>	0.369
<b>Interaction parameter (<math>k_{ij}</math>)</b>	0.14
<b>%AARD</b>	4.35

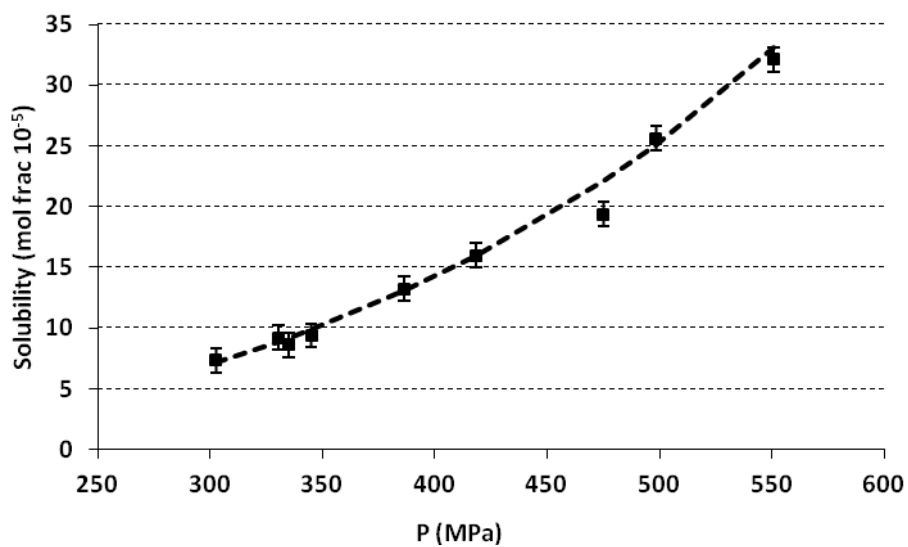


**Figure IV-8.** Experimental data and fitting provided by PR-EoS

It can be seen that the deviations between experimental data and estimated with PR-EoS are lower than with Chrastil equation, being able to predict the behavior of the mixture.

#### IV.4. Adsorption isotherms of RuCp<sub>2</sub>

In the literature, there are two precedents in the study of the adsorption of ruthenium organometallic precursors in supercritical medium. Zhang et al. [48] have reported the adsorption of Ru(cod)(tmhd)<sub>2</sub> on carbon aerogel. All the isotherms were best represented by the modified Langmuir model, founding that maximum concentration corresponded to monolayer coverage of all the accessible surface. On the other hand, silica aerogel has been loaded with Ru(acac)<sub>3</sub> at different pressures and temperatures by Caputo et al. [49]. This study revealed that its kinetic of adsorption is relatively fast, being able to fit its behavior with a simple linear relation. From our part, the adsorption process of RuCp<sub>2</sub> on two different kinds of supports in supercritical CO<sub>2</sub> will be studied in detail in this section. For this purpose, a microporous material (activated carbon, AC) and, a mesoporous ordered silica (MCM-48) have been selected as supports, since they have interesting properties in catalysis. A different behavior in adsorption is expected due to their different chemical nature and surface and textural properties.

First, adsorption isotherms are determined experimentally and fitted with models with the aim of understanding the physics behind the process and choosing the most favorable operational conditions. Secondly, kinetics of adsorption has been determined to estimate the optimum operating time and identify the limiting step.

##### IV.4.1. Results and discussion: Adsorption of RuCp<sub>2</sub>

Adsorption isotherms have been determined at constant temperature (T=60 °C) using the same facility and the procedure described in Chapter II for cobalt. In all the experiments a fixed amount of precursor have been used (10 mg), while varying the amount of precursor up to its solubility limit at different pressures (from 9 to 20 MPa).

In this case, the selected temperature is 10 °C lower than that used for cobaltocene and nickelocene (60 °C instead of 70 °C), looking for a slightly increase of CO<sub>2</sub> density to favor RuCp<sub>2</sub> dissolution, since its solubility is poorer compared to the rest of organometallic precursor employed in this thesis.

The adsorption isotherm data of RuCp<sub>2</sub> on AC (Fig. IV-9) indicates that the metallic loading in the solid phase increases with the concentration of precursor in the supercritical phase, as expected in an isotherm of type I (monolayer).

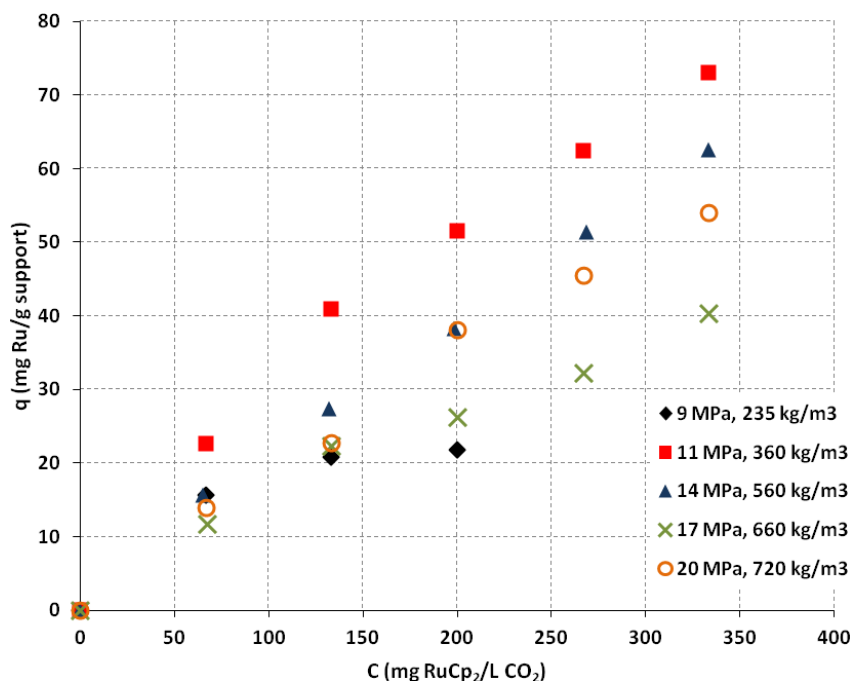


**Figure IV-9.** Effect of pressure on adsorption isotherms of RuCp<sub>2</sub> on activated carbon in SC-CO<sub>2</sub> at 60°C.

As is shown in figure 9, the isotherm at 9 MPa was conducted only up to a concentration of 200 mg/L, basically because the solubility limit of the precursor is reached (4 mol/mol), obtaining a maximum load of 22 mg/g. It can be observed as the equilibrium adsorptive capacity ( $q$ ) decreases with increasing CO<sub>2</sub> density from 11 MPa to 17 MPa at temperature and initial concentration constant. This fact indicates that a higher density (or higher pressure), the interaction forces between the solute and the CO<sub>2</sub> molecules increase, owing to a rising of its solvation power, compared to the bonding forces between the solute and support surface. These results are consistent with previous data from the literature [50].

However, the last isotherm at 20 MPa exhibits a different tendency, having increased its adsorptive capacity with increasing pressure. This crossover phenomenon is not new, and generally occurs at relatively high pressures [51]. There are several examples in the literature, such as the adsorption of toluene [52], CH<sub>4</sub> [53, 54], N<sub>2</sub> and Ar [54] on activated carbon.

On the other hand, the adsorption isotherms of RuCp<sub>2</sub> on MCM-48 are presented in Figure IV-10.

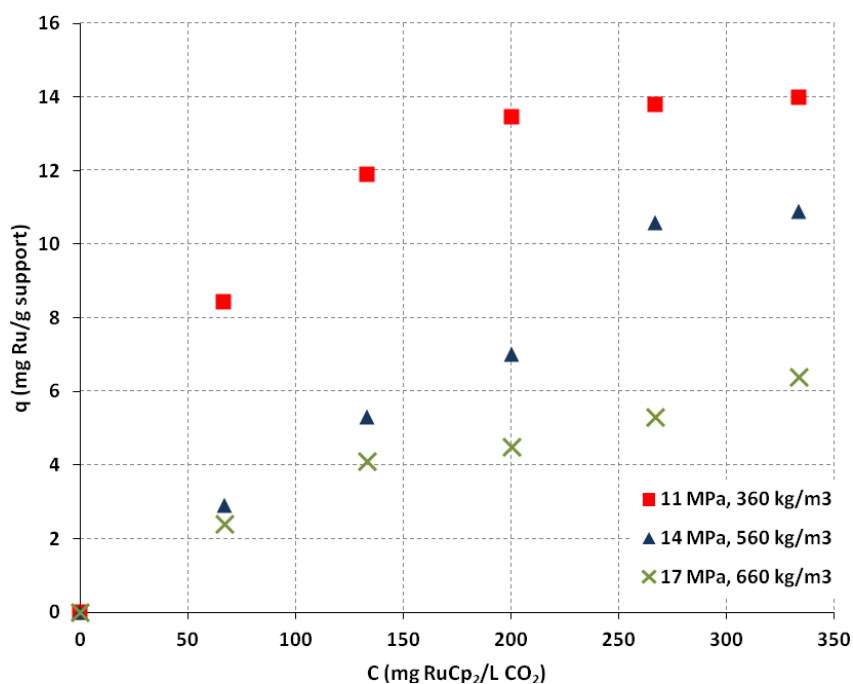


**Figure IV-10.** Effect of pressure on adsorption isotherms of RuCp<sub>2</sub> on MCM-48 in SC-CO<sub>2</sub> at 60°C.

As in the previous case, the adsorption capacity of MCM-48 versus concentration curve clearly shows an isotherm of type I. Similar conclusions than that obtained for deposition on AC can be drawn; that is, the metallic loading increases with the concentration of precursor, and decreasing with increasing pressure, and therefore the density of the supercritical phase.

However, it is remarkable the great difference on the maximum metallic loading of these two supports. Whereas it is possible to achieve maximum metallic loadings up to 80 mg/g on AC, when using MCM-48 as support, only depositions around 15 mg/g were reached. This divergence in the results could be due to the treatment that has been performed to the charcoal to activate it, which, in addition to incorporate numerous functional groups, also could caused significant changes in its porosity both in pore size and pore arrangement [55].

#### IV.4.2. Adsorption Isotherm Modeling: Fittings and discussion

Experimental data were fitted using the sorption models explained in Chapter III (Langmuir, Freundlich, Redlich-Peterson and BET).

#### RuCp<sub>2</sub> on AC

The experimental isotherms at 11, 14, 17 and 20 MPa were fitted with the five sorption models. Adjusted parameters and mean square error (MSE) for each model are summarized in the Table IV-3, where several conclusions can be drawn together with the analysis from the figures IV-11 to IV-15.

**Table IV-3.** Fitted model parameters and average deviation for the adsorption equilibrium of RuCp<sub>2</sub> on AC in sc-CO<sub>2</sub>: Langmuir, Freundlich, Redlich-Peterson and BET

	<i>Isotherm 1</i> 11 MPa	<i>Isotherm 2</i> 14 MPa	<i>Isotherm 3</i> 17 MPa	<i>Isotherm 4</i> 20 MPa
<b>Langmuir</b>				
<i>k</i> (L/mg)	0.0057	0.0053	0.0056	0.0053
<i>q<sub>s</sub></i> (mg/g)	103.55	87.46	52.12	74.03
<i>MSE</i>	4.95	5.72	2.22	4.43
<b>Modified Langmuir</b>				
<i>k'</i> (L/mg)	0.0045	0.0042	0.0032	0.0034
<i>q'<sub>s</sub></i> (mg/g)	65.07	44.44	20.56	42.60
<i>λ</i> (L/mg)	0.107	0.102	0.094	0.092
<i>MSE</i>	1.41	1.52	1.94	1.33
<b>Freundlich</b>				
<i>K<sub>F</sub></i> ((mg/g)/(mg/L) <sup>1/n</sup> )	0.97	0.78	0.58	0.47
<i>n</i>	1.34	1.34	1.37	1.22
<i>MSE</i>	1.45	2.01	1.23	1.37
<b>Redlich-Peterson</b>				
<i>K<sub>RP</sub></i> (mg/g)	39.26	34.00	32.59	27.42
<i>a<sub>R</sub></i> (L/mg) <sup>g</sup>	38.18	44.12	55.38	57.77
<i>g</i>	0.26	0.25	0.27	0.18
<i>MSE</i>	1.50	1.95	1.23	1.37
<b>BET</b>				
<i>K<sub>BET</sub></i> (L/mg)	7.93	6.14	8.10	4.53
<i>Q<sub>s</sub></i> (mg/g)	87.22	71.65	48.85	65.49
<i>C<sub>s</sub></i> (mg/L)	1618	1481	1798	1269
<i>MSE</i>	1.45	1.84	1.23	1.24

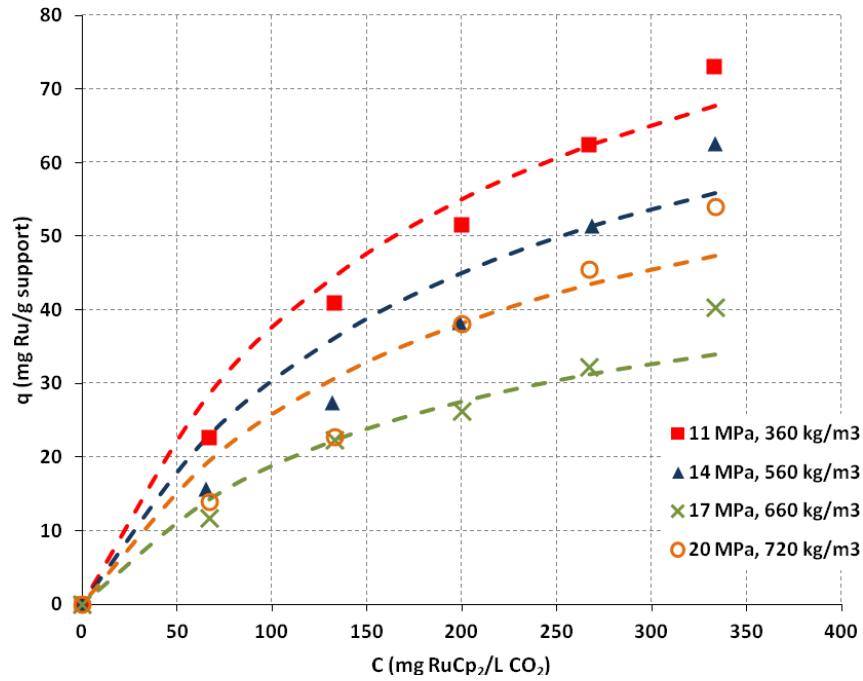


**Figure IV-11.** Experimental data (symbols) and fit by Langmuir (lines) for adsorption isotherms of  $\text{RuCp}_2$  on AC at 60 °C and: (◆) 9 MPa; (■) 11 MPa; (▲) 14 MPa; (X) 17 MPa; (○) 20 MPa.

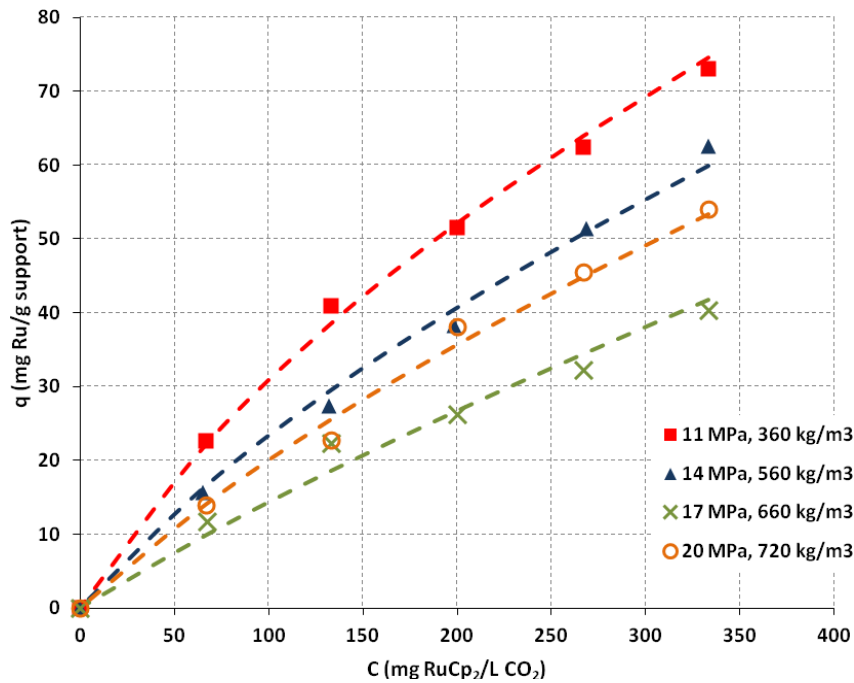


**Figure IV-12.** Experimental data (symbols) and fit by Modified Langmuir (lines) for adsorption isotherms of  $\text{RuCp}_2$  on AC at 60 °C and: (◆) 9 MPa; (■) 11 MPa; (▲) 14 MPa; (X) 17 MPa; (○) 20 MPa.

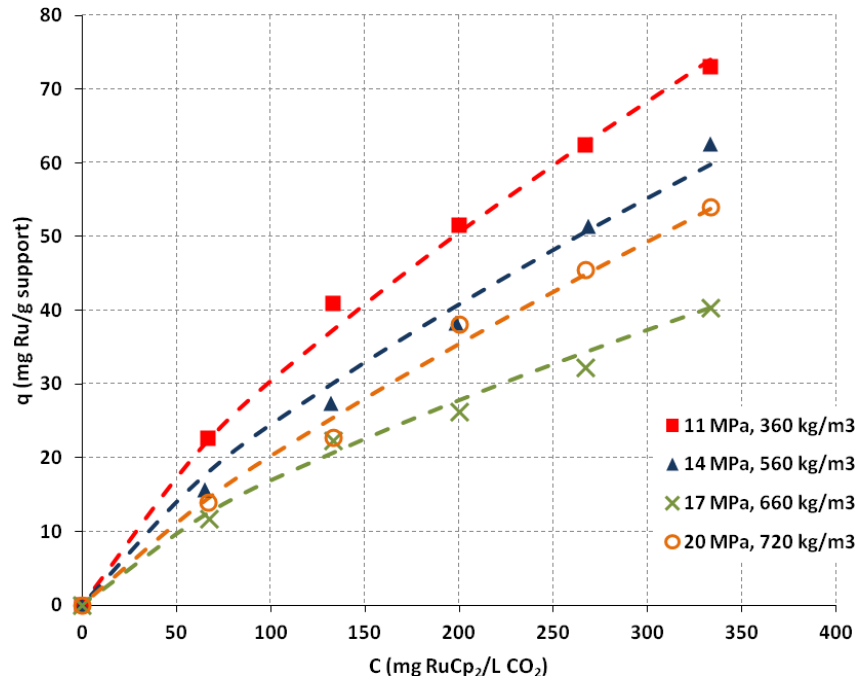


**Figure IV-13.** Experimental data (symbols) and fit by Freundlich (lines) for adsorption isotherms of RuCp<sub>2</sub> on AC at 60 °C and: (◆) 9 MPa; (■) 11 MPa; (▲) 14 MPa; (X) 17 MPa; (○) 20 MPa.

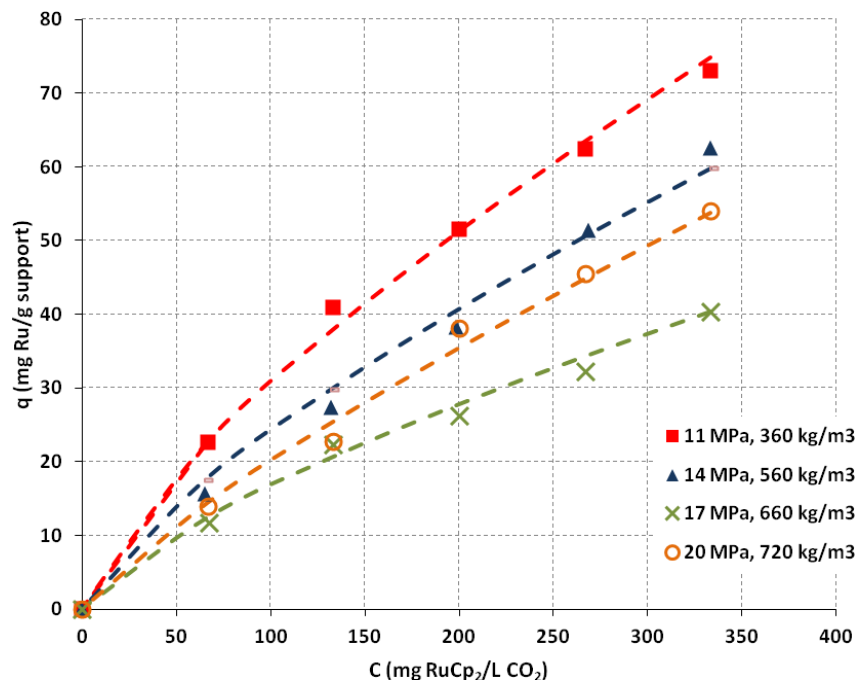


**Figure IV-14.** Experimental data (symbols) and fit by Redlich-Peterson (lines) for adsorption isotherms of RuCp<sub>2</sub> on AC at 60 °C and: (◆) 9 MPa; (■) 11 MPa; (▲) 14 MPa; (X) 17 MPa; (○) 20 MPa.

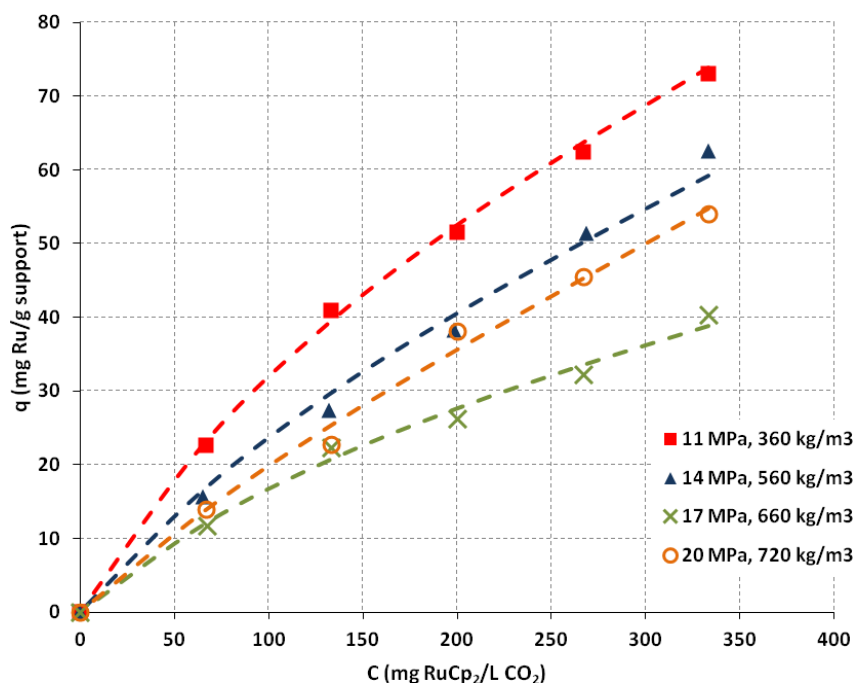


**Figure IV-15.** Experimental data (symbols) and fit by BET (lines) for adsorption isotherms of  $\text{RuCp}_2$  on AC at 60 °C and: (◆) 9 MPa; (■) 11 MPa; (▲) 14 MPa; (×) 17 MPa; (○) 20 MPa.

First, considering the values of the average error, it is possible to conclude that all models provided similar fits ( $\text{MSE} < 6$ ), although obviously the three-parameter models (modified Langmuir, Redlich-Peterson and BET isotherms) give the lowest deviations.

For the Langmuir and modified Langmuir models, the values of  $k$  are much smaller, around one order of magnitude, than other values reported in supercritical  $\text{CO}_2$ , such as the adsorption of ethylacetate and furfural on AC [50], hydroxybenzoic acid on PMMA [56], or  $\text{Pt}(\text{COD})\text{Me}_2$  onto organic aerogels [57]; but similar to that found for the adsorption of  $\text{Ru}(\text{COD})(\text{tmhd})_2$  on AC [48], or  $\text{Pd}(\text{hfac})_2$  onto SBA-15 [58]. In this case, the product of  $k \cdot q_s$  gets very small in both models, indicating a weak adsorption of this precursor,  $\text{RuCp}_2$ , over the surface of the AC support.

Comparing the fits, Langmuir model gives close values to the experimental data at low concentration, but it is unable to reproduce the plateau occurring at higher concentrations; thereby, it can be concluded that this system under supercritical conditions differs significantly from ideal monolayer adsorption on a plane surface.

Likewise, Freundlich model correlated satisfactorily the experimental data considering that this is a model of only two parameters, with deviations similar to Redlich-Peterson.

However, this model does not consider the competitive adsorption of CO<sub>2</sub> for adsorption sites, which was recently reported by Wu et al. [59].

Taking this consideration into account, three-parameter models, such as Redlich-Peterson and BET correlations, have been used to improve slightly the fit of the experimental data. Both models provide the best fit over the whole range of experimental concentrations, with average deviation about 1%. Therefore, these two correlations are clearly the most appropriated models to represent the sorption equilibrium for this system.

Finally, noteworthy as in all cases, the value of the saturation limit capacity ( $Q_s$ ) provided by BET model is slightly lower than estimated by Langmuir correlation ( $q_s$ ), being this last one more closer to the experimental data.

### RuCp<sub>2</sub> on MCM-48

Once finished the discussion about the deposition on AC, the parameters of the fitting of the experimental data for the adsorption on MCM-48 can be found in table IV-4, and the graphical representations for each model in figures IV-16 to IV-20.

**Table IV-4.** Fitted model parameters and average deviation for the adsorption equilibrium of RuCp<sub>2</sub> on MCM-48 in sc-CO<sub>2</sub>: Langmuir, Freundlich, Redlich-Peterson and BET

	<i>Isotherm 1</i> 11 MPa	<i>Isotherm 2</i> 14 MPa	<i>Isotherm 3</i> 17 MPa
<b>Langmuir</b>			
<i>k</i> (L/mg)	0.0188	0.0055	0.0042
<i>q<sub>s</sub></i> (mg/g)	16.25	15.00	10.34
<i>MSE</i>	0.24	1.19	0.33
<b>Modified Langmuir</b>			
<i>k'</i> (L/mg)	0.0502	0.0032	0.0059
<i>q'<sub>s</sub></i> (mg/g)	9.11	8.17	7.20
<i>λ</i> (L/mg)	0.019	0.022	0.004
<i>MSE</i>	0.78	0.43	0.31
<b>Freundlich</b>			
<i>K<sub>F</sub></i> ((mg/g)/(mg/L) <sup>1/n</sup> )	2.21	0.43	0.22
<i>n</i>	3.07	1.80	1.74
<i>MSE</i>	0.56	0.98	0.28
<b>Redlich-Peterson</b>			
<i>K<sub>RP</sub></i> (mg/g)	61.89	14.85	7.48
<i>a<sub>R</sub></i> (L/mg) <sup><i>M</i></sup>	27.78	30.00	33.66
<i>g</i>	0.67	0.48	0.43
<i>MSE</i>	0.56	1.13	0.28
<b>BET</b>			
<i>K<sub>BET</sub></i> (L/mg)	33.63	15.24	14.35
<i>Q<sub>s</sub></i> (mg/g)	15.43	12.01	7.26
<i>C<sub>s</sub></i> (mg/L)	2464	2270	2226
<i>MSE</i>	0.64	1.01	0.31

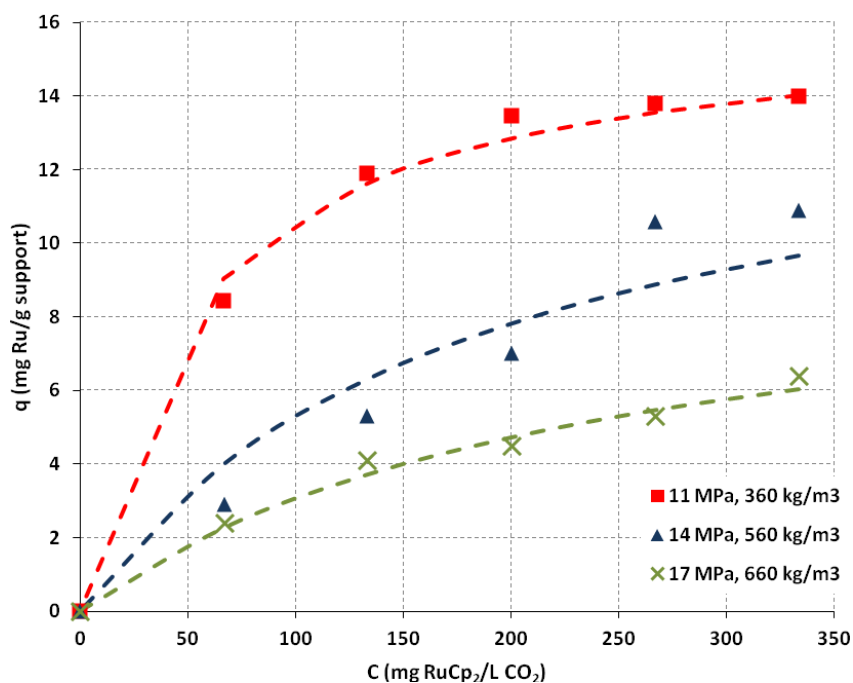


**Figure IV-16.** Experimental data (symbols) and fit by Langmuir (lines) for adsorption isotherms of RuCp<sub>2</sub> on MCM-48 at 60 °C and: (■) 11 MPa; (▲) 14 MPa; (X) 17 MPa.

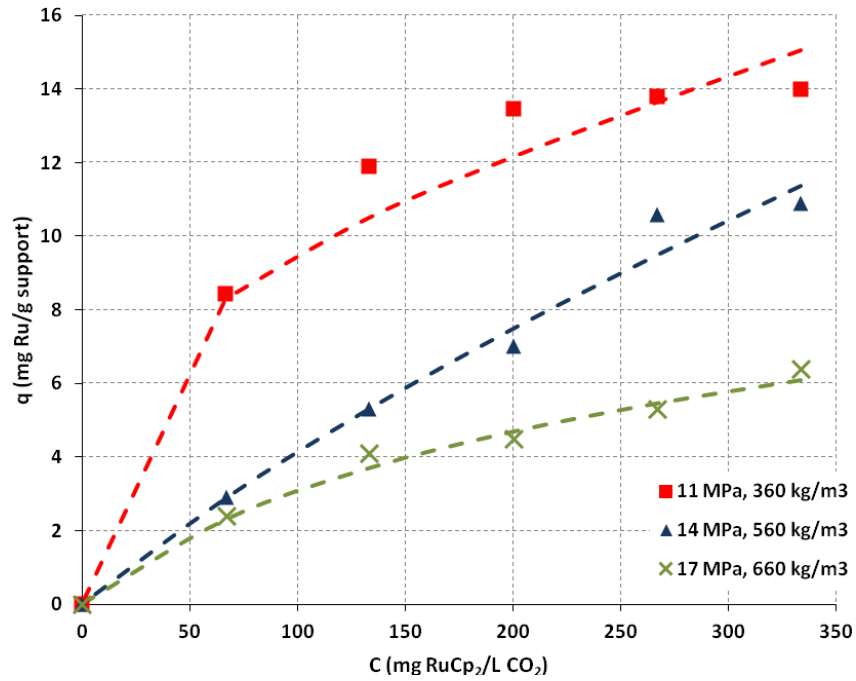


**Figure IV-17.** Experimental data (symbols) and fit by Modified Langmuir (lines) for adsorption isotherms of RuCp<sub>2</sub> on MCM-48 at 60 °C and: (■) 11 MPa; (▲) 14 MPa; (×) 17 MPa.

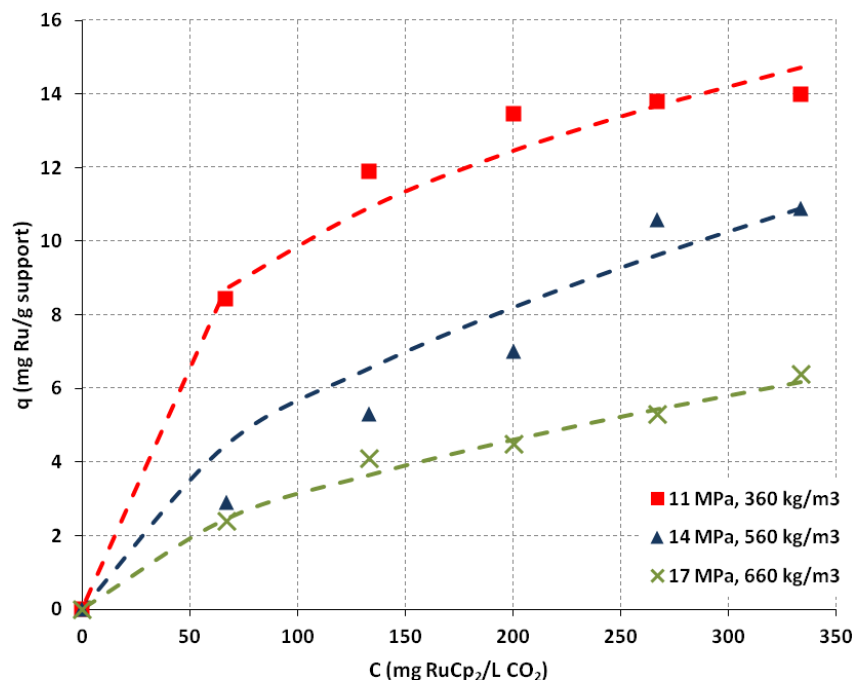


**Figure IV-18.** Experimental data (symbols) and fit by Freundlich (lines) for adsorption isotherms of RuCp<sub>2</sub> on MCM-48 at 60 °C and: (■) 11 MPa; (▲) 14 MPa; (×) 17 MPa.

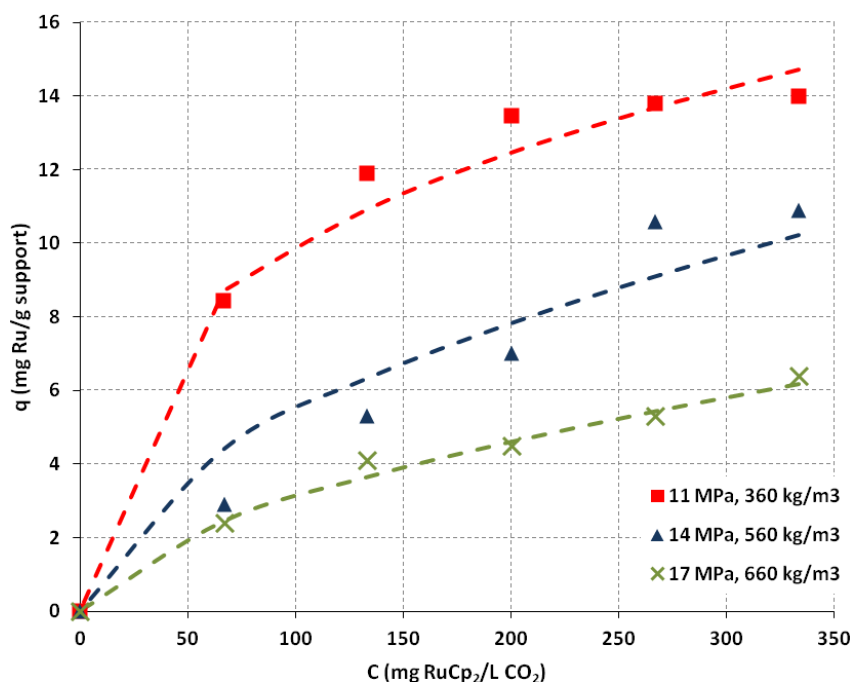


**Figure IV-19.** Experimental data (symbols) and fit by Redlich-Peterson (lines) for adsorption isotherms of RuCp<sub>2</sub> on MCM-48 at 60 °C and: (■) 11 MPa; (▲) 14 MPa; (X) 17 MPa.

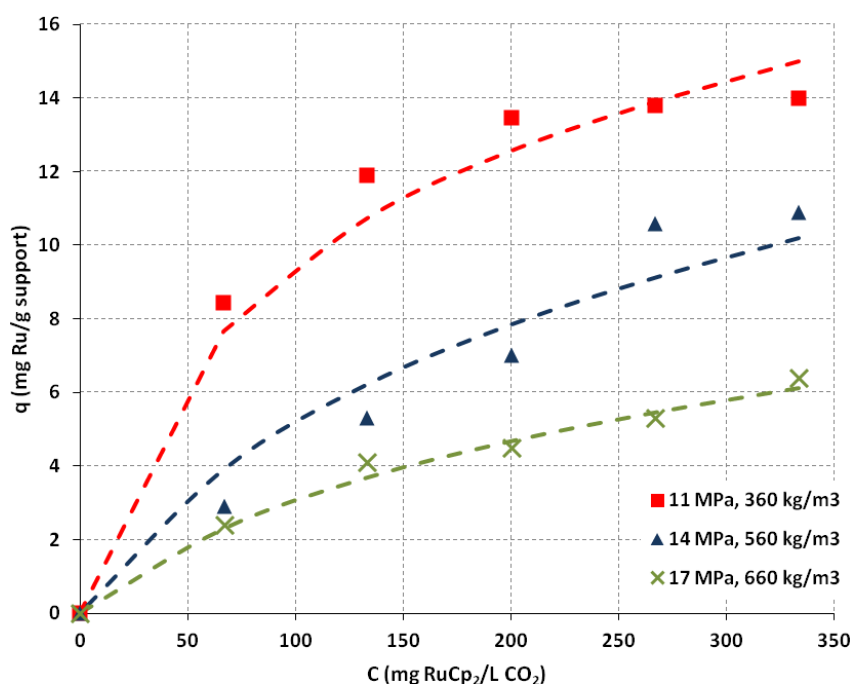


**Figure IV-20.** Experimental data (symbols) and fit by BET (lines) for adsorption isotherms of RuCp<sub>2</sub> on MCM-48 at 60 °C and: (■) 11 MPa; (▲) 14 MPa; (X) 17 MPa.

Although the provided adjustments show average deviations equal to or less than 1 in all cases, not all of them are able to describe the process reliably.

Langmuir model represents the adsorption curve accurately, further providing values for the parameter  $q_s$  very close to those achieved experimentally, demonstrating to be

capable of predicting the metallic loading which could be obtained at equilibrium. Moreover, it is rechecked as the product of  $k \cdot q_s$  is very low, just like in the previous case, denoting a poor affinity of the metal on the support.

All other models provide virtually the same setting, with no significant differences.

Most of them do not have a good fit in the whole concentration range, showing certain deviations at low concentrations, as is particularly noticeable in the isotherm at 14 MPa correlated with Freundlich or Redlich-Peterson models.

Meanwhile, BET model returns to satisfactorily response by returning an adjustment where the  $Q_s$  values listed in the Table IV-4 are also in good agreement with the experimental ones and closer to those provided by Langmuir correlation.

In conclusion, taking into account the results shown in this section, henceforth all experiences will be developed at a pressure of 11 MPa to go on with the study of the process and establish the optimal working conditions.

#### IV.4.3. Adsorption Kinetics of RuCp<sub>2</sub>

Figure IV-21 shows the experimental data of the adsorption rate of RuCp<sub>2</sub> on AC, where metallic loading versus time at 60 °C and 11 MPa is presented, together with the corresponding profiles predicted by means of pseudo-first and second order models (explained in Chapter II). Table IV-5 summarizes the values for the kinetics constants and characteristic parameters, with its associated calculated error by Equation 18.

$$\Delta q(\%) = \sqrt{\frac{\sum[(q_{exp} - q_{model})/q_{exp}]^2}{N-1}} \cdot 100 \quad (\text{Eq. 18})$$

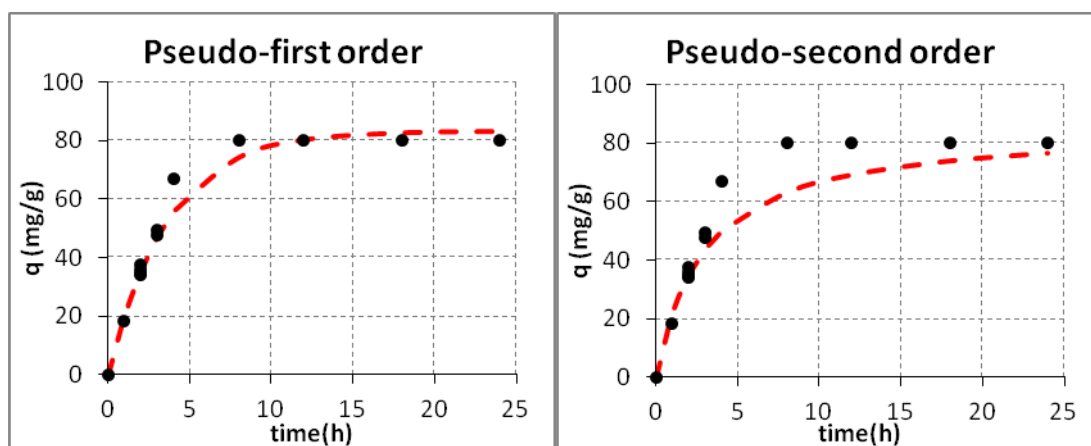


**Figure IV-21.** Adsorption of  $\text{RuCp}_2$  on AC at 60 °C and 11 MPa: Experimental data (●) and pseudo-first and second order fits (dotted line).

**Table IV-5.** Kinetics parameters for adsorption of  $\text{RuCp}_2$  on AC: pseudo-first and second order.

Model	Rate constant ( $k$ )	Saturation limit ( $q_s$ )	Std. deviation ( $\Delta q$ )
Pseudo-first order	0.278	83.20	7.8
Pseudo-second order	0.004	85.85	15.5

From Figure IV-21, it can be seen that pseudo-first order model appears to fit the process better than pseudo-second order model throughout the entire range of time, in the same way than other studies reported in literature [60], with standard deviation less than 8%.

Moreover, the values of saturation limit ( $q_s$ ) calculated from pseudo-first order model are little bit more consistent with the experimental data than those estimated by means of pseudo-second order model, providing a good agreement between the measures and predicted values. This fact can be explained because pseudo-first order model is applicable under low surface coverage, and hence describes the early stages of adsorption [60]; whereas pseudo-second order model better suits the adsorption process involving chemical interactions [61].

Similarly, the same analysis about the adsorption of  $\text{RuCp}_2$  on MCM-48 has been performed. Experimental data of adsorption kinetics and the fittings provided by both models are shown in Figure IV-22, and Table IV-6 presents the kinetics parameters and calculated errors.

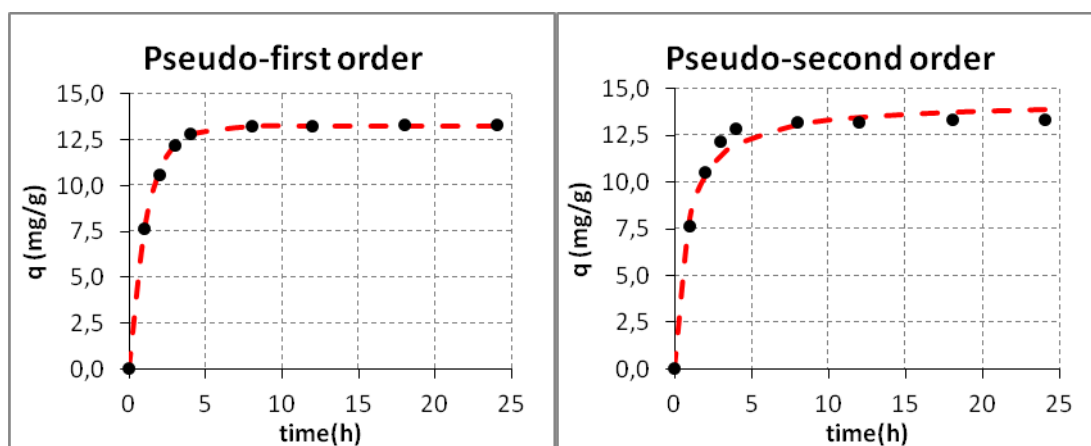


**Figure IV-22.** Adsorption of  $\text{RuCp}_2$  on MCM-48 at 60 °C and 11 MPa: Experimental data (●) and pseudo-first and second order fits (dotted line).

**Table IV-6.** Kinetics parameters for adsorption of  $\text{RuCp}_2$  on MCM-48: pseudo-first and second order.

Model	Rate constant ( $k$ )	Saturation limit ( $q_s$ )	Std. deviation ( $\Delta q$ )
Pseudo-first order	0.844	13.25	1.03
Pseudo-second order	0.090	14.34	4.28

Results suggested from Fig. IV-22 that, pseudo-first order model is again the best fitting for the experimental data, as in the previous case, with an average standard deviation even lower, around 1%. The repetition of this result could corroborate the theory discussed above about the application of pseudo-first order model in the early stages of adsorption or low surface coverage, since the metallic loading obtained on MCM-48 is much lower.

Comparing both supports, several conclusions can be drawn. First, the saturation capacity ( $q_s$ ) or affinity for the metal on AC is much greater than on MCM-48, as already noted in the previous section. However, correlations indicate that although adsorption on MCM-48 only reaches a maximum of 1.5%, its kinetics is much faster than on AC, as indicated by the values of constants  $k_f$  and  $k_s$ , being less time required to reach the equilibrium. Therefore, according to the conclusions obtained in this section, it can be establish between 4 and 5 hours as the maximum working time, thus optimizing the operation with equilibrium between maximizing the metallic loading and reducing the operating costs.

IV.4.4. Mechanism of adsorption of RuCp<sub>2</sub>

Finally, experimental data was analyzed in order to identify the controlling step of the adsorption process by means of intraparticle diffusion and film-diffusion models previously detailed in Chapter III.

Adsorption mechanism for RuCp<sub>2</sub> on AC

As can be seen in Fig. IV-23, the Weber-Morris plot for the adsorption of RuCp<sub>2</sub> on AC suggests that there could be different stages involved in the process, founding three clearly distinct regions.

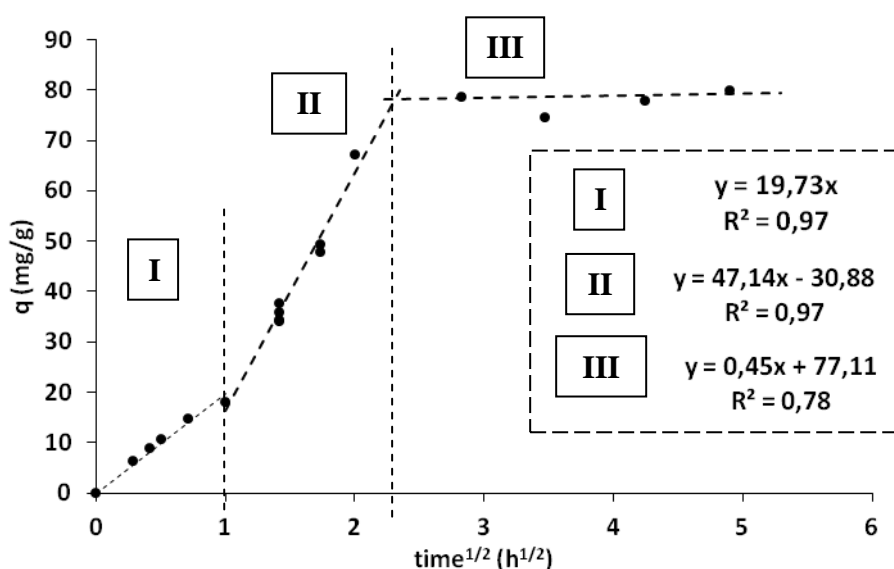


**Figure IV-23.** Prediction of intraparticle diffusion model, Weber-Morris plot for adsorption of RuCp<sub>2</sub> on AC at 11 MPa and 60 °C

The initial part, region I, is attributed to the instantaneous adsorption and the transport of the adsorbate through the bulk of the fluid to the external surface of the adsorbent, correlated to the boundary layer diffusion. The second one, region II, describes the gradual adsorption stage, where intraparticle diffusion is the rate limiting. Finally, the third portion, region III, is assumed as the final equilibrium stage at which the intraparticle diffusion starts to slow down due to saturation of active sites.

This plot shows that intraparticle diffusion is not the only rate limiting mechanism, since according to the values of kinetic constant  $k_i$ , the slope corresponding to the bulk diffusion is the least. This implies that the diffusion from the bulk phase to the exterior

surface of the support, which starts at the onset of the process, is the slowest and therefore the rate-controlling step [62]. It can be noticed that this stage lasts the first hour of the process, increasing after the adsorption rate once overcome.

Notably, as in this case the setting for the region III obtained by this model gives a very low correlation coefficient  $R^2$ , to some extent due to the difference between the values of the experimental data.

To further verify the above observations, Boyd's plot of  $B_t$  versus  $t$  is shown in Fig. IV-24.

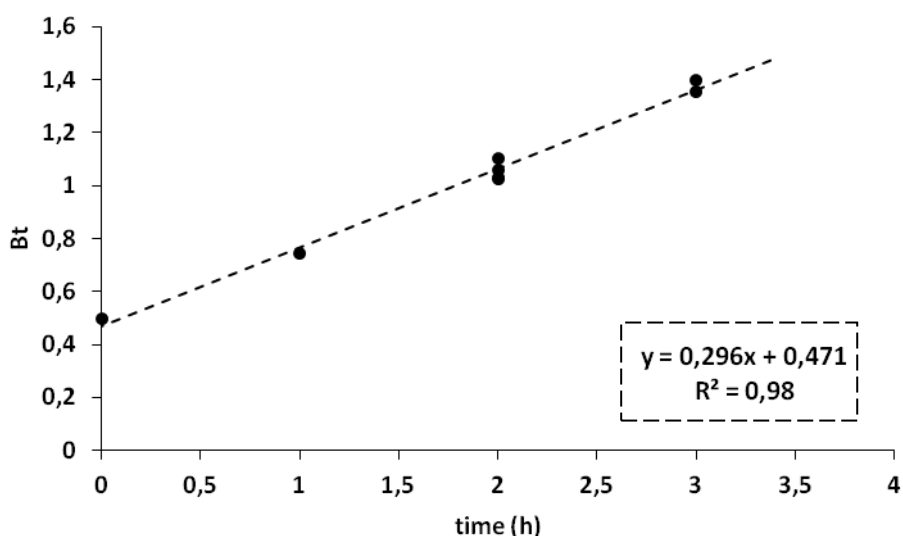


**Figure IV-24.** Boyd plot for adsorption of  $\text{RuCp}_2$  on AC at 11 MPa and 60 °C

This model shows a good fit for short times, as seen in the regression coefficient value  $R^2$ , very close to unity.

Boyd's plot shows a straight line, but it does not pass through the origin. The presence of intercept value together a relatively high value for the slope, indicates that the external mass transport governs the rate-controlling process. Nevertheless, as the intercept approaches zero, pore diffusion plays a relevant role in the overall adsorption mechanism [63].

It may be conclude that the adsorption of  $\text{RuCp}_2$  on AC is rather a complex mechanism where the intraparticle diffusion in not the only rate-controlling step.

Adsorption mechanism for RuCp<sub>2</sub> on MCM-48

In the adsorption of RuCp<sub>2</sub> on MCM-48, Weber-Morris plot shows three different regions, as can be seen from Fig. IV-25 together with the correlation and coefficient  $R^2$ .

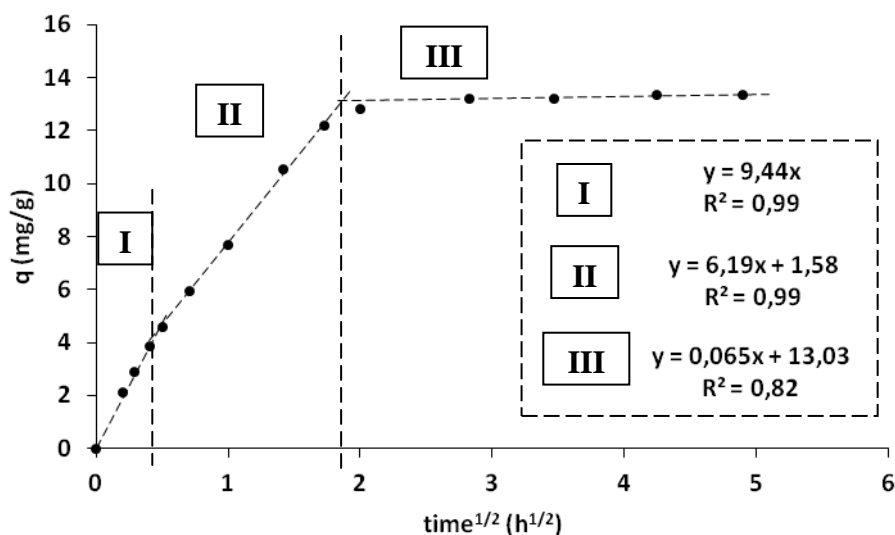


**Figure IV-25.** Prediction of intraparticle diffusion model, Weber-Morris plot for adsorption of RuCp<sub>2</sub> on AC at 11 MPa and 60 °C

Regression coefficient  $R^2$  values lie in the range of 0.82-0.99, indicating that the interparticle model fits the experimental data correctly. However, even though  $R^2$  values seem to reproduce quite well the results, rigorous evaluation is required in order to choose the more reliable diffusion mechanism.

Referring to Fig. IV-25, it can be observed different regions, which indicate that the adsorption rate is initially faster and then slows down when the time increases.

The first stage, region I, is completed within the first 15 minutes, unlike in the previous case on AC. This first shaper portion is related to the boundary layer diffusion (film diffusion). This phenomenon has been noted by other authors [62] with similar results at high pressures, where the film thickness decreases with the rise in pressure, and thereby the rate of film diffusion will increase.

Later, linear portion, region II, reaches up to 3 hours. During this time, the rate of mass transfer is sole controlled by the pore diffusion up to  $q$  values very close to equilibrium. After this stage, region III, the adsorption rate drops sharply due to the saturation of the active centers, as mentioned above, until equilibrium is reached.

It can be noticed that, region II does not pass through the origin which indicates a boundary layer effect; but this value is very low, which suggests that the role of the film diffusion is insignificant and pore diffusion is the main dominating factor in controlling the rate of the adsorption [64].

A conclusion regarding mass transfer mechanism can be reached from the analysis of data by Boyd's model, given in the Fig. IV-26.

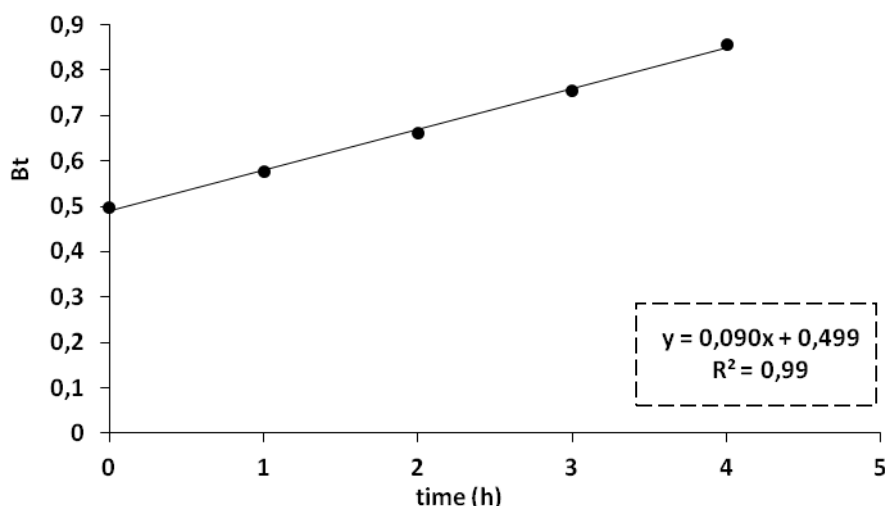


Figure IV-26. Boyd plot for adsorption of  $\text{RuCp}_2$  on MCM-48 at 11 MPa and 60 °C

Based on the high  $R^2$  value that is very close to unity, it can be concluded that Boyd's model fits well the experimental data.

In this case, a straight line with a very slope value is obtained. This fact indicates that the adsorption of  $\text{RuCp}_2$  on MCM-48 is mainly governed by the pore diffusion, being this the rate limiting step, as the intercept is close to zero. This conclusion is in accordance with the previous results obtained from the intraparticle diffusion model.

Finally, if the results obtained from the different models and proposed mechanisms for both supports are compared, several conclusions can be obtained: In the first place, both supports exhibit a complex adsorption mechanism, comprising several stages in series, according to Fick's second law. However, in the case of AC, it is seen as the controlling step of the process is mainly the external transport or film diffusion, being this the predominant effect during the first hour of operation. On the other hand, the adsorption on MCM-48 is largely governed by pore diffusion, since the external transport initial stage is very fast and of short length.

## IV.5. Continuous Supercritical Deposition of RuCp<sub>2</sub>

In this section, the supercritical fluid deposition method (SCFD) will be developed for synthesis of ruthenium-based catalysts. The novelty that arises is the achievement of this technique by continuous process. To reach this objective, the synthesis plant was modified as described subsequently; and then a series of experiments was performed at different times and flow rates, analyzing its effect on the deposition process.

### IV.5.1. Continuous Set-up for Catalyst Synthesis

One of the aims of this PhD thesis is to attempt to transfer the SFRD process from a batch operation to a continuous procedure. For this purpose, several modifications have been performed in the batch experimental set-up, described in a previous paragraph, in order to achieve a continuous operation.

To facilitate the control of the process, the CO<sub>2</sub> is continuously pumped by means of a HPLC pump Jasco model PU-2080 Plus, with a flow rate range of 1 μL to 10 ml per minute and maximum pressure of 22 MPa. The suction line of the pump is cooled down in order to guarantee the liquid state of the CO<sub>2</sub>.

Moreover, to maintain a constant flow throughout the experiments, a mass flow meter controller from Bronkhorst Coriolis sensor calibrated to CO<sub>2</sub> combined with a controller model mini Cori-Flow (nominal range of 10 to 1000 g/h) was set up.

Furthermore, a back pressure valve RHPS, with maximum allowable operating pressure <40 MPa, is employed downstream of the reactor to keep the desired pressure.

Finally, for security aims, a relief valve Swagelok SS-4R3A was installed to protect the system from potentially damaging overpressures, with a pressure rating up to 41 MPa at room temperature.

In this new configuration, the high pressure vessel used in the batch operation has been replaced by two tube sections placed in horizontal position inside the oven, as shown in figures. IV-27 and IV-28. The first of them contains the organometallic precursor mixed

with glass spheres to help its dissolution into the CO<sub>2</sub> flow. Afterwards, the solution goes through the second tube in which the support is located.

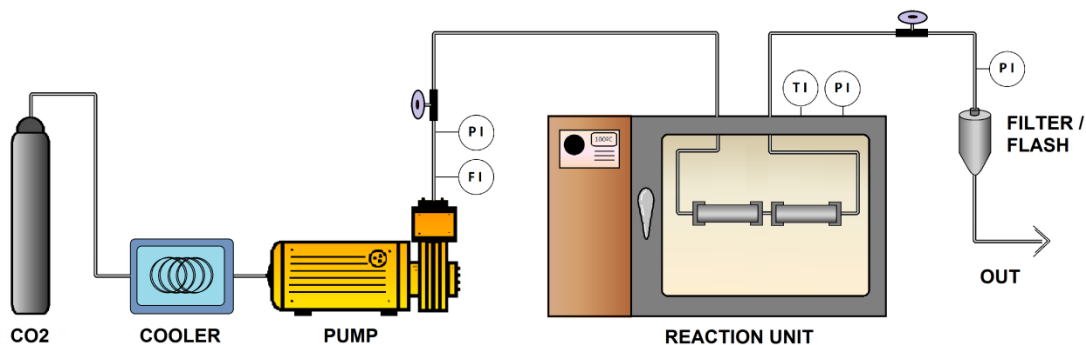


**Figure IV-27.** Experimental device for the synthesis of catalysts by SFRD (operation flow)

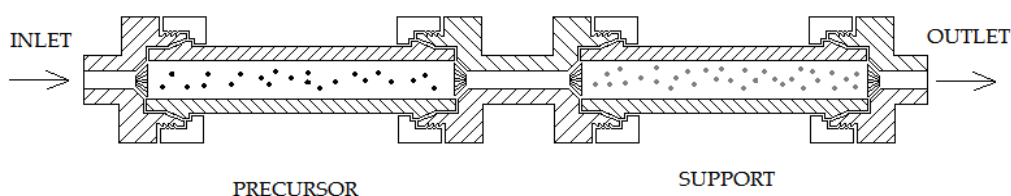


**Figure IV-28.** Detail of the new configuration for continuous process: two tube section

Depositions were conducted under conditions of pressure and temperature established following the previous isotherms analysis,  $P = 11 \text{ MPa}$  and  $60 \text{ }^\circ\text{C}$ .

The initial flow of CO<sub>2</sub> was 45 g/h, which was estimated to be enough to dissolve the precursor along the bed, and be saturated prior to contact with the support. This premise was based on observations made in the experiments carried out in the visual cell.

### IV.5.2. Results and discussion

Figure IV-29 shows the results obtained at different times for the adsorption of RuCp<sub>2</sub> on MCM-48.

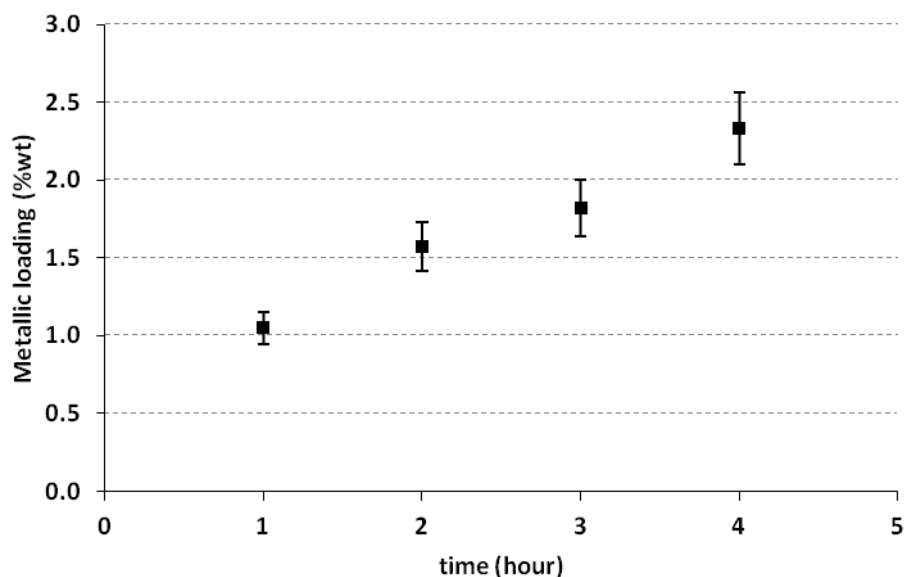


**Figure IV-29.** Evolution of metal loading (Ru %wt) versus time of exposure for the adsorption of  $\text{RuCp}_2$  on MCM-48 at 60 °C, 11 MPa and 45  $\text{gCO}_2/\text{h}$

Results show as Ru loading increases with time of operation. As can be seen, it is possible to reach loadings exceeding its maximum saturation capacity ( $\sim 15 \text{ mg/g}$ ) in less than 2 hours. This means that the effectiveness of the adsorption process is improved because of the following potential factors: first, the precursor concentration in the fluid medium is maintained constant at any moment, unlike in the batch process; and on the other hand, the support is much better distributed within the reactor thanks to the filling of glass spheres, improving the stage of mass transport and diffusion.

In this case, the  $\text{CO}_2$  is completely saturated in the first vessel, which is filled with excess of precursor, putting it in contact with the support in the second vessel with a concentration equal to the initial. The amount of undissolved precursor can be recovered after operation, thus saving on costs.

As to the deposition on activated carbon, as shown in Fig. IV-30, it is sensed that a maximum concentration lower than the one reached at equilibrium is obtained, irrespective of length of exposition over 2-3 hours.

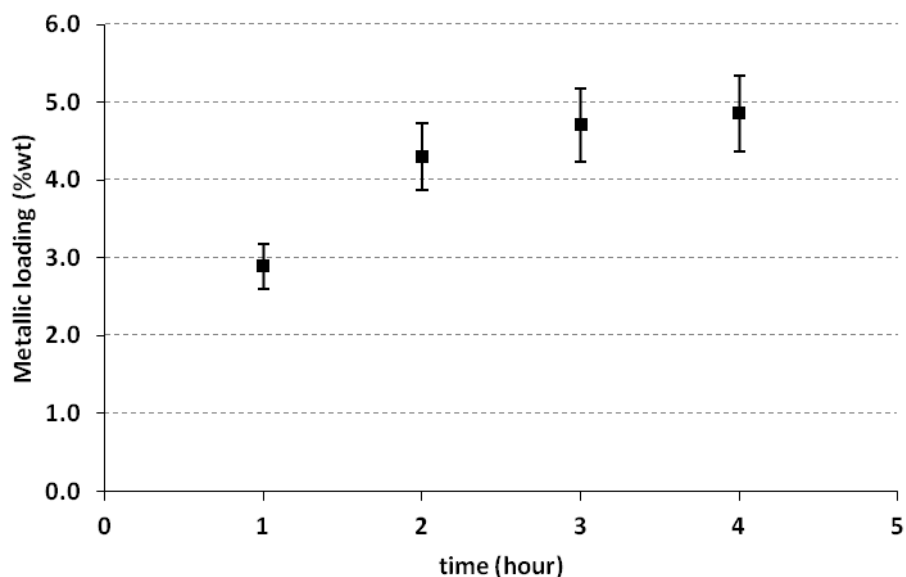


**Figure IV-30.** Evolution metal loading (Ru %wt) versus time of exposure for the adsorption of  $\text{RuCp}_2$  on AC at 60 °C, 11 MPa and 45  $\text{gCO}_2/\text{h}$

This fact could be related to the transport limitations found after studying its adsorption mechanism in the previous section, where it has been concluded that for this metal-support system,  $\text{RuCp}_2/\text{AC}$ , the diffusion from the bulk phase to the exterior surface of the support is the rate-controlling step.

To solve this matter, it has been proposed to work with lower  $\text{CO}_2$  flows (30 and 15  $\text{g/h}$ ), in this way it is expected to increase the contact time between the fluid phase and the support matrix to facilitate the adsorption process. The results are shown in the figure IV-31.

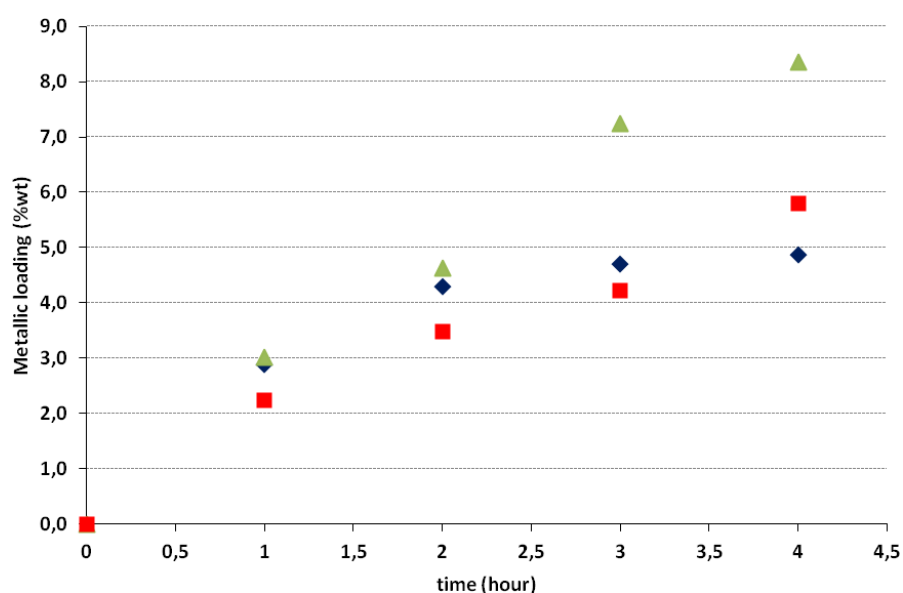


**Figure IV-31.** Evolution of metal loading versus time of exposure for the adsorption of  $\text{RuCp}_2$  on AC at different  $\text{CO}_2$  flows: (♦) 45  $\text{g/h}$ ; (▲) 30  $\text{g/h}$ ; (■) 15  $\text{g/h}$

As can be seen, by reducing the flow of CO<sub>2</sub>, the desired effects is achieved, leaving more time for fluid to penetrate into the pores, obtaining metallic loadings up to 8 % wt in 4 hours with a flow of 30 g/h. The smallest flow (15 g/h) also shows a lower loading, although actually, this fact is explained as the total dissolved amount of precursor is also lower. For this reason, to choose the optimal flow for this process, not only the metal loading will be taken into account, but also the CO<sub>2</sub> consumption, minimizing its costs and increasing the effectiveness.

### IV.5.3. Kinetics of the continuous process

Firstly, the data was fitted to first-order kinetics, by the following equation:

$$q_i = q_s \cdot (1 - e^{-k \cdot t}) \quad (19)$$

where  $q_i$  and  $q_s$  are the adsorptive capacity (mg/g) at a given point of time and at saturation limit respectively;  $k$  is the first order rate constant; and  $t$  is the time in hours.

The kinetics parameters were estimated by using the error function based on the normalized standard deviation:

$$\Delta q(\%) = \sqrt{\frac{\sum[(q_{exp} - q_{model})/q_{exp}]^2}{N-1}} \cdot 100 \quad (20)$$

Figure IV-32 show the fitting provided for the adsorption of RuCp<sub>2</sub> on MCM-48 and AC. Table IV-7 summarizes the kinetics parameters.

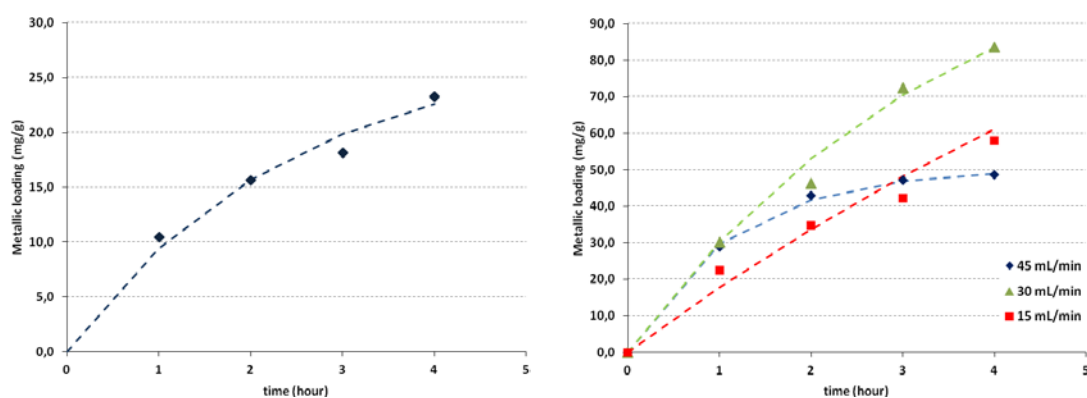


**Figure IV-32.** Fittings (dotted line) for the adsorption process in continuous of RuCp<sub>2</sub> on MCM-48 and AC: Experimental data: at different CO<sub>2</sub> flows: (♦) 45 g/h; (▲) 30 g/h; (■) 15 g/h

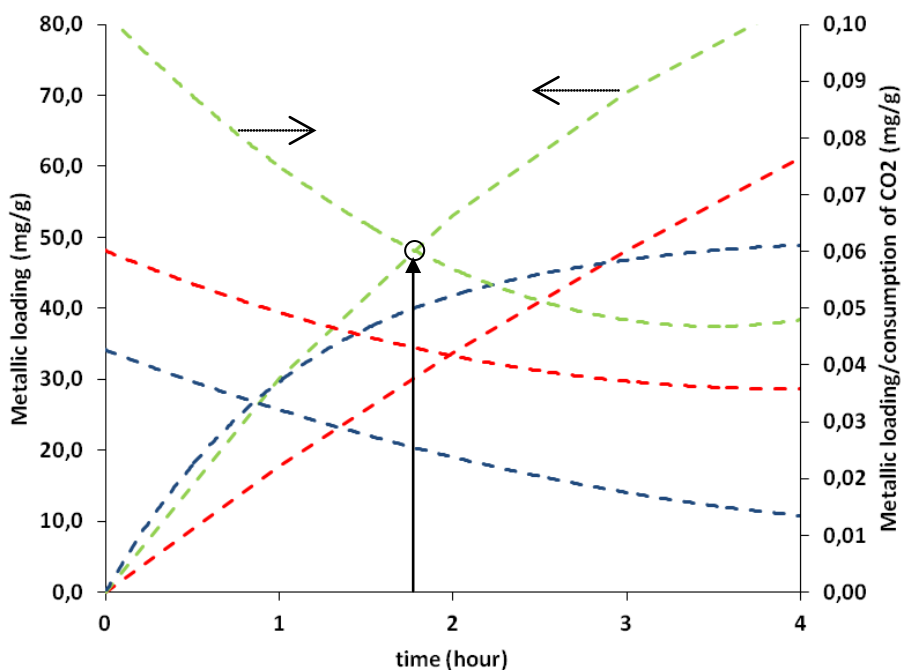
**Table IV-7.** Kinetics parameter and standard deviation provided by first-order kinetics fitting

	$q_s$ (mg/g)	$k$ (h <sup>-1</sup> )	Error %
<b>Adsorption on MCM-48</b>			
45 g/h	28.0	0.41	6.93
<b>Adsorption on AC</b>			
45 g/h	50.3	0.89	1.95
30 g/h	184.7	0.10	13.06
15 g/h	124.8	0.28	7.60

Model provides acceptable fitting, comparable to that of other authors. Experiments carried out with the greatest flows (45 g/h) have higher kinetic constants, seemingly reaching its maximum adsorption capacity shortly. However, this load seems to be limited. Deposition of metal nanoparticles with high flows covers the surface of the support quickly; but by contrast, this reduces its specific area by plugging the pores and thus avoiding successive loads.

On the other hand, experiments carried out with a flow of 30 g/h are those that have the higher metal loading at short times; as despite having a slightly lower value for its kinetic constants compared to the experiences with flow of 15 g/h, these two lines cross over after 8 hours of operation according to the prediction estimated by the fittings.

Finally, the process can be analyzed in terms of kinetics behavior and the consumption of CO<sub>2</sub> which entails achieving that metal load versus time:

**Figure IV-33.** Final metallic loading and evolution of this with the consumption of CO<sub>2</sub> versus time

Red line: 15 g/h; Green line: 30 g/h; and Blue line 45 g/h

#### CHAPTER IV. Ruthenium-based Catalysts

From Figure IV-33, it can be obtained the optimum operating conditions to achieve a metal loading around 5 %wt, working with a CO<sub>2</sub> flow of 30 g/h in less than 2 hours. The graph shows how from that point, spending CO<sub>2</sub> is very high compared to the deposited metal.

Therefore, as a conclusion of this section, it has been proved that SCFD technique is feasible to be implemented in continuous process.

## IV.6. Characterization of ruthenium-based catalysts

In this case, the study will be focused on the main differences associated to the use of two different supports; one of them, mesoporous (MCM-48), and the other one, microporous (AC).

The amount of Ru deposited over both supports (MCM-48 and AC) was determined by XRF. With the aim to precise comparison, it has attempted to synthesized catalysts with similar metal loadings, around 4 %wt. Additionally, another sample was prepared with double metal content to analyze its effect on the homogeneity of the synthesis method; and in turn, for its subsequent activity test. Table IV-8 gives the BET area and pore volume for each sample.

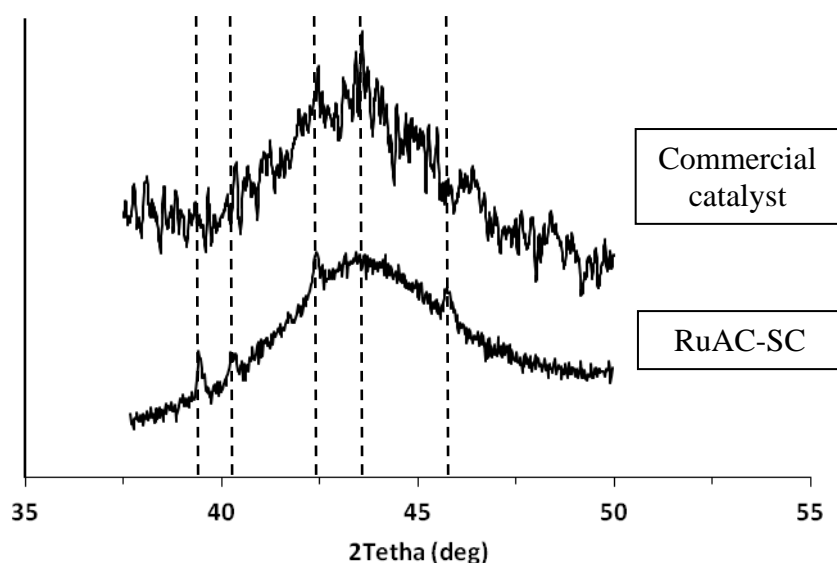
**Table IV-8.** Structural properties and metallic loading of ruthenium-based catalysts prepared

Sample	Ru (wt.%)	S <sub>BET</sub> (m <sup>2</sup> /g)	d <sub>p</sub> (nm)	V <sub>p</sub> (cm <sup>3</sup> /g)
<b>MCM48</b>	---	1641	3.6	0.90
<b>AC</b>	---	794	3.0	1.01
<b>Ru/MCM48-WI</b>	4.0	1450	3.2	0.50
<b>Ru/MCM48-SC</b>	4.7	748	1.6	0.58
<b>Ru(L)AC-SC<sup>(a)</sup></b>	4.3	739	2.2	0.77
<b>Ru(H)AC-SC<sup>(b)</sup></b>	7.9	524	2.3	0.61

(a) Low metallic content; (b) High metallic content

Just as in the previous cases, both pore volume and pore size decrease with the amount of metal impregnated. It is noteworthy as in the case of AC due to its irregularity of its structure, this difference becomes less plausible.

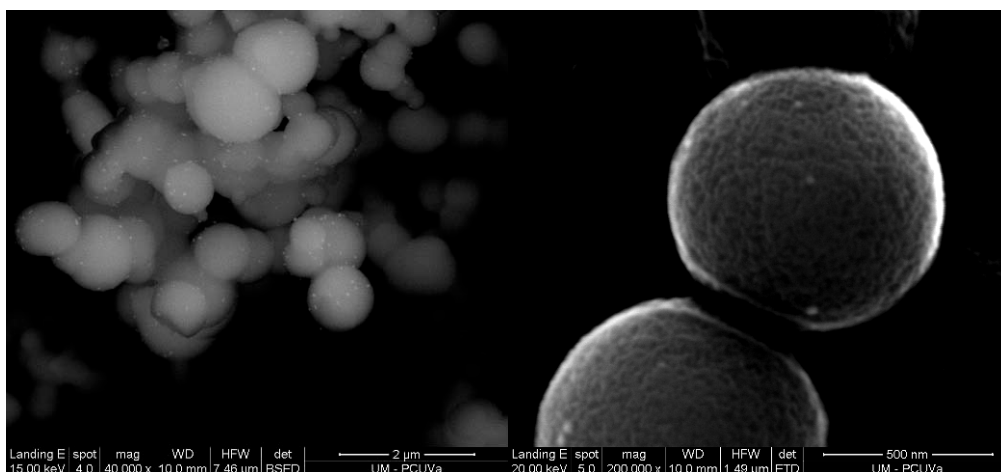
XRD analysis was employed to identify the species and crystal phase of ruthenium nanoparticles.



**Figure IV-34.** XRD pattern of Ruthenium catalysts: Commercial Ru/AC (Ru5 %wt on activated carbon, reduced, 50 % water wet paste (Escat<sup>TM</sup> 4401)) and Ru(H)/AC-SC

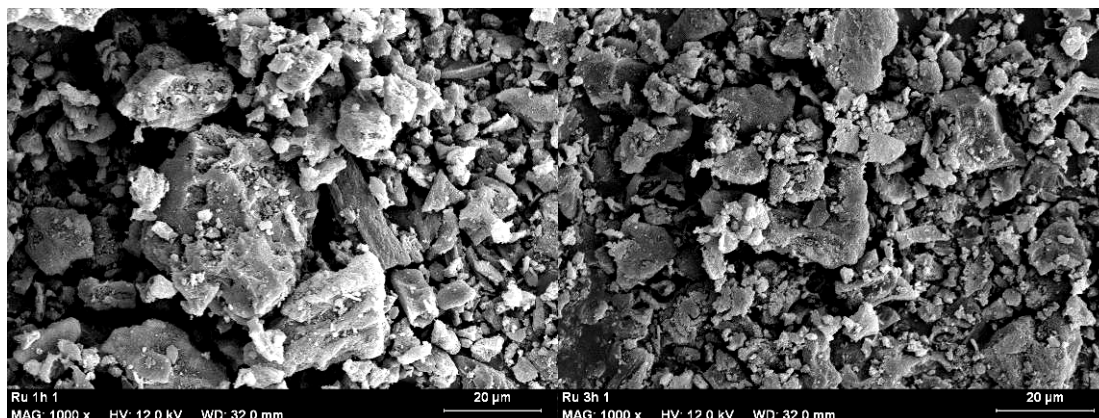
The analysis of the catalyst by XRD gave the results as shown in Fig. IV-34, in which multiple peaks were present at  $2\theta = 37$  to  $47^\circ$ , with a maximum around  $44^\circ$ . This peak was analyzed by peak separation method in order to identify different peaks. The main peak corresponding to  $44^\circ$  belongs to the plane (101). Like this, there are two other peaks at  $38^\circ$  and  $42^\circ$ , related to the planes (100) and (002) respectively. All this leads us to believe in the presence of ruthenium crystallized in hexagonal close packing structure (JCPDS 06-0663). On the other hand, peaks at  $41^\circ$  and  $47^\circ$  are associated with cubic ruthenium. Therefore, the XRD spectrum shows a similar appearance in both samples (commercial and SC) with two different ruthenium crystallizations.

Besides, the morphology of this nanocomposites and the distribution of metal were studied by means of scanning electron micrographs (Fig. IV-35 and IV-36).



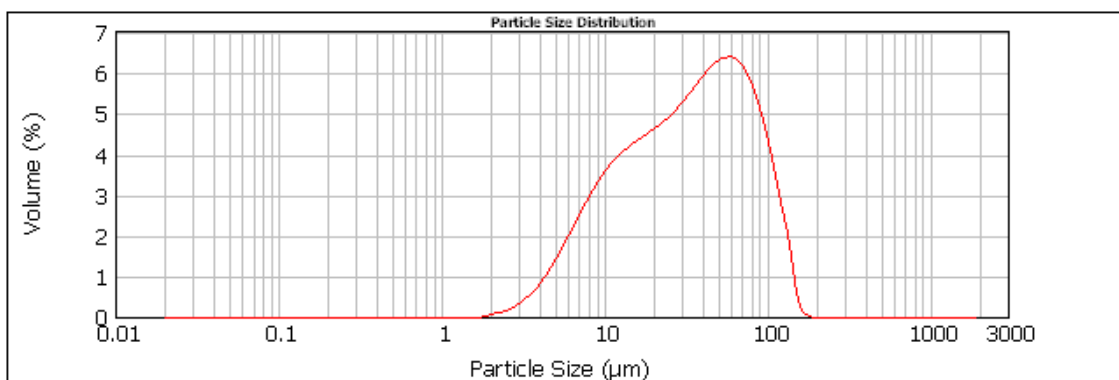
**Figure IV-35.** SEM images of Ru/MCM48-SC prepared in continuous

Analysis of the SEM pictures for samples on MCM-48 (Fig. IV-35) reveal, spherical particles with an average diameter between 300 and 500 nm, where it can be observed metallic nanoparticles dispersed over the surface. The appearance of these particles suggests a multilayer adsorption, leading the growth of metallic nanocrystals located on outer surface



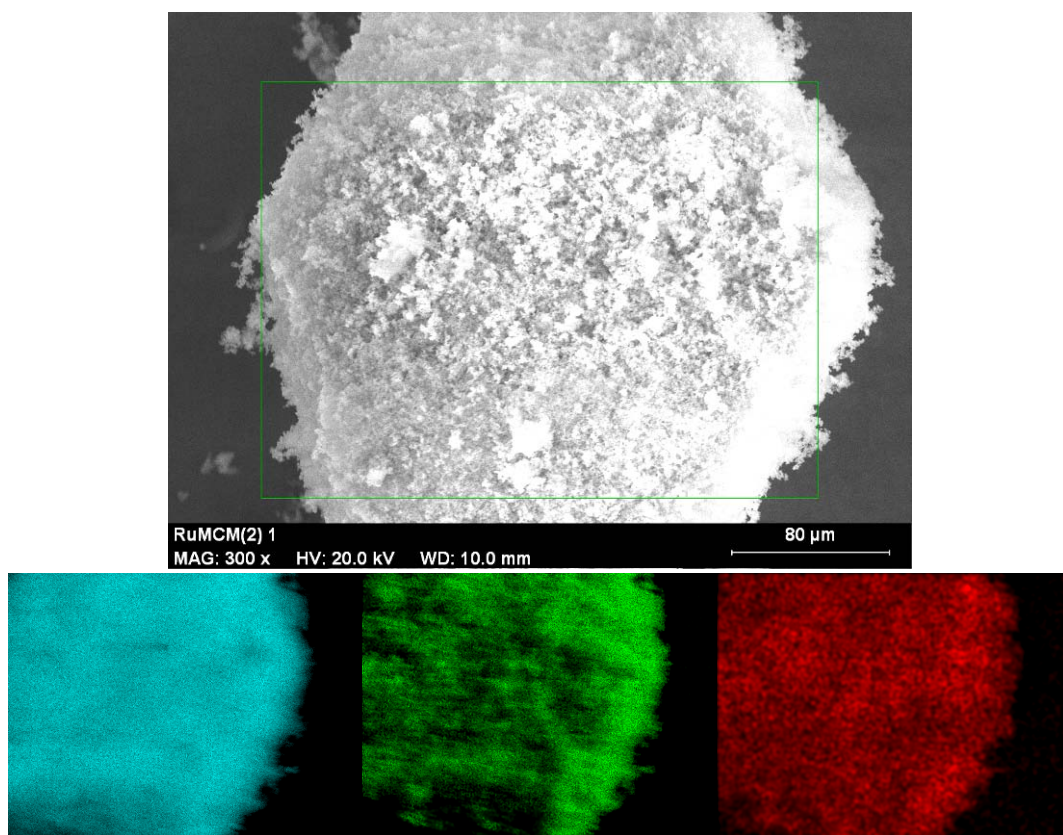
**Figure IV-36.** SEM images of Ru(H)/AC-SC prepared in continuous

Otherwise, images for catalysts prepared on AC (Fig. IV-36) show the rough and uneven surfaces of carbon particles, with a wide size distribution, as it is checked in the Dynamic Light Scattering (DLS) report (Fig. IV-37).



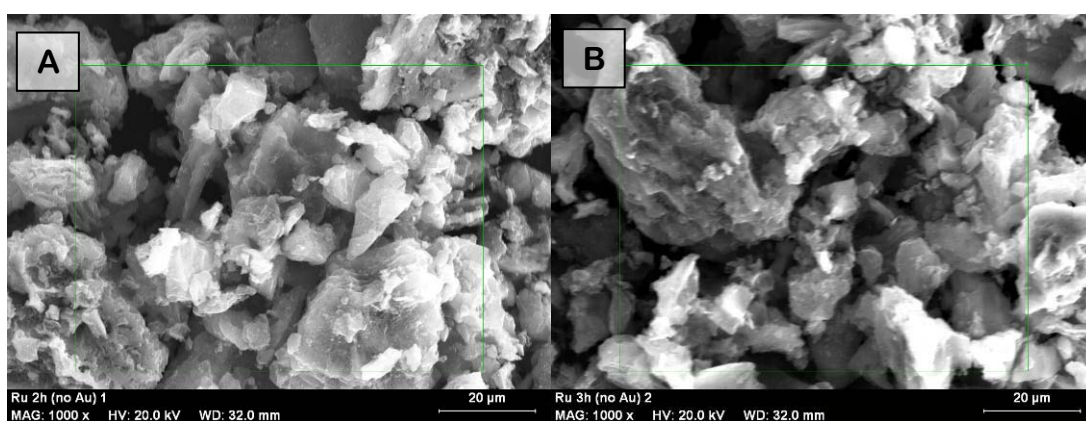
**Figure IV-37.** Particle size distribution curve of AC

X-Ray SEM/EDX Mapping was used in order to verify the distribution and homogeneity of ruthenium nanoparticles on both supports.



**Figure IV-38.** X-Ray SEM/EDX Mapping for Ru/MCM48-SC:  
Electron image, Blue color Si  $\kappa\alpha$ , Green color O  $\kappa\alpha$ , and Red color Ru  $\lambda\alpha$

Figure IV-38 reveals that ruthenium has been deposited on the substrate surface, filling its pores with a very good distribution; likewise it was achieved on this kind of mesoporous micelle-templated silicas (MS41 family) with the other two metals studied in this PhD thesis.



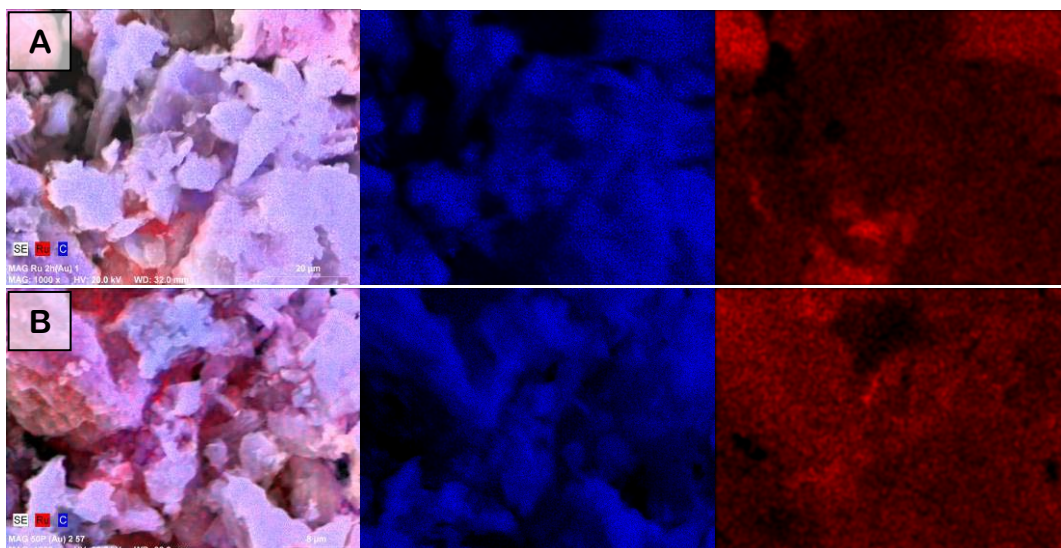


**Figure IV-39.** X-Ray SEM/EDX Mapping for Ru(H)/AC-SC prepared in continuous  
(A) Ru ~ 4%wt, (B) Ru ~ 7 %wt – Blue color C  $\kappa\alpha$  and Red color Ru  $\lambda\alpha$

On the other hand, as shown in figure IV-39, metal completely covers the entire carbon surface with homogeneous distribution. Increasing the concentration of metal in the catalyst, it still maintains a uniform distribution, without finding concentration gradients.

This proves that this technique of metal deposition is perfectly feasible for all types of support, both mesopore and microporous.

## IV.7. Activity Test: Hydrolysis of Cellobiose for Glucose production

As already mentioned throughout the course of this PhD thesis, there is a new trend that tries to replace petroleum-based products with other renewable raw materials. Among all the options that are being considered, many researches are focusing their attention on vegetal biomass as an abundant source of carbon material that can be used as feedstock for the production of chemicals and/or fuels.

One of the most promising ways is the use of cellulose [65-67], which is the most abundant fraction in biomass wastes. Cellobiose can represent a model compound in the cellulose hydrolysis since it is formed by two glucose units. In particular, glucose can be achieved from the hydrolysis of cellobiose, but other numerous intermediates and subproducts can also be obtained according to the pathway proposed in the literature [68], and presented in figure IV-40.

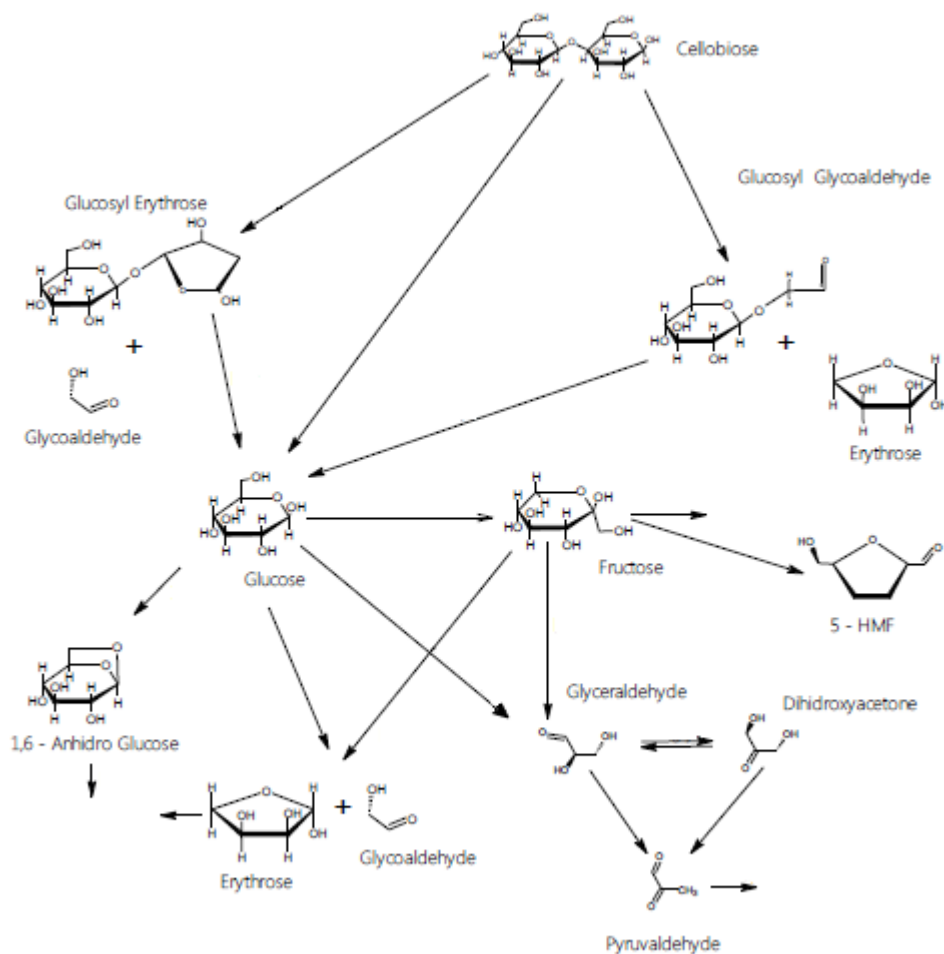


Figure IV-40. Reaction pathway for cellobiose [68]

So far, the most widespread treatments to hydrolyze the cellobiose consist on the enzymatic hydrolysis [69, 70], or on the homogeneous acid-catalyzed process [71-73].

The first one, the enzymatic hydrolysis, is a very selective process, which also is performed at mild conditions, usually temperatures between 40 and 50 °C, and under slightly acidic (pH ~ 5). Nevertheless, this method presents some drawbacks. As since it is a biological process, the reaction rate is very low (conversion 60% in 5 days [74]), requiring large volumes of reaction; and besides, the enzymes are active only over a very narrow range of operating conditions (very sensitive process) [75].

On the other hand, homogeneous acid hydrolysis is much faster, but as it is carried out at higher temperatures, degradation of some products occurs, thereby decreasing the selectivity of the process. Moreover, there exists a very high risk of corrosion problems in the equipment, which implies a greater initial cost (special resistant materials).

However, recently some researchers have suggested a new method to hydrolyze cellulose rapidly by means of the hydrothermal process, which employs near-critical or supercritical water as a reaction medium [76-79]. In this case, it is not necessary to pre-dry the raw material, independently of this moisture [80], making it in a very versatile process for food purposes, derivation of useful compounds for chemical synthesis, or energy resource [81].

In order to enhance the selectivity of the reaction, supported acid catalysts can be added, because they avoid corrosion problems caused by homogeneous catalysts, and in addition, they are easily separable [82].

Previous studies have already demonstrated that ruthenium-based catalysts improve the selective conversion of cellobiose to hexitols [83]; for this reason, in this chapter, the activity of Ru/MCM48 and Ru/AC composite materials is confirmed following the hydrolysis of cellobiose in hot compressed water and compared to commercial catalysts.

### IV.7.1. Experimental Device

Reactions were carried out in an AISI 304 stainless steel batch reactor, with a volume equal to 150 mL presented in figure IV-41 together with the rest of the elements.

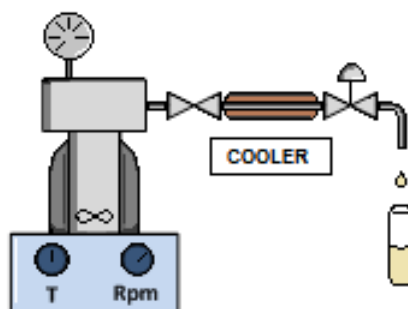


**Figure IV-41.** Experimental device: reactor, controller, cooler and sampler

At the beginning, 140 mL of a solution of cellobiose with an initial concentration of 10 g/L is introduced into the vessel, together the catalyst (ratio Ru/cellobiose = 0.15). After that, the reactor is closed, and heated up to 180 °C by means of an electrical band heater (275 W) connected to a PID controller (OSAKA, OK31) in 10 min. Because of this warming up, an increase in pressure is produced. This autogeneous pressure is measured, for security reasons, with a gauge (0 – 2.5 MPa). Then, when the operational temperature is reached, the reaction starts (this point is considered time = 0). During the operation (40 min in order to prevent the degradation of products), the solution is continuously stirred by using a magnetic stirrer at a constant speed of 200 rpm. At the end, the valve is opened, and the sample is cooled down through a coil placed around the side tube with fresh water to facilitate the sampling.

These operational conditions, specific for the cellobiose hydrolysis, were chosen as optimal according to previous studies inside our research group.

Samples are then filtered and analyzed in High Performance Liquid Chromatography (HPLC), by using a Sugar Shodex SH-1011 in aqueous solution of sulfuric acid (0.01 N) as mobile phase with a flow rate of 0.8 mL/min at 50 °C.

The conversion of cellobiose, and the yield of the products were calculated as follows:

$$\%C = \frac{(\text{moles Cellobiose}_i - \text{moles Cellobiose}_f)}{\text{moles Cellobiose}_i} \cdot 100 \quad (21)$$

$$\%S = \frac{\text{moles Glucose}_f}{(\text{moles Cellobiose}_i - \text{moles Cellobiose}_f)} \cdot 100 \quad (22)$$

$$\%Y = \frac{\text{moles Glucose}_f}{\text{moles Cellobiose}_i} \cdot 100 \quad (23)$$

### IV-7.2. Results and discussion

It is worth noting that, in contrast to previous studies, non-calcined catalysts were employed since in this reaction it is not necessary that the ruthenium is present in its metallic state

Figure IV-42 shows the effect of the addition of ruthenium-based catalysts in the hydrolysis reaction of cellobiose at 180 °C, 40 min, and ratio Ru/cellobiose = 0.15.

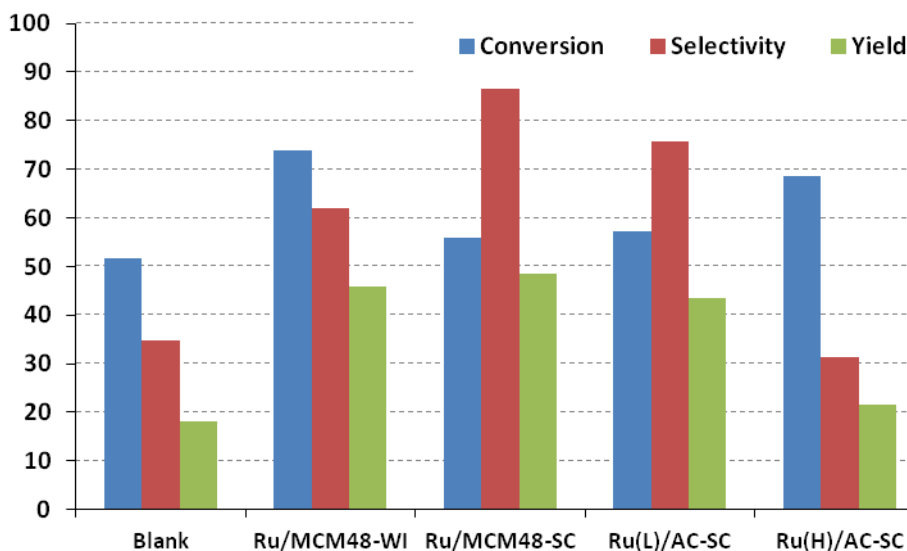


**Figure IV-42.** Conversion, selectivity to glucose and yield on different Ru-based catalysts influence of the support, synthesis technique and metallic loading

As shown in the figure IV-42, in all cases, the yield to glucose was improved. In order to check if the reaction is promoted either by the ruthenium or by the acidic character of the support, an experiment under the same conditions with an analogous amount of MCM-48 and AC, but without ruthenium was employed. The results in both experiences were similar to the blank (51 % conversion and 35 % selectivity); thus the active metal is the responsible of improving the performance of the reaction.

Comparing Ru-based catalysts supported on MCM-48 prepared by WI and SC, it can be observed as both provides similar yields, 46% and 48% respectively. However, it is noteworthy that although this yield is almost the same, the catalyst prepared by WI significantly improves both conversion (74 %) and selectivity (62 %); whereas the catalyst prepared by SC, slightly increases the conversion (56 %), but practically triples the value of selectivity (87 %).

## CHAPTER IV. Ruthenium-based Catalysts

This fact is remarkable, since the conversion could be increased with a longer operation, being the catalysts synthesized by SC the better option for this process.

On the other hand, if attention is paid to the results comparing the Ru catalysts with different supports, MCM-48 and AC, several conclusions can be drawn. Both catalysts prepared by SC provide a similar conversion; however, both selectivity and yield obtained by the Ru catalysts supported on AC are lower, and therefore, a higher amount of byproducts are generated when AC is used as support.

According to literature, it has been demonstrated that the strength of the acid sites is crucial for effective hydrolysis of cellulose [84, 85]. To verify this theory and give explanation to this behavior, an ammonia TPD and titration were performed to determine the acidity of the supports. Figure IV-43 shows the TPD curve of MCM-48.

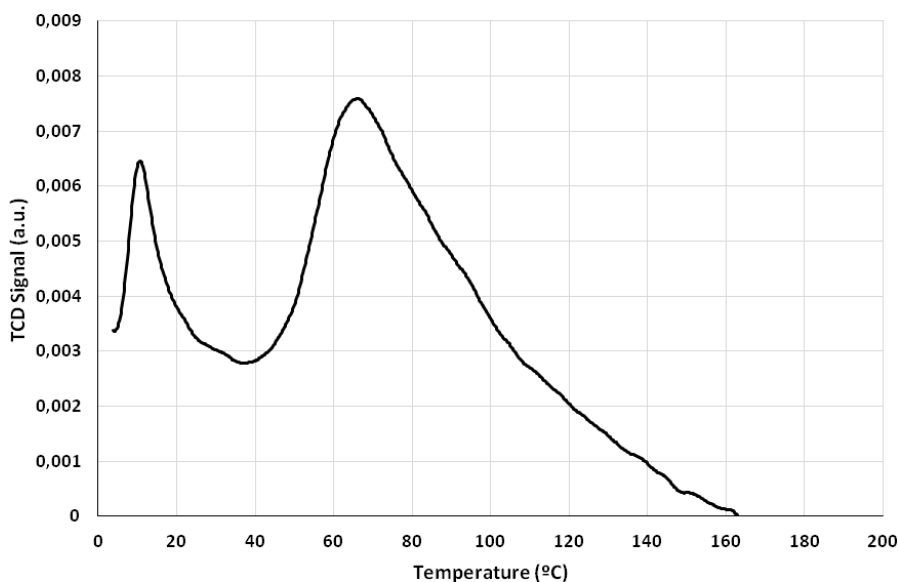


**Figure IV-43.** TPD measurement of MCM-48 support (heating rate 15 °C/min)

Analysis revealed that MCM-48 has both weak and strong acid sites (0.056 mmol<sub>NH3</sub>/g and 0.695 mmol<sub>NH3</sub>/g respectively), which in addition, due to its highly ordered structure are easily accessible. On the other hand, titration curve showed that AC had certain basic character.

Finally, the catalyst with higher metallic loading (~8%) provides the lowest yield (22%), very close to that obtained uncatalyzed. In this case, two phenomena act against.

First, the conversion increases while the selectivity decreases, demonstrating that glucose continues to react in other byproducts, as showed in Fig. IV-40; and secondly,

several authors have been proved that approximately monolayer coverage of metal on the inner surface of the support provides the best results, because the sample preserves its mesoporosity and ordered structure. The higher the metal load, the greater are the diffusion limitations, and therefore, the worse the contact with the active centers [86].

In conclusion, in this section, Ru-catalysts prepared by SC have been tested in the hydrolysis of cellobiose. The samples have shown a good catalytic activity, increasing the selectivity in producing glucose, with comparable yield to conventional catalysts. In this particular case, the Ru-catalyst prepared by SC in continuous on MCM-48 with a metallic loading of 4 %wt has proven to be the best option, achieving yields up to 48%.

## IV.8. Conclusions

In summary, in this chapter we have synthesized different ruthenium-based catalysts on MCM-48 and AC using ruthenocene ( $\text{RuCp}_2$ ) as organometallic precursor by means of supercritical fluid deposition process in continuous. For its development, the following issues have been studied:

- ✓ Firstly, the solubility of  $\text{RuCp}_2$  has been determined at 60 °C and different pressures by cloud point technique in a visual cell. Experimental data have been fitted by Chrastil and Peng-Robinson with good agreement.
- ✓ The adsorption isotherms of  $\text{RuCp}_2$  on MCM-48 and AC have been obtained. In both cases the metallic loading in the support increased with the supercritical phase concentration, type I, characteristic of monolayer deposition. It has been observed as the process is favored at low pressures. Experimental data have been fitted by different models, being the three-parameter equations such as Redlich-Peterson or BET correlations which provide the best fittings.
- ✓ Adsorption kinetics of  $\text{RuCp}_2$  on AC is better fitted by a pseudo-first order model, achieving a value of saturation limit of 80 mg/g after 10 hours. In contrast, the adsorption on MCM-48 only reaches a maximum of 15 mg/g, but in less than 4 hours, having a faster kinetics. The analysis of their adsorption mechanism revealed that both systems have complex mechanisms with different stages involved in the process. However, in the case of adsorption on AC, it is seen that the controlling step is mainly the external transport, whereas on MCM-48 is largely governed by pore diffusion.
- ✓ Ruthenium catalysts have been satisfactorily synthesized by means of SCFD in a continuous process, at 60 °C and 11 MPa. Experimental data have been fitted by a first order model with acceptable average errors. The deposition on MCM-48 was carried out with a  $\text{CO}_2$  flow of 45 g/h; while in the study on AC, 3 different flows were tested to obtain the optimum value to improve the process and avoid the problems owing to transfer limitations. Taking into account both kinetics and efficiency of the process, it has been determined that the best  $\text{CO}_2$  flow to operate is 30 g/h.

- ✓ Ruthenium-based catalysts have been characterized using different techniques. The samples prepared in both supports showed a decrease in their BET areas after the incorporation of metal, being this effect much smaller in the case of adsorption on AC due to its irregular structure. SEM and TEM pictures revealed homogeneous metallic distributions, filling the pores and maintaining the original structure of the support even with increasing concentrations.
- ✓ The activity of the prepared catalysts has been tested in the selective hydrolysis of cellobiose for glucose production. Ru/MCM-48 catalysts with 4 %wt prepared by SC have shown the highest yield, improving the process without catalysts from 18% to 48%, with selectivity around 90%. Experiments with different loadings have revealed that, the higher the amount of metal, the worse contact with the active centers.

IV.9. References

1. Babuněk, M., O. Šimůnek, J. Hošek, M. Rybáčková, J. Cvačka, A. Březinová, and J. Kvičala, *Heavy fluorous phosphine-free ruthenium catalysts for alkene metathesis*. Journal of Fluorine Chemistry, 2014. **161**: p. 66-75.
2. Liu, G., H. Zhang, X. Zhao, and J. Wang, *Efficient ruthenium metathesis catalysts containing carborane ligands*. Journal of Organometallic Chemistry, 2014. **749**: p. 13-17.
3. Hamad, F.B., T. Sun, S. Xiao, and F. Verpoort, *Olefin metathesis ruthenium catalysts bearing unsymmetrical heterocyclic carbenes*. Coordination Chemistry Reviews, 2013. **257**(15-16): p. 2274-2292.
4. Zhang, Y., M. Shao, H. Zhang, Y. Li, D. Liu, Y. Cheng, G. Liu, and J. Wang, *Synthesis and reactivity of oxygen chelated ruthenium carbene metathesis catalysts*. Journal of Organometallic Chemistry, 2014. **756**: p. 1-9.
5. Bek, D., R. Gawin, K. Grella, and H. Balcar, *Ruthenium metathesis catalyst bearing chelating carboxylate ligand immobilized on mesoporous molecular sieve SBA-15*. Catalysis Communications, 2012. **21**: p. 42-45.
6. Gao, Y., S. Jaenicke, and G.-K. Chuah, *Highly efficient transfer hydrogenation of aldehydes and ketones using potassium formate over AlO(OH)-entrapped ruthenium catalysts*. Applied Catalysis A: General, 2014. **484**: p. 51-58.
7. Durap, F., M. Aydemir, A. Baysal, D. Elma, B. Ak, and Y. Turgut, *A new efficient bis(phosphinite)-ruthenium(II) catalyst system for the asymmetric transfer hydrogenation of aromatic ketones*. Inorganica Chimica Acta, 2014. **411**: p. 77-82.
8. Humphries, M.E., W.H. Pecak, S.A. Hohenboken, S.R. Alvarado, D.C. Swenson, and G.J. Domski, *Ruthenium(II) supported by phosphine-functionalized N-heterocyclic carbene ligands as catalysts for the transfer hydrogenation of ketones*. Inorganic Chemistry Communications, 2013. **37**: p. 138-143.
9. Wang, Z., J. Lin, R. Wang, and K. Wei, *Ammonia synthesis over ruthenium catalyst supported on perovskite type BaTiO<sub>3</sub>*. Catalysis Communications, 2013. **32**: p. 11-14.
10. Li, Y., C. Pan, W. Han, H. Chai, and H. Liu, *An efficient route for the preparation of activated carbon supported ruthenium catalysts with high performance for ammonia synthesis*. Catalysis Today, 2011. **174**(1): p. 97-105.
11. Akbayrak, S., M. Kaya, M. Volkan, and S. Özkar, *Ruthenium(0) nanoparticles supported on magnetic silica coated cobalt ferrite: Reusable catalyst in hydrogen generation from the hydrolysis of ammonia-borane*. Journal of Molecular Catalysis A: Chemical, 2014. **394**: p. 253-261.
12. Akbayrak, S., S. Tanyıldızı, İ. Morkan, and S. Özkar, *Ruthenium(0) nanoparticles supported on nanotitania as highly active and reusable catalyst in hydrogen generation from the hydrolysis of ammonia borane*. International Journal of Hydrogen Energy, 2014. **39**(18): p. 9628-9637.
13. Ma, Y., Y. Huang, Y. Cheng, L. Wang, and X. Li, *Biosynthesized ruthenium nanoparticles supported on carbon nanotubes as efficient catalysts for hydrogenation of benzene to cyclohexane: An eco-friendly and economical bioreduction method*. Applied Catalysis A: General, 2014. **484**: p. 154-160.

14. Liao, H., D. Ouyang, J. Zhang, Y. Xiao, P. Liu, F. Hao, K. You, and H.a. Luo, *Benzene hydrogenation over oxide-modified MCM-41 supported ruthenium–lanthanum catalyst: The influence of zirconia crystal form and surface hydrophilicity*. Chemical Engineering Journal, 2014. **243**: p. 207-216.
15. Arena, B.J., *Deactivation of ruthenium catalysts in continuous glucose hydrogenation*. Applied Catalysis A: General, 1992. **87**: p. 219-229.
16. Mishra, D.K., A.A. Dabbawala, J.J. Park, S.H. Jung, and J.-S. Hwang, *Selective hydrogenation of d-glucose to d-sorbitol over HY zeolite supported ruthenium nanoparticles catalysts*. Catalysis Today, 2014. **232**: p. 99-107.
17. Hao, C., S. Wang, M. Li, L. Kang, and X. Ma, *Hydrogenation of CO<sub>2</sub> to formic acid on supported ruthenium catalysts*. Catalysis Today, 2011. **160**(1): p. 184-190.
18. Li, G., P. Dong, D. Ji, Y. Xu, Y. Li, and R. Mu, *Effect of support materials on liquid-phase hydrogenation of hydroquinone over ruthenium catalysts*. Solid State Sciences, 2013. **23**: p. 13-16.
19. Jang, H., S.-H. Kim, D. Lee, S.E. Shim, S.-H. Baeck, B.S. Kim, and T.S. Chang, *Hydrogenation of lactic acid to propylene glycol over a carbon-supported ruthenium catalyst*. Journal of Molecular Catalysis A: Chemical, 2013. **380**: p. 57-60.
20. Nadgeri, J.M., N. Hiyoshi, A. Yamaguchi, O. Sato, and M. Shirai, *Liquid phase hydrogenation of methyl levulinate over the mixture of supported ruthenium catalyst and zeolite in water*. Applied Catalysis A: General, 2014. **470**: p. 215-220.
21. Yen, C.H., H.W. Lin, and C.-S. Tan, *Hydrogenation of bisphenol A – Using a mesoporous silica based nano ruthenium catalyst Ru/MCM-41 and water as the solvent*. Catalysis Today, 2011. **174**(1): p. 121-126.
22. Kim, D., H.-B.-R. Lee, J. Yoon, and H. Kim, *Ru nanodot synthesis using CO<sub>2</sub> supercritical fluid deposition*. Journal of Physics and Chemistry of Solids, 2013. **74**(5): p. 664-667.
23. Zhang, Y., H. Jiang, Y. Wang, and M. Zhang, *Synthesis of Highly Dispersed Ruthenium Nanoparticles Supported on Activated Carbon via Supercritical Fluid Deposition*. Industrial & Engineering Chemistry Research, 2014. **53**(15): p. 6380-6387.
24. Xu, S., L. Li, R. Li, and Y. Su, *Preparation of Ru/C catalysts by supercritical CO<sub>2</sub> deposition*. Xiyou Jinshu Cailiao Yu Gongcheng/Rare Metal Materials and Engineering, 2011. **40**(12): p. 2142-2146.
25. Zhao, Y., J. Zhang, J. Song, J. Li, J. Liu, T. Wu, P. Zhang, and B. Han, *Ru nanoparticles immobilized on metal-organic framework nanorods by supercritical CO<sub>2</sub>-methanol solution: highly efficient catalyst*. Green Chemistry, 2011. **13**(8): p. 2078-2082.
26. Aschenbrenner, O., S. Kemper, N. Dahmen, K. Schaber, and E. Dinjus, *Solubility of  $\beta$ -diketonates, cyclopentadienyls, and cyclooctadiene complexes with various metals in supercritical carbon dioxide*. The Journal of Supercritical Fluids, 2007. **41**(2): p. 179-186.
27. Teoh, W.H., R. Mammucari, and N.R. Foster, *Solubility of organometallic complexes in supercritical carbon dioxide: A review*. Journal of Organometallic Chemistry, 2013. **724**: p. 102-116.
28. Span, R. and W. Wagner, *A new equation of state for carbon dioxide covering the fluid region from triple-point temperature to 1100 K at pressures up to 800 MPa*. Journal of Physical Chemistry, 1996. **25**(6).

29. Morère, J., M.J. Tenorio, C. Pando, J.A.R. Renuncio, and A. Cabañas, *Solubility of two metal-organic ruthenium precursors in supercritical CO<sub>2</sub> and their application in supercritical fluid technology*. The Journal of Chemical Thermodynamics, 2013. **58**: p. 55-61.
30. Darr, J.A. and M. Poliakoff, *New Directions in Inorganic and Metal-Organic Coordination Chemistry in Supercritical Fluids*. Chemical Reviews, 1999. **99**(2): p. 495-542.
31. Kontogeorgis, G.M. and G.K. Folas, *Thermodynamics for Industrial Applications. From Classical and Advanced Mixing Rules to Association Theories*. 2010: Wiley.
32. Abdallah, E., C. Si-Moussa, S. Hanini, and M. Laidi, *Application of PC-SAFT and cubic equations of state for the correlation of solubility of some pharmaceutical and statin drugs in SC-CO<sub>2</sub>*. Chemical Industry and Chemical Engineering Quarterly, 2013. **19**(3): p. 449-460.
33. Maity, S.K., *Correlation of solubility of single gases/hydrocarbons in polyethylene using PC-SAFT*. Asia-Pacific Journal of Chemical Engineering, 2012. **7**(3): p. 406-417.
34. Gross, J. and G. Sadowski, *Perturbed-chain SAFT: an equation of state based on a perturbation theory for chain molecules*. Industrial & Engineering Chemistry Research, 2001. **40**: p. 1244-1260.
35. Varona, S., A. Braeuer, A. Leipertz, Á. Martín, and M.J. Cocero, *Lycopene solubility in mixtures of carbon dioxide and ethyl acetate*. The Journal of Supercritical Fluids, 2013. **75**: p. 6-10.
36. Montequi, I., E. Alonso, A. Martín, and M.J. Cocero, *Solubility of diisopropoxititanium bis(acetylacetonate) in supercritical carbon dioxide*. Journal of Chemical & Engineering Data, 2008. **53**: p. 204-206.
37. Buckingham, A.D. and R.L. Disch, *The quadrupole moment of the carbon dioxide molecule*, in *Optical, Electric and Magnetic Properties of Molecules*, D.C.C.J. Orr, Editor. 1997, Elsevier Science B.V.: Amsterdam. p. 81-95.
38. Nunes da Ponte, M., *The Thermodynamics of Supercritical Fluids*. BSPQ, 2003. **89**: p. 40-42.
39. Méndez-Santiago, J. and A.S. Teja, *The solubility of solids in supercritical fluids*. Fluid Phase Equilibria, 1999. **158–160**(0): p. 501-510.
40. Mendez-Santiago, J. and A.S. Teja, *Solubility of solids in supercritical fluids: Consistency of data and a new model for cosolvent systems*. Industrial & Engineering Chemistry Research, 2000. **39**: p. 4767-4771.
41. Chrastil, J., *Solubility of solids and liquids in supercritical gases*. The Journal of Physical Chemistry, 1982. **86**(15): p. 3016-3021.
42. Hong, S.-A., J.-D. Kim, J. Kim, J.W. Kang, and I.-J. Kang, *Phase equilibria of palm oil, palm kernel oil, and oleic acid + supercritical carbon dioxide and modeling using Peng–Robinson EOS*. Journal of Industrial and Engineering Chemistry, 2010. **16**(5): p. 859-865.
43. Huang, Z., Y.C. Chiew, M. Feng, H. Miao, J.-H. Li, and L. Xu, *Modeling aspirin and naproxen ternary solubility in supercritical CO<sub>2</sub>/alcohol with a new Peng–Robinson EOS plus association model*. The Journal of Supercritical Fluids, 2007. **43**(2): p. 259-266.
44. Lashkarbolooki, M., B. Vaferi, and M.R. Rahimpour, *Comparison the capability of artificial neural network (ANN) and EOS for prediction of solid solubilities in supercritical carbon dioxide*. Fluid Phase Equilibria, 2011. **308**(1–2): p. 35-43.

45. Kim, S.-K. and Y. Kim, *Thermophysical properties of dimethyl ether at near- and supercritical pressures using generalized cubic EoS*. The Journal of Supercritical Fluids, 2014. **92**(0): p. 16-23.
46. Angus, S., B. Armstrong, and K.M. de Reuck, *International Thermodynamic Tables of the Fluid State - 3: Carbon Dioxide*. 1976.
47. Nikitin, E.D. and A.P. Popov, *Critical point measurement of ferrocene and some of its derivatives*. Fluid Phase Equilibria, 2012. **324**: p. 13-16.
48. Zhang, Y., B. Cangul, Y. Garrabos, and C. Erkey, *Thermodynamics and kinetics of adsorption of bis(2,2,6,6-tetramethyl-3,5-heptanedionato) (1,5-cyclooctadiene) ruthenium (II) on carbon aerogel from supercritical CO<sub>2</sub> solution*. The Journal of Supercritical Fluids, 2008. **44**(1): p. 71-77.
49. Caputo, G., I. De Marco, and E. Reverchon, *Silica aerogel-metal composites produced by supercritical adsorption*. The Journal of Supercritical Fluids, 2010. **54**(2): p. 243-249.
50. Lucas, S., M.J. Cocero, C. Zetzl, and G. Brunner, *Adsorption isotherms for ethylacetate and furfural on activated carbon from supercritical carbon dioxide*. Fluid Phase Equilibria, 2004. **219**(2): p. 171-179.
51. Monsalvo, M.A. and A.A. Shapiro, *Study of high-pressure adsorption from supercritical fluids by the potential theory*. Fluid Phase Equilibria, 2009. **283**(1-2): p. 56-64.
52. Lai, C.-C. and C.-S. Tan, *Heat effects for toluene adsorption on activated carbon from supercritical carbon dioxide*. Fluid Phase Equilibria, 1995. **111**: p. 127-141.
53. Li, M., A.-z. Gu, X.-s. Lu, and R.-s. Wang, *Supercritical Methane Adsorption Equilibrium Data on Activated Carbon with Prediction by the Adsorption Potential Theory*. Journal of Chemical & Engineering Data, 2004. **49**(1): p. 73-76.
54. Herbst, A. and P. Harting, *Thermodynamic Description of Excess Isotherms in High-Pressure Adsorption of Methane, Argon and Nitrogen*. Adsorption, 2002. **8**: p. 111-123.
55. Bandosz, T.J. and C.O. Ania, *Chapter 4 Surface chemistry of activated carbons and its characterization*, in *Interface Science and Technology*, J.B. Teresa, Editor. 2006, Elsevier. p. 159-229.
56. Diankov, S., D. Barth, A. Vega-Gonzalez, I. Pentchev, and P. Subra-Paternault, *Impregnation isotherms of hydroxybenzoic acid on PMMA in supercritical carbon dioxide*. The Journal of Supercritical Fluids, 2007. **41**(1): p. 164-172.
57. Bozbag, S.E., N.S. Yasar, L.C. Zhang, M. Aindow, and C. Erkey, *Adsorption of Pt(cod)me<sub>2</sub> onto organic aerogels from supercritical solutions for the synthesis of supported platinum nanoparticles*. The Journal of Supercritical Fluids, 2011. **56**(1): p. 105-113.
58. Tenorio, M.J., C. Pando, J.A.R. Renuncio, J.G. Stevens, R.A. Bourne, M. Poliakoff, and A. Cabañas, *Adsorption of Pd(hfac)<sub>2</sub> on mesoporous silica SBA-15 using supercritical CO<sub>2</sub> and its role in the performance of Pd-SiO<sub>2</sub> catalyst*. The Journal of Supercritical Fluids, 2012. **69**: p. 21-28.
59. Wu, Y.Y., D.S.H. Wong, and C.-S. Tan, *Thermodynamic Model for the Adsorption of Toluene from Supercritical Carbon Dioxide on Activated Carbon*. Industrial and Engineering Chemistry Research, 1991. **30**: p. 2492-2496.
60. Serna-Guerrero, R. and A. Sayari, *Modeling adsorption of CO<sub>2</sub> on amine-functionalized mesoporous silica. 2: Kinetics and breakthrough curves*. Chemical Engineering Journal, 2010. **161**(1-2): p. 182-190.

61. Borah, J.M., J. Sarma, and S. Mahiuddin, *Adsorption comparison at the  $\alpha$ -alumina/water interface: 3,4-Dihydroxybenzoic acid vs. catechol*. Colloids and Surfaces A: Physicochemical and Engineering Aspects, 2011. **387**(1-3): p. 50-56.
62. Loganathan, S., M. Tikmani, S. Edubilli, A. Mishra, and A.K. Ghoshal, *CO<sub>2</sub> adsorption kinetics on mesoporous silica under wide range of pressure and temperature*. Chemical Engineering Journal, 2014. **256**: p. 1-8.
63. Kalavathy, M.H., T. Karthikeyan, S. Rajgopal, and L.R. Miranda, *Kinetic and isotherm studies of Cu(II) adsorption onto H<sub>3</sub>PO<sub>4</sub>-activated rubber wood sawdust*. J Colloid Interface Sci, 2005. **292**(2): p. 354-62.
64. Hameed, B.H., I.A.W. Tan, and A.L. Ahmad, *Adsorption isotherm, kinetic modeling and mechanism of 2,4,6-trichlorophenol on coconut husk-based activated carbon*. Chemical Engineering Journal, 2008. **144**(2): p. 235-244.
65. Sasaki, M., B. Kabyemela, R. Malaluan, S. Hirose, N. Takeda, T. Adschiri, and K. Arai, *Cellulose hydrolysis in subcritical and supercritical water*. The Journal of Supercritical Fluids, 1998. **13**(1-3): p. 261-268.
66. Zhao, Y., W.-J. Lu, and H.-T. Wang, *Supercritical hydrolysis of cellulose for oligosaccharide production in combined technology*. Chemical Engineering Journal, 2009. **150**(2-3): p. 411-417.
67. Zhao, Y., H.-T. Wang, W.-J. Lu, and H. Wang, *Combined supercritical and subcritical conversion of cellulose for fermentable hexose production in a flow reaction system*. Chemical Engineering Journal, 2011. **166**(3): p. 868-872.
68. Sasaki, M., Z. Fang, Y. Fukushima, T. Adschiri, and K. Arai, *Dissolution and Hydrolysis of Cellulose in Subcritical and Supercritical Water*. Industrial & Engineering Chemistry Research, 2000. **39**(8): p. 2883-2890.
69. Béguin, P. and J.P. Aubert, *The biological degradation of cellulose*. FEMS Microbiology Reviews, 1994. **13**(1): p. 25-58.
70. Coughlan, M.P. and L.G. Ljungdahl, *Comparative biochemistry of fungal and bacterial cellulolytic enzyme system*. Biochemistry and Genetics, 1988: p. 11-30.
71. Song, Y., J. Zhou, L. Zhang, and X. Wu, *Homogenous modification of cellulose with acrylamide in NaOH/urea aqueous solutions*. Carbohydrate Polymers, 2008. **73**(1): p. 18-25.
72. Zhang, Z., W. Wang, X. Liu, Q. Wang, W. Li, H. Xie, and Z.K. Zhao, *Kinetic study of acid-catalyzed cellulose hydrolysis in 1-butyl-3-methylimidazolium chloride*. Bioresource Technology, 2012. **112**(0): p. 151-155.
73. Keshk, S.M.A.S., *Homogenous reactions of cellulose from different natural sources*. Carbohydrate Polymers, 2008. **74**(4): p. 942-945.
74. Wu, J. and L.K. Ju, *Enhancing enzymatic saccharification of waste newsprint by surfactant addition*. Biotechnol Prog, 1998. **14**(4): p. 649-52.
75. Bravo, V., M.P. Paez, M. Aoulad, and A. Reyes, *The influence of temperature upon the hydrolysis of cellobiose by  $\beta$ -1,4-glucosidases from *Aspergillus niger**. Enzyme and Microbial Technology, 2000. **26**(8): p. 614-620.
76. Klein, M.T., L.A. Torry, B.C. Wu, S.H. Townsend, and S.C. Paspek, *Hydrolysis in supercritical water: Solvent effects as a probe of the reaction mechanism*. The Journal of Supercritical Fluids, 1990. **3**(4): p. 222-227.
77. Adschiri, T., S. Hirose, R. Malaluan, and K. Arai, *Noncatalytic Conversion of Cellulose in Supercritical and Subcritical Water*. JOURNAL OF CHEMICAL ENGINEERING OF JAPAN, 1993. **26**(6): p. 676-680.

78. Kabyemela, B.M., T. Adschiri, R.M. Malaluan, and K. Arai, *Kinetics of Glucose Epimerization and Decomposition in Subcritical and Supercritical Water*. Industrial and Engineering Chemistry Research, 1997. **36**(5): p. 1552-1558.
79. Kabyemela, B.M., *Degradation kinetics of dihydroxyacetone and glyceraldehyde in subcritical and supercritical water*. Industrial and Engineering Chemistry Research, 1997. **36**(6): p. 2025-2030.
80. Tekin, K., S. Karagöz, and S. Bektaş, *A review of hydrothermal biomass processing*. Renewable and Sustainable Energy Reviews, 2014. **40**(0): p. 673-687.
81. Brunner, G., *Chapter 8 - Processing of Biomass with Hydrothermal and Supercritical Water*, in *Supercritical Fluid Science and Technology*, B. Gerd, Editor. 2014, Elsevier. p. 395-509.
82. Morales-Delarosa, S. and J.M. Campos-Martin, *6 - Catalytic processes and catalyst development in biorefining*, in *Advances in Biorefineries*, K. Waldron, Editor. 2014, Woodhead Publishing. p. 152-198.
83. Niu, Y., H. Wang, X. Zhu, Z. Song, X. Xie, X. Liu, J. Han, and Q. Ge, *Ru supported on zirconia-modified SBA-15 for selective conversion of cellobiose to hexitols*. Microporous and Mesoporous Materials, 2014. **198**(0): p. 215-222.
84. Cabiac, A., E. Guillon, F. Chambon, C. Pinel, F. Rataboul, and N. Essayem, *Cellulose reactivity and glycosidic bond cleavage in aqueous phase by catalytic and non catalytic transformations*. Applied Catalysis A: General, 2011. **402**(1-2): p. 1-10.
85. Palkovits, R., K. Tajvidi, J. Procelewska, R. Rinaldi, and A. Ruppert, *Hydrogenolysis of cellulose combining mineral acids and hydrogenation catalysts*. Green Chemistry, 2010. **12**(6): p. 972-978.
86. Gracia, M.D., A.M. Balu, J.M. Campelo, R. Luque, J.M. Marinas, and A.A. Romero, *Evidences of the in situ generation of highly active Lewis acid species on Zr-SBA-15*. Applied Catalysis A: General, 2009. **371**(1-2): p. 85-91.

# Conclusions

## Conclusions

Taking into account the objectives set at the beginning of this PhD thesis, during the course of it, they have been fully complied, as indicated below:

- Co/MCM-41 and Ni/MCM-48 catalysts have been synthesized by means of supercritical fluid reactive deposition (SCFRD), with metallic loadings up to 15 %wt and 5 %wt respectively.
- Ru/MCM-48 and Ru/AC catalysts have been prepared using supercritical fluid deposition (SCFD) in continuous process with metal loadings of 4 and 8 %wt.
- The solubility of RuCp<sub>2</sub> in sc-CO<sub>2</sub> has been determined at 60 °C and different pressures, and fitted with good agreement by empirical (Chrastil) and EoS (Peng-Robinson) methods.
- The adsorption isotherms of all systems adsorbent-adsorbate presented in this PhD thesis have been determined, showing different behaviors, and modeled with multiple correlations (Langmuir, Freundlich, Redlich-Peterson, Toth and BET). Moreover, the adsorption kinetics and mechanisms have been studied in order to propose a correct operational time and identify the rate-controlling step.
- SCFRD process has been optimized for deposition of cobalt and nickel from their respectively metallocenes, in a batch system, operating at 200 °C and 14 MPa for 1 hour, placing the precursor and support alternatively to avoid transfer limitations into the reactor.
- SCFD process in continuous has been developed for the deposition of ruthenium on MCM-48 and AC, at 60 °C and 11 MPa with different CO<sub>2</sub> flows (15, 30 and 45 g/h).
- Catalysts have been characterized in terms of metallic loading, morphology, structure, metal distribution and metal size by different techniques, such as XRF, BET, TPR, SEM or TEM among others.

## CONCLUSIONS

- In the case of study of cobalt, the isotherm showed that the adsorption of  $\text{CoCp}_2$  on MCM-41 was practically non-existing. But this technique of SCFRD has proven to be a viable process for its synthesis. It has been achieved a product with a metal loading around 6 %wt after just one hour of operation. This fact presents a considerable advantage compared to conventional synthesis methods, which require exposure times of up to one or two days. Moreover, metal dispersion achieved by this technique has been far superior to other methods, around 10% with particles between 1 to 9 nm.
- The versatility of this process has been tested by means of the preparation of nickel-based catalysts. However, in this case the difficulty to be overcome was the adsorption mechanism was mainly governed by external mass transport, requiring very long times to reach the equilibrium (10 hours). The results have shown that this synthesis technique (SCFRD) also allows the manufacture of catalysts for this kind of systems, obtaining metallic loading between 2-5 %wt with nickel particles homogeneously distributed on the surface and BET areas close to  $1000 \text{ m}^2/\text{g}$ .
- By using SCFRD can achieve high metal loadings through consecutive batches, as it has been tested in the synthesis of cobalt (6, 14 and 17 %wt) and nickel (2, 4 and 5 %wt) catalysts.
- Another important factor that should be noted is that, despite using high pressure, this technique does not modify the ordered structure of the supports as has been proven in microscopy pictures, unlike other methods such as direct synthesis that caused the pores collapse.
- Ruthenium-based catalysts have been satisfactorily prepared by means a continuous method based on the SCFD on two different supports (MCM-48 and AC). The analysis of their adsorption mechanism revealed that both systems have complex mechanism with different stages involved. In the case of adsorption on AC, the external transport is the controlling step; whereas on MCM-48 the pore diffusion is which governs the process. However, this difference is not a problem for the synthesis method, since the diffusion limitations can be resolved using lower  $\text{CO}_2$  flows. This represents a huge

advantage compared to batch process from an economic point of view, which shows its potential commercial and industrial viability.

- Co/MCM-41 catalysts have been tested in the gasification of cellulose, obtaining a H<sub>2</sub> selectivity around 30% as a result of the promotion of tar production, as it has been demonstrated by the fit provided by a proposed three-reaction model.
- Ni/MCM-48 catalysts have been proved in the selective conversion of glucose to sorbitol, reaching conversions around 6 %, with selectivity up to 90 % and yield of 5 %, similar to conventional catalysts.
- The activity of ruthenium-based catalysts have been tested in the hydrolysis of cellobiose for glucose production, achieving the best yield with the Ru/MCM-48 catalysts prepared by SC, and improving the process without catalysts from 18% to 48%, with selectivity around 90%.

# Future Work

## Future Work

As future work, the synthesis of bimetallic catalysts by means of supercritical technology is proposed.

The main characteristic that a good catalyst must have is a long useful life; that is, maintain its activity in the course of time and multiple uses.

In this sense, nickel-based catalysts are often easily deactivated due to poisoning by coke. One of the possible solutions that arises is the use of another metal to confer certain stability, protecting nickel particles against carbonaceous deposits.

Therefore, the synthesis of nickel-ruthenium bimetallic catalysts using supercritical fluids is proposed; with its consequent stability test in cycles reactions.

# Appendix

## Characterization Techniques

In this section, characterization techniques employed during the development of this thesis are described. As well as the analytical conditions under which the different equipments have been operated to determine the structural and physicochemical properties of the synthesized catalysts and organometallic precursors.

In the following table, characterization techniques are summarized and briefly explained the objective with each of them.

<b>Technique</b>	<b>Information</b>
<b>Nitrogen adsorption / desorption</b>	<b>Textural properties, surface area and porosity</b>
<b>Temperature Programmed Reduction (TPR)</b>	<b>Reducibility of the species</b>
<b>X-Ray Diffraction (XRD)</b>	<b>Structural properties and cristallinity</b>
<b>X-Ray Photoelectron Spectroscopy (XPS)</b>	<b>Surface species and oxidation state</b>
<b>Inductively Coupled Plasma Optical Emission Spectrometry (ICP-OES)</b>	<b>Concentration of metal</b>
<b>X-Ray Fluorescence (XRF)</b>	<b>Semi-quantitative elemental composition</b>
<b>Fourier Transform Infrared Spectroscopy (FTIR)</b>	<b>Chemical structure and functional groups</b>
<b>Scanning Electron Microscopy (SEM / EDX)</b>	<b>Morphology, size and external particles</b>
<b>Transmission Electron Microscopy (TEM / MAPPING)</b>	<b>Morphology of the pores and metal distribution</b>
<b>Thermogravimetric Analysis (TGA)</b>	<b>Decomposition temperature</b>
<b>Temperature-Programmed Desorption (TPD) of ammonia</b>	<b>Acidity</b>
<b>Hydrogen Chemisorption (HC)</b>	<b>Dispersion of the active phase</b>

## APPENDIX

### Nitrogen adsorption / desorption

The two additional factors in the adsorption phenomena, imperative for catalysis applications, are the surface area and porosity or texture of the solid, which are intimately connected to the process of synthesis. The adsorption / desorption gases measurements can provide information about them through the adsorption isotherms.

There are 6 different types of isotherms it can be found in literature [Fig. 1], from I to V belonging to the original classification of Brunauer, Deming and Teller, and type VI, added later by the International Union of Pure and Applied Chemistry (IUPAC).

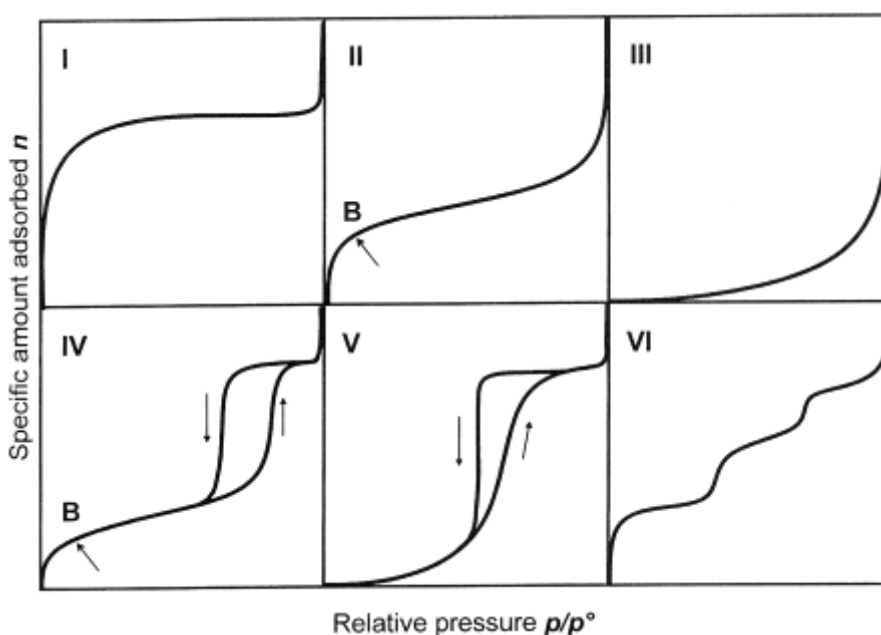


**Figure 1.** Classification of adsorption isotherms defined by IUPAC depending on the pore size and surface character of the material

In this same way, the pore sizes were classified into three groups according to their diameter to explain the nature of solids and their isotherms:

- Microporous: 0-2 nm
- Mesoporous: 2-50 nm
- Macroporous: >50 nm

Type I isotherm are given by microporous solids having relatively small external surfaces, such as activated carbons, molecular sieve zeolites and certain porous oxides, the limiting uptake being governed by the accessible micropore volume rather than by the internal surface area.

Type II isotherm represents the unrestricted monolayer/multilayer adsorption of adsorbate on the surface of non-porous or macroporous materials.

Type III isotherm is not common; however there are a number of systems, such as nitrogen on polyethylene, which give isotherms with gradual curvature. In such cases, the adsorbent-adsorbate interaction is weak as compared with the adsorbate-adsorbate interactions.

Types IV and V isotherms show a hysteresis loop associated to capillary condensation taking place in mesopores.

Type VI isotherm shows stepwise multilayer adsorption on a uniform non-porous surface. The step-height now represents the monolayer capacity for each adsorbed layer and, in the simple case, remains nearly constant for two or three adsorbed layers.

BET surface area and pore size distribution were determined using a Quantasorb Sorption System (Quantachrome Instruments) by the isotherms of adsorption and desorption of N<sub>2</sub> at -196 °C on 200 mg of sample previously degassed at 350 °C under high vacuum atmosphere for 8 h. Total specific areas were determined by the multipoint ET method at  $P/P_0 \leq 0.3$ , and total specific pore volume were evaluated from N<sub>2</sub> uptake at relative pressure to near saturation ( $P/P_0 = 0.99$ ).

The pore size distribution curves were calculated from the desorption branches of the isotherm using Barret-Joyner-Halenda method (BJH).

### Temperature Programmed Reduction (TPR)

Temperature Programmed Reduction (TPR) is a technique widespread for chemical characterization of solids.

TPR basically consists in the reduction of a solid in contact with a gaseous stream, usually H<sub>2</sub> as a reducing gas diluted with other inert gas (nitrogen or argon), during a controlled heating of the system. The composition of the gaseous mixtures is measured at the exit of the reactor, in one or more peaks. Each of these represents a reduction

## APPENDIX

process involving a chemical species in particular, and its position depends on their chemical nature.

During the development of this thesis, TPR technique was used to analyze the reducibility of metal species and their oxidation states, and thus to identify them.

TPR profiles were determined using a Micrometrics TPR/TPD 2900 analyzer, where catalyst precursor is first outgassed and heated in an N<sub>2</sub>/H<sub>2</sub> flow ( $\geq 99.999\%$  purity, 95/5 volumetric ratio) at 10 °C/min to 900 °C. Finally, the effluent gas is directed through a liquid N<sub>2</sub> trap and H<sub>2</sub> consumption is determined by TCD.

### X-Ray Diffraction (XRD)

This technique provides information about structural properties, orientation and size of the crystals present in the sample. Since each crystal compound has certain characteristic parameters, such as interplanar distances, then, this data is enough to unequivocally identify the species present by comparison of the diffractograms obtained with the standards provided by the database system.

In the case of microporous supports, XRD was used to verify the degree of crystallinity. This was estimated from the ratio of the sum of intensities corresponding to the peaks of the main planes (1 1 1), (3 3 0), (1 5 0), (2 0 2) and (3 5 0).

Precursors and prepared solids were ground in an agate mortar to homogenize the particle size and placed in the sample holder. A diffractometer XRD Phillips PW 1710 was employed, using Cu K-alpha radiation (wave length  $\lambda = 1.54056\text{\AA}$ ), in the angle range  $2\theta$  from 5° to 85° and step size of 0.02°.

### X-Ray Photoelectron Spectroscopy (XPS)

X-Ray Photoelectron Spectroscopy (XPS) can help us to identify the surface species, especially to determine its oxidation state, considering that this is essentially a technique for analyzing the solid surface, only reaching a depth of 30 Å.

The XPS measurements were performed with multitechnique system (SPECS) fitted with a dual anode (Mg/Al) non-monochromatic X-ray source and hemispherical PHOIBOS 150 analyzer operating in the fixed analyzer transmission mode (FAT). The spectra were obtained with pass energy of 30 eV and AlK $\alpha$  radiation ( $h\nu = 1486.6$  eV) at 200 W and 12 kV.

### Inductively Coupled Plasma Optical Emission Spectroscopy (ICP-OES)

The chemical analysis to determine the metal concentrations were obtained by means of the Inductively Coupled Plasma Optical Emission Spectroscopy (ICP-OES).

A Perkin Elmer Optima 2100 DV ICP-OES spectrometer was used to get the metallic loading, previously calibrated with standard solutions prepared in the laboratory.

For the measurement, all samples followed the same procedure.

0,1 g of solid is weighed in a platinum capsule completely dry. Then, deionized water is added to wet the sample, and right after, 2 ml of H<sub>2</sub>SO<sub>4</sub> and 10 ml of HF are added for their digestion. After this, the samples are placed in a heating mantle where the water evaporates and a thicker white vapor due to sulfuric acid is subsequently observed. At that time, the capsule is removed from the heater, allowed to cool and poured into a 250ml Erlenmeyer flask, making up to the mark with ultrapure distilled water. Finally, this solution is measured in the ICP-OES spectroscopy and compared to the standard calibration curve.

### X-Ray Fluorescence (XRF)

X-Ray Fluorescence (XRF) has been used as semi-quantitative determination of elemental composition of materials, although always results have been contrasted with other technique such as ICP-OES.

This technique has been chosen to obtain approximate values quickly and easily. Analyzed samples are not destroyed or changed by exposure to X-Ray, and 2 mm thick are enough to measure, making this methodology very useful for analysis of small

## APPENDIX

samples sizes or high value. Detection limit depend upon the specific element and the sample matrix, but in general heavier elements have higher detection limit.

The measurements are based on the study of the generated fluorescence emission (angle of diffraction  $\theta$ , and wavelength  $\lambda$ , according to the Bragg's law, where  $\sin\theta=n\cdot\lambda/2\cdot d$ ) after excitation of a sample by X-ray source. For this purpose, a Bruker S8 Tiger (4KW) equipped with an end window X-Ray tube with Rh-target was employed.

### Fourier Transform Infrared Spectroscopy (FTIR)

The chemical structure and functional groups of both the precursors and degradation products thereof to be subjected to high pressures and temperatures were characterized by Infrared Spectroscopy (FTIR).

FT-IR spectra were obtained by means of a Bruker Tensor 27 Fourier transform spectrometer equipped with a SPECAC Golden Gate diamond ATR unit. Measurements were made with a resolution of  $4\text{ cm}^{-1}$  in the region between  $4000$  and  $600\text{ cm}^{-1}$ , with a total of 64 scans.

### Scanning Electron Microscopy (SEM / EDX)

The application of Scanning Electron Microscopy (SEM) combined with detection by Energy Dispersive X-ray Spectroscopy (EDX) was performed to analyze the morphology of the support, both its tridimensional structure and its porous superficial texture, and besides to determine the chemical composition of the deposited particles.

For this, an environmental scanning electron microscope (ESEM) FEI Quanta model 200FEG operating at 30 kV was used, processing the information collected with the system software.

Furthermore, a backscattered electron detector was employed to observe the metallic particles. This method is characterized by a stronger contrast in relation to the atomic number  $Z$  ( $Z$ -contrast). Therefore, if there are phases with very different  $Z$  in the sample, more clear images are obtained, with brighter values for the elements with higher  $Z$ .

### Transmission Electron Microscopy (TEM / MAPPING)

Transmission Electron Microscopy (TEM) was used to determine the organization, morphology and the mesoporous channels dimensions, as well as to observe the presence of the metallic particles dispersed within and/or out the pores. In addition, this technique allows measuring the nanoparticles interplanar distance, with resolutions up to 3 Å.

The samples were dissolved in methanol and then placed in a carbon grid to be introduced directly into the microscope. A JEOL field emission microscope model JEM-FS2200 HRP operating at 200 kV was used.

Moreover, the real particles distribution was achieved by means of X-ray mapping. This technique allows knowing the distribution and homogeneity of the metallic particles in the space identifying each chemical element with different colors.

### Thermogravimetric Analysis (TGA)

In order to determine the decomposition temperature of organometallic precursors was employed a thermobalance Mettler Toledo TGA/SDTA 851E. This device is equipped with a horizontal furnace average temperature (1100 °C) and automatic gas exchanger, acclimatized with an external water loop, with a resolution of 0.005 °C.

Assays were performed by weighing 10 mg of precursor in an aluminum oxide crucible and heated from 50 °C to 850 °C at a constant ramp rate of 20 °C/min under continuous N<sub>2</sub> flow of 60 ml/min.

### Temperature-Programmed Desorption (TPD) of ammonia

The acidity of catalysts is widely measured by means of Temperature-Programmed Desorption (TPD) of ammonia. This characterization method involves saturation of the surface with ammonia under some set of adsorption conditions, followed by linear ramping of temperature of the sample in a flowing inert gas stream. Ammonia

## APPENDIX

concentration in the effluent gas is followed by absorption/titration or mass spectroscopy.

For the determination of surface acid site concentration, a Micrometrics TPD/TPR 2900 analyzer was employed. The catalysts were reduced/activated under conditions used prior catalysis. Cooled to 100 °C and the samples contacted with a flow of NH<sub>3</sub> for 15 min with a subsequent purge with helium for 1 h to remove physisorbed NH<sub>3</sub>. The samples were ramped at 15 °C/min from 100 to 600 °C and TPD<sub>NH<sub>3</sub></sub> data acquired.

### Hydrogen Chemisorption (HC)

Selective chemisorption of hydrogen has been used to estimate the degree of dispersion, crystal diameter and calculate metal surface areas. For this purpose, the hydrogen-to-metal stoichiometry must be known, as for example in the case of cobalt or ruthenium where the relation H/M = 1/1 is well established.

For this kind of experiments, the dispersion of metal was calculated employing a methodology similar to the determination of the isotherm of adsorption. All the samples were previously degassed at 300 °C under vacuum (120 mmHg) for 8 h.

## Conventional Deposition Methods

In this PhD, catalysts have been prepared by different techniques in order to compare them with catalysts synthesized by SC techniques. The metal salt precursor employed in the traditional syntheses were  $\text{Co}(\text{NO}_3)_2$  and  $\text{Ni}(\text{NO}_3)_3$ .

### Wet Impregnation (WI)

Incipient wetness impregnation is the most widespread method for the manufacture of metal catalysts.

In this technique, the support (MCM-41 and MCM-48) is mixed with an aqueous metal-containing solution, whose concentration depends on the desired amount of metal. This solution is added in excess of the support pore volume in order to ensure that the entire surface is wetted. After that, the mixture is slowly heated (1 °C/min) up to 90 °C.

Then, the sample is dried and calcined to drive off the volatile components within the solution, depositing the metal over the catalysts surface.

### Direct synthesis or co-precipitation (DS)

Direct synthesis process involves the addition of the metal at the same time of the formation of the support structure. This means that catalysts samples were synthesized like for the silica supports (MCM-41 and MCM-48), but with the addition of the appropriate metal salt to the surfactant-water-ethanol solution. The amount necessary of precursor in each case depending on the metal concentration desired in the final product.

After this, TEOS is dropwise added to promote the gel formation. This solution is maintaining under continuous stirring for about 20 hours at constant temperature, 35 °C. Finally, the same procedure for drying, filtering and calcining for supports is followed.

About  
the autor

## About the author



Álvaro Sastre Cuadrillero (Valladolid, 1986) started the studies of *Chemical Engineering* at the University of Valladolid in 2004. During the degree, he also started in the world of research through a project funded by the *Junta de Castilla y León*, entitled “*Experimental Determination and Modeling of Impregnation Isotherms of Linalool on Wood by  $sc\text{-CO}_2$* ” in 2007. After that, he continued his research, graduating in 2010 with his final thesis called “*Design of an Industrial Plant for Wood Protection against Moisture using Supercritical Technology: Impregnation by Adsorption and Precipitation by Spray (PGSS)*”.

The next year, in 2011, the author graduated in *Master’s Degree in Engineering Thermodynamics of Fluids* with the highest grade of his year, and was officially joined to the *High Pressure Processes Group* of the *Department of Chemical Engineering* in the University of Valladolid, in charge of purchasing reagents. In those days, a new research project was being started about “*Preparation, Characterization and Evaluation of Soli Catalysts for the Selective Conversion of Cellulose into Chemicals in Supercritical Water*” in cooperation with others research centers and universities (CTQ2010-15475 and CTG2011-27347). In this framework, he started his PhD thesis focused on the optimization of the synthesis process to prepare cobalt, nickel and ruthenium catalyst supported on different porous materials.

During his PhD studies, the author has made a stay in a foreign research institute in the year 2013, at the *Chemical and Biological Engineering Department* in the Koç University (Istanbul, Turkey) under the supervision of Prof. Dr. Can Erkey.

His study has been financially supported by the *European Social Foundation in the framework of the Regional Strategy of Science Research, Technological Development and Investigation*, in collaboration with the *Government of Castilla y León* (ORDEN EDU/1204/2010).

## Contributions, publications and conferences

Soledad Guadalupe Aspromonte; Álvaro Sastre Cuadrillero; Alicia Viviana Boix; María José Cocero Alonso; Gloria Esther Alonso Sánchez.

*Cobalt oxide nanoparticles on mesoporous MCM-41 and Al-MCM-41 by Supercritical CO<sub>2</sub> Deposition.* Microporous & Mesoporous Materials. 148 - 1, pp. 53 - 61. (2012)

Antonio Nieto Márquez; Álvaro Sastre Cuadrillero; Alberto Romero Camacho; Esther Alonso Sánchez; María José Cocero Alonso.

*Preparación supercrítica de catalizadores de Cobalto y Níquel para la valorización selectiva de biomasa* 31º Congreso Latinoamericano de Química CLAQ-2014, XXVII Congreso Peruana de Química, Lima (Perú)

14/10/2014

Álvaro Sastre Cuadrillero; Alberto Romero Camacho; Antonio Nieto Márquez-Ballesteros; Gloria Esther Alonso Sánchez.

*Síntesis de catalizadores de cobalto soportados en MCM41 por deposición reactiva supercrítica: Evaluación de la actividad catalítica en gasificación de celulosa*

I Encuentro de Jóvenes Investigadores de la SECAT, Málaga (España)

22/06/2014

Alberto Romero Camacho; Álvaro Sastre Cuadrillero; Antonio Nieto Márquez-Ballesteros; Gloria Esther Alonso Sánchez.

*Preparación de catalizadores mesoporosos de Ni para la hidrogenación selectiva de D-glucosa.*

I Encuentro de Jóvenes Investigadores de la SECAT, Málaga (España)

22/06/2014

Alberto Romero Camacho; Álvaro Sastre Cuadrillero; Antonio Nieto Márquez-Ballesteros; Gloria Esther Alonso Sánchez.

*Design of ruthenium catalysts for efficient conversión of biomass into sorbitol*

10th International Conference on Renewable Resources and Biorefineries, Valladolid (España)

04/06/2014

Alberto Romero Camacho; Álvaro Sastre Cuadrillero; Antonio Nieto Márquez-Ballesteros; Gloria Esther Alonso Sánchez.

*Ruthenium nanoparticles on mesoporous MCM48 by supercritical CO<sub>2</sub> deposition: Efficient conversión of glucose into sorbitol*

14th European Meeting on Supercritical Fluids, Marsella (Francia)

18/05/2014

Alberto Romero Camacho; Álvaro Sastre Cuadrillero; Antonio Nieto Márquez-Ballesteros; Gloria Esther Alonso Sánchez.

*Direct conversión of Cellulose into sorbitol by Ni/mesoporous catalysts prepared in supercritical CO<sub>2</sub>*

UBIOCHEM IV, Utilization of Biomass for Sustainable Fuels & Chemicals, 4th International Workshop of COST Action, CM0903, Valencia (España)

14/10/2013

Álvaro Sastre Cuadrillero; Alberto Romero Camacho; María José Cocero Alonso; Esther Alonso Sánchez.

*Supercritical Fluid Deposition of Cobalt Oxide Nanoparticles over MCM-41: Adsorption Isotherms and Adsorption Curves*

6th International Symposium on High Pressure Process Technology, Belgrado (Serbia)

08/09/2013

Álvaro Sastre Cuadrillero; Alberto Romero Camacho; Antonio Nieto-Márquez Ballesteros; Evangelina Atanes Sánchez; Gloria Esther Alonso Sánchez.

*Descomposición de celulosa sobre catalizadores de Co introducidos en MCM41 en medio supercrítico*

SECAT 2013. Catalizadores y Reactores Estructurados, Sevilla (España)

26/06/2013

Álvaro Sastre Cuadrillero; Alberto Romero Camacho; María José Cocero Alonso; Gloria Esther Alonso Sánchez.

*High Loading Co/MCM41 catalysts prepared by Supercritical Fluid Deposition*  
9th European Congress of Chemical Engineering, Word Forum, La Haya (Holanda)  
21/04/2013

Alberto Romero Camacho; Álvaro Sastre Cuadrillero; María José Cocero Alonso; Gloria Esther Alonso Sánchez.

*Supercritical preparation of nickel mesoporous silica catalysts: Comparision with Wet Techniques*  
9th European Congress of Chemical Engineering, Word Forum, La Haya (Holanda)  
21/04/2013

Álvaro Sastre Cuadrillero; Alberto Romero Camacho; María José Cocero Alonso; Gloria Esther Alonso Sánchez.

*Supercritical Fluid Deposition of metallic nanoparticles over mesoporous supports*  
Prosciba 2013. III Iberoamerican Conference on Supercritical Fluids, Cartagena de Indias (Colombia)  
01/04/2013

Soledad Guadalupe Aspromonte; Florencia Schneeberger; Álvaro Sastre Cuadrillero; Gloria Esther Alonso Sánchez; Eduardo Miró; Alicia Viviana Boix; María José Cocero Alonso.

*Catalizadores Co-AMCM-41 preparados mediante CO2 supercrítico*  
XVII Congreso argentino de catálisis (XVII CAC) y VI Congreso de catálisis del Mercosur (VI Mercocat), Salta (Argentina)  
17/10/2011

Álvaro Sastre Cuadrillero; Soledad Guadalupe Aspromonte; Alicia Viviana Boix; María José Cocero Alonso; Gloria Esther Alonso Sánchez.

*Deposition of Co Nanoparticles on Mesoporous-Silica Supports Using Supercritical CO2*  
13th European Meeting on Supercritical Fluids. SCFs as product and process solvents in emerging applications, La Haya (Holanda)  
09/10/2011

Álvaro Sastre Cuadrillero

*Deposición de cobalto sobre soportes MCM-41 mediante deposición reactiva en CO2 supercrítico*  
3rd International Seminar on Engineering Thermodynamics of Fluids. Ionic Liquids for Absorption Refrigeration, Tarragona (España)  
25/07/2011

Gloria Esther Alonso Sánchez; Álvaro Sastre Cuadrillero; Soledad Guadalupe Aspromonte; Eduardo Miró; Alicia Viviana Boix; María José Cocero Alonso.

*Preparación de catalizadores de Co/MCM41 con CO2 supercrítico*  
SECAT 2011. La catálisis ante la crisis energética y ambiental, Zaragoza (España)  
29/06/2011

Álvaro Sastre Cuadrillero; Gloria Esther Alonso Sánchez; María José Cocero Alonso.

*Deposición química en CO2 supercrítico de nanopartículas de cobalto sobre soportes mesoporosos*  
Flucomp 2011. V Reunión de Expertos en Tecnologías de Fluidos Comprimidos, Burgos (España)  
15/06/2011

Soledad Guadalupe Aspromonte; Álvaro Sastre Cuadrillero; Gloria Esther Alonso Sánchez; Alicia Viviana Boix; Eduardo Miró; María José Cocero Alonso.

*Tecnología de fluidos supercríticos para la deposición de nanopartículas metálicas sobre soportes mesoporosos*  
XVII Congreso Argentino de Físicoquímica y Química Inorgánica. Punto de encuentro de la Física, la Química y la Biología, Córdoba (Argentina)  
03/05/2011

Soledad Guadalupe Aspromonte; Álvaro Sastre Cuadrillero; Gloria Esther Alonso Sánchez; Alicia Viviana Boix; Eduardo Miró; María José Cocero Alonso.

*Deposición supercrítica de nanopartículas metálicas sobre soportes micro y mesoporosos*

RITeQ 2010. II Reunión Interdisciplinaria de Tecnología y Procesos Químicos, Córdoba (Argentina)

24/10/2010

# Resumen

## (castellano)

## Resumen (castellano)

### Introducción

En los últimos años el interés hacia los materiales nanoestructurados ha crecido de manera exponencial debido a sus ventajas asociadas a su pequeño tamaño, tales como su gran área superficial, convirtiéndolos en un producto muy interesante desde el punto de vista de la catálisis.

En este sentido, numerosos estudios se han centrado en mejorar la difusión de las moléculas de reactivos más voluminosas hacia los centros activos, creando nuevos materiales depositando nanopartículas metálicas sobre materiales porosos, los cuales aparte de otorgar estabilidad como soporte, también aportan cierta uniformidad.

A día de hoy, existen varias técnicas para depositar metales sobre diversos sustratos, tanto en forma de películas como de nanopartículas. Los métodos convencionales más empleados en todos los ámbitos son impregnación húmeda, co-precipitación o sol-gel. Cada una de ellas presenta diversas ventajas e inconvenientes, pero en general, el principal problema de todos estos métodos de síntesis es el control del tamaño de las partículas, así como la distribución y el contenido del metal en el interior de la matriz del soporte. Por ejemplo, tanto la impregnación húmeda como la deposición por sol-gel emplean soluciones líquidas, lo que provoca la aglomeración de las partículas y el colapso de los poros del soporte debido a la elevada tensión superficial. Además, la necesidad de eliminar el surfactante promueve de nuevo la aglomeración de las partículas metálicas debido a las altas temperaturas requeridas.

Por todo ello, el reto principal aún sin resolver en la síntesis de materiales nanoestructurados es el de conseguir un método de alta reproducibilidad, con un gran control de tamaños y estable, evitando la aglomeración de las partículas.

En este sentido, el uso de fluidos supercríticos representa una alternativa con un método prometedor para la deposición de partículas tanto sobre la superficie como dentro de los poros de los sustratos. Esta técnica, denominada deposición en fluidos supercríticos (SCFD), se aprovecha de las excelentes y peculiares propiedades físicas del CO<sub>2</sub> supercrítico, las cuales son fácilmente modificables con pequeños cambios en la presión y/o temperatura del proceso. Además, su baja viscosidad, alta difusividad y tensión

superficial prácticamente nula, permiten una mayor penetración y empapado de los poros que por los métodos convencionales. Por otra parte, con una simple descompresión se puede eliminar el medio solvente, evitando así el colapso de los poros y obteniendo un producto libre de residuos, reduciendo tiempos de operación al no necesitar de etapas posteriores para su purificación.

Esta técnica es un proceso muy sencillo que puede llevarse a cabo en un solo recipiente que consta de las siguientes etapas. En primer lugar, se disuelve un precursor organometálico del metal deseado en el CO<sub>2</sub> supercrítico. Esta disolución se pone en contacto con el soporte, entrando por todos sus poros, produciéndose la adsorción del precursor sobre el sustrato. Después, el precursor se descompone, mediante un agente reductor o un aumento brusco de temperatura por encima de su temperatura de descomposición, lo que promueve la precipitación de las nanopartículas metálicas y su consecuente adsorción. Por otro lado, la parte orgánica permanece disuelta en el medio supercrítico, siendo eliminada junto a él en la descompresión.

Desde un punto de vista industrial, la producción de partículas metálicas a escala nano en CO<sub>2</sub> supercrítico podría ser muy útil en numerosas aplicaciones. Sin embargo, aún nos encontramos lejos de ser capaces de diseñar un proceso a gran escala; ya que para ello es necesario un estudio termodinámico y cinético profundo del proceso, el cual no es muy extenso en la bibliografía actual.

Atendiendo a esta necesidad, este trabajo se ha centrado en el desarrollo del proceso de síntesis de varios catalizadores utilizando esta tecnología de deposición de partículas, analizando las diferentes etapas implicadas (solubilidad, adsorción, reacción) con el fin de optimizar el proceso de síntesis. En concreto, se han preparado catalizadores de Co/MCM-41, Ni/MCM-48, Ru/MCM-48 y Ru/AC, caracterizados y probados en reacciones relacionadas con la revalorización de la biomasa.

## Objetivos

El objetivo principal de esta tesis doctoral se centra en la **preparación de una serie de catalizadores metálicos soportados en CO<sub>2</sub> supercrítico para la conversión selectiva y eficiente de biomasa**. El proceso de deposición en fluidos supercríticos (SCFD) se utilizará para depositar tres metales diferentes, Co, Ni y Ru, sobre diferentes soportes, sílica mesoporosa (MS41) y carbón activo microporoso (AC).

En especial, esta tesis se enfocará en la optimización del proceso de síntesis, para el cual se desarrollarán los siguientes objetivos parciales:

- El análisis de cada etapa del proceso de deposición (solubilidad del precursor, isothermas de adsorción y cinética).
- El estudio de las distintas condiciones de operación, tales como la presión, temperatura, tiempo de exposición... y sus efectos en el proceso.
- La caracterización físico-química de los nanocomposites (morfología, tamaño de partícula, distribución del metal...) por medio de diversas técnicas, como por ejemplo área BET, DRX, microscopía SEM, TEM...
- La evaluación de la actividad y comportamiento de los catalizadores preparados en reacciones asociadas con la revalorización de la biomasa.

## Resultados y discusión

Esta tesis se empezó con una búsqueda bibliográfica sobre el tema a tratar, resumiendo en el **Capítulo 1** los datos más relevantes a modo de introducción, presentándose en primer lugar las propiedades y ventajas de los fluidos supercríticos, seguido de los procesos de síntesis de partículas por medio de fluidos supercríticos, y acabando con unas pequeñas nociones sobre catalizadores.

A partir de ahí, la tesis se ha organizado en otros 3 capítulos, cada uno de ellos centrados en el estudio de un metal distinto: cobalto, níquel y rutenio.

En el **Capítulo 2**, se comienza el estudio con la producción de catalizadores de cobalto debido a sus numerosas aplicaciones y bajo costo; además, no hay presente ningún trabajo previo en el que se utilice la tecnología supercrítica para su síntesis. Se ha seleccionado como soporte MCM-41, siendo éste uno de los soportes mesoporosos más utilizado a todos los niveles debido a su estrecha distribución de tamaño de poros, gran superficie y estabilidad térmica. En el caso del precursor elegido para la síntesis, tras evaluar las alternativas encontradas en la literatura, se ha decidido trabajar con los compuestos denominados metallocenos, en este caso en particular con cobaltoceno ( $\text{CoCp}_2$ ), debido a su relativa alta solubilidad en  $\text{CO}_2$  supercrítico.

Para encontrar los parámetros óptimos para el proceso de deposición, se han determinado las isothermas de adsorción del  $\text{CoCp}_2$  en MCM-41 mediante un proceso en batch en una celda agitada a 70 °C y 11 MPa, donde se ha podido observar que este sistema presenta una baja interacción adsorbente-adsorbato por la forma de la curva de adsorción, perteneciente a una isoterma de tipo III.

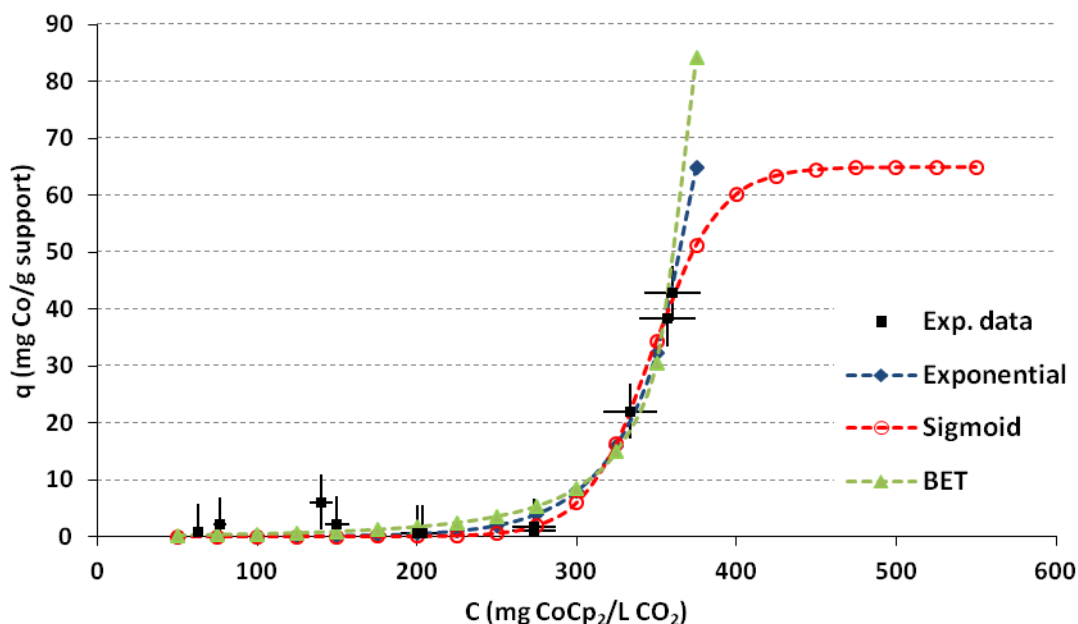


**Figura 1.** Datos experimentales (■) de la adsorción de cobaltoceno sobre MCM-41 y ajuste dado por el modelo Exponencial (-◆-), Sigmoidal (-○-) y BET (-▲-)

La adsorción sólo permite obtener cargas en torno a 65 mg/g utilizando concentraciones de saturación del precursor en el medio supercrítico y durante tiempos de exposición largos (48 horas). Los datos experimentales se han ajustado por medio de varios modelos (exponencial, sigmoidal y BET) con un error medio menor al 2%.

Ante este resultado, se ha determinado que la deposición de cobalto sobre MCM-41 no es viable tan sólo por medio de la adsorción por medio de la exposición de la disolución del precursor sobre el soporte, siendo necesario acudir a otro procedimiento. Como respuesta a esta problemática, se ha decidido utilizar la deposición reactiva en fluidos supercríticos (SCFRD), promoviendo la precipitación de las partículas metálicas sobre la superficie por medio de un incremento brusco de temperatura.

En este trabajo se han determinado las condiciones óptimas del proceso de adsorción del CoCp<sub>2</sub> sobre MCM-41 evaluado sus efectos sobre la carga metálica obtenida: temperatura, presión y tiempo sobre cada una de las etapas implicadas (disolución y adsorción). Además, durante el desarrollo de este trabajo, se ha podido observar como la distribución de los reactivos dentro del reactor también es un factor importante, debido a limitaciones de transferencia de materia, por lo que se propuso una distribución de los mismos de forma alterna, facilitando así los mecanismos del proceso. Por otro lado, los resultados fueron ajustados a un modelo cinético consistente en dos reacciones secuenciales, la primera relativa a la disolución del precursor sólido en el seno del

fluido supercrítico, y una segunda etapa de precipitación promovida por la descomposición térmica del precursor.

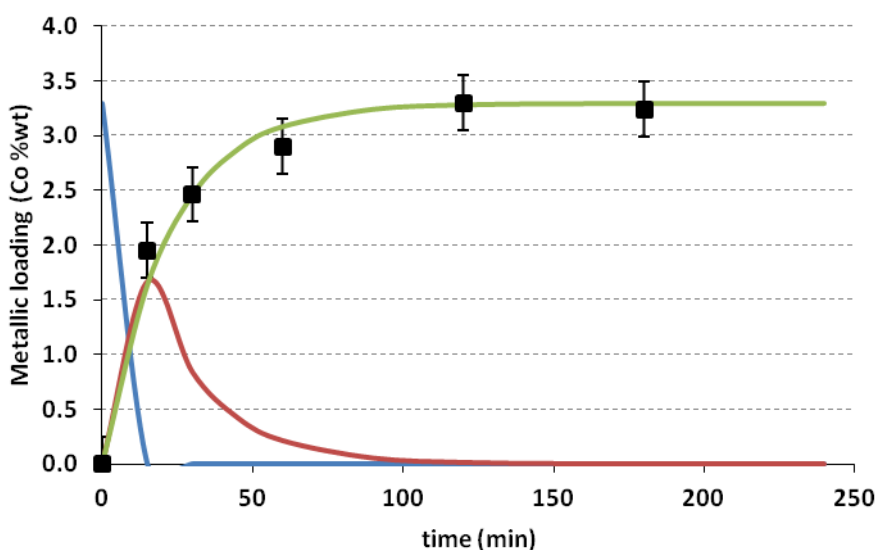


**Figura 2.** Simulación del proceso de síntesis por SCFRD como una consecuencia de reacciones en serie: Datos experimental (■); Evolución del precursor en estado sólido (Línea azul -); Precursor disuelto en el CO<sub>2</sub> supercrítico (Línea roja -); y partículas metálicas adsorbidas sobre el soporte (Línea verde -)

Como conclusión, se ha determinado trabajar a 14 MPa y 200 °C durante una hora con esta configuración precursor-soporte, obteniendo cargas metálicas del 5,8 %.

Por último, se ha comprobado como la deposición mediante cargas sucesivas consigue aumentar el porcentaje de carga metálica a un 13% tras dos secuencias, y a un 17% después de tres operaciones.

Las muestras preparadas de Co/MCM-41 han sido caracterizadas por medio de múltiples técnicas y comparados con otras sintetizadas por métodos convencionales, revelando que los catalizadores supercríticos mostraban la mejor dispersión del metal (cercano al 10%), con partículas entre 1 y 9 nm, accesibles incluso dentro de los poros. Al aumentar la carga metálica, se ha comprobado como el área BET del catalizador disminuye drásticamente de 1300 m<sup>2</sup>/g hasta 420 m<sup>2</sup>/g, reduciéndose así su volumen de poro de 0,8 cm<sup>3</sup>/g a 0,36 cm<sup>3</sup>/g a causa del taponamiento de los mismos. Las imágenes de microscopía mostraron distribuciones homogéneas del metal para las diversas cargas, apareciendo cristales de cobalto de mayor tamaño en superficie para las muestras de mayor contenido en metal.

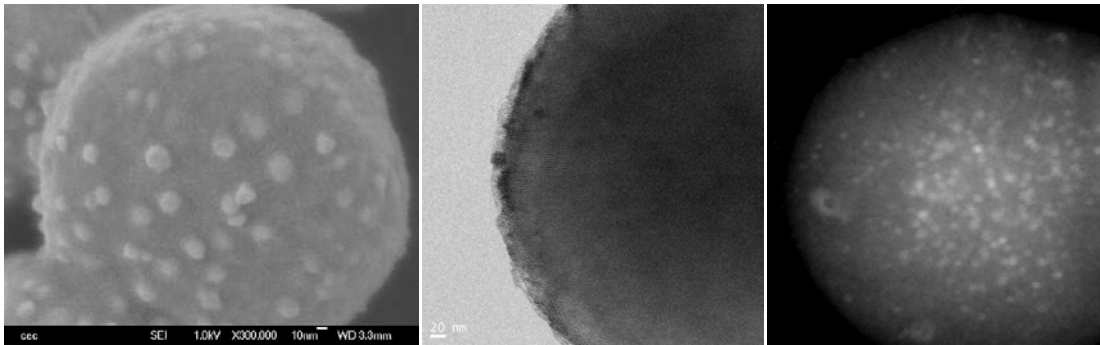


**Figura 3.** A) Imagen SEM de Co/MCM-41 con partículas en superficie;  
 B) Imagen TEM donde se observa la estructura de poro intacta y partículas metálicas;  
 y C) Imagen BSE de la misma muestra, con distribución homogénea de las partículas

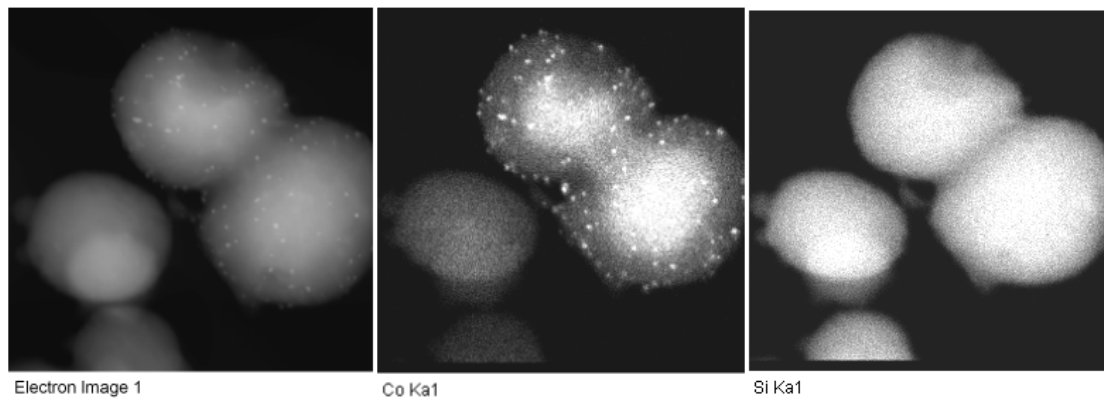


**Figura 4.** TEM/EDX Mapping para Co/MCM41 preparado por SCFRD con carga del 15%:  
 (A) imagen general, (B) Co  $\kappa\alpha$  and (C) Si  $\kappa\alpha$

Finalmente, los catalizadores fueron probados en la reacción de gasificación de celulosa para la producción de hidrógeno. Estas experiencias demostraron que los catalizadores de cobalto supercríticos aumentaban la selectividad del proceso desde un 7% a un 30% como resultado de promover la producción de compuestos líquidos intermedios. Los resultados han sido ajustados por medio de un modelo propuesto de tres reacciones para realizar un estudio de la evolución de los diferentes compuestos obtenidos a lo largo del proceso de pirolisis de la celulosa.

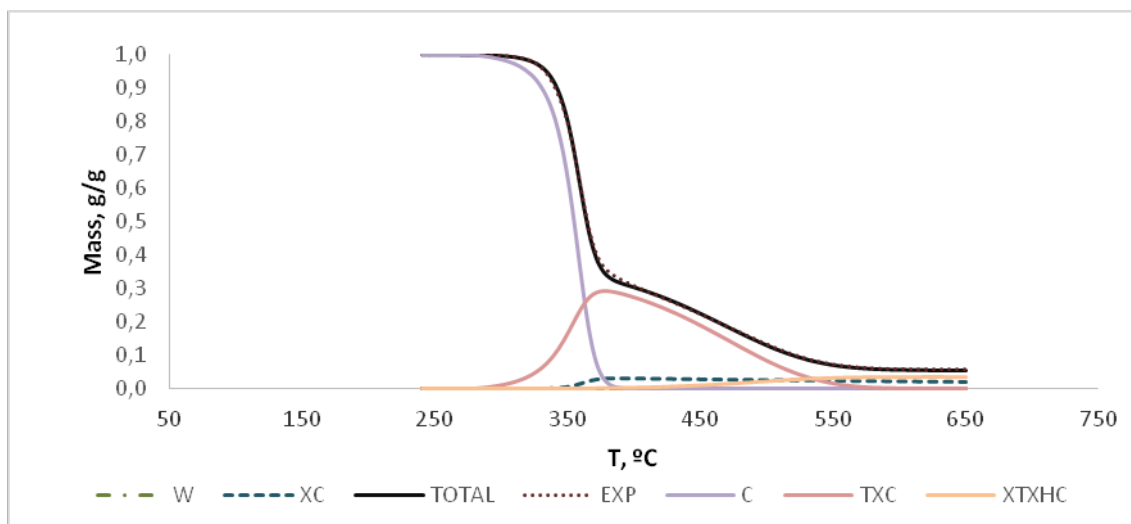


**Figura 5.** TGA experimental y curva obtenida a partir del modelo propuesto junto a la evolución de los productos intermedios en la combustión de celulosa con una rampa de calentamiento de 20°C/min catalizado con una muestra preparada de Co/MCM-41 por SCFRD y carga 5%  
 \*W) agua, XC) cenizas, C) celulosa, TXC) productos líquidos, y XTXHC) cenizas a partir de líquido

Los resultados respaldaron la hipótesis propuesta, ya que al añadir el catalizador de cobalto, la cinética de la formación de productos líquidos se vio aumentada. Suponemos que los gases producidos por la descomposición térmica de la celulosa en contacto con el catalizador, son recombinados y conducidos por un mecanismo nuevo de reacción hacia la producción de hidrógeno. Al aumentar la carga de cobalto, este efecto se ve disminuido debido a un efecto pantalla, encontrándose una carga óptima del 5-6% para esta reacción.

Para continuar con el trabajo, se decidió comprobar la versatilidad y robustez del proceso de síntesis supercrítico con un sistema precursor-soporte distinto, aunque por otro lado, con propiedades muy similares. Con este objetivo en mente, en el **Capítulo 3** se han preparado catalizadores de níquel a partir del niqueloceno (precursor con la misma configuración que el usado en el anterior capítulo) sobre MCM-48. Este soporte es otro miembro de la familia de los soportes mesoporosos de sílice llamado MS41, con un diámetro de poro muy parecido al del MCM-41 (2-4 nm), aunque con una estructura ordenada cúbica en vez de hexagonal.

De igual forma que en el caso anterior, el estudio se inició con la determinación de las isotermas de adsorción a la temperatura de 70 °C y distintas presiones (11, 14 y 17 MPa). Los resultados revelaron un comportamiento completamente distinto al observado con anterioridad, ya que la carga metálica aumentaba con la concentración, apareciendo un cambio de curvatura en torno a los 100-150 mg/L, característico de un

isoterma de tipo IV relacionada con la coexistencia de mesoporos y microporos. Los datos experimentales fueron ajustados a diversos modelos, siendo Toth el de mejor resultado, prediciendo un valor máximo de adsorción de 130 mg/g a 70 °C y 14 MPa.

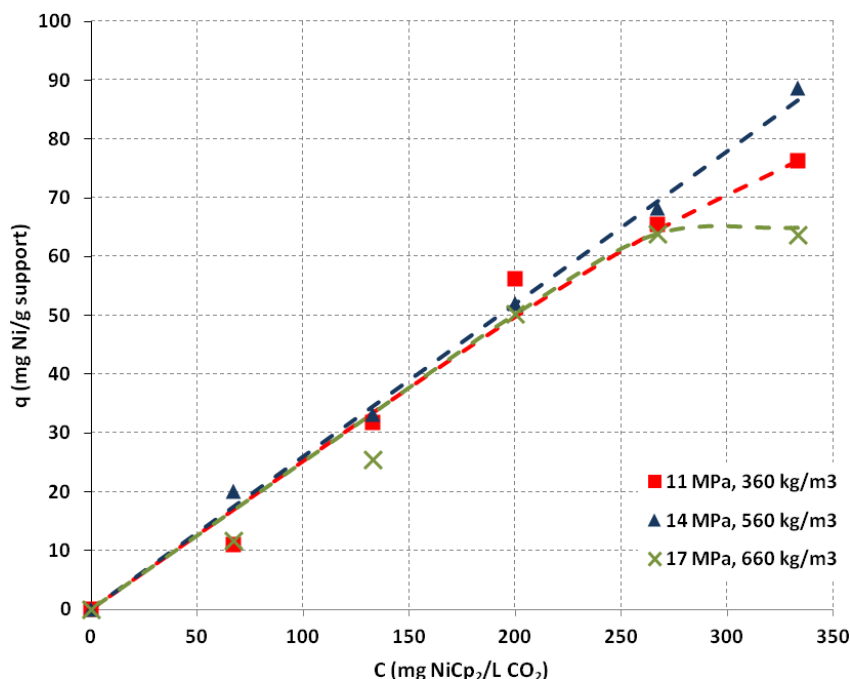


**Figura 6.** Datos experimentales (símbolos) y ajuste provisto por Toth (líneas) para la isoterma de adsorción de NiCp<sub>2</sub> sobre MCM-48 a 70 °C y: (■) 11 MPa; (▲) 14 MPa; (x) 17 MPa.

Los análisis cinéticos y estudios sobre el mecanismo de adsorción demostraron que este proceso requería de tiempos superiores a 10 horas para alcanzar el equilibrio debido a limitaciones difusionales; corroborado por los modelos de difusión en película e intraparticular, donde se resolvió que el transporte externo era la etapa limitante del proceso. Por todo ello, se decidió utilizar el mismo procedimiento de síntesis de deposición reactiva con fluidos supercríticos para la preparación de catalizadores de Ni/MCM-48.

Las muestras obtenidas con cargas entre 2-5% fueron caracterizadas, revelando la existencia de óxidos de níquel homogéneamente distribuidos y fuertemente anclados sobre la superficie del soporte con áreas BET mayores a 1000 m<sup>2</sup>/g. El uso de esta técnica no modifica la superficie del soporte, a diferencia de otros métodos de preparación convencionales donde se pudo observar irregularidades en su estructura y colapso de poros a través de las imágenes de microscopía.

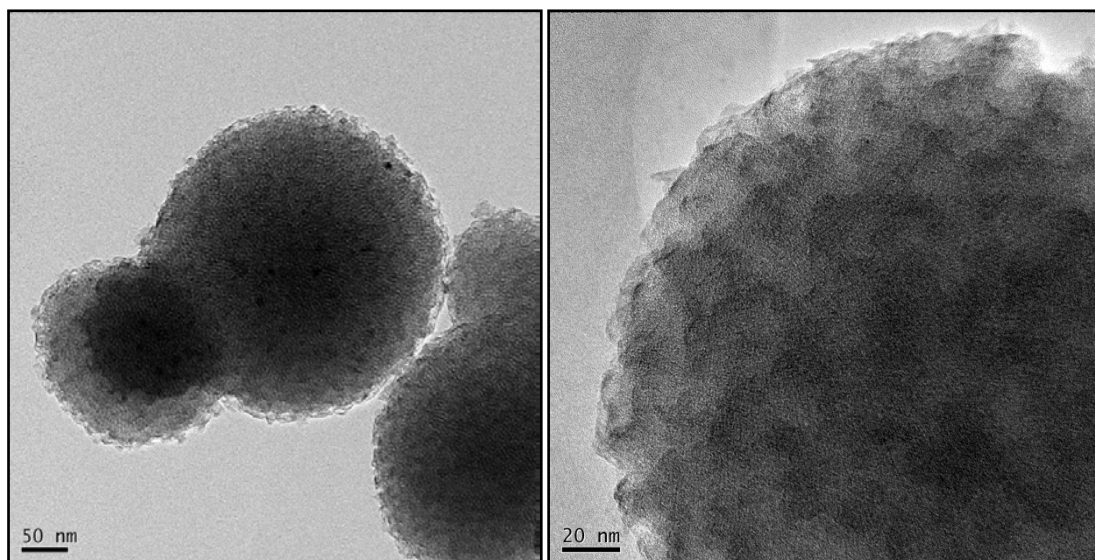


**Figura 7.** Imágenes TEM de los catalizadores de Ni/MCM-48 preparados por síntesis directa: detalle de la irregularidad de su superficie rota y colapso de poros

La actividad de los catalizadores de Ni/MCM-48 fue probada en la reacción de producción de sorbitol a partir de glucosa. Las muestras preparadas por supercrítico alcanzaron conversiones del 6%, con selectividades superiores al 90% y rendimientos alrededor del 5%; valores similares a los catalizadores sintetizados por impregnación húmeda y sustancialmente mejores a los datos obtenidos por los catalizadores de síntesis directa.

Como conclusión, tanto en el primer caso de estudio sobre cobalto donde la adsorción era prácticamente inexistente, y este último sobre níquel cuyo proceso es muy lento, el método de síntesis por deposición reactiva en fluidos supercrítico ha demostrado ser una técnica viable para la preparación de catalizadores.

Por último, en el **Capítulo 4**, se ha desarrollado un proceso de síntesis en continuo basado en la tecnología de deposición en fluidos supercrítico. Con este propósito, era necesario seleccionar un sistema metal-soporte adecuado que permitiera realizar un estudio desde el principio (solubilidad, adsorción y cinética). Tras una búsqueda bibliográfica y debido a sus posibles aplicaciones incluso con bajas cargas, se decidió preparar catalizadores de rutenio. Para ello se escogió rutenoceno ( $\text{RuCp}_2$ ) como precursor organometálico, y probar sobre dos soportes distintos: uno mesoporo (MCM-48) y otro microporo (carbón activo).

En primer lugar, debido a que éste precursor posee una mayor estabilidad, se determinó su solubilidad en CO<sub>2</sub> supercrítico a 60 °C por medio del *cloud point* en una celda visual en la Universidad de Koç durante una estancia en Estambul (Turquía), bajo la supervisión del Prof. Dr. Can Erkey. Los resultados obtenidos fueron consistentes con los reportados en bibliografía para este tipo de compuestos, y ajustados con éxito mediante una ecuación empírica (Chrastil) y una ecuación de estado (Peng-Robinson).

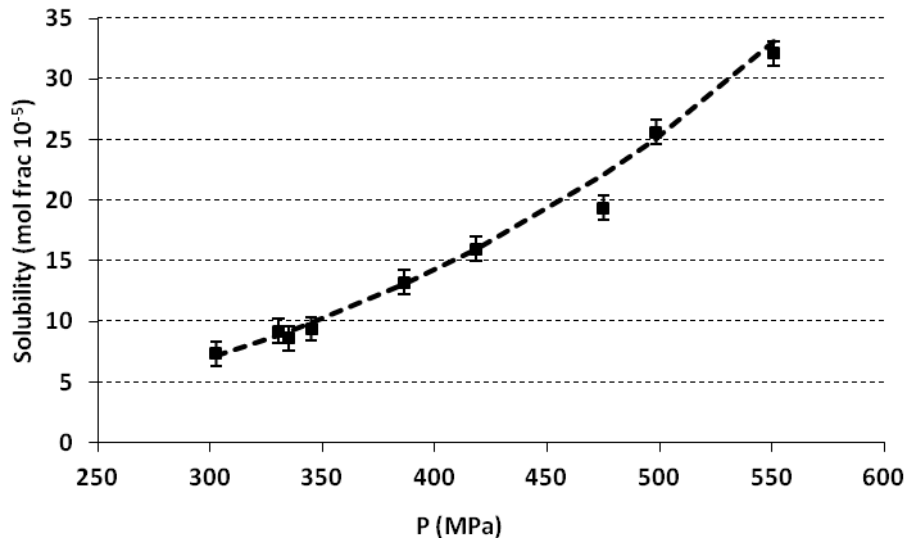


**Figura 8.** Datos experimentales y ajuste dado por Peng-Robinson

Tras esto, se determinaron las isotermas de adsorción sobre los soportes mencionados a 60 °C y distintas presiones (9, 11, 14, 17 y 20 MPa) con el fin de encontrar las condiciones óptimas para el proceso en continuo. En este caso las isotermas revelaron un comportamiento de adsorción en monocapa, perteneciente a isotermas de tipo I, favorables para nuestro propósito a presiones bajas.

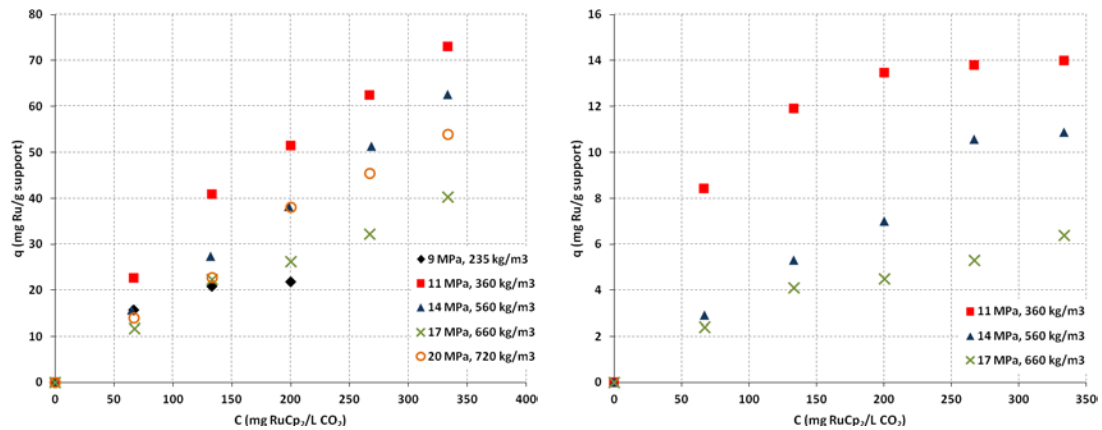


**Figura 9.** Isotermas de adsorción de RuCp<sub>2</sub> sobre carbón activo y MCM-48 a 60 °C y distintas presiones

De igual forma que en el estudio con níquel, los datos experimentales fueron ajustados, siendo en este caso los modelos de tres parámetros como Redlich-Peterson o BET los que proveían el mejor ajuste.

El análisis cinético y determinación del mecanismo de adsorción mostraron comportamientos diferentes para ambos soportes, lo que sería después clave a la hora de llevar el proceso en continuo. La adsorción sobre carbón activo resultó ser similar al caso de níquel sobre MCM-48, con una cinética lenta (superior a 10 horas) y un mecanismo complejo con varias etapas involucradas, principalmente controlado por el transporte externo, obteniendo un valor de carga en el equilibrio de 80 mg/g. Sin embargo, la adsorción de rutenio sobre MCM-48 alcanzó un valor mucho más bajo, próximo a 15 mg/g, pero con una cinética más corta (4 horas), siendo gobernada por la difusión dentro del poro.

Gracias a esta información, se diseñaron una serie de experimentos para la preparación de catalizadores de rutenio en continuo, a 60 °C y 11 MPa, con distintos tiempos (1, 2, 3 y 4 horas) y varios flujos de CO<sub>2</sub> (15, 30 y 45 g/h).

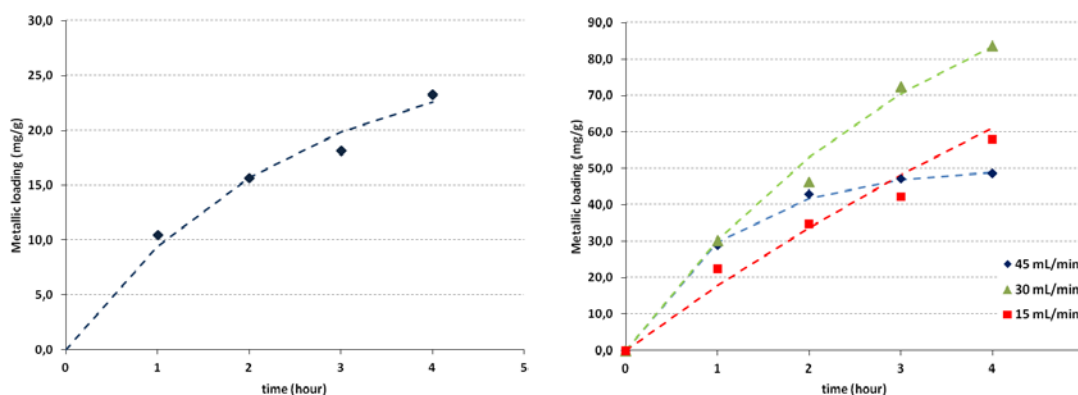


**Figura 10.** Ajustes (línea de puntos) para la adsorción de RuCp<sub>2</sub> sobre MCM-48 y carbón activo a 60°C y 11 MPa en un proceso en continuo a distintos flujos de CO<sub>2</sub>: (◆) 45 g/h; (▲) 30 g/h; (■) 15 g/h

Los catalizadores preparados fueron caracterizados y probados en la hidrólisis de celobiosa para la producción de glucosa. Los catalizadores de Ru/MCM-48 preparados por supercrítico con una carga metálica del 4% fueron los que mostraron el mejor resultado, mejorando el rendimiento de la reacción de un 18% sin catalizar a un 48%, con una selectividad hacia glucosa cercana al 90%. Por otra parte, los experimentos a diferentes cargas revelaron que incrementar la carga metálica por encima de su valor de monocapa produce un descenso en el rendimiento de la reacción debido a un efecto pantalla, impidiendo el contacto con todos los centros activos del catalizador.

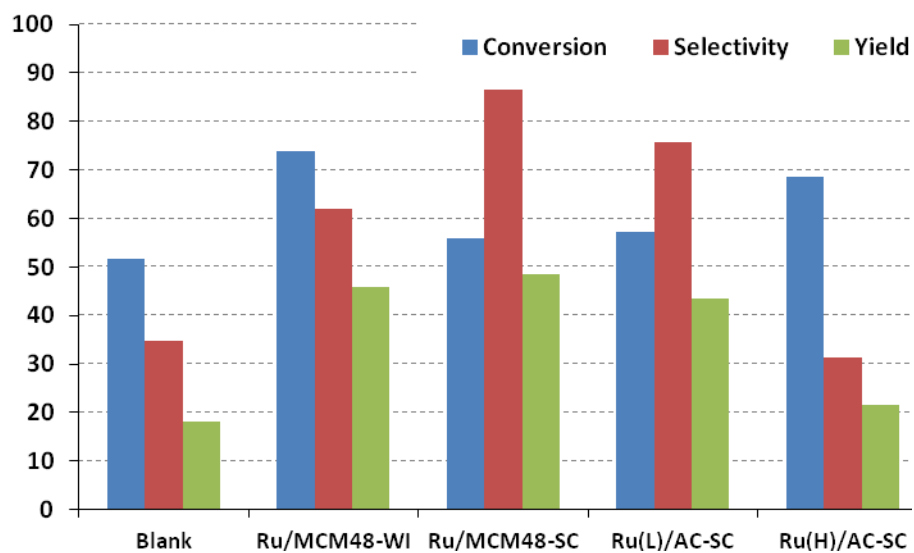


**Figura 11.** Conversión, selectividad a glucosa y rendimiento para diferentes catalizadores de rutenio influencia del soporte, técnica de síntesis y carga metálica

## Conclusiones

Teniendo en cuenta los objetivos marcados al principio de esta tesis, durante el transcurso de la misma se han ido completando tal y como se indica a continuación.

- Catalizadores de Co/MCM-41 y Ni/MCM-48 han sido preparados por medio de la deposición reactiva en fluidos supercríticos (SCFRD), con cargas metálicas de hasta 15% y 5% respectivamente.
- Catalizadores de Ru/MCM-48 y Ru/AC han sido preparados en un proceso en continuo basado en la deposición en fluidos supercríticos (SCFD) con cargas metálicas de 4% y 8%.
- La solubilidad del precursor de  $\text{RuCp}_2$  ha sido determinada a 60 °C y diferentes presiones, siendo posteriormente ajustada por una ecuación empírica (Chrastil) y una ecuación de estado (Peng-Robinson).
- Las isotermas de adsorción de todos los sistemas adsorbato-adsorbente presentados en esta tesis han sido determinados, mostrando comportamientos completamente distintos los unos de los otros, y correlacionados por medio de múltiples modelos (Langmuir, Freundlich, Redlich-Peterson, Toth y BET). Además, tanto su cinética como su mecanismo de adsorción han sido ampliamente estudiados con el objetivo de proponer un tiempo eficiente de operación e identificar la etapa controlante del proceso.
- El proceso de SCFRD ha sido optimizado para la deposición de cobalto y níquel desde sus respectivos precursores organometálicos (metalocenos), en un proceso en *batch* a 200 °C y 14 MPa con un tiempo de operación de 1 hora, y colocando el precursor y el soporte de manera alterna con el fin de evitar problemas de transferencia de materia dentro del reactor.
- Se ha desarrollado el proceso de síntesis SCFD en continuo para la deposición de rutenio sobre MCM-48 y carbón activo a 60 °C y 11 MPa con distintos flujos de  $\text{CO}_2$  (15, 30 y 45 g/h).
- Todos los catalizadores han sido caracterizados, analizando su carga metálica, morfología, estructura, distribución y tamaño del metal mediante distintas técnicas, tales como FRX, BET, RTP o microscopía entre otros.

- En el caso del estudio de cobalto, la isoterma reveló como la adsorción de  $\text{CoCp}_2$  sobre MCM-41 era prácticamente nula. Sin embargo, esta técnica de síntesis ha demostrado ser perfectamente viable para su síntesis, consiguiendo nanocomposites con carga metálicas cercanas al 6% tras solamente una hora de operación. Este hecho representa una considerable ventaja frente a los métodos convencionales que requieren de tiempos de exposición superiores a uno o dos días. Además, la dispersión del metal obtenida por esta técnica ha sido muy superior a la de otros métodos, en torno al 10% con partículas comprendidas entre 1 y 9 nm.
- La versatilidad de este proceso ha sido comprobado al preparar catalizadores de níquel. En este caso en particular, la dificultad que se presentaba era un mecanismo de adsorción lento gobernado principalmente por el transporte externo, siendo necesario tiempo muy largos para alcanzar el equilibrio (más de 10 horas). Los resultados han demostrado como esta técnica de síntesis también permite la preparación de este tipo de sistemas, obteniendo cargas metálicas entre 2% al 5%, con partículas de níquel homogéneamente distribuidas sobre la superficie del soporte y áreas BET cercanas a  $1000 \text{ m}^2/\text{g}$ .
- El uso de SCFRD permite obtener altas cargas metálicas por medio de cargas consecutivas, probándose en la síntesis de catalizadores de cobalto (6, 14 y 17%) y níquel (2, 4 y 5%).
- Otro factor importante que debería ser remarcado es que, a pesar de usar altas presiones, esta técnica no modifica la estructura ordenada de los soportes tal y como se demostró en las imágenes de microscopía, a diferencia de otras técnicas convencionales como síntesis directa, que provocó el colapso de los poros.
- Catalizadores de rutenio han sido satisfactoriamente preparados por medio de un proceso en continuo basado en la deposición supercrítica sobre dos soportes con distinto comportamiento (MCM-48 y carbón activo). El análisis de sus mecanismos de adsorción revelaron que ambos sistemas presentan complejos mecanismo donde hay distintas etapas involucradas. En el caso de la adsorción sobre carbón activo, el transporte externo es la etapa controlante; mientras que sobre MCM-48, la difusión de poro es quien gobierna el proceso. Sin embargo, esta diferencia no ha presentado ningún problema, ya que pueden resolverse las limitaciones ocasionadas por la difusión de los reactivos disminuyendo el flujo

de CO<sub>2</sub>. Esto representa una enorme ventaja comparado a los procesos en *batch* desde un punto de vista económico, lo que además muestra su alto potencial comercial y viabilidad industrial.

- Los catalizadores de Co/MCM-41 han sido evaluados en la gasificación de celulosa, obteniendo una selectividad de hidrógeno cercana al 30% como resultado de favorecer la producción de productos líquidos intermedios, demostrándose esta teoría por medio del ajuste realizado a través del modelo de tres reacciones propuesto en este trabajo.
- Los catalizadores de Ni/MCM-48 fueron probados en la conversión selectiva de glucosa hacia sorbitol, alcanzando conversiones cercanas al 6%, selectividades de hasta 90% y un rendimiento total del 5%, valores muy similares a los obtenidos por catalizadores preparados por métodos convencionales.
- La actividad de los catalizadores de rutenio han sido testados en la hidrólisis de celobiosa para la producción de glucosa. En este caso, el mejor resultado ha sido obtenido por los catalizadores de Ru/MCM-48 sintetizados por medio del proceso en continuo supercrítico, mejorando el rendimiento del proceso desde un 18% sin catalizar hasta un 48%, y selectividades del 90%.

